Optical Diagnostics and Particulate Emissions Analysis of Hydrogen-Hydrocarbon Combustion

Huayong Zhao

St. Catherine's College

A thesis submitted in partial fulfilment of the requirements for the degree of Doctor of Philosophy

Department of Engineering Science

University of Oxford

Trinity Term 2012

Optical Diagnostics and Particulate Emissions Analysis of Hydrogen -Hydrocarbon Combustion

Huayong Zhao
St. Catherine's College, Oxford

Doctor of Philosophy
Department of Engineering Science

A thesis submitted in partial fulfilment of the requirements for the degree of Doctor of Philosophy at the University of Oxford, Trinity Term 2012

Abstract

With the depletion of hydrocarbon fuels, the hydrogen-hydrocarbon combustion system provides a good solution for the transition period from a hydrocarbon-based energy system to a hydrogen-based energy system because of its desirable combustion characteristics and the low level of modification to current combustion systems. Though extensive research has been carried out to investigate the combustion process of hydrogen-hydrocarbon fuels, no experiments have been reported to study the Particulate Matter (PM) formations in hydrogen-hydrocarbon combustion systems.

To measure the PM concentrations in a laminar diffusion flame, a new optical diagnostic technique, called Cone-Beam Tomographic Three Colour Spectrometry (CBT-TCS) has been developed to measure the spatially distributed temperature, soot diameter and soot volume fraction. This technique is based on the principle of three colour pyrometry, but uses a more rigorous light scattering model to calculate the soot diameter and soot volume fraction. The cone beam tomography technique has also been used to reconstruct the 3D property fields from the 2D flame images. The detailed theoretical principles, the experimental setup, the optical considerations, the reconstruction algorithm and the sensitivity analysis are all introduced.

The CBT-TCS technique has been successfully applied to several laminar diffusion flames to study the PM formation. The temperature and soot volume fracction profiles measured by CBT-TCS for a ethylene laminar diffusion flame are consistent with the data reported by Snelling et al. [77]. The helium-ethylene-air flame tests show that adding helium reduces the PM formation (due to the dilution effect). The hydrogen-ethylene-air flame tests show that adding hydrogen is more effective in reducing the PM formation due to the combined effect of dilution and direct chemical reaction. A PM sampling system has also been developed to verify the PM size distributions measured by CBT-TCS. The comparison results show that the CBT-TCS tends to overestimate the particle size.

Several optical engine experiments have also been undertaken to investigate the effect of adding hydrogen on the PM emissions from a Gasoline Direct Injection (GDI) engine. The hydrogen-ethylene engine tests show that adding hydrogen can reduce the PM emissions without sacrificing the power output. The hydrogen-base fuel (65% isooctane and 35% toluene) tests show that adding hydrogen can improve the combustion stability and reduce the PM emissions, especially at low load. Adding 5% stoichiometric of hydrogen can reduce the total PM number concentration by 90% for a stoichiometric mixture and 97% for richer mixture at low load. At high load, adding 10% stoichiometric of hydrogen can also reduce the total PM number concentration by 85% for richer mixture but has little effect upon the stoichiometric mixture.

Acknowledgements

My foremost thanks go to my supervisor, Prof. Richard Stone, not only for his patient supervision on my research project and generous sharing of his profound knowledge and rich experience, but also for his help and invaluable advices on my career development.

I would like to thank all my colleagues in my research group, Dr. Ben William, Ben Twiney, Steve Marshall, Longfei Chen, Michael Braisher, Mengchen Hu, Fan Xu, Kun Liang, Felix Leach, Nathan Hinton and Lei Zhou, for their friendly help and support on my research and daily life. My gratitude is also expressed to Prof. Markus Kraft, Dr. Sebastian Mosbach, Laurence McGlashan and Anthony Knobel in the Computational Modelling Group in Cambridge for their modelling work and constructive suggestions for my research.

I also want to thank all my dear friends I have met in oxford these years. You have made this otherwise lonesome journey one of the sweetest and memorable experiences in my life.

Finally, my most sincere gratitude is for my family. Their endless support and encouragement has led to my progress so far.

Contents

List of Figures

List of Tables

Nomenclature

Acronyms

2D	2-Dimensional
3D	3-Dimensional
atdc	after top dead centre
ATR	Auto-Thermal Reforming
btdc	before top dead centre
CARS	Coherent Anti-Stoke Raman Spectroscopy
CBT-TCS	Cone Beam Tomographic Three Colour Spectrometry
CFA	Colour Filter Array
CNC	Condensation Nuclei Counter
CoBRA	Combustion Burn Rate Analysis
COV	Coefficient of Variation
CRDS	Cavity Ringdown Spectrometry
CT	Computational Tomography
DAQ	Data Acquisition
DFT	Discrete Fourier Transform

DFWM	Degenerate Four Wave Mixing
DMA	Differential Mobility Analyzer
DMS	Differential Mobility Spectrometer
DR	Downsampling Ratio
EGR	Exhaust Gas Recirculation
ETCS	Engine Timing Control System
EVC	Exhaust Valve Closure
EVO	Exhaust Valve Opening
FBP	Filtered Backprojection
FFT	Fast Fourier Transform
FT	Fourier Transform
GDI	Gasoline Direct Injection
GUI	Graphical User Interface
HACA	Hydrogen Abstraction and Carbon Addition
HDAQ	High speed Data Acquisition
IFFT	Inverse Fast Fourier Transform
IMEPn	Net Indicated Mean Effective Pressure
IVC	Intake Valve Closure
IVO	Intake Valve Opening
LDAQ	Low speed Data Acquisition
LDV	Laser Doppler Velocimetry

LIBS	Laser Induced Breakdown Spectroscopy
LIGS	Laser Induced thermal Grating Spectroscopy
LII	Laser Induced Incandescence
LOSA	Line-of-Sight Light Attenuation
MBT	Minimum (ignition) advance for Best Torque
MFC	Mass Flow Controller
NMHC	Non-Methane Hydrocarbon
OHD-RIKES	Optically Heterodyned Raman Induced Kerr Effect Spectroscopy
PAH	Polycyclic Aromatic Hydrocarbon
PARS	Photoacoustic Raman Spectroscopy
PIV	Particle Imaging Velocimetry
PM	Particulate Matter
PMRF	Particulate Matter Reduction Factor
REMPI	Resonance-Enhanced Multi-Photon Ionization
RIKES	Raman Induced Kerr Effect Spectroscopy
SAD	Source-to-Axis Distance
SMPS	Scanning Mobility Particle Sizer
SR	Steam Reforming
SRGS	Stimulated Raman Gain Spectroscopy
TCP	Three Colour Pyrometry
TEM	Transmission Electron Microscopy

TGA	Thermogravimetric Analyzer
THC	Total Hydrocarbon
WALS	Wide Angle Light Scattering
ZP	Zero Padding

Roman

A	Area
C	Cross section
c	Speed of light
D	Logarithmic derivative / Diamter
d	Particle diameter
E	Electrical field
f	Soot volume fraction / focus length
H	Magnetic field/ window function
h	Planck's constant
I	Radiance
K	Absorption coefficient per unit flame thickness
k	Boltzmann constant / wave number / imaginary part of the complex refractive index/Agglomeration coefficient
L	Optical path thickness
M	Magnification factor
m	Complex refractive index

m	Mass
N	Number of projections
n	Real part of the complex refractive index
P	Projection data in parrallel beam tomography
Q	Filtered projection/ Efficiency factor in light scattering phenomena
R	Projection data in equally spaced fan beam tomography
r	Radius
S	Fourier transform of projection data
s	Sensitivity factor of the camera sensor
T	Transmission efficiency
V	Voltage
x	Size parameter/Percent of stoichiometric

Greek

α	Fraction of available reactive surface / constant in the Hottel and Broughton correlation
β	Tilted angle of the fan beam
χ	Number density of surface sites
δ	Dirac delta function
η	Efficiency
Γ	Half the beam-width cone angle
γ	Angle of elevation of fan beam in the cone beam tomography

λ	Wavelength / equivalence ratio
μ	Permeability
ω	Frequency
ε	Emissivity/ permittivity

Superscripts

M	Mie theory
P	Rayleigh-Gans theory with Penndorf extension
R	Rayleigh-Gans theory

Subscripts

β	Tilted angle of the fan beam
λ	Wavelength
θ	Gantry angle in tomography
i	Incident
abs	Absorption
ext	Extinction
max	Maximum
sca	Scattering

Chapter 1

Background

1.1 Introduction

Over the past few decades, the world has been at a transition in the use of energy because of two main challenges: the impending depletion of hydrocarbon fuels and the global climate changes due to the combustion of hydrocarbons. These challenges are further exaggerated by the increasing global energy demand. Hydrogen, as a sustainable and clean energy resource, is widely considered as a strong candidate to be the fuel of the future. However, hydrogen-based energy systems still need to overcome two main barriers before their wide applications: large-scale infrastructures to provide seamless transitions from production to storage to use, and its economic competitiveness. Since both barriers take a long time to overcome, a hybrid hydrogen-hydrocarbon combustion system can be a useful option during the transition period because of its attractive combustion characteristics and the low level of modifications needed to current combustion system. In this chapter, the characteristics of hydrogen-hydrocarbon combustion systems will be reviewed.

One of the most widely encountered combustion system is the internal combustion engine. From its first invention, the internal combustion engine has brought about a very influential revolution in transportation. It creates an unbelievable freedom of movement, and alters our

very perception of time and distance. The spray-guided Gasoline Direct Injection (GDI) engine, as the most recent generation of engine, has the potential to achieve a much better fuel economy (improved by up to 25%) without sacrificing power output. However, it produces much more Particulate Matter (PM) emissions compared to the conventional port fuel injection engine. PM is essentially soot (carbon) with an adsorbed layer of hydrocarbons. They are very small (10-1000 nm) so are not visible, but can have a high deposition efficiency in the human respiratory system, especially for those ultra-fine particles with large surface-to-volume ratios. More and more recent studies indicate that small PM from engines is of great hazard to human health [63]. PM has also been linked to global warming [34]. The new European Emission Standard also sets restrictions on PM emissions from GDI engines for the first time in 2011, as shown in Table 1.1.

Table 1.1: EU light duty tailpipe emissions requirements for gasoline passenger cars (EU Regulation EC/715/2007)

Effective Timing	CO (g/km)	THC[1] (mg/km)	NMHC[2] (mg/km)	NOx (mg/km)	PM Mass (mg/km)	PM Number (1/km)
EU3: 01/2000	2.30	200	n/a	150	n/a	n/a
EU4: 01/2005	1.00	100	n/a	80	n/a	n/a
EU5: 09/2009	1.00	100	68	60	n/a	n/a
EU5b: 10/2011	1.00	100	68	60	5.0/4.5[3]	n/a
EU6: 09/2014	1.00	100	68	60	5.0/4.5	6×10^{12}/km;6×10^{11}/km[4]

From diesel engine researches, it is known that adding hydrogen can reduce the PM emissions, but no such test has been undertaken with GDI engines. The characteristics of hydrogen-enhanced GDI engines will also be reviewed in this chapter.

Also will be reviewed in this chapter are various optical diagnostic techniques. Research in

[1] Total Hydrocarbon
[2] Non Methane Hydrocarbon
[3] for direct injection engine only
[4] effective 1 January 2012, mandates a particle limit of 6×10^{12}/km reducing to 6×10^{11}/km within 3 years

Table 1.2: Comparison between the properties of hydrogen, gasoline (iso-octane), and methane[19]

property	Hydrogen	Gasoline (Iso-octane)	Methane
Chemical formula	H_2	(C_8H_{18})	CH_4
Minimum ignition energy (MJ)	0.02	0.24	0.29
Laminar burning velocity (cm/s)	~237	~41.5	~42
Diffusion coefficient (cm^2/s)	0.61	0.16	0.05
Quenching distance (cm)	0.06	0.2	0.2
Flammability limit in air (euqivalence ratio)	0.1-7.14	0.68-3.95	0.5-1.42
Lower calorific value (MJ/kg)	120	(44)	50.4
Adiabatic flame temperature in air at stoichiometric (K)	2318	2148	2223
Net energy density (MJ/kg of a stoichiometric mixture)	17.8	20.97	18.98

PM emissions is very challenging both in terms of its measurement and modelling. Since the PM formation is very sensitive to the sampling conditions, such as the dilution ratio and temperatures, optical diagnostic techniques are advantageous over the traditional sampling-based measurements because they can be applied *in situ* and are non-intrusive. Moreover, various optical diagnostic techniques can be used in a single run to measure important parameters (such as temperature, soot volume fraction and number density) with much better temporal and spatial resolution than sampling-based techniques.

1.2 Characteristics of hydrogen-hydrocarbon combustion

1.2.1 Properties of hydrogen

As the most abundant chemical element in the universe, hydrogen has many attractive properties compared to other hydrocarbons, as in table 1.2.

Hydrogen has a lower minimum ignition energy compared to other hydrocarbons, which ensures more stable ignition and eases the cold start engine operation at the cost of making

the combustion system more vulnerable to abnormal combustions. Its higher laminar burning velocity (around five times faster than that of gasoline) is expected to increase the burn rate, which is beneficial for increasing the combustion efficiency and stability. The higher diffusion coefficient of hydrogen can also contribute to improve the engine efficiency and produce less soot and unburned hydrocarbon emissions by creating a more homogeneous mixture. Hydrogen also has a smaller quenching distance compared to gasoline, which means the flame can travel further into crevices to ensure a more complete combustion. Moreover, the flammability limit of hydrocarbon fuels can be extended by adding hydrogen. However, the lower net energy density of a stoichiometric hydrogen mixture will reduce the power output. Adding hydrogen also tends to produce more NOx emissions because of its high adiabatic flame temperature. However, a higher percent of Exhaust Gas Recirculation (EGR) can be used when adding hydrogen without sacrificing the combustion stability, which can reduce the flame temperature and the NOx emissions.

1.2.2 Combustion and emissions

The hydrogen flame, either in air or oxygen, usually exhibits little or no visible radiation. In a static hydrogen combustion system, no reaction occurs below 675 K, but explosions caused by the chain branching reactions occurs spontaneously above 850 K for the H_2-O_2combustion system. For the H_2-air combustion system, the nitrogen molecules will act as third body molecules to take the energy away from the radicals via radicals recombination reaction, so higher temperature is needed for explosions. Because the chain branching of H_2-O_2 plays very important role in the oxidation of hydrocarbons, the main chain branching reactions are summarized as follows:

$$H + O_2 \longrightarrow O + OH \tag{1.1}$$

$$O + H_2 \longrightarrow H + OH \tag{1.2}$$

$$H_2 + OH \longrightarrow H_2O + H \tag{1.3}$$

$$O + H_2O \longrightarrow OH + OH \tag{1.4}$$

Since radicals react very rapidly, the reverse reactions in the chain branching of the H_2-O_2 system can be neglected [30]. The presence of hydrocarbons usually slows down the combustion of hydrogen because the reaction rates between most hydrocarbon species and H atoms are considerably larger than reaction (1.1).

The oxidation of hydrocarbons is tremendously complicated and their detailed chemical kinetics are still not fully understood. It is generally accepted that the oxidation of hydrocarbons is initiated by collisions between the hydrocarbon molecules and other third body molecules (M) at moderate temperature via reaction (1.5):

$$RH + M \longrightarrow R + H + M \tag{1.5}$$

But reaction (1.6) becomes important at high temperature.

$$RH + O_2 \longrightarrow R + HO_2 \tag{1.6}$$

Then the main oxidation process is started by the constant attack of various radicals (X) on the fuel molecules to decompose the hydrocarbon molecules into lower order hydrocarbons:

$$RH + X \longrightarrow R + XH \tag{1.7}$$

The formation of the radical (X) pools should take into account the whole H_2-O_2 chain branching reactions. Then for different types of hydrocarbons, different chain branching reactions start to take place to finally decompose the hydrocarbons into CO, H_2, H_2O. For heavy hydrocarbon molecules (more than 5 carbon atoms), the isomerization reactions becomes important:

$$RH(+x) \longrightarrow R(+O_2) \longrightarrow RO_2 \longrightarrow ROOH(+O_2) \longrightarrow \text{chain branching} \tag{1.8}$$

This is followed by the oxidation of the CO and H_2 into CO_2 and H_2O. The oxidation of

CO into CO_2 is the main contributor to the heat release during the whole process of the oxidation of hydrocarbons because it is highly exothermic. The dominant path during the oxidation of CO is:

$$CO + OH \longrightarrow CO_2 + H \tag{1.9}$$

However, the reactions between the hydrocarbons and OH are much faster than reaction (1.9). Therefore, the main oxidation process of CO is usually after the consumption of original and intermediate hydrocarbons. In practical combustion systems, reaction (1.9) is not fast enough to fully oxidize the CO into CO_2.

When hydrogen is added into hydrocarbon fuels, the combustion will become faster because the decomposition of the hydrogen molecules and the chain branching reactions between the extra H_2 and O_2 increase the radical (X) concentrations, which speed up the decomposition of hydrocarbons due to reaction (1.7). This is verified by the experiments and simulations done by Choudhuri et al. [14]. Choudhuri et al. [12] also found that the height of either the laminar diffusion flame or the turbulent flame of hydrocarbons became shorter when blending hydrogen and the laminar diffusion flame heights are well predicted by the correlation suggested by Roper [67]. This is because the increased burn rate and flame temperature speed up the oxidation of hydrocarbons so that the flame is depleted before it can reach a higher position. The increase in the flame temperature is caused by the reduced heat radiation loss from soot particles and CO.

The main emissions from the combustion of hydrocarbon fuels are nitric oxide/ nitrogen oxides (NO/NOx), CO/CO_2, and the PM.

NO/NOx Though the nitrogen oxides are a minor species in the emissions, they are important due to their contributions to air pollution. NO_2 and volatile organic compounds will react in the presence of sunlight to form a photochemical smog. Nitrogen oxides are also known as a major contributor to the formation of acid rain when they are combined with atmospheric moisture [1]. Most NOx emissions from combustion of hydrocarbons are NO and its formation is mainly through three chemical paths. The first one is called Thermal

or Zeldovich mechanism [91]. This mechanism is closely related to the temperature and dominates over a wide range of equivalence ratio when the flame temperature is higher than 1800K. It consists of two chain reactions:

$$O + N_2 \longleftrightarrow NO + N \tag{1.10}$$

$$N + O_2 \longleftrightarrow NO + O \tag{1.11}$$

It is extended by adding another reaction [46]:

$$N + OH \longleftrightarrow NO + H \tag{1.12}$$

The rates of these reactions are much slower than the hydrocarbon oxidation reactions, so it is usually assumed that the concentration of CO, O, CO_2, O_2, OH, H, H_2O and N_2 are in their equilibrium values at the local pressure and equilibrium temperature. Under this N steady state assumption, the initial formation of NO is related to temperature by [36]:

$$\frac{d[NO]}{dt} = \frac{6 * 10^{16}}{T^{1/2}} \exp(\frac{-69090}{T})[O_2]_e^{1/2}[N_2]_e \tag{1.13}$$

The second mechanism for nitric oxide formation is called the N_2O-intermediate mechanism. This one is important in fuel-lean ($\lambda > 1.25$), and low temperature conditions. The chemical reactions suggested by this mechanism are:

$$O + N_2 + M \longleftrightarrow N_2O + M \tag{1.14}$$

$$H + N_2O \longleftrightarrow NO + NH \tag{1.15}$$

$$O + N_2O \longleftrightarrow NO + NO \tag{1.16}$$

The last mechanism is the Fenimore mechanism [28]. This mechanism suggests that hydrocarbon radicals react with molecular nitrogen to form amines or cyano compounds. Then, the amines or cyano compounds will be finally converted into NO. This mechanism can be

represented by:

$$CH + N_2 \longleftrightarrow HCN + N \tag{1.17}$$

$$C + N_2 \longleftrightarrow CN + N \tag{1.18}$$

$$N + O_2 \longleftrightarrow NO + O \tag{1.19}$$

When $\lambda > 0.8$,

$$HCN + O \longleftrightarrow HCO + N \tag{1.20}$$

$$NCO + H \longleftrightarrow NH + CO \tag{1.21}$$

$$NH + H \longleftrightarrow N + H_2 \tag{1.22}$$

$$N + OH \longleftrightarrow NO + H \tag{1.23}$$

When $\lambda < 0.8$, other routes open up and the process will be more complex. When this mechanism is coupled with the thermal mechanism, it destroys rather than forms NO by the reverse of the reaction (1.10) [57]. But for fuels containing nitrogen, the nitrogen may rapidly be converted to hydrogen cyanide (HCN) or ammonia (NH_3) which is oxidized by similar reactions to the Fenimore mechanism.

The main chemical reaction to form NO_2 is:

$$NO + HO_2 \longrightarrow NO_2 + OH \tag{1.24}$$

The HO_2 radical is formed by a three-body reaction:

$$H + O_2 + M \longleftrightarrow HO_2 + M \tag{1.25}$$

This reaction can occur in relatively low-temperature regions. At high temperatures, the destruction reactions of NO_2 are very active. Therefore, unless the NO_2 is quenched by mixing with cooler fluid shortly after its formation, the emission of NO_2 is very low, typically less than 2% of the NOx [37]. The experiments carried out by Choudhuri et al. [12] [13] found that the NOx emissions increased as more hydrogen is added into the hydrocarbon fuels.

This is mainly because the higher flame temperature increases the formation rate of NO through the reaction suggested by the Zeldovich mechanism.

Carbon monoxide/ carbon dioxide The CO/CO_2 emissions are directly related to the available carbon atoms. When blending hydrogen, the available carbon atoms are reduced so that the CO/CO_2 emissions will also reduce. This effect has been verified by many researchers [12].

Particulate Matter (PM) The PM emissions have received increasing attention due to their hazardous impact on human health. The pathogenesis of asthma in relation to PM is reported by Pandya et al. [60] Moreover, PM may cause heart attacks or strokes [22]. The PM can be classified into three modes according to their size: nucleation mode (< 40 nm), accumulation mode (< 1000 nm), and the coarse mode (> 1000 nm). Most nucleation mode particles are often described as volatile particles. But some researchers indicated they can also be solid particles [25]. The accumulation mode particles are aggregations of spherules (also called primary particles) so their sizes depend on how many spherules they contain. The coarse mode particles usually consist of a solid core and an outer layer of volatile materials. The PM formed during combustion of hydrocarbons are mostly carbonaceous particles, and are widely referred to as soots. Though their detailed formation mechanisms are still under debate, it is generally accepted that the soot particles are formed through interception, agglomeration and simultaneous surface growth. The interception process is initiated by the pyrolysis process, which includes the fragmentation of hydrocarbon molecules, their polymerisation to form larger particles and dehydrogenation to form particles with a low H/C ratio. These reactions will proceed to form soot precursors in high temperature and oxygen depleted regions. The most important precursor molecules are acetylene (C_2H_2) and Polycyclic Aromatic Hydrocarbons (PAH). There are two different paths to form the soot nuclei. The aromatic compounds can form the soot particles in a direct path and the aliphatic compounds will form the soot particles by an indirect path.

The aliphatic compounds need to form the fundamental rings first by cyclisation:

$$C_4H_3 + C_2H_2 \longrightarrow C_6H_5 \tag{1.26}$$

$$C_4H_5 + C_2H_2 \longrightarrow C_6H_6 + H \tag{1.27}$$

Or propargyl recombination reaction:

$$C_3H_3 + C_3H_3 \longrightarrow C_6H_6 \tag{1.28}$$

$$C_3H_3 + C_3H_3 \longrightarrow C_6H_5 + H \tag{1.29}$$

Then both the aromatic compounds and the fundamental rings will proceed to form larger PAH by a widely-accepted mechanism: Hydrogen Abstraction and Carbon Addition (HACA[29]). This mechanism can be represented by the following reactions:

$$A_i + H \longrightarrow A_1^{\cdot} + H_2 \tag{1.30}$$

$$A_1^{\cdot} + C_2H_2 \longrightarrow A_1C_2H_2 \tag{1.31}$$

$$A_1C_2H_2 + H \longrightarrow A_1C_2H + H_2 \tag{1.32}$$

$$A_1C_2H + C_2H_2 \longrightarrow A_{i+1} \tag{1.33}$$

where A_i is the ring-structure aromatics and i is the number of fused rings, and $A_1^{\cdot}$ is the phenyl radical (C_6H_5). It is possible that the largest PAH molecules become unstable in the gas phase due to their size and will eventually condense and solidify into soot nuclei [25]. After the soot nuclei are formed, they will go through the process of agglomeration and surface growth concurrently. The surface growth is a chemical process and one possible mechanism [6], which is very similar to HACA mechanism is:

$$(C_{soot}-H) + H \longleftrightarrow C^*_{soot} + H_2 \tag{1.34}$$

$$(C_{soot}-H) + OH \longleftrightarrow C^*_{soot} + H_2O \tag{1.35}$$

$$C^*_{soot} + H \longrightarrow (C^*_{soot}-H) \tag{1.36}$$

$$C^*_{soot} + C_2H_2 \longrightarrow (C^*_{soot+2}-H) + H \tag{1.37}$$

The soot model used by Guo et al. [32] suggests a correlation to calculate the surface growth rate:

$$k_{s.g.} = k_{C_2H_2}[C_2H_2]\alpha\chi_{CS}A_s/N_A \tag{1.38}$$

where $k_{C_2H_2}$ is the per-site rate coefficient for acetylene addition, $[C_2H_2]$ is the mole concentration of acetylene, α is the fraction of available reactive surface, A_s is the particle surface area, N_A is Avogadro's number, and χ_{CS} is the number density of surface sites for acetylene addition. Surface growth is usually considered as the main contributor to the soot particle mass.

The agglomeration is a physical process and it is due to the collisions between soot molecules. The generally accepted correlation to calculate the agglomeration rate is:

$$\frac{dN}{dt} = -k_0N^2 \tag{1.39}$$

where k_0 is the agglomeration coefficient which is dependent on the temperature and surface area of the soot particle.

The effect of adding hydrogen on the soot formation in an ethylene laminar diffusion flame was investigated by Guo et al. [32] by using a detailed soot model. Their simulation results suggest that adding hydrogen reduces the soot formation by both a dilution effect and a direct chemical inhibition effect because the presence of molecular hydrogen reduces the production rate of PAH and also inhibits the particle surface growth process. Whether these simulation results are valid or not will be checked by several groups of laminar diffusion flame tests in this project.

Fig. 1.1: Comparison between the port fuel injection engines and the direct injection engines [88]

1.3 Characteristics of hydrogen-enhanced Gasoline Direct Injection (GDI) engine

1.3.1 Introduction to the GDI engine

Though the first appearance of the Gasoline Direct Injection (GDI) technology can be traced back to 1925 when the Swedish engineer Jonas Hesselman applied it to a petrol and diesel hybrid engine [50], the first large scale application of modern GDI technology in gasoline engines was in 1995. Mitsubishi introduced an in-line 4-cylinder 1.8L engine with a gasoline direct injection system to the Japanese market in 1995, and similar engines were brought to the European market in 1997. Upright inlet ports were used in these engines to produce a reverse tumble air motion to assist the stratified mixture preparation. After that, due to the great potential for better fuel economy and lower CO_2 emissions, the GDI technologies have been widely developed by all mainstream vehicle manufactures and a great number of research groups.

The difference between the port fuel injection system and the direct injection systems is shown in fig. 1.1. Compared to the port fuel injection system, the amount of fuel can be controlled more accurately with direct injection as there is no fuel hang-up in the inlet system, so that a better transient performance can be achieved. In addition, the vaporisation of the fuel spray absorbs thermal energy and reduces the intake charge temperature - the charge cooling effect. This improves the volumetric efficiency due to the increased air density and the knock tolerance so that a more flexible ignition timing or higher compression ratio can be used to increase the engine efficiency and power output. GDI technology can also improve the fuel economy at part-load conditions by using a stratified combustion mode. In this mode, possibly with split injections, the timings of the fuel injection are used to produce an overall lean mixture, but with a richer mixture near the spark plug at ignition,

so as to ensure stable ignition and combustion. As the overall mixture is lean, (leading to relatively low temperature combustion so that the NOx emission and CO_2 emission can be reduced) a better fuel economy can be achieved. There are many different strategies to control the in-cylinder charge motion so as to ensure more stable combustion, such as the wall-guided system, the air guided system, and the spray guided system. The most recent generation of GDI engine uses a spray-guided DI system with scope for multiple injections.

Because of reduced time for mixture preparation, the PM emissions from GDI engines are much higher than from conventional port-fuel injection engines, especially in terms of the number concentration. Research in diesel engines suggests that adding hydrogen can reduce the PM emissions but no similar research has been carried out in GDI engines. In this project, several diffusion flame burner tests and engine tests are used to investigate the effect of adding hydrogen in PM emissions and their underlying mechanisms.

1.3.2 Combustion and emissions

According to laboratory flame tests (reviewed in section 1.2.2), blending hydrogen could speed up combustion and increase flame temperatures. Therefore, blending hydrogen in a gasoline engine is expected to increase its combustion stability and the indicated efficiency.

As for the emissions, the laboratory flame tests suggest that blending hydrogen reduces the CO /CO_2 emissions but increases the NOx emissions. Another pollutant from the engine tailpipe is the Unburned Hydrocarbon (UBHC). As its name suggests, the UBHC is from the incomplete combustion of the fuel. The major sources for their formation include: flame quenching at walls, hydrocarbons trapped into the crevices during the main combustion stage (mainly the crevice regions between the piston, piston rings and cylinder walls), absorption/desorption from oil films and combustion deposits, poor mixture preparation (such as the appearance of fuel droplets, especially during the cold start or transient conditions), and poor combustion quality (such as misfire or the partial burning when the flame propagation rate is too slow or the combustion starts too late). Cheng et al. [11] sketched an

Fig. 1.2: Formation of UBHC in SI engines [11](Fig. 10 in original paper)

overall picture for the formation of UBHC in typical SI engines, which is show in Fig. 1.2. When blending hydrogen, the higher diffusion coefficient of hydrogen helps to produce a more homogeneous mixture, and the smaller quenching distance of hydrogen can lead to a more complete combustion. Both effects are expected to decrease the UBHC emissions. However, the fast burn rate of hydrogen may lead to a lower oxidation temperature, which can lead to a negative impact on the UBHC emissions. Therefore, the UBHC emissions when adding hydrogen may depend on the operating conditions.

The experiments on a DI-SI engine done by Conte and Boulouchos confirm these postulations [17]. They reported a 20% reduction in COV of IMEP (from 13.9% to 11.09%) and 16.5% improvement in indicated efficiency (from 28% to 32.6%) when 17% of hydrogen was blended in the stratified mode, and around a 51% reduction in COV (from 13.9% to 6.75%) and a 28% improvement in indicated efficiency (from 28% to 35.9%) when 27% of hydrogen was blended. In addition, blending 28% of hydrogen in the homogeneous mode reduced the COV by 17.6% (from 2.5% to 2.06%) and improved the indicated efficiency by 7.4% (from 29.6% to 31.8%). But since the COV in the stratified mode is inherently large, this engine may not be optimized for operation in a stratified mode so that the effect of blending hydrogen is particularly significant. Considering that the efficiency for a typical on-board gasoline reformer is around 85-90%, Conte and Boulouchos concluded that the efficiency benefit of blending hydrogen was large enough to compensate for the energy loss in generating the hydrogen on-board. They also attributed the increase in indicated efficiency and combustion stability to the fast burn rate and reduced pumping loss. They reported an increase in NOx emissions. However, by increasing the EGR percentage or delaying the ignition timing, they achieved a lower NOx/IMEP ratio than that for the pure gasoline operation with a normal EGR percentage. The UBHC emissions were reduced in their experiments and they suggested that this was due to the improvement in combustion stability and lower fraction of gasoline when blending with hydrogen.

Andrea et al. [19] studied the combustion characteristics of a hydrogen-blended SI engine

operated at lean conditions. They suggested a critical equivalence ratio (λ = 1.18). When the engine was running richer than this critical equivalence ratio, there was no big difference for both the torque output and burn rate when blending hydrogen. But when the engine was operated leaner than this critical equivalence ratio, both the torque output and the burn rate increased when adding hydrogen. They also attributed these effects to the fast burn rate when blending hydrogen. In addition, the operational equivalence ratio range was extended by blending with hydrogen. However, the gain in efficiency when blending hydrogen in their experiments was smaller than the extra energy required to generate the hydrogen on-board. They also investigated the NO emissions and found that the NO emission increased when blending hydrogen for lean operation but there was no difference for stoichiometric operation.

Several other groups also investigated the effect of adding hydrogen-rich on-board gasoline reforming gases on engine performance. Allgeier et al. [3] used the partial oxidation reformer syngas (21% hydrogen, 24% carbon monoxide, and 55% nitrogen). They reported that the output power was reduced as reformer gases were introduced due to their low energy density. The engine efficiency, on the other hand, was improved due to a lower pumping loss, better scavenging and better combustion stability when adding the reformer gases. They also suggested that the efficiency gain when blending reformer gases was large enough to compensate for the reformer loss if 85% is accepted as the typical efficiency of a gasoline partial oxidation reformer. They also found that a much higher EGR rate (up to 50%) can be used when blending reformer gases and this can reduce the NOx emission level below the sensitivity of the measuring apparatus. The UBHC emissions were also reduced significantly in their experiments. The CO emissions during low load (BMEP < 1.5 bar) and low speed (rpm < 1500) were reduced when blending with the syngas. However, the CO emission was increased for other operation conditions because of the high fraction of CO in the reformer gases. Suzuki and Sakurai [79] investigated the effect of blending hydrogen, steam-reforming (SR) gases, and auto-thermal reforming (ATR) gases on engine performance. They found that the MBT ignition timings were retarded significantly as more hydrogen was blended. In addition, the indicated thermal efficiency was found to be high-

est when blending hydrogen at low load but no big difference was reported when various gaseous fuels were blended at high load.

The effect of blending hydrogen on the knock behaviour was reported by Shinagawa et al. [74]. They found that blending hydrogen could reduce the gap between ignition timings for the MBT point and knocking point, the "knock margin". They also found that the knock behaviour was closely related with the distribution of hydrogen. Knock-free operation was reported when hydrogen was unevenly distributed both near the wall and the spark plug. They attributed these effects to the production of hydroxyl radials when blending hydrogen because these can inhibit the fuel decomposition so as to reduce the tendency for knock.

Though no experimental results can be found on the effect of adding hydrogen on the particulate emissions from GDI engines, the effects on DI diesel engines have been investigated by many research groups. Varde and Frame [84] investigated the smoke emissions from a DI diesel engine when supplying different fractions of hydrogen in the intake manifold. They reported that the optimum hydrogen percentage for smoke reduction to be between 10-15% of the total energy. Up to 50% reduction in smoke levels at part load and 17% reduction at full load were reported. They also reported an increase in NOx emissions. Bose and Maji [8] reported that adding hydrogen increased the brake thermal efficiency by 12.9%, reduced the volumetric efficiency, reduced the smoke level (by 42%), the CO (by 40.5%) and CO2 (by 45.8%) and also the HC emissions (by 57.69%). Saravanan and Nagarajan [70] reported that replacing 90% (by volume) of diesel with hydrogen increased the brake thermal efficiency by 29.1% but it also caused knocking. They believed that 30% of hydrogen gave the best results because it increased the brake thermal efficiency by 27.9% without causing any knocking. They also reported reductions in both smoke and NOx emissions.

PM emissions from engine Besides the carbonaceous PM discussed in the previous section, the PM emissions from engines also include the ash fraction, the organic fraction and sulphate fraction. The ash fraction PM is the smallest proportion. The main sources for ash

PM are lubricant components, airborne inorganic debris, wear metals and the sundry inorganic compounds or elements in the fuel. The ash materials usually go through extremely early gas-to-particle conversion due to their low volatility. This process can be described in three zones: nucleation zone, growth zone and the burn-out zone [25]. The iron oxides are usually regarded as nucleation centres for carbon atoms. Their growth rate depends on the rate of outward diffusion of iron compared with the rate of accretion of carbon, as promoted by iron, and reversed by FeO [66]. Finally, accreted carbon is oxidized in the burn-out zone. The gas-to-particle conversion is essentially completed prior to emission at the tailpipe, but in some instances, separation occurs within the exhaust system between the gas and particulate phases, such as the separation of boron [81]. The organic fraction PM can be classified into two distinct groups according to their formation mechanisms. The first group are called petrogenic, which includes the fuel compounds which successfully escape from the combustion process due to the imperfect charge preparation or wall quenching effect. The other group is pyrogenic, which includes those new-born compounds synthesised from partially broken fuel compounds, especially at low load conditions because the temperature is not high enough for soot-formation [25]. The gas-to-particle conversion for the organic fraction occurs very late in the emission process, either in the exhaust plume or the dilution tunnel. The main sulphur oxide emitted by an engine is SO_2 when there is no catalyst since the thermodynamic equilibrium favours SO_2. However, the presence of an oxidation catalyst promotes the conversion from SO_2 to SO_3. Significant problems are caused by SO_3 because it readily hydrolyses to form sulphuric acid through the reaction:

$$SO_3 + H_2O \longrightarrow H_2SO_4 \tag{1.40}$$

Moreover, the H_2SO_4 will shift the dew point temperature, so that condensation will initiate at a higher temperature. Many studies also indicated that the NO_2 may assist the oxidation of SO_2 to SO_3 via the reaction:

$$SO_2 + NO_2 \longrightarrow SO_3 + NO \tag{1.41}$$

This reaction might well occur on particle surfaces and indirectly encourage the formation of sulphate particulate matter [15].

There is currently no literature found about the effect of adding hydrogen in PM emissions from GDI engines, so a series of experiments have been conducted in this project and the results will be presented in chapter 4.

1.3.3 Sampling-based emissions measurement techniques

NO/NOx The NOx emissions are usually measured by a chemiluminescence analyser. The NO in the exhaust gases will react with ozone to produce NO_2 , some being in an excited state. Then the excited NO_2 molecules will release their energy and go back to their base state by collision with third-body molecules.

$$NO + O_3 \longrightarrow NO_2^* + O_2 \tag{1.42}$$

$$NO_2^* + M \longrightarrow NO_2 + M + \text{photon} \tag{1.43}$$

This process will emit light and its intensity is proportional to the concentration of nitric oxide under controlled reaction conditions.

UBHC The UBHC is usually measured by a FID (Flame Ionisation Detector). The UBHC is burned in a hydrogen flame within an electric field. The electrons and positive ions produced during the breaking of carbon-hydrogen bonds can produce a current flow which is proportional to the number of carbon atoms present.

CO/CO2 The CO/CO_2 is usually measured by an NDIR (Non-Dispersive Infrared Sensor). Because different molecules will absorb infrared radiation at different wavelengths, which is known as the absorption spectrum, the CO/CO_2 concentration can be measured by measuring this absorption spectrum.

Fig. 1.3: Principle of the photo-acoustic soot sensor [71](Fig. 1 in orignal paper)

PM The PM emissions from engines can be measured either according to their mass or their number concentrations. The conventional techniques are mainly filter based. Different instruments, such as a Thermogravimetric Analyser (TGA), or a Transmission Electron Microscopy (TEM), can then be used to measure their weights, compositions, or morphologies of the filter samples. However, this type of measurements is heavily dependent on the sampling condition (and even the materials of the filter itself) and has no temporal resolution. Another long-standing instrument is the smokemeter, which measures the blackness of the particulate matter, usually in the visible spectrum. There are two types of smokemeter. One is the opacimeter, which measures the transmission of light through the exhaust gases. The other type is the spotmeter, which measures the scattered light from the filter where smoke has been accumulated. Both types of smoke meter are of diminishing utility in the automobile industry because of their poor accuracy, especially for modern engines with much lower particulate emissions compared to old engines. Several techniques have been developed to measure the real-time PM emissions. One of them is the photo-acoustic soot sensor. It is based on the photo-acoustic effect, and is illustrated by fig. 1.3.

When the black carbon particles absorb the energy of a modulated laser beam, they produce an acoustic pressure wave through absorption-induced gas expansion. Then, a microphone is used to measure the amplitude of the standing acoustic wave, which is proportional to the mass of soot. The major difficulty for this technique is the existence of other light absorbing substances, such as some gas molecules but it can be partially avoided by judicious choice of the laser beam wavelength.

Another very popular technique is measuring the PM electrical mobility. One type of instrument measuring the electrical mobility is the Scanning Mobility Particle Sizer (SMPS). The first part of SMPS is a Differential Mobility Analyser (DMA). In DMA, particulates need to go through a bipolar charger before entering the classification chamber. In the chamber, particulates experience radial forces in an electrical field created by a centrally mounted electrode and only those possessing a certain electrical mobility can access the central exit

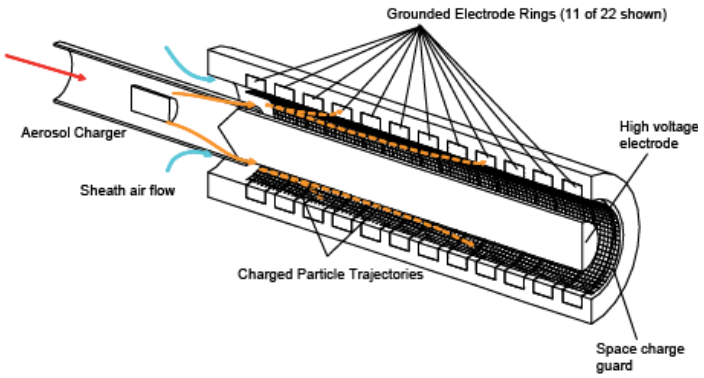

Fig. 1.4: Principle of the differential electrical mobility spectrometer (Cambustion DMS500 user manual)

at the opposite end of the chamber. Then a Condensation Nuclei Counter (CNC) is used to measure the concentrations of particulates selected by the DMA. By scanning through electrical field with gradually increasing strength, concentrations of particulates with different electrical mobility can be measured. The major limitation of SMPS is the finite duration of the scanning. To measure the real-time PM emissions, another instrument called the Differential Mobility Spectrometer (DMS) has been developed. A typical setup is shown in fig. 1.4. The particles go through a diffusion charging process in a corona discharge. Then the charged particles are introduced into a strong electrical field inside the classifier column. Particles with less electrical mobility will experience less force so that they can travel further down the column before depositing on the electrometer rings. Because the PM electrical mobility is a function of its diameter, by measuring the current on each electrometer ring, the number concentrations of particles of different sizes can be deduced.

1.4 Optical diagnostics in combustion

1.4.1 Overview

Since the famous lecture given by Michael Faraday on the combustion of a candle in 1860, combustion science has bdeveloped over 150 years. Further developments in combustion science, either to understand the essence of combustion or improve the combustion system,

are heavily reliant on different diagnostic techniques. All these diagnostic techniques can be roughly classified into two categories. One is probe-based techniques and the other is optical diagnostic techniques. Since the combustion process is very sensitive to the property of the flow field, optical diagnostic techniques become more and more popular due to their non-intrusive characteristic. In addition, the probes used in high temperature and high pressure combustion environments need to be more physically robust, which increases the chance of perturbation and degradation in accuracy. Moreover, the probe-based techniques usually have low spatial and temporal resolutions, which limit their application in investigating a fast changing process, such as chemical reactions or the properties of turbulent flames. Optical diagnostic techniques can overcome all these difficulties. The main disadvantage of the optical diagnostic techniques is the requirement for robust optical access in the combustion system, which can be very difficult in high temperature and high pressure combustion systems.

The simplest optical diagnostic techniques mainly rely on the flame emissions and typically use a high speed photography system. The schlieren or the shadowgraph photography system is also frequently used to visualize the flow field according to the change of its density. With the discovery and continuous development of laser techniques and a deeper understanding about the interactions between light (electromagnetic waves) and matter, the optical diagnostic techniques experienced a dramatic improvement. Weak or fast phenomena can be detected by using powerful and fast pulsed laser beams. The next section will give a brief review of different optical diagnostic techniques.

1.4.2 Non-laser based techniques

Compared to the laser-based optical diagnostic techniques, the main advantages of the non-laser based techniques are their simple experimental setups and ease of use. But these techniques usually have weaker signals and sometimes suffer from background noise because of the low signal-to-noise ratio. The most common techniques used in combustion science include direct high speed imaging systems to visualize the flames or flow field, the

schlieren and shadowgraph systems used to measure the density gradient or the flame speed, and the emission spectrum measurement systems to measure the species' concentrations.

1.4.2.1 Direct high speed imaging techniques

High speed imaging systems have been widely used to study combustion science in the last decade because of the astonishing advancement in microsystems, electronics and computer technologies, especially the development of digital imaging devices. State-of-art high speed digital cameras are able to run at 10^9 frames per second (e.g. Specialized Imaging Limited recently introduced a high speed camera which can run at 200 000 000 frames per second with up to 32 images), which is fast enough to study most physical and chemical processes during combustion.

High speed imaging systems are usually characterized by the frame rate, the integration time, the pixel number, the recording time, the memory size, the data format and transfer rate, and the triggering modes. Most high-end high speed cameras allow independent control of the frame rate and the integration time to capture more sharp images at relatively low frame rates. For most inexpensive cameras, the integration time is the inverse of the frame rate. Most high speed cameras used in research can record the radiation signals in uncompressed raw data format. In this case, the necessary memory size (MEM), can be calculated by the following equation:

$$\mathrm{MEM} = N_{pix} \times col \times \mathrm{FR} \times t_{rec} \tag{1.44}$$

where the N_{pix} is the pixel number, col is the colour depth (usually 8 bits/pixel, or 256 colours), FR is the frame rate, and t_{rec} is the recording timing. The recording timing for most high speed cameras is constant due to the limited data transfer rate. Therefore, the pixel number is smaller at higher frame rates if a constant memory size is used. A more detailed introduction to the high speed camera can be found in ref. [85].

Direct high speed imaging systems in engine applications with various imaging processing

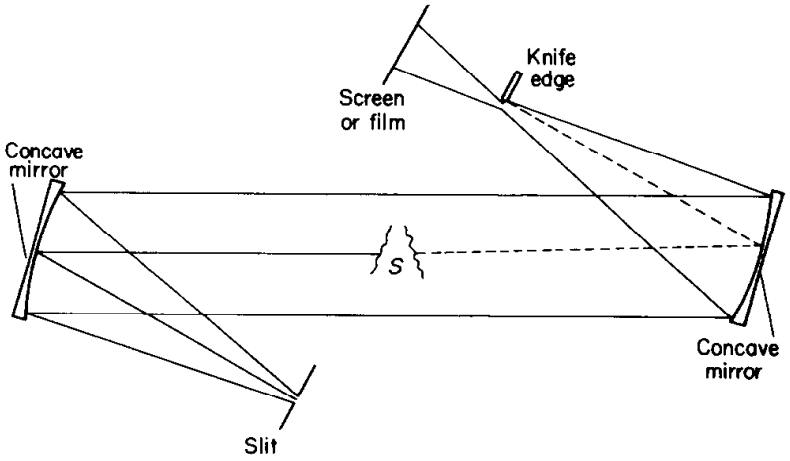

Fig. 1.5: Z-type schlieren systems

techniques can be used to study the fuel preparation process, such as the fuel penetration or the spray pattern, the spark ignition process, and the flame propagation process (such as the flame extinction or misfires). When combined with other optical devices, such as lasers and optical filters, the high speed imaging system can be used for quantitative measurements as will be discussed later.

1.4.2.2 Schlieren and shadowgraph techniques

The schlieren technique can be traced back to 17th century when Robert Hooke demonstrated the schlieren effect by using two candles to reveal the transparent convective plume of the candle. Then this technique was greatly improved by Foucault and Toepler and the name "schlieren" was adopted by Toepler. The schlieren method is based on the propagation of light through inhomogeneous media. The angular light ray deflection is proportional to the gradient of the refractive index of the medium. For air and other gases, the refractive index is in linear relationship with the gas density, therefore the angular light ray deflection is proportional to the density gradient for gases. While the schlieren technique displays the light ray deflection angle, the shadowgraph technique displays the light ray displacement resulting from the deflection and the shadowgraph responds to the Laplacian of the refractive index. Both the schlieren and shadowgraph techniques are line-of-sight measurement techniques so they can only show 2D property fields.

The most often used schlieren systems are in z-type configuration, as shown in fig. 1.5. The sensitivity of the system is inversely proportional to the slit width, but the minimum slit size is limited by diffraction [73]. Since the displacement of a beam at the knife edge is proportional to the length of the light beam between the striation (S) and the knife edge, the system sensitivity increases with focal length [21]. Besides the conventional grey-scale image, colour schlieren photography systems have also been developed by using a tri-colour filter in place of the knife edge for better visualization. The more detailed operation principles and experiment setups of various schlieren techniques can be found in [72].

Besides visualizing the flow field and flame front structure, both the schlieren and shadowgraph techniques can be used to measure the laminar flame speed. Since the schlieren photography measures the density gradient, which has the greatest value at about the inflection point of the flame temperature curve and corresponds more closely to the ignition temperature, and the surface is more readily definable than most other images, it is recommended by many workers [30].

1.4.2.3 Emission spectrum measurement techniques

The emission spectrum measurement techniques are used to measure species' concentrations. As their names suggest, these techniques are based on species' characteristic emission spectra. Theoretically, the concentrations of all different species can be measured by using different optical filters because the emission spectra from different species are unique and can be used as their signatures. However, in practice, measurements are limited by the signal level, the signal-to-noise ratio, and the spectrum bandwidth of the optical filter. In fact, most emission spectrum measurements in hydrocarbon combustion systems are measuring the chemiluminescence from OH*, CH*, C_2* and CO_2* (asterisk denotes the excited state) molecules because of their relatively high signal levels and significant roles in chemical reactions, and the thermal radiation from soot particles.

The chemiluminescence signals from OH*, CH* and C_2* molecules can be used to locate the primary reaction zones and are used as indicators of the equivalence ratio [35]. Whether

they can be used as indicators of the heat release rate is under debate [58][35]. In addition, the quantitative measurements of the chemiluminescence from OH*, CH* and C_2* are invaluable to verify the chemical kinetic models because they are very important intermediate radicals. The measurement of chemiluminescence in engines can also provide information about equivalence ratio or heat release rate [40] or work as indicators to misfires, flash back or auto-ignition [7].

The thermal radiation from soot particles has been studies by many researchers. Typical measurement methods include two colour pyrometry [38], three colour pyrometry [52], single wavelength emission spectrometry [33], and multi-wavelengths emission spectrometry [77]. These measurements can measure the flame temperature and soot loadings using certain assumptions, such as negligible radiance attenuation along the optical path (known as the optical-thin approximation) or spherical soot particles. The three colour pyrometry and emission spectrometry with tomography techniques will be discussed in more detail in chapter 2 because they are closely related to the new optical diagnostic techniques introduced in this thesis.

1.4.3 Laser based techniques

The laser based optical diagnostic techniques have become more and more popular in the last few decades due to the astonishing advances in laser techniques. Compared to the non-laser based optical diagnostics, laser diagnostics usually have better spatial and temporal resolutions and are more tolerant to background noise because of their high signal level. The emergence of ultra-fast pulsed lasers, such as the femtosecond (10^{-15} sec) and the subpicosecond ($<10^{-12}$ sec) lasers, makes the detection of most fast chemical reactions possible. The main disadvantages of laser diagnostics are the requirement of high level operational skills and the relatively high cost. But these drawbacks have been gradually overcome by the increasing commercialization of integrated laser diagnostic systems. In this section, a very brief overview of the laser diagnostics in combustion science will be given. A more detailed introduction to laser diagnostics can be found in various textbooks [26][44] and

papers.

Laser diagnostics can be roughly divided into two approaches: the coherent and incoherent, according to their signal generation processes. The incoherent techniques usually use a single laser beam and the signal is generated by the interactions between the laser beam and the medium. Then, an optical collection system is used to collect the signal over some solid angle at a certain angle (typically 90 deg) to the incident beam. Therefore, the spatial resolution is determined by the intersection volume formed by the optical collection system and the laser beam. The spectral signals generated in the incoherent approach are relatively simple and are usually linearly dependent on the species' concentrations so they are easy to calibrate compared to the coherent approach. However, the collection efficiency is much lower than that of the coherent approach so that a large solid angle is often used to increase the signal level. Moreover, the incoherent techniques are more vulnerable to interference signals because of the low signal level generated. In the coherent approach, the signal is generated by the mixing of multiple laser beams so that the spatial resolution is determined by the intersection volume between the laser beams. Then, most of the generated signal can be collected by a coherent process, which can be either the modulation of the probe laser or the generation of new laser signal. Compared to the incoherent approach, the coherent techniques usually generate stronger laser-like signal beams so that they are more tolerant to interference. However, the spectral signal is more complicated and is normally non-linearly dependent on the species' concentrations so its calibration and further analysis is more difficult. In many applications, the incoherent approach is preferred due to the simplicity in the experimental setup and the data analysis. But sometimes the coherent approach should be adopted if there is strong signal interference from the background or the signal level generated by the incoherent approach is not high enough to produce trustworthy results.

There are different interaction processes in the incoherent approach, including elastic and inelastic scattering, and absorption. During the elastic scattering process, such as Rayleigh scattering or Mie scattering, there is no energy exchange between the laser beam and the medium. The signal generated during inelastic scattering processes, such as Raman or near-Raman scattering, on the other hand, is dependent on the different energy exchange

processes between the incident laser beam and the medium molecules. Therefore, the inelastic scattering signal is highly species specific. However, the inelastic signal is very weak (typical Raman scattering signal has 10^{-14} signal to laser energy ratio) so that it is only suitable for a clean combustion environment and is normally only used to measure the major species. The emitted photons from an atom or a molecule can also have been promoted to the excited state by various means: electron bombardment, heating, chemical reaction (chemiluminescence) or photon absorption (fluorescence or phosphorescence). The fluorescence is of great combustion diagnostic interest because it is species specific and has a much stronger signal level than Raman scattering. Therefore, fluorescence techniques, such as Laser-Induced Fluorescence (LIF), can be used to measure the minor species, such as various intermediate radicals, during combustion. But they are incapable of measuring the concentrations of major species because of the inaccessibility of their electronic transitions [26]. In addition, the fluorescence effect needs to compete with other quenching effects, such as dissociation, ionization, energy transfer to other molecules or other internal states, or chemical reactions. Therefore, the quantitative measurement of species concentration by using the fluorescence effect must be able to avoid the competition with quenching processes or determine the quenching effect in-situ. The absorption techniques can be very useful in measuring the temperature, pressure and the species concentrations simultaneously by measuring the detailed absorption spectra, especially when using fast tuning lasers and fast line scanning techniques. Since most of the absorption techniques are line-of-sight integral measurements, the spatial resolution of the results is lost but it can be partially recovered by using tomographic techniques. The long path absorption techniques, such as Cavity Ringdown Spectrometry (CRDS), are very sensitive and not affected by the quenching process so they have attracted increasing attention.

Many different coherent techniques have also been widely applied to measure the temperature, pressure, and species concentrations. They are normally based on nonlinear optical processes. One main category is the Raman based nonlinear process. The signals in two-colour Raman based coherent techniques are produced by the modulation of a probe laser due to the Raman effect, either in terms of the intensity (e.g. Stimulated Raman Gain Spec-

troscopy (SRGS), Photo-Acoustic Raman Spectroscopy (PARS)) or the polarization (e.g. Raman-Induced Kerr Effect Spectroscopy (RIKES), Optically Heterodyned RIKES (OHD-RIKES)). The signals in three-colour or four-colour techniques are photons at different frequency created by the mixing process of the pump laser and probe laser (e.g. Coherent Anti-Stoke Raman Spectroscopy (CARS)). Though CARS can produce a signal that is many orders of magnitude higher than the signals from the traditional Raman scattering technique, most of the signal resides in fluorescent-free regions, so it can only be used to measure the concentration of major species ($> 0.1\%$). The sensitivity of CARS is comparable to that of the SRGS but CARS is more tolerant to background noise. The other category in the coherent approach is based on the nonlinear electronic resonance process in which the frequency of the pump laser is tuned to the electronic resonance frequency of the molecules. Typical techniques include Resonance Coherent Anti-Stokes Raman Spectroscopy, Degenerate Four Wave Mixing (DFWM), and polarization spectroscopy. The detection sensitivity of DFWM is comparable to that of LIF so it can be used to detect the minor species in combustion.

Besides the laser diagnostic techniques mentioned above, other demonstrated diagnostic techniques includes Laser-Induced Incandescence (LII - used to measure the soot volume fraction), time-resolved LII and Wide Angle Light Scattering (WALS - used to measure the soot morphology), Laser-Induced thermal Grating Spectroscopy (LIGS - used to measure the temperature, pressure and possibly air-fuel ratio), Laser-Induced Breakdown Spectroscopy (LIBS - used to measure the soot particle distribution and compositions), Laser Doppler Velocimetry (LDV - used to measure the velocity of paticles), Particle Imaging Velocimetry (PIV - used to visualize the flow field), and Resonance-Enhanced Multi-Photon Ionization (REMPI - used to measure the species concentrations). A comprehensive review of the application of various laser diagnostics in the combustion science is given by Kohse-Hoinghaus et al. [45].

1.5 Motivation and Objectives

Though extensive research has been carried out to investigate the combustion and emission characteristics of hydrogen-hydrocarbon combustion systems, no literature can be found to investigate the effect of adding hydrogen on Particulate Matter (PM) emissions from GDI engines. Since the increased PM is one the main drawbacks for GDI engines, especially the number concentration, it is important to know the PM emission characteristics of the hydrogen-enhanced GDI engines. In addition, the fundamental mechanisms for the PM formations in hydrogen-hydrocarbon combustion systems should be investigated in more details to provide clues for the PM emission abatement techniques.

1.6 Summary of thesis contents

In this chapter, both the combustion and emission characteristics and fundamental chemical kinetics of the hydrogen-hydrocarbon combustion system have been reviewed, including a typical combustion system – the gasoline direct injection engine. In addition, a brief review has been given of the advances in optical diagnostic techniques. Several optical engine tests were undertaken first to investigate the effect of adding hydrogen on particulate emissions in spark ignition engines. The engine test results will be reported in chapter 5. To understand the fundamental mechanisms behind the engine test results, a simpler combustion system – the laminar diffusion flame burner was constructed to investigate the effect of adding hydrogen on particulate emissions on pure ethylene flames. Meanwhile, to measure the 3D temperature, soot diameter and soot volume fraction distributions, a new optical diagnostic, called cone beam tomographic three colour spectrometry has been developed. The theories behind this technique and related assumptions will be introduced in chapter 2; the experimental setup and sensitivity analysis will be introduced in chapter 3. This new optical diagnostic technique has been applied to several ethylene laminar diffusion flames, including pure ethylene flames, a helium diluted ethylene flames, and hydrogen-ethylene flames. The flame tests results will be reported in chapter 4. The conclusions are

made in chapter 6 along with suggested future work.

Chapter 2

Theory of Cone-Beam Tomographic Three Colour Spectrometry (CBT-TCS)

2.1 Introduction

Cone Beam Tomographic Three Colour Spectrometry (CBT-TCS) is a technique used to measure the spatially distributed temperature and soot loading in flames. It is based on the principle of Three Colour Pyrometry (TCP) with the aid of a 3-Dimensional (3D) Computational Tomography (CT) technique.

Conventional two colour pyrometry measures the temperature by taking the ratio of light intensity at two different wavelengths so as to eliminate an unknown coefficient in Planck's radiation law. Then the *KL* value, which is the product of the absorption coefficient per unit flame thickness (K) and the line-of-sight integrated length (L), can be calculated by substituting the flame temperature into the Planck equation with the absolute light intensity. The *KL* can be used as a qualitative indication of the soot loadings. Matsui et al. [53] were among the first to use the two-colour method (with visible wavelength radiation from soot particles in flames) as a technique for measuring the flame temperature and soot concentration in diesel engines using two discrete wavelengths. Matsui et al. [54] also investigated

the effect of choosing different wavelengths on the accuracy of the measurement. One of the major difficulties in two colour pyrometry is the measurement of the absolute light intensity, which can be avoided in the TCP by using the colour ratios from three measurements to solve for temperature and KL.

With the tremendous improvement in computer power over the past few decades, the CT technique has become a very powerful and popular diagnostic technique in various fields. It can be used to reconstruct the volumetric property field from the measured 2-Dimensional (2D) projection data by applying various mathematical algorithms. Many researchers have applied the 2D tomographic technique to measure the planar temperatures and soot volume fraction distributions from 1D projection data in a diffusion flame burner. Hall and Boncyzk (1990) [33] used a single wavelength emission-absorption spectrometry to reconstruct the 2D soot concentration and temperature fields in ethylene and iso-octane diffusion flames. Snelling et al. (2002) [77] applied multi-wavelength emission spectrometry to measure the 2D temperature and soot concentration fields and also discussed the influence of various optical parameters on the accuracy of the experiment. Ayranci et al. (2007)[4] proposed a new approach to correct the assumption of a constant complex refractive index of soot over a certain range of wavelengths. Lu et al. (2009) [51] introduced an iterative method to eliminate the error caused by the optically-thin assumption. All these researchers have greatly improved the spatial resolution and accuracy of the 2D emission spectrometry. Their experiments are all based on the measurement of the absolute light intensity, which can be difficult because of the need for a source with an absolute calibration, such as a black body[1] at a known temperature and the results are also very sensitive to the optical properties of the environments and instruments. Their experiments also rely on the assumption that the Rayleigh-Gans theory is valid throughout the whole spectrum, which is not necessarily the case. In addition, the 2D emission spectrometry only gives the temperature and soot concentration distributions at a specific height in one measurement and their measurments did not include any information about the soot particle size. The CBT-TCS can give the 3D temperature and soot diameter distributions without needing an absolute calibration. But

[1] A black body is an ideal object which can absorb all incident radiations.

the measurement of soot volume fraction does need an absolute calibration of the colour camera.

2.2 Three colour pyrometry

Since the CBT-TCS is based on the principle of TCP, it is worth introducing the TCP first. TCP is based on the relationship between the temperatures of glowing particles and their thermal radiation. The thermal radiation from a black body, $I_{\lambda b}$, is given by Planck's radiation law:

$$I_{\lambda b} = \frac{2hc^2}{\lambda^5[\exp(hc/\lambda kT) - 1]} \tag{2.1}$$

where h is the Planck constant ($6.626 * 10^{-34}$Js); c is the speed of light in vacuum ($2.998 * 10^8$m/s), and k is the Boltzmann constant ($1.38 * 10^{-23}$J/K) respectively. The unit of calculated black body radiance by using the Planck's law is energy per unit time per unit surface area per unit solid angle and per unit wavelength ($\mathrm{J \cdot s^{-1} \cdot m^{-2} \cdot sr^{-1} \cdot m^{-1}}$in SI unit). Therefore, to calculate the radiance accurately, the particle size should be taken into account to calculate the total emitting surface area. For objects other than a black body, such as soot particles, the spectral emissivity ε_λ needs to be introduced to quantify the ratio between the actual intensity emitted by the object and that by the black body. Then, the radiance is calculated by the following equation for a grey body

$$I_\lambda = \varepsilon_\lambda \frac{2hc^2}{\lambda^5[\exp(hc/\lambda kT) - 1]} \tag{2.2}$$

Assume the scattering by soot particles is negligible in comparison with absorption. Within the Rayleigh limit[2], the emissivity ε_λ can be calculated by:

$$\varepsilon_\lambda = f_v * 6\pi * E(m_\lambda)/\lambda \tag{2.3}$$

[2]Rayleigh limit: $\pi d/\lambda << 1$ (usually use $\pi d/\lambda < 0.3$), d is the diameter of the soot particle. Since the particle size can be as large as several hundred nano-meter, this limit does not hold all the time

where f_v is the soot volume fraction, $E(m_\lambda)$ is a function of the complex refractive index m_λ. The value for $E(m_\lambda)$ is debated, and in this work, its value is taken as a constant with the value of 0.26[3] . For particles larger than 50 nm, the Rayleigh limit does not hold in the visible light spectrum, especially at lower end of the visible spectrum. Therefore, more accurate scattering models, such as the Rayleigh-Gans theory with the Penndorf extension, or the Mie theory, need to be used to calculate the emissivity. When using the Penndorf extension, or Mie theory, the emissivity is also a function of the diameter of the particle (D_p). Since TCP takes the ratios of light intensities at different wavelengths, the soot volume fraction will be eliminated so that the two colour ratios can be used to calculate two unknowns: T and D_p. The Mie theory should be given the priority when mapping D_p because it is the analytical solution of the Maxwell equations while the Penndorf extension is a fitting equation to the experimental data. A more detailed discussion about the scattering theories and optical constants of particles will be given in section 2.4.

Hottel and Broughton (1932)[38] also introduced an empirical formula to calculate the emissivity ε_λ:

$$\varepsilon_\lambda = 1 - \exp(-A_\lambda L) \tag{2.4}$$

where A_λ is the absorption coefficient and is given by:

$$A_\lambda = K/\lambda^\alpha \tag{2.5}$$

where K is proportional to the soot volume fraction, and L is the geometric flame thickness along the optical path. α is dependent on the physical and optical properties of the soots in the flame, and its value was found to be around 1.39 in the visible light spectrum for amyl acetate flames[38].

Assuming that there is no attenuation of the emitted radiation along the optical path and that the radiation absorbed and emitted by other species is negligible in comparison with

[3] $E(m_\lambda)$= 0.26 when m_λ = 1.57 – 0.56i

that from the soot particles, the line-of-sight integral intensity can be written as:

$$I_\lambda = \int_{-\infty}^{\infty} \frac{6\pi f_v E(m_\lambda)}{\lambda} \frac{2hc^2}{\lambda^5[\exp(hc/\lambda kT)-1]} ds \tag{2.6}$$

Or

$$I_\lambda = \int_{-\infty}^{\infty} [1 - exp(-\frac{KL}{\lambda^\alpha})] \frac{2hc^2}{\lambda^5[\exp(hc/\lambda kT)-1]} ds \tag{2.7}$$

The strategy in calculating the soot loading by using eq. (2.7) is different from that used to calculate the soot volume fraction using eq. (2.6). Using eq. (2.6) requires the absolute calibration of the camera. In contrast, eq. (2.7) can only provide qualitative soot loading information indicated by *KL*, but it does not require absolute calibration of the camera sensor. The strategy for using eq. (2.7) is depicted in Fig. 2.1. As seen in Fig. 2.1, the light radiance from soot particles at different temperature and concentrations can be calculated first according to eq. (2.7) across the whole spectrum. Then, a Photron FASTCAM 1024PCI high speed video colour camera is carefully calibrated to obtain the spectral response curve of its Colour Filter Array (CFA). The spectral intensities recorded by the camera were calculated by multiplying the thermal radiance and the camera response. Then, by taking integrals of the relative intensity over the whole wavelength range and calculating the ratios, a look-up table can be built up with the Red/Blue, and Red/Green ratios as double entries, and temperature and *KL* as outputs. When using a different lens, the transmission coefficients of the lens over the whole wavelength range have to be measured and included when constructing the look-up table.

A simple quartz halogen bulb can be used as a reliable calibration light source after it has been fully warmed-up. Since the spectrum from the bulb is red biased, care should be taken to make sure that the readings at the shorter end of the visible spectrum are detectable. Then a spectrometer was used to separate the incoming light into different wavelengths in the range from 400 nm to 800 nm with 10 nm increments, and the monochromatic light (bandwidth 10 nm) was sent to the camera sensor. In addition, an Ocean Optics spectrometer was used to record the absolute light intensity at each increment. Several issues arose during the experiment. One is that the emitting spectrum near 400nm was difficult to de-

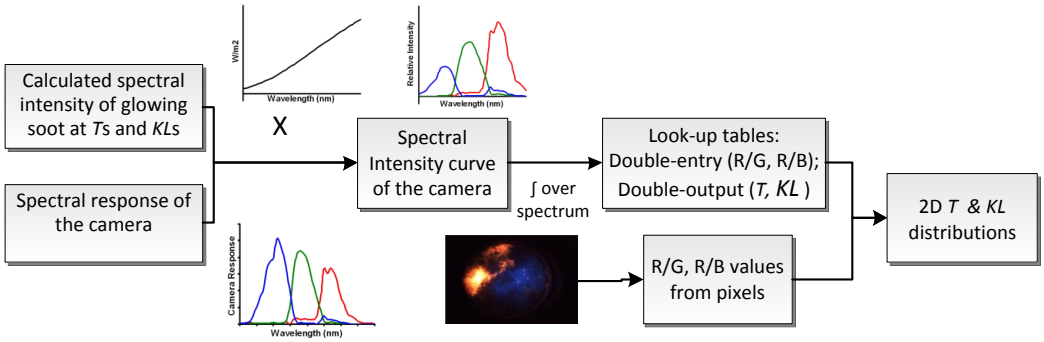

Fig. 2.1: The strategy for the determination of temperature and soot loading (*KL*) using Three Colour Pyrometry (TCP) when using the Hottel and Brought correlation

tect and the output signal from the spectrometer had a large sideband. This problem was overcome by using an anti-reflective coated lens between the bulb and the spectrometer to produce an image of the bulb on the incident slit of the spectrometer. It was also found that a harmonic appears at wavelengths greater than 700nm, and the harmonic is at 400nm when the intended wavelength was 800nm. This phenomenon has to be taken into account when processing the data. This produced a much clearer signal and made the measurement more accurate. Because the light intensity received by the fibre optic cable was sensitive to its position, a magnetic-base clamp was used to fix the cable throughout the whole experiment. The supporting software provided a control of the integration time, to control the amount of light received. At different wavelengths, different integration times were used to obtain sufficient signal level in the spectrometer. Background noise should also be subtracted when processing the data. Different shutter speeds can also be used on the camera to avoid light saturation. Only the raw pixel values were recorded (the camera sensor only records the data of certain colour channels due to the CFA) when saving the image. Then bilinear interpolation was applied to calculate values for the other two colour channels at each pixel location. The CFA and the weighting factors for different colour channels are shown in Fig. 2.2.

According to the obtained camera response curve (Fig. 2.3), the camera was unable to receive much red light. But the camera user manual indicates that this camera can receive

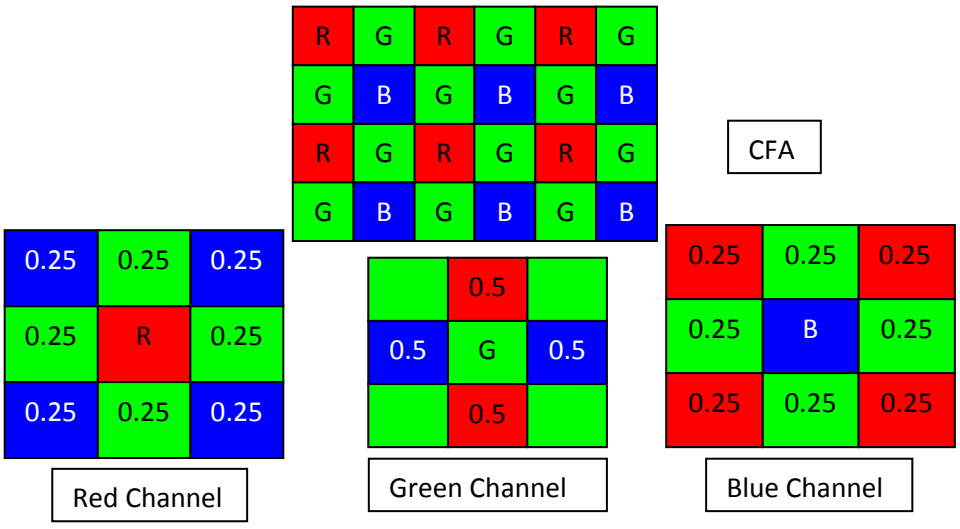

Fig. 2.2: The Colour Filter Array (CFA) and its weighting factors when doing interpolation

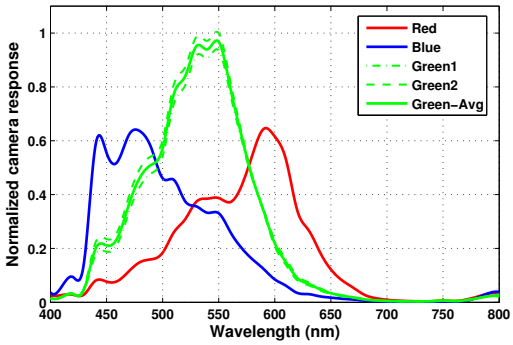

Fig. 2.3: Camera calibration curve

light with wavelengths up to 900nm. To validate the calibrated camera response curve, a helium-neon laser (of wavelength 633nm) was used to test the colour ratios obtained by the camera calibration data. The error between the camera response curve and the data from the laser test was smaller than 5%, which confirmed that the camera itself filters most lights above 600nm. From the calibration of the camera, it can be seen that there is a blue-green tint to the pickup. This is beneficial for the imaging of the combustion chamber since its image is usually red saturated. The two different green channels responses shown in the camera response curve are due to slight misalignment of the CFA and the CMOS Sensor. The average value between these two green chaneels will be used to represent the spectrum response of the green channel.

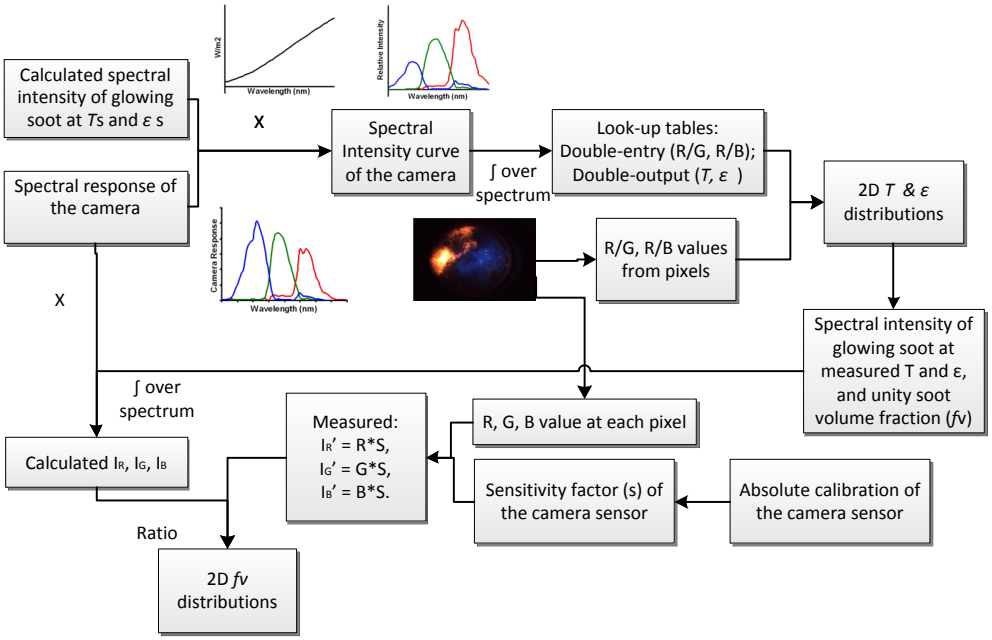

Fig. 2.4: The strategy for the determination of temperature and soot loading (soot volume fraction) in Three Colour Pyrometry by using scattering models other than Hottel and Broughton corellation

The strategy to calculate the soot volume fraction using eq. (2.6) is somewhat different. It should be noticed that when taking the colour-ratios, the soot volume fraction will be cancelled out. In other words, the soot volume fraction (f_v) in eq. (2.6) cannot be calculated directly by using the same strategy as using eq. (2.7). The strategy when using eq. (2.6) is summarized in Fig. 2.4.

In this strategy, the absolute calibration of the camera sensor is needed to get the sensitivity factor (s). Then the soot volume fraction can be calculated according to the ratio of the measured intensity and the calculated intensity (assume unity soot volume fraction) at the measured temperature.

The idea of the CBT-TCS is to use tomographic techniques to obtain the spatially distributed colour ratios and then apply the TCP technique to get the temperature and soot loadings at individual voxel (volumetric pixel).

2.3 Cone beam tomography – 3D Filtered Backprojection (FBP) algorithm

Tomography is used to reconstruct a cross sectional field from its projection data. The simplest tomographic algorithm is for parallel beam reconstruction, and this lays down the foundation for other more complex reconstruction algorithms. The detailed algorithm deductions can be found in the book *Principles of Computerized Tomographic Imaging* by Kak and Slaney [42]. Equations in the following three subsections are cited from ref [42].

2.3.1 Parallel beam reconstruction

The parallel beam reconstruction is the simplest form of tomography. This subsection will introduce the most fundamental algorithm, called the Radon transform. This algorithm is the foundation for other higher-dimension tomography algorithms. Many other approaches to deconvolve the one-dimensional parallel beam line-of-integral projection have been suggested, including the Abel Transform, and the onion-peeling method. A detailed comparison between these methods has been made by Dasch (1992)[20]. According to this paper, the two-point Abel Transform can achieve similar accuracy to the onion-peeling method, but they are less accurate than three-point Abel Transform and the FBP algorithm. Due to the efficiency of the three-point Abel Transform, this method is recommended if one-dimensional tomography is encountered.

Consider the parallel beam layout as shown in Fig. 2.5.

The projection $P_\theta(t)$ is known as the Radon transform of the field function $f(x,y)$:

$$P_\theta(t) = \int \int_{-\infty}^{\infty} f(x,y)\delta(x\cos(\theta) + y\sin(\theta) - t)dxdy \tag{2.8}$$

where $\delta(t)$ is the Dirac delta function. The Fourier Slice Theorem states that the Fourier Transform (FT) of a parallel projection of an image $f(x,y)$ taken at angle θ gives a slice

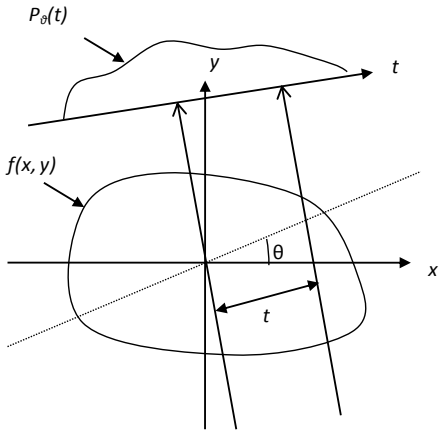

Fig. 2.5: Parallel beam tomography layout

Fig. 2.6: Fourier slice theory [59](Fig. 1 in original paper)

of the two-dimensional transform, $F(u,v)$, subtending an angle θ with the u-axis. In other words, the FT of $P_\theta(t)$ gives the values of $F(u,v)$ along line BB in Fig. 2.6.

Therefore, $S_\theta(\omega)$, the FT of $P_\theta(t)$,is:

$$S_\theta(w) = \int_{-\infty}^{\infty} P_\theta(t) e^{(-i2\pi\omega t)} dt = F(\omega\cos\theta, \omega\sin\theta) \tag{2.9}$$

where $F(\omega\cos\theta, \omega\sin\theta)$ is the FT of the field function $f(x,y)$. In practice, only a finite number of projection data can be measured, so the field function need to be calculated using the Discrete Fourier Transform (DFT):

$$f(x,y) \approx \frac{1}{A^2} \sum_{m=-N/2}^{N/2} \sum_{n=-N/2}^{N/2} F(\frac{m}{A}, \frac{n}{A}) e^{i2\pi((m/A)x+(n/A)y)} \tag{2.10}$$

where -A/2 < x < A/2 and –A/2 < y < A/2, and N is an arbitrary even number. In this case, interpolations must be applied to the points along radial directions into the squared grids as in eq. (2.10). Since the density of the radial points becomes sparser as they depart farther away from the centre, the interpolation error will become larger. In other words, the high frequency components in an image have lower errors in interpolation than the low frequency components.

While the FT and the Fourier slice theorem provide the conceptual model for tomogra-

phy, practical implementations use a different approach, called the Filtered Backprojection (FBP) algorithm. In a loose intuitive sense, the projections are nearly independent. The FBP algorithm assembles all the weighted projections at different angles to get the whole picture of the field property according to the Fourier slice theorem. As its name implies, the FBP algorithm consists of two steps: the filtering and the backprojection. The filtering part is initiated by measuring the projection $P_\theta(t)$. Then the FT of $P_\theta(t)$ will be multiplied by the weighting function $2\pi|\omega|/K$, where ω is the sampling frequency and K is the number of projections. The backprojection part is the summation over the imaginary plane of the inverse FT of the filtered projections.

The FBP algorithm has two advantages. Most importantly, since the reconstruction can be started as soon as the first projection has been measured, the reconstruction procedure is speeded up, and the stored amount of data each time is reduced. The second advantage is that the FBP does the interpolation in the space domain, which is more accurate and efficient compared to that in the frequency domain. The FBP algorithm comes into play by rewriting the inverse FT in polar coordinates:

$$f(x,y) = \int \int_{-\infty}^{\infty} F(\omega,\theta) e^{i2\pi\omega(x\cos\theta + y\sin\theta)} \omega d\omega d\theta \tag{2.11}$$

This integral can be split into two by considering θ from 0°-180° and then from 180°-360°. Using the property:

$$F(\omega,\theta+180) = F(-\omega,\theta) \tag{2.12}$$

Eq. (2.11) can be rewritten as

$$f(x,y) = \int_0^{\pi} [\int_{-\infty}^{\infty} F(\omega,\theta)|\omega| e^{i2\pi\omega t} d\omega] d\theta \tag{2.13}$$

where $t = x\cos\theta + y\sin\theta$. Applying the Fourier slice Theorem, eq. (2.13) becomes:

$$f(x,y) = \int_0^{\pi} [\int_{-\infty}^{\infty} S_\theta(\omega)|\omega| e^{i2\pi\omega t} d\omega] d\theta \tag{2.14}$$

Or,

$$f(x,y) = \int_0^{\pi} Q_\theta(x\cos\theta + y\sin\theta)d\theta \tag{2.15}$$

$$Q_\theta(t) = \int_{-\infty}^{\infty} S_\theta(\omega)|\omega|e^{i2\pi\omega t}d\omega \tag{2.16}$$

Eq. 2.16 represents a filtering operation, and eq. (2.15) is for the backprojection operation. It can be further explained as follows: for each point (x,y) in the field plane, there is a value of t for a given value of θ, and the filtered projection Q_θ contributes to the reconstruction of its value at t. In practice, only a finite numbers of projections are collected, and the sampling frequency should be higher than the Nyquist frequency (2ω). Therefore, eq. (2.16) can be rewritten in discrete form:

$$Q_\theta(\frac{k}{2\omega}) \approx (\frac{2\omega}{N}) \sum_{m=-N/2}^{N/2} S_\theta(m\frac{2\omega}{N}) \cdot |m\frac{2\omega}{N}|H(m\frac{2\omega}{N})e^{i2\pi(mk/N)} \tag{2.17}$$

where $k = -N/2, \cdots, -1, 0, 1, \cdots, N/2$. $H(m)$ is the window function used to redistribute the spectral leakage to places where it does the least harm to the real data, normally to where the high frequency signals locate because they are mostly noise. When implementing the FBP algorithm, sufficient zero-padding of the projections is needed to reduce the interperiod interference artefacts inherent to the periodic convolution that is required in eq. (2.17).

2.3.2 Equally spaced fan beam FBP algorithm

The equally spaced fan beam Filtered Backprojection (FBP) layout is shown in fig. 2.7.

The projection $R_\beta(s)$ is measured along a line parallel to D1'D2' but is further away from the source S (not shown in fig. (2.7)). The line D1'D2', which passes through the origin O, is used as the imaginary detector line. Any ray in a fan beam, such as SA, can be considered as one of the rays in a series of parallel beam projections $P_\theta(t)$. From fig. (2.7), the relationship between β and t is given by:

$$t = s \cdot \cos\gamma;\ \theta = \beta + \gamma$$

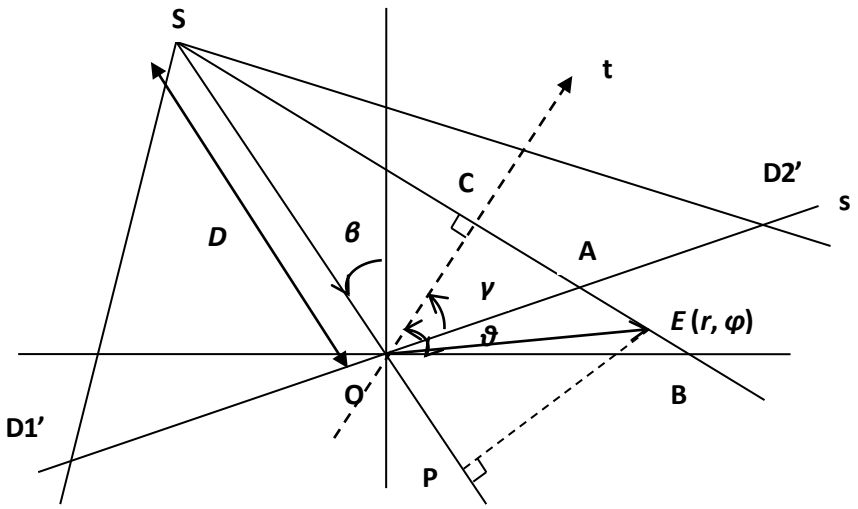

Fig. 2.7: Equally spaced fan beam tomograpy layout

$$t = \frac{sD}{\sqrt{D^2+s^2}}; \theta = \beta + \tan^{-1}\frac{s}{D} \tag{2.18}$$

Moreover, according to convolution theory, eq. (2.14) can be rewritten as:

$$f(r,\phi) = \frac{1}{2}\int_0^{2\pi}\int_{-t_m}^{t_m} P_\theta(t)h(r\cos(\theta-\phi)-t)dtd\theta \tag{2.19}$$

where h is the inverse FT of the weight function. Combining eq. (2.18) and eq. (2.19), and replace $P_\theta(t)$ by $R_\beta(s)$, the expression for the fan beam FBP algorithm can be written as:

$$f(x,y) = \int_0^{2\pi}\frac{1}{U^2}Q_\beta(s')d\beta \tag{2.20}$$

$$Q_\beta(t) = \int_{-\infty}^{\infty} R_\beta(s)g(s'-s)\frac{D}{\sqrt{D^2+s^2}}ds;\ g(s) = 0.5*h(s) \tag{2.21}$$

where U is the ratio between SP and the source-to-axis distance (SAD), as in fig. 2.7:

$$U(r,\phi,\beta) = \frac{\overline{SO}+\overline{OP}}{\overline{SP}} = \frac{Dr\cos(\beta-\phi)}{D+rsin(\beta-\phi)} \tag{2.22}$$

and s' is the value of s for the ray that passes through the point (r,ϕ):

$$s' = \frac{\overline{EP}\cdot\overline{SO}}{\overline{SP}} = D\frac{r\cos(\beta-\phi)}{D+r\sin(\beta-\phi)} \tag{2.23}$$

and $g(s) = 0.5 * h(s)$.

2.3.3 Cone beam FBP algorithm

The practical FBP algorithm for cone beam tomography was first introduced by Feldkamp et al. (1984)[27], and is known as the FDK algorithm. A new coordinate system (t,s,r) is created to facilitate the derivation of the cone beam FBP Algorithm. This coordinate system is obtained by two rotations of the (x,y,z) coordinate, as in Fig. 2.8. The first rotation is by θ degrees (gantry angle) around the z-axis to give the (t,s,z) coordinate:

$$\begin{bmatrix} t \\ s \\ z \end{bmatrix} = \begin{bmatrix} \cos\theta & \sin\theta & 0 \\ -\sin\theta & \cos\theta & 0 \\ 0 & 0 & 1 \end{bmatrix} \begin{bmatrix} x \\ y \\ z \end{bmatrix} \tag{2.24}$$

The second rotation is by γ degrees around the t-axis to give the(t,s',r) coordinate:

$$\begin{bmatrix} t \\ s' \\ r \end{bmatrix} = \begin{bmatrix} 1 & 0 & 0 \\ 0 & \cos\gamma & \sin\gamma \\ 0 & -\sin\gamma & \cos\gamma \end{bmatrix} \begin{bmatrix} t \\ s \\ z \end{bmatrix} \tag{2.25}$$

The (t,θ) is in the x-y plane and locates a ray in a given tilted fan, and (r,γ) is in the s-z plane and specifies the location of the tilted fan itself. In the cone beam system, the source is rotated by β, and the projections are measured on the detector plane and described as $R_\beta(p,\zeta)$. Then the parallel projection ray is given by:

$$t = p\frac{D_{SO}}{\sqrt{D_{SO}^2 + p^2}}; \theta = \beta + \tan^{-1}(p/D_{SO});$$

$$r = \zeta\frac{D_{SO}}{\sqrt{D_{SO}^2 + \zeta^2}}; \gamma = \tan^{-1}(\zeta/D_{SO}) \tag{2.26}$$

where D_{SO} is the distance between the source and axis of rotation. Rewriting the equations for the fan beam tomography (eq. (2.20-23)) in different symbols (because of the overlap of

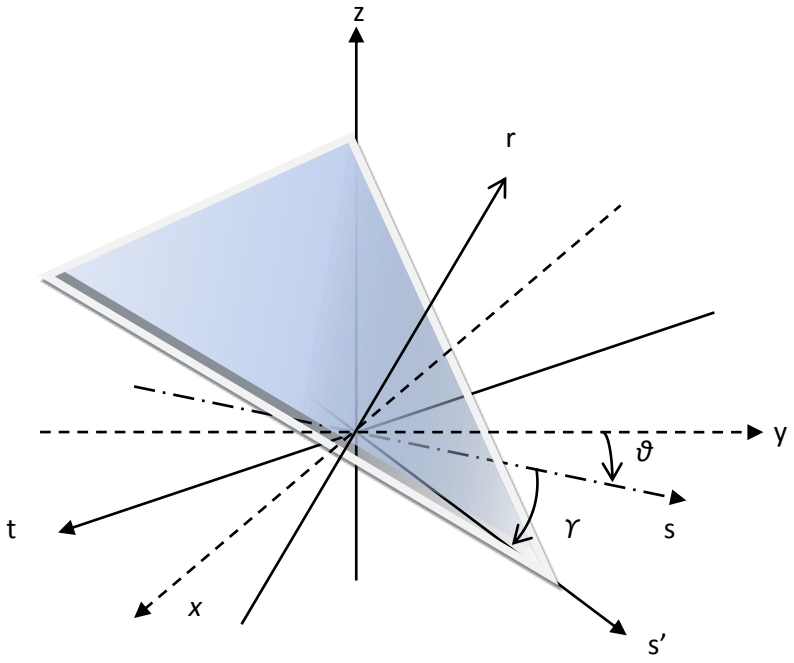

Fig. 2.8: Cone beam tomography coordinate

some symbols between the fan beam tomography and the coordinate systems in cone beam tomography) gives:

$$g(r,\phi) = \frac{1}{2}\int_0^{2\pi} \frac{1}{U^2}\int_{-\infty}^{\infty} R_\beta(p)h'(p'-p)\frac{D_{SO}}{\sqrt{D_{SO}^2+p^2}}dpd\beta \tag{2.27}$$

$$p' = \frac{D_{SO}r\cos(\beta-\phi)}{D_{SO}+r\sin(\beta-\phi)}; h(p) = \int_{-W}^{W}|\omega|e^{i\omega p}d\omega; U(r,\phi,\beta) = \frac{D_{SO}+r\sin(\beta-\phi)}{D_{SO}}$$

To further simplify these expressions, the (r,ϕ) coordinate is replaced by the (t,s) coordinate by using the following transformations:

$$t = x\cos\beta + y\sin\beta; s = -x\sin\beta + y\cos\beta; x = r\cos\phi; y = r\sin\phi \tag{2.28}$$

Consider an arbitrary tilted fan in a cone beam in the (t,s')coordinate system:

$$D'_{SO} = D_{SO}^2 + \zeta^2; D_{SO}d\beta = D'_{SO}d\beta' \tag{2.29}$$

Rewrite eq. (2.27) by substituting variables with eq. (2.28) and (2.29):

$$g(t,s') = \frac{1}{2}\int_0^{2\pi} \frac{(D'_{SO})^2}{(D'_{SO}-s')^2} \int_{-\infty}^{\infty} R_{\beta'}(p,\zeta) h(\frac{D'_{SO}t}{D'_{SO}-s} - p) \frac{D'_{SO}}{\sqrt{(D'_{SO})^2+p^2}} dp d\beta' \quad (2.30)$$

To map back into the (t,s,z)coordinate, the following relationships should be applied:

$$\frac{s'}{D'_{SO}} = \frac{s}{D_{SO}}; \frac{\zeta}{D_{SO}} = \frac{z}{D_{SO}-s} \quad (2.31)$$

The cone beam FBP algorithm can be summarized as:

$$g(t,s,z) = \int_0^{2\pi} \frac{D_{SO}^2}{(D_{SO}-s)^2} Q_\beta(\frac{D_{SO}t}{D_{SO}-s}, \frac{D_{SO}z}{D_{SO}-s}) d\beta \quad (2.32)$$

$$Q_\beta(p,\zeta) = \frac{1}{2}\int_{-\infty}^{\infty} R_\beta(p,\zeta) h(\frac{D_{SO}t}{D_{SO}-s} - p) \frac{D_{SO}}{\sqrt{D_{SO}^2+\zeta^2+p^2}} dp \quad (2.33)$$

In application, the cone beam reconstruction algorithm can be summarized in the following three steps:

Step 1: Measure the projection data, $R_\beta(p,\zeta)$. Then calculate the $R'_\beta(p,\zeta)$ according to:

$$R'_\beta(p,\zeta) = \frac{D_{SO}}{\sqrt{D_{SO}^2+\zeta^2+p^2}} R_\beta(p,\zeta) \quad (2.34)$$

Step 2: Filtering the calculated projection data:

$$Q_\beta(p,\zeta) = \text{IFFT}(\text{FFT}(\text{R}'_\beta(\text{p},\zeta)\text{withZP}) \times H(p,\zeta)) \quad (2.35)$$

Where $H(p,\zeta)$ is the product of the weighting function and the window function; IFFT: Inverse Fast FT; and FFT: Fast FT; ZP: Zero Padding

Step 3: Each weighted projection is backprojected into the three-dimensional reconstruction grids according to eq. (2.33).

Only those points that are illuminated from all directions can be properly reconstructed. In

a cone beam system, this region is a sphere of radius $D_{SO} \cdot \sin(\Gamma_m)$ where Γ_m is half the beam-width angle of the cone [42]. The quality of the reconstruction varies for different evaluation planes. On the plane of rotation ($z = 0$), the cone beam reconstruction algorithm can be reduced to the fan beam reconstruction algorithm. Further from the central plane, the accuracy of the reconstructed field suffers from noticeable quality degradation. Therefore, for real applications, projection data at various elevations can be collected to ascertain the accuracy level.

2.4 Absorption and scattering of light by particles

2.4.1 Introductory physics

The absorption and scattering of electromagnetic waves (e.g. light) is related to the heterogeneity of the system (e.g. particle). Different kinds of matter can be considered as discrete electric charges. When they are illuminated by electromagnetic waves, they are set into oscillation. The accelerated electric charges then radiate electromagnetic energy in all directions. This secondary radiation is called scattering. Meanwhile, the excited electric charges may transform part of the incident energy into other forms (e.g. thermal energy). This process is called absorption. The term extinction is used to describe the combined effect of scattering and absorption.

The scattering by a single particle can be regarded as the secondary radiation of the oscillating dipoles within a particle induced by an applied oscillating electromagnetic field, as in Fig. 2.9. If the particle size is small compared to the wavelength, the scattered wavelets are approximately in phase so that the scattering in different directions is similar. As the particle size increases, the possibilities of mutual enhancement and cancellation of the scattered wavelets increase so that the larger the particle, the more complex the scattering pattern.

In practise, the scattering phenomena under consideration are usually for a collection of particles. In this project, the assumption of single scattering and incoherent scattering are

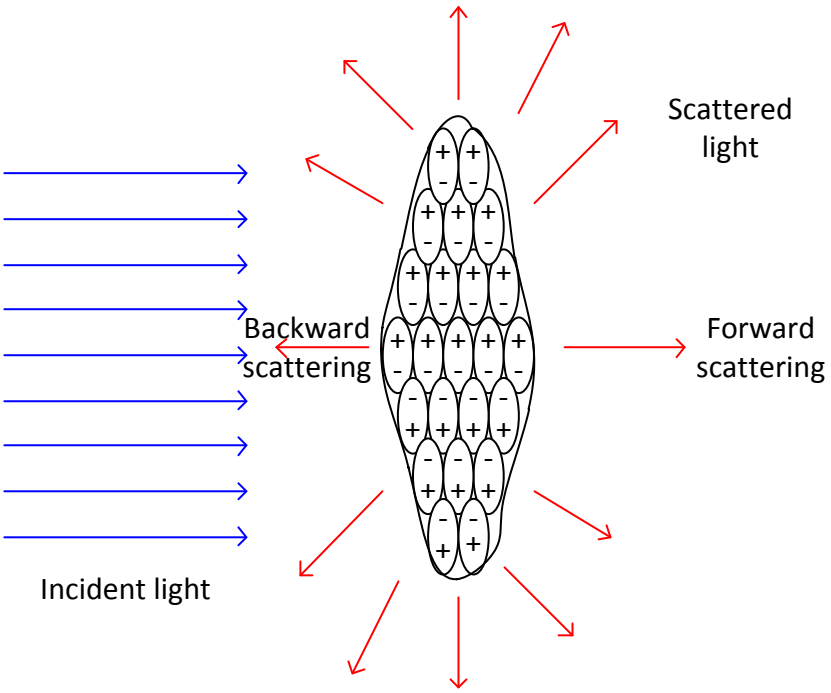

Fig. 2.9: Scattering by a single particle

made to simplify the analysis. Single scattering means the adjacent particles are separated sufficiently so that the total scattered field is just the sum of the fields scattered by individual particles. Incoherent scattering implies there is no systematic relation between the phases of the waves scattered by the individual particles.

Since the scattering and absorption are caused by the interaction between the electromagnetic wave and the inner electromagnetic field of the particle, the general formula can be deduced from the Maxwell equations. The field inside the particle can be denoted by (E_1, H_1); the field in the medium surrounding the particle is denoted by (E_2, H_2) and it is the superposition of the incident field (E_i, H_i), and the scattered field (E_s, H_s).Where E is the electrical field and H is the magnetic field. The fields must satisfy Maxwell equations:

$$\nabla \cdot E = 0 \tag{2.36}$$

$$\nabla \cdot H = 0 \tag{2.37}$$

$$\nabla \times E = i\omega\mu H \tag{2.38}$$

$$\nabla \times H = -i\omega\varepsilon E \tag{2.39}$$

where ω is the frequency of the wave, μ is the permeability, and ε is the permittivity. By doing some vector manipulation, the vector wave equation can be obtained:

$$\nabla^2 E + k^2 E = 0 \tag{2.40}$$

$$\nabla^2 H + k^2 H = 0 \tag{2.41}$$

where $k^2 = \varepsilon\mu\omega^2$ and $\nabla^2 A = \nabla \cdot (\nabla A)$. Besides satisfying Maxwell equations at points where ε and ω are continuous, the vector wave equation should also satisfy the other boundary condition, which is that the tangential component of the electromagnetic field is continuous across a boundary or discontinuity. More detailed explanation of the physics of absorption and scattering and the deduction of equations can be found in the book written by Bohren and Huffman [7].

2.4.2 Absorption and scattering theories for spheres

2.4.2.1 Mie scattering theory

Confusingly there are two sets of equations that are attributed to Mie, for light scattering, one of which is an approximation for non-absorbing particles that are much larger than the wavelength of the light. Hua and Ladommatos [92] give the following equation for the scattering intensity of light for particles larger than 0.5 μm in visible spectrum:

$$I_{sca}(n, \theta, d) = I_0 \cdot C_n \cdot f(n, \theta) \cdot d^2 \tag{2.42}$$

Where n is the real part of the refractive index, θ is the scattering angle, C_n is the number density of particles, and $f(n, \theta)$ is a complicated function of the refractive index, particle

shape, and the scattering angle. Another set of equations are introduced by Gastav Mie in 1908 to understand the varied colours in absorption and scattering exhibited by small colloidal particles of gold suspended in water [55]. In this paper, an analytical solution to the vector wave equations for a sphere in spherical polar coordinates was provided. Although Mie was not the first to solve the sphere problem, the most common term, the Mie theory, is used here. Before presenting the Mie theory formula, several parameters need to be defined. The first is the extinction cross section (C_{ext}), which is the ratio of the rate of extinction energy across the surface (W_{ext}) to the incident irradiance (I_i). It is the sum of the absorption cross section (C_{abs}) and the scattering cross section (C_{sca}):

$$C_{ext} = C_{abs} + C_{sca} \tag{2.43}$$

where

$$C_{ext} = W_{ext}/I; C_{abs} = W_{abs}/I; C_{sca} = W_{sca}/I \tag{2.44}$$

The extinction efficiency factor (Q_{ext}) is defined as the ratio of the extinction cross section area to the particle cross-sectional area projection onto a plane perpendicular to the incident beam (G). Definitions of scattering efficiency factor (Q_{sca}) and the absorption efficiency factor (Q_{abs}) are similar to the extinction efficiency factor:

$$Q_{ext} = C_{ext}/G; Q_{abs} = C_{abs}/G; Q_{sca} = C_{sca}/G \tag{2.45}$$

According to the Mie theory, the scattering efficiency factor and the extinction efficiency factor for a sphere can be described as:

$$Q^M_{sca} = \frac{2}{x^2}\sum_{n=1}^{\infty}(2n+1)(|a_n|^2 + |b_n|^2) \tag{2.46}$$

$$Q^M_{ext} = \frac{2}{x^2}\sum_{n=1}^{\infty}(2n+1)\Re\{|a_n|^2 + |b_n|^2\} \tag{2.47}$$

where x is the size parameter and defined as $x = \pi d/\lambda$ (d is the diameter of the particle and λ is the wavelength of the incident light), a_n and b_n are scattering coefficients and can be

calculated according to the formula, and superscript M represent the Mie theory:

$$a_n = \frac{m\psi_n(mx)\psi_n'(x) - \psi_n(x)\psi_n'(mx)}{m\psi_n(mx)\xi_n'(x) - \xi_n(x)\psi_n'(mx)} \tag{2.48}$$

$$b_n = \frac{\psi_n(mx)\psi_n'(x) - m\psi_n(x)\psi_n'(mx)}{\psi_n(mx)\xi_n'(x) - m\xi_n(x)\psi_n'(mx)} \tag{2.49}$$

$$\psi_n(x) = x j_n(x) = x\sqrt{\frac{\pi}{2x}} J_{n+0.5}(x) \tag{2.50}$$

$$\xi_n(x) = x h_n^{(1)}(x) = x(\sqrt{\frac{\pi}{2x}} J_{n+0.5}(x) + i\sqrt{\frac{\pi}{2x}} Y_{n+0.5}(x)) \tag{2.51}$$

where J_n and Y_n are the Bessel functions of the first and second kind; ψ_n and ξ_n are the Riccati-Bessel functions; m is the relative complex refractive index of the particle.

The direct calculation of the Mie scattering coefficients is well-known for being time-consuming due to the large iteration numbers for large particles. In addition, calculation of $\psi_n(mx)$ can be problematic because it will overflow when mx has a large imaginary part [24]. In 1947, Infeld [41] introduced the logarithmic derivative of $\psi_n(mx)$:

$$D_n(mx) = d[\log \psi_n(mx)]/d(mx) = \psi_n'(mx)/\psi_n(mx) \tag{2.52}$$

The function $D_n(mx)$ overcomes the problem of overflow and makes it possible to calculate the Mie scattering coefficients iteratively. Using the recurrence relations:

$$\psi_n'(z) = \psi_{n-1}(z) - \frac{n\psi_n(z)}{z};\ \xi_n'(z) = \xi_{n-1}(z) - \frac{n\xi_n(z)}{z} \tag{2.53}$$

Eq. (2.48) and (2.49) can be rewritten as:

$$a_n = \frac{[D_n(mx)/m + n/x]\psi_n(x) - \psi_{n-1}(x)}{[D_n(mx)/m + n/x]\xi_n(x) - \xi_{n-1}(x)} \tag{2.54}$$

$$b_n = \frac{[mD_n(mx)/m + n/x]\psi_n(x) - \psi_{n-1}(x)}{[mD_n(mx)/m + n/x]\xi_n(x) - \xi_{n-1}(x)} \tag{2.55}$$

The logarithmic derivative satisfies the recurrence relation:

$$D_{n-1}(z) = \frac{n}{z} - \frac{1}{D_n + n/z} \tag{2.56}$$

The function D_n can be calculated either by the upward recurrence or the downward recurrence. The upward recurrence is more efficient than downward recurrence simply because it needs no extra iteration to start with. However, the upward recurrence can be highly unstable if the imaginary part of the complex refractive index is large enough [62]. The downward recurrence is always stable but it takes a much longer time. Wiscombe (1980)[89] suggests a criterion to decide whether the upward recurrence can be used from a fitting polynomial to the experiment data. This criterion was as follow:

$$\Im(mx) \leq 13.78\Re\{m\}^2 - 10.8\Re\{m\} + 3.9 \tag{2.57}$$

where $\Im$is the imaginary part, and $\Re$ is the real part. Wiscombe also proposed a correlation to decide the number of interations (N) for different ranges of size parameter:

$$N = \begin{cases} x + 4x^{1/3} + 1 & 0.02 \leq x \leq 8 \\ x + 4.05x^{1/3} + 2 & 8 < x < 4200 \\ x + 4x^{1/3} + 2 & 4200 \leq x \leq 20,000 \end{cases} \tag{2.58}$$

After calculating the function D_n, the remaining Mie theory calculation is relatively easy. The Riccati-Bessel function $\psi_n(x)$ and $\xi_n(x)$ can be calculated by either downward or upward recurrence. Du (2004)[24] proposed another algorithm to calculate the Mie scattering coefficients by using the ratio of the Riccati-Bessel functions and also provided a way to estimate the number of significant digits of the calculated Riccati-Bessel functions and their ratios.

2.4.2.2 Rayleigh-Gans theory and Penndorf extension

When the particle size is small compared to the wavelength of incident light, the Mie theory can be simplified to the Rayleigh-Gans theory. The conditions for the validity of the Rayleigh-Gans approximation are:

$$|m-1| \ll 1 \,\&\, kd|m-1| \ll 1 \tag{2.59}$$

where d is the characteristic linear dimension of the particle, and k is the wave number. The Rayleigh-Gans approximation can also be considered as the field inside the particle is approximated by the incident field [7]. In this case, the Mie theory can be simplified to the following equations:

$$Q^R_{abs} = 4x\Im\{\frac{m^2-1}{m^2+2}\}[1+\frac{4x^3}{3}\Im\{\frac{m^2-1}{m^2+2}\}] \tag{2.60}$$

$$Q^R_{sca} = \frac{8}{3}x|\frac{m^2-1}{m^2+2}|^2 \tag{2.61}$$

where the superscript R represents the Rayleigh-Gans theory. When the size parameter is sufficiently small,

$$\frac{4x^8}{3}\Im\{\frac{m^2-1}{m^2+2}\} \ll 1 \tag{2.62}$$

Then, eq. (2.60) can be further simplified as

$$Q^R_{abs} = 4x\Im\{\frac{m^2-1}{m^2+2}\} \tag{2.63}$$

In practise, the upper limit of the size parameter is set at 0.3 when using the Rayleigh-Gans theory. In this case, the sphere diameter should not exceed 60 nm for the visible incident light. Penndorf (1962)[61] extends the size parameter to 0.8 by using a fitting equation to the experimental data:

$$Q^P_{sca} = Q^R_{sca}[1+2\frac{x^2}{M_1}(\frac{3}{5}M_3 - 2N_1x)] \tag{2.64}$$

$$Q_{ext}^{P} = Q_{abs}^{R} + 2x^2[N_1(\frac{1}{15} + \frac{5}{3}\frac{1}{M_4} + \frac{6}{5}\frac{M_5}{M_1^2}) + \frac{4}{3}\frac{M_6}{M_1^2}x] \tag{2.65}$$

Where subscript P represents the Penndorf extension, , and the Ms and Ns are defined as:

$$N_1 = 2nk;\ M_1 = N_1^2 + (2+N_2)^2;\ M_2 = 1+2N_2;\ M_3 = N_3 - 4;$$
$$M_4 = 4N_1^2 + (3+2N_2)^2;\ M_5 = 4(N_2-5) + 7N_3;\ M_6 = (N_2+N_3-2)^2 - 9N_1^2 \tag{2.66}$$

The practical significance of the Rayleigh-Gans theory and the Penndorf extension compared to the Mie theory will be demonstrated in the next section.

2.4.2.3 Comparison between different scattering models

As described in previous sections, the Mie theory is the analytical solution to Maxwell equations for spheres; the Rayleigh-Gans theory is the approximation of the Mie theory for small spheres; and the Rayleigh-Gans theory with the Penndorf extension is based on the Rayleigh-Gans theory but uses a polynomial function of the size parameter to extend the validity of the Rayleigh-Gans theory to larger particles. To quantify the accuracy of the Rayleigh-Gans theory and the Penndorf extension equations for different sizes spheres, the absolute error is defined as:

$$\text{error} = |\frac{Q^{R/P} - Q^{M}}{Q^{M}}| * 100\% \tag{2.67}$$

Since both the scattering efficiency factor and the absorption efficiency factor are functions of the complex refractive index, to simplify the analysis, the complex refractive index is taken as a constant value: 1.55 – 0.55i because it is very close to the most often cited value (1.57 – 0.56i). The influence of the variation of the complex refractive index will be discussed in detail in section 2.4.4. The comparison results are plotted as in Fig. 2.10. This figure shows that the efficiency factors calculated using the Mie theory usually lie between those calculated by using the Rayleigh-Gans theory and the Penndorf extension. The subplot of the scattering fraction in Fig. 2.10 indicates that when using the light extinction method to measure the temperature and soot loading, the scattering must be taken

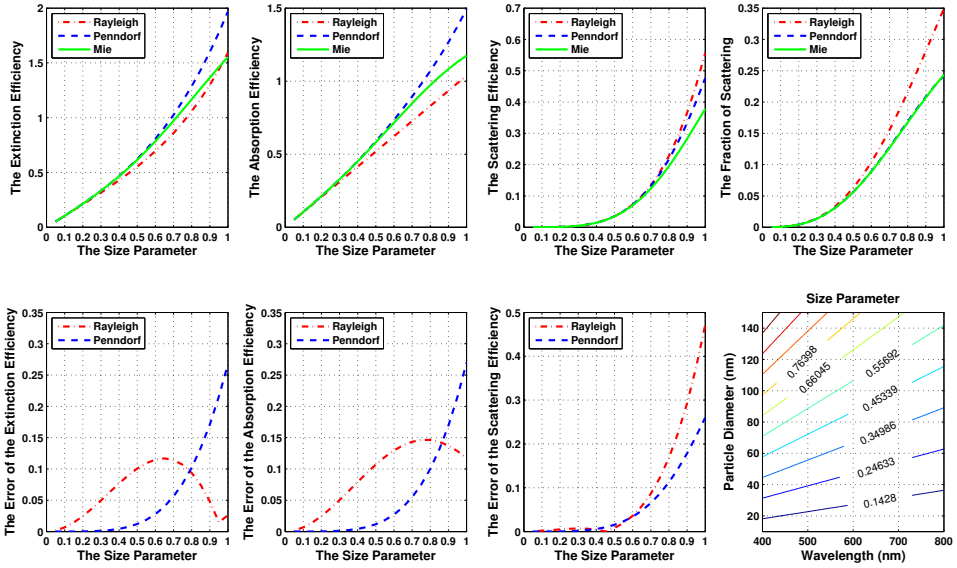

Fig. 2.10: Comparisons between different scattering theories

into account for accurate results when the size parameter is larger than 0.6. The absolute error plots in Fig. 2.10 show that the maximum size parameter when using Rayleigh-Gans theory is around 0.45, and is 0.8 when using the Penndorf extension if the tolerance of the absolute error is 10%. According to the contour plot of the size parameter in Fig. 2.10, the corresponding maximum sphere diameters when using the Rayleigh-Gans theory and the Penndorf extension in the visible spectrum are 58-110 nm and 100-145 nm.

2.4.3 Thermal radiation

When the temperature of the particle is above absolute zero, the particle will emit, absorb and scatter the electromagnetic radiation. Consider a spherical particle, which is enclosed inside an insulated radiation field, and is in thermodynamic equilibrium. If an imaginary spherical surface with radius R ($R >>$ radius of the particle r) is assumed as the source of illumination, the energy absorbed per unit time by the particle from each element ds is $C_{abs} * I_b * ds/R^2$. I_b is the black body radiation. Therefore, the total amount of energy

absorbed per unit time by the particle across all frequencies is:

$$W_{abs} = \int\int (C_{abs} I_b ds/R^2) d\omega = 4\pi \int_0^\infty C_{abs} I_b d\omega \tag{2.68}$$

Since the particle is in thermodynamic equilibrium, the rate of power emitted by the particle should be the same as is absorbed:

$$\int_0^\infty I_b (Q_{abs} - \varepsilon) d\omega = 0 \tag{2.69}$$

where ε is the emissivity of the particle and is defined as:

$$\varepsilon = \frac{W_e}{4\pi^2 r^2 I_b} \tag{2.70}$$

A sufficient condition for eq. (2.69) is that:

$$Q_{abs} = \varepsilon \tag{2.71}$$

This is the Kirchhoff's law for emission and absorption by an arbitrary spherical particle. At a first glance, it might be argued that eq. (2.71) is not a necessary condition because the excess absorption in a specific frequency (ω) can be balanced by the excess emission at another frequency. However, the detailed balance is a consequence of time-reversal symmetry and requires that the probability of any process be equal to the probability of the reverse process[65]. A more rigorous derivation of eq. (2.71) has been given by Kattawar and Eisner (1970)[43]. In this project, the optical thin assumption indicates that there is no incident light (no scattering) and no attenuation of the thermal radiation along the optical path. Therefore, eq. (2.71) can be applied in this project.

2.4.4 Complex refractive index

The complex refractive index of a particle relative to the surrounding media is a very important parameter to describe the wave property of the light when it goes through a media. The

Fig. 2.11: Ratio of the soot volume fraction to the extinction coefficient at different wavelengths (Fig. 2 in original paper)[76]

complex refractive index ($m = n - ik$) can be divided into the real part (n) and the imaginary part (k). The real part determines the phase velocity ($v = c/n$, where c is the speed of light in vacuum) in the media. The imaginary part determined the attenuation of the wave as it propagates through the medium.

2.4.4.1 The effect of wavelength on the complex refractive index

Both n and k are functions of wavelength of the light. However, the value $m = 1.57 - 0.56i$ is most often cited for particles within visible spectrum. Smyth and Shaddix (1996)[76] gave a brief review of the history of using $m = 1.57 - 0.56i$ and they concluded that this value is not directly from any experiment but is an approximation to the average value of the complex refractive index of particles in acetylene and propane flames in the visible spectrum reported by Dalzell and Sarofim (1969)[18]. Smyth and Shaddix also showed the difference in derived soot volume fraction when using different complex refractive index, as in Fig. 2.11.

2.4.4.2 Effect of temperature and composition on the complex refractive index

The dependence of the complex refractive index on the temperature is debated among different researchers. Howarth et al. (1966) [39] reported a heavy temperature dependence of the refractive index for pyrolytic graphite, while Lee and Tien (1981) [48] reported no dependence of the refractive index on temperature. Lee and Tien used a more rigorous dispersion model of graphite with two bond electrons and one free electron together with some in-situ flame transmission data to calculate the optical constants. They also investigated the effect of temperature and fuel composition on the complex refractive index and concluded that within a typical flame temperature range, the refractive index is insensitive to the temperature difference and the H/C (hydrogen to carbon) ratio of the fuel. Charalampopoulos

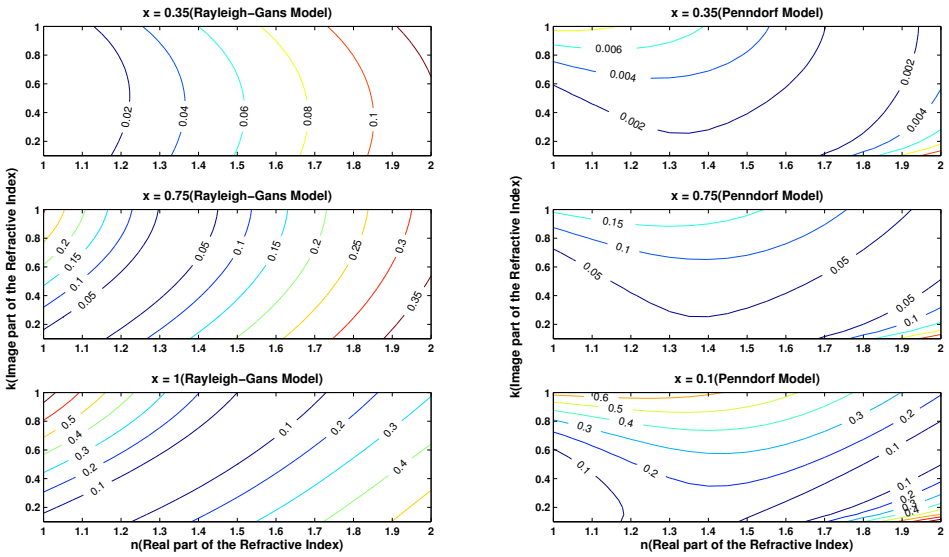

Fig. 2.12: Error band of the absorption efficiency calculated by using Rayleigh-Gans theory and the Penndorf extension when using different value of the complex refractive index

et al. (1989) [10] used the same dispersion model to investigate the effect of electron number densities on the refractive index. Their results indicated that both the real part and the imaginary part of the refractive index are not sensitive to the number densities of the free electrons and the first bond electrons at the visible optical transition wavelength. However, the number density of the second bond electron does affect both the real part and the imaginary part of the refractive index significantly. They also showed that the refractive index is not sensitive to the temperature under typical flame temperature ranges (> 1100 K).

2.4.4.3 The effect of the complex refractive index on the accuracy of different scattering models

The effect of variations in the complex refractive index on the accuracy of the absorption efficiencies calculated by using Rayleigh-Gans theory and the Penndorf extension is plotted in Fig. 2.12.

As Fig. 2.12 shows, when using the Rayleigh-Gans theory to calculate the absorption efficiency factor of small particles ($x = 0.35$ – the maximum particle diameter (D_{p-max})

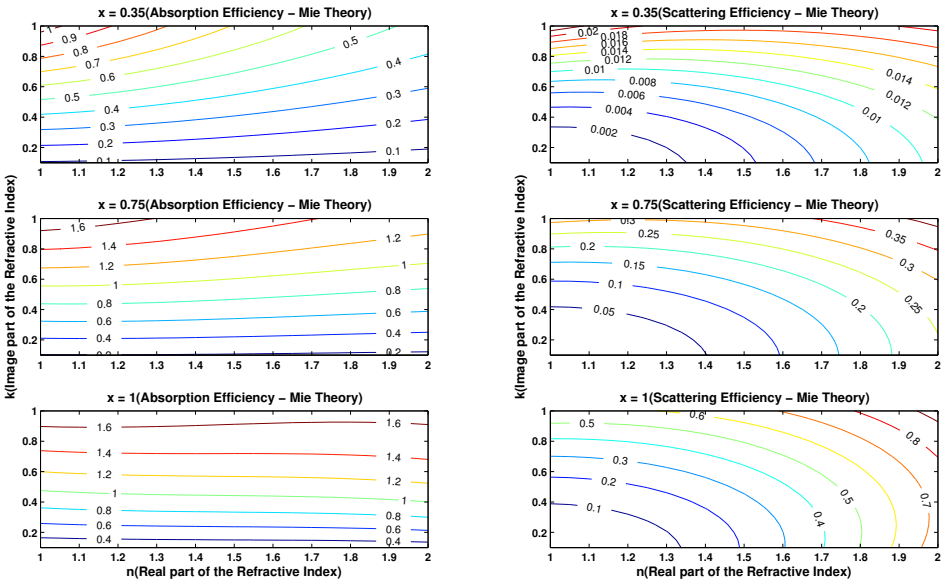

Fig. 2.13: Absorption and scattering efficiencies calculated by Mie theory when using different complex refractive index

ranges from 40 – 60 nm in visible spectrum), the error is well below 10%. However, if the Rayleigh-Gans theory is used to calculate the absorption efficiency of large particles ($x = 0.75$ – D_{p-max} ranges from 100 – 140 nm in the visible spectrum) by using different values of the complex refractive index, the error can range from 0 – 35%. Therefore, a acknowledge of the accurate value of the complex refractive index is of great benefit when measuring the temperature field and particle number concentration in a flame with large particles ($D_{p-max} > 60$nm). The Rayleigh-Gans theory with Penndorf extension is less sensitive to the change of complex refractive index, especially for small to median size particle ($x < 0.75$).

Fig. 2.13 shows the effect of the complex refractive index on the absorption and scattering efficiencies calculated by the Mie theory.

As Fig. 2.13 shows, the contours of the absorption efficiencies are very flat, which means that the absorption efficiency is only sensitive to the imaginary part of the complex refractive index, especially for large particles. This trend makes perfect sense, since the imaginary part determines the attenuation of the wave (absorption) as it propagates through the medium. As for the scattering efficiencies, both the real part and imaginary part of the

Fig. 2.14: Spectral extinction coefficient and the total emissivity of cylindrical and spherical particles [47](Fig.2 and Fig. 3 in orignial paper)

complex refractive index can impose a significant effect. Therefore, when measuring the temperature and soot loading by using the light extinction method, both the real part and imaginary part of the complex refractive index need to be chosen carefully while only the imaginary part of the complex refractive index is important for light emission measurement.

2.4.5 Effect of the morphology and size distribution of soot particles

In flame radiation analysis, the particles are usually assumed to be spherical and their absorption and scattering efficiencies are calculated by using the Mie theory. Many articles have reported that the soot particles in hydrocarbon flames are fractal aggregates (i.e. complex, branched, chain-like structures) consisting of different sizes of spherical primary particles [16, 56, 78]. A review on the scattering properties of soot aggregates has been made by Sorensen [78]. In practise, it is too complex to calculate the radiation by particles with all different shapes. Li et al. [49] investigated the numerical accuracy of the spherical approximations when calculating the scattering properties of the soot aggregates by calculating the phase matrix of the soot particles using the generalized multiple Mie theory. They calculated the phase matrix of the soot aggregate, and the spherical soot particle with either equivalent volume or surface area. Their simulation showed that the spherical particle with equivalent volume has weaker forward scattering and stronger backscattering compared to the soot aggregate, with an average error in the normalized phase function of around 20% for incident light of wavelength 628 nm, while the spherical particle with equivalent surface area has stronger forward scattering and weaker backscattering and an average error also around 20%.

A special approach suggested by Lee and Tien (1983)[47] to investigate the effect of the shape is to model the optical properties of particles with extreme shapes. According to their simulations, the extreme shapes were spheres and long chains (which are approximated by a

cylinder). The extinction efficiency of the particle with other shapes lay between these two extreme cases. Fig. 2.14 shows their simulation results. According to this figure, the extinction coefficient of spherical particles is characterized by a rapid decrease in the infrared spectrum range; therefore the radiation from cylindrical particles dominates the low temperature range, where the blackbody radiation peaks at long wavelengths. In consequence, the shape of the particle is very important for low temperature range thermal radiation but it can be neglected for a typical flame temperature.

With regard to the effect of this assumption of the validity of the measurements, the effect of changing particle size (and thus emissivity) on the colour ratio is relatively small, which means that the accuracy of the derived temperature is unlikely to be radically affected by the assumption of sphericity. The derived particle size itself is clearly subject to interpretation, given that the particles are likely to be anything but spherical. Finally, the absolute soot volume fraction measured by CBT-TCS will be affected by the spherical particle assumption because the absolute thermal radiation is proportional to the total surface area of the soot particles, which will be different for the soot aggregate compared to spherical soot particles. Another assumption made in CBT-TCS is that the soot particles within an individual voxel have the same shape, size and mass, which is normally referred to as the mono-disperse assumption. This will introduce some errors in both the temperature measurement and the soot volume fraction measurement depending on the homogeneity of the thermal radiation properties of the soot particles. But since the voxel size is small (a cube with 46 or μm side length), the error introduced is expected to be small.

2.5 Validity of the assumptions

The CBT-TCS is based on several assumptions. Their impact on the temperature and soot loading will be discussed in detail in this section.

2.5.1 Particulate temperature is the same as local flame temperature

The first assumption is that the temperature of the soot particle is equal to the local gas temperature. Many researchers have argued that this assumption is valid. Matsui et al. (1980)[54] showed that the particle temperature would respond to changes in the surrounding gas temperature within around 10^{-8} s. They also showed that the particle would achieve a steady-state temperature within 0.3 K of the surrounding gas temperature. Zhao and Ladommatos [92] summarise previous work and conclude that the temperature difference between soot particles and surrounding gases is below 1 K, providing thermal equilibrium has been attained, which typically happens on a time scale below 1 microsecond. Furthermore, it has been shown that soot-based pyrometry techniques agree within experimental uncertainty with gas-based (e.g. nitrogen) CARS measurements, for example, Hall and Bonczyk [33].

2.5.2 Interferences with soot luminosity is negligible

Besides the gaseous products and the particles, there are electronically excited radicals during the oxidation reaction process which can also emit radiation in discrete spectra, an effect called chemiluminescence. Therefore, it is necessary to quantify the chemiluminescence from those predominant intermediate radicals, especially the CH and C_2 radicals because their radiation is in the visible spectrum. To measure the chemiluminescence effect, an spectrometer with an absolute calibration made by Ocean Optics was used to detect the radiation from different parts of an ethylene-air flame. The fuel flow rate was set to 200 mL/min and the air flow rate was set to 42 L/min to produce a sooting laminar diffusion flame. The optic fibre could observe a circlular area with diameter of about 1.5 cm with a small pinhole and about 2.5 cm without a pinhole. The radiation from the central-bottom and central-middle of the flame was recorded by using a much larger integration time (500 ms) than that of the middle centre part (10 ms) due to their low level radiation intensities. The results are shown in Fig 2.15 and Fig. 2.16.

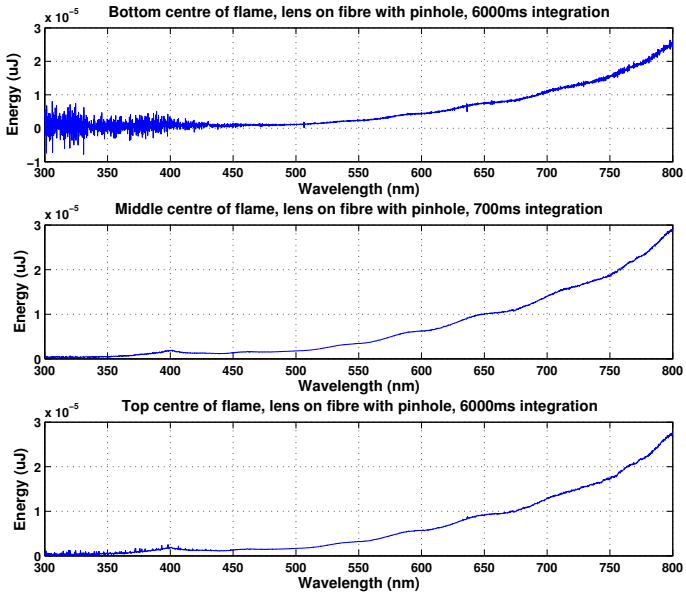

Fig. 2.15: Radiation from different parts of an ethylene laminar diffusion flame detected by the optic fibre with a pinhole (shorter integration time for the middle part of the flame because it's much brighter)

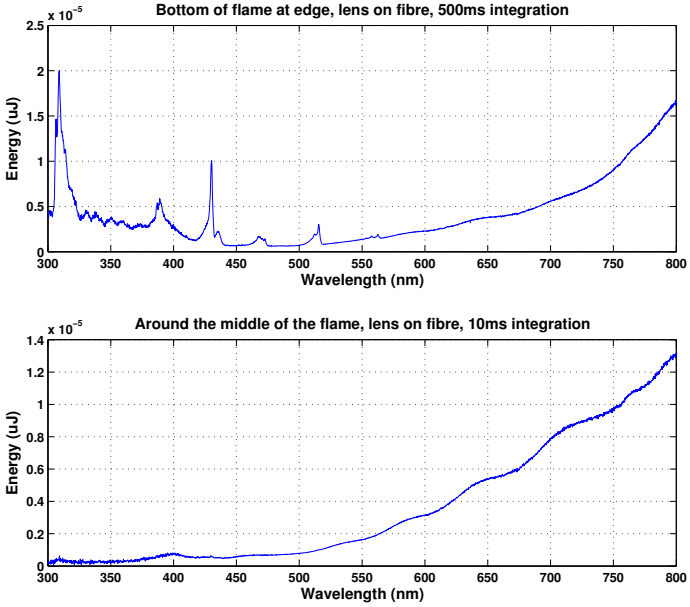

Fig. 2.16: Radiation from different parts of an ethylene laminar diffusion flame detected by the optic fibre without a pinhole (shorter integration time for the middle part of the flame because it's much brighter)

As can be seen from fig. 2.15, the chemiluminescence effect is negligible compared to the main yellow radiation in the central part of the flame. Fig. 2.16 shows the chemiluminescence effect in the bottom edge part of the flame. The spike at around 305-315 nm is the radiation from excited OH (0, 0) radical; the spike at around 380-390 nm is from excited CN/CH radicals; the spike at around 425-435 nm is from the excited CH (0, 0) radicals; the spike at around 430-435 nm is from the excited CH (2, 2) radicals; the spike at around 465 – 475 nm is from the excited C_2 (5, 4), (4, 3), (3, 2), (2, 1) and (1, 0) radicals; and finally the spike at around 505 – 520 is from the excited C_2 (0, 0) radicals. Fortunately, this part of the flame is unlikely to be measured by CBT-TCS, simply because the flame luminosity is far too low to record a reliable signal. Looking instead at the centre of the flame, the spectrum becomes continuous in character, with no significant contributions from narrow peaks indicating that chemiluminescence is negligible compared to the flame luminosity. Overall, it is possible that some regions of the flame could see some interference from chemiluminescence, but in this work CBT-TCS was only applied when the flame luminosity was high (maximum integration time is 1/60 second), making interference from radical species less likely.

The main species generated during the combustion of hydrocarbon fuels are CO_2 and water vapour. Since the radiation from gaseous products is from the transitions between the vibrational and rotational energy levels of the gas molecules, the radiation is concentrated in discrete spectral lines and bands. The emission bands of CO_2 are centred in the infra-red region around wavelengths of 2.0 2.7, 4.3, 9.4, 10.4 and 15 μm, and those of water vapour are around 1.38, 1.87, 2.7, and 6.3 μm[86]. Therefore, CO_2 and water vapour are strong infrared emitters only. Since the wavelength range covered by the Photron camera is well below 800 nm, the emission bands from water vapour and CO_2should be negligible.

When considering sooting flames, the effects of soot precursors – polycyclic aromatic hydrocarbons (PAH) – must be considered. Absorption spectra for most simple PAH molecules demonstrate absorption features in the ultraviolet except for a few very large PAH molecules in the lower end of the visible spectrum, such as terrylene ($C_{30}H_{16}$ has 450 to 600 nm substructure) and quaterrylene ($C_{40}H_{20}$ has 500 to 600 nm substructure) [23, 68]. PAH ions can

be strong absorbers in the visible spectrum [5, 68], but their concentrations (~ppt) are much lower than neutral PAH species (~ppm) [5]. The PAH family has many members which may limit the generality of this simple review, but since the wavelength range covered by the Photron camera is from 400-750 nm and PAH concentrations reduce with the increase in their molecular mass [87], the impact of molecular and ion PAH should be small.

It can be concluded that the effects of the emissions and absorption by the combustion gases are well controlled. A more detailed review of flame radiation is presented by Tien and Lee [83], who also concluded that the effect of chemiluminescence from intermediate radicals can be neglected in the main part of the flame.

2.5.3 Homogeneous particulate emissivity along the optical path

A very fundamental assumption for using the Hottel and Broughton correlation is that the emissivity of the soot particles (ε_λ) is distributed uniformly along the optical path. The errors introduced by this assumption can be significant and very difficult to correct, especially for the 2D pyrometry technique. Yan and Borman (1988)[90] investigated the effects of non-uniformity of the temperature and soot concentrations along the optical path on the accuracy of two-colour pyrometry. They concluded that the temperature measured by two-colour pyrometry generally corresponds to the mean flame temperature, but severe non-uniformities either in temperature or KL can lead up to 100K temperature deviation away from the mean value, and KL factors are even more sensitive to the non-uniformities. Theoretically, in CBT-TCS, this assumption can be avoided since the ε_λ is distributed discretely along the optical path and will be considered separately in different locations. However, some error will still be introduced when using a constant α for Hottel and Broughton scattering model.

2.5.4 The radiation attenuation along the optical path is negligible

Another assumption made in CBT-TCS is that the attenuation of the emitted radiation along the optical path is negligible. This assumption is usually referred to as the optically-thin approximation. The error caused by this assumption can be partially corrected by an iterative method introduced by Lu et al. (2009)[51]. The error in this method is introduced by the assumption that the attenuation term is a constant. The attenuation actually depends on the position of the voxels inside the flame and the particle distribution along the optical path. Since the soot volume fractions in typical hydrocarbon flames are very low (~ppm), the attenuation caused by the multiple scattering or absorbed by other soot particles will be very low.

2.6 Summary

The CBT-TCS is an optical diagnostic techniques based on the measurement of the thermal radiation from soot particles by using a calibrated colour camera and with the aid of 3D tomography technique. The detailed underlying physics, the mathematical algorithm used in 3D tomography, and the implementation strategies have been discussed in this chapter. Then, comparisons are made in the effects of using three different scattering models: the Rayleigh-Gans theory, the Rayleigh-Gans theory with Penndorf extension, and the Mie theory, to calculate the emissivity of the particle. It shows that within the visible spectrum, the Rayleigh-Gans theory can only be applied with reasonable accuracy (<10% error) when the size parameter (x, $x = \pi d/\lambda$,where d is the diameter of the particle and λ is the incident light wavelength) is less than 0.45 and the Penndorf extension can be applied when the size parameter is less than 0.8 when assuming a constant complex refractive index ($1.55 - 0.55i$). In addition, the effect of different parameters on the complex refractive index and emissivity, including the incident light wavelength, the temperature, the shape of the particle and the particle composition are discussed in detail. The discussion indicates that the complex refractive index and the emissivity of the soot particls are not sensisitive to these parame-

ters in typical flame temperatures. Moreover, the discussions on the assumptions made in CBT-TCS show that they are valid in typical flame conditions except some corrections may need to be introduced to compensate for the optical-thin approximation.

Chapter 3

Implementation of Cone-Beam Tomographic Three Colour Spectrometry (CBT-TCS)

3.1 Introduction

The detailed principles and assumptions made by Cone-Beam Tomographic Three Colour Spectrometry (CBT-TCS) have been introduced and discussed in previous chapter. In this chapter, the experiment setup, the software package used to implement the data analysis, and the sensitivity analysis will be introduced.

3.2 Experimental facilities and calibration

3.2.1 Experimental setup

The overall experimental setup is shown in Figs 3.1 and 3.2. As shown in Fig. 3.1, the experiment setup consists of a co-annular laminar diffusion flame burner, the air and fuel delivery system, and the imaging system.

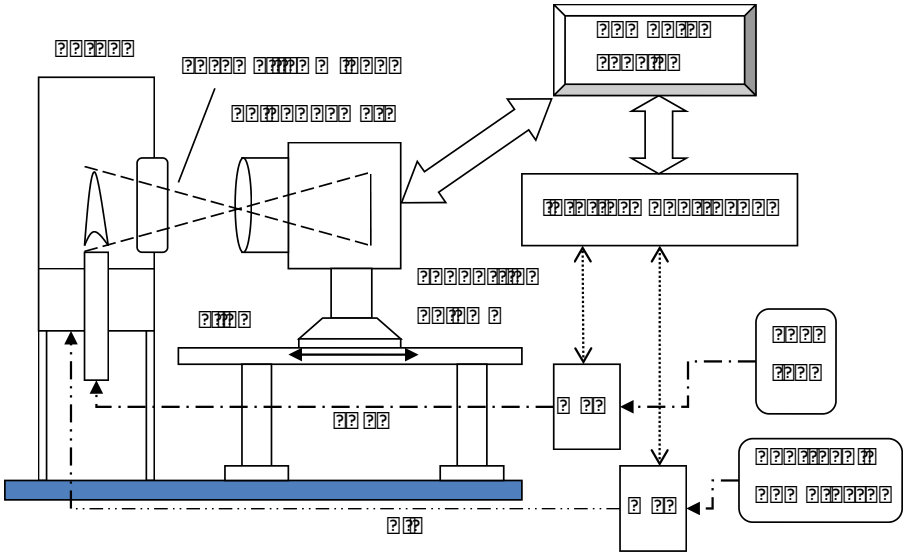

Fig. 3.1: Experimental set-up

The co-annular laminar diffusion flame burner is a copy of the burner described by Santoro et al. (1983) [69], and its design is shown in Fig. 3.3. Glass beads and ceramic honeycombs are used to ensure a uniform air flow. To minimize the glare and light reflection from the inner walls of the burner chimney, the wall surface is black anodized and only one fused silica window is used to obtain the image of the flame.

The gaseous fuel is stored in a compressed gas cylinder and its exit pressure is controlled by a pressure regulator. The air is from a central gas compressor. The mass flow rates of air and fuel are accurately controlled by two mass flow controllers (MFCs). An interface control box was built up to control and record the flow rates of fuel and air. The control box consists of a power supply (± 15 V DC), two National Instruments Data Acquisition (DAQ) cards and several BNC[1] sockets. Each DAQ card has eight analogue input channels with a sampling rate up to 48ks/s, two analogue output channels, and 12 TTL/CMOS digital I/O lines. The analogue input channels are used to log the actual flow rate signals; the analogue output channels are used to control the mass flow rates remotely; and the digital I/O channels are used to fully open or close the mass flow controllers. A premixing chamber filled with metallic beads is used when there is a second fuel or diluent.

Finally, a Photron® FASTCAM 1024PCI high speed camera is used to record the flame

[1] Bayonet Neill-Concelman connector

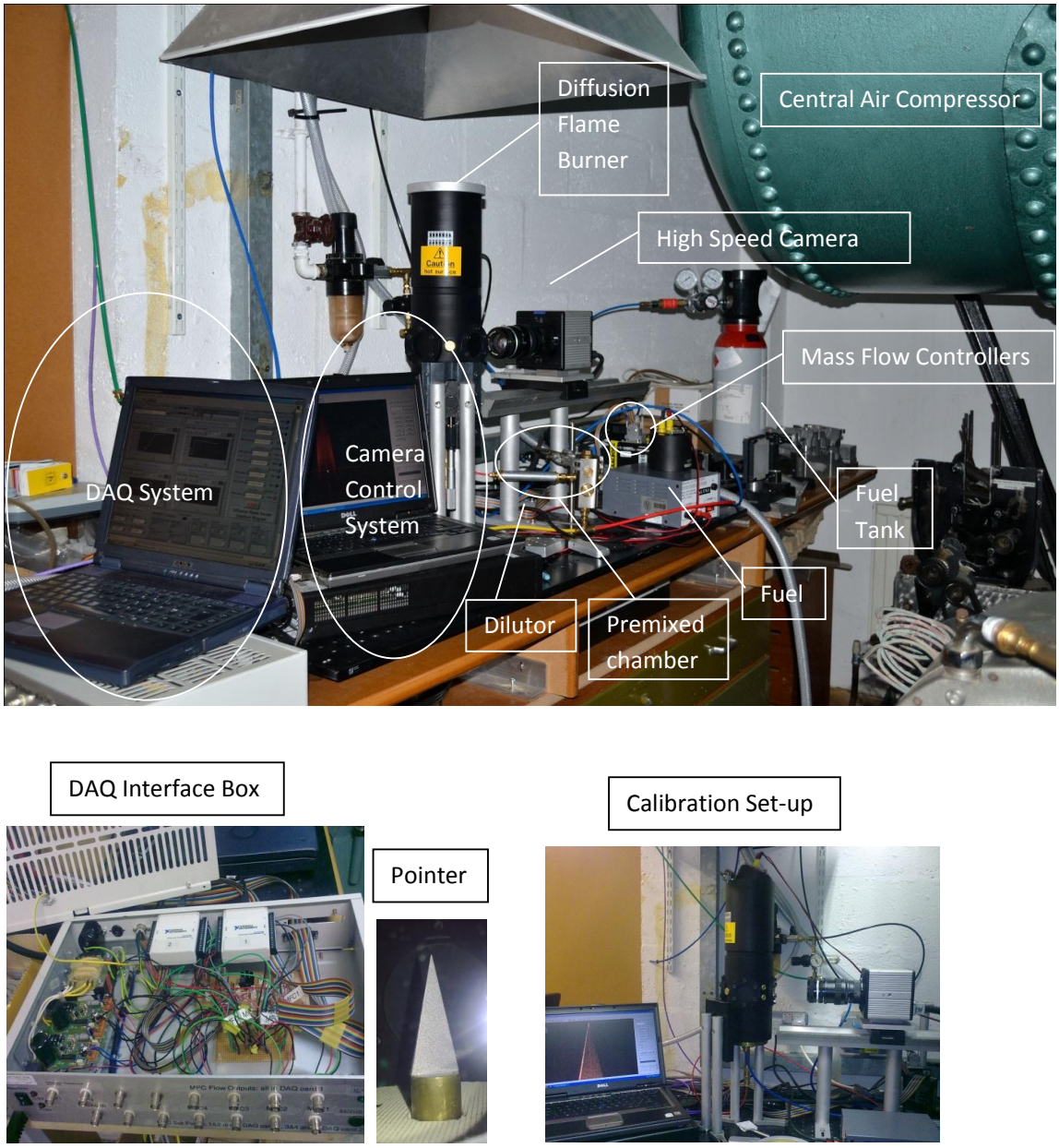

Fig. 3.2: Experimental apparatus

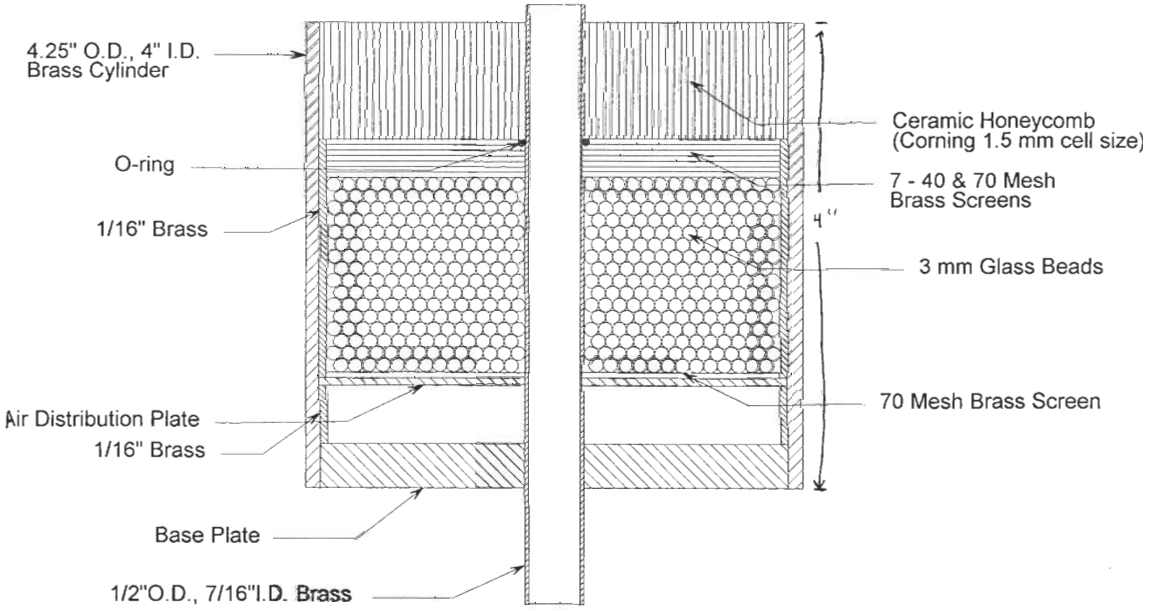

Fig. 3.3: Santoro diffusion flame burner [69]

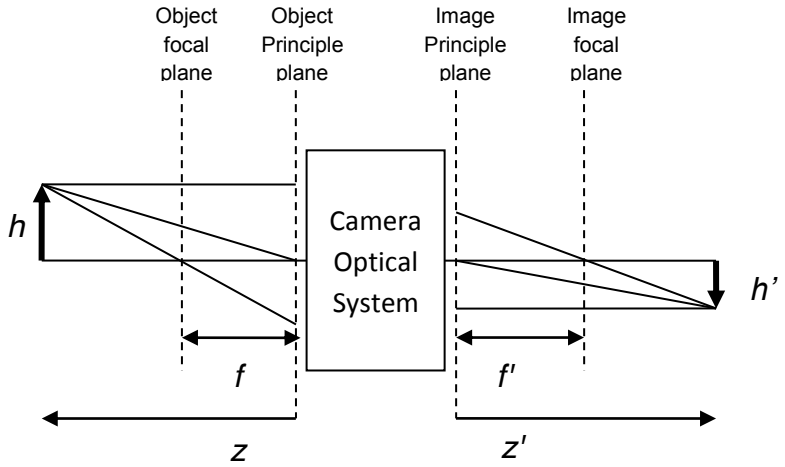

Fig. 3.4: Camera optical system

image. The maximum resolution is 1024*1024 pixels with a 17 μm pixel width. The image can be saved in the Bayer format which only records the true colour channel value for each pixel without doing any on-board processing such as colour demosaicing. A half-cone pointer (see Fig. 3.2) is used to find the focal plane and the central axis of the flame. The camera optical system forms a cone beam projection system as in Fig. 3.4. According to Newton's lens equation, the size of the image (h') and that of the object (h) is related as: $h'/h = f/(z+f) = (z'+f')/f'$. Rearrange this equation to get: $h'/z' = -(f/f')(h/z)$. Since f and f' are the focal lengths in the object side and image side respectively and their ratio is constant for a fixed optical system, the objects which share the same slope h/z will be in the same position on the detector. Therefore, the projections form a cone and the vertex point is the centre of the object's principle plane. The validity of Newton's lens formula is based on the assumption that all objects are within the depth of field of the optical system. The detailed depth of field analysis will be shown later in section 3.3.1.

3.2.2 Diffusion flame burner interface control program

The diffusion flame burner control interface program is written in Labview 2009. Its front panel is shown in Fig. 3.5. It can be divided into three parts: the analogue input interface, the analogue output interface, and the digital output interface.

The analogue input interface is used to monitor and record the output signals from the mass flow controllers. All four output voltage signals are logged by a single DAQ card. Then, according to the selection of the mass flow controller flow range and gas type from pull-down menus, the mass flow controller will be identified, and the calibration data can be selected and then the voltage will be converted into the actual mass flow rate (g/min) and displayed on screen. When the mass flow rate departs from the set point, an alarm 'LED' will be lit.

The analogue output interface is used to control the mass flow rates by sending 0-5 V analogue voltage signals. There are two modes by which to control the mass flow rates.

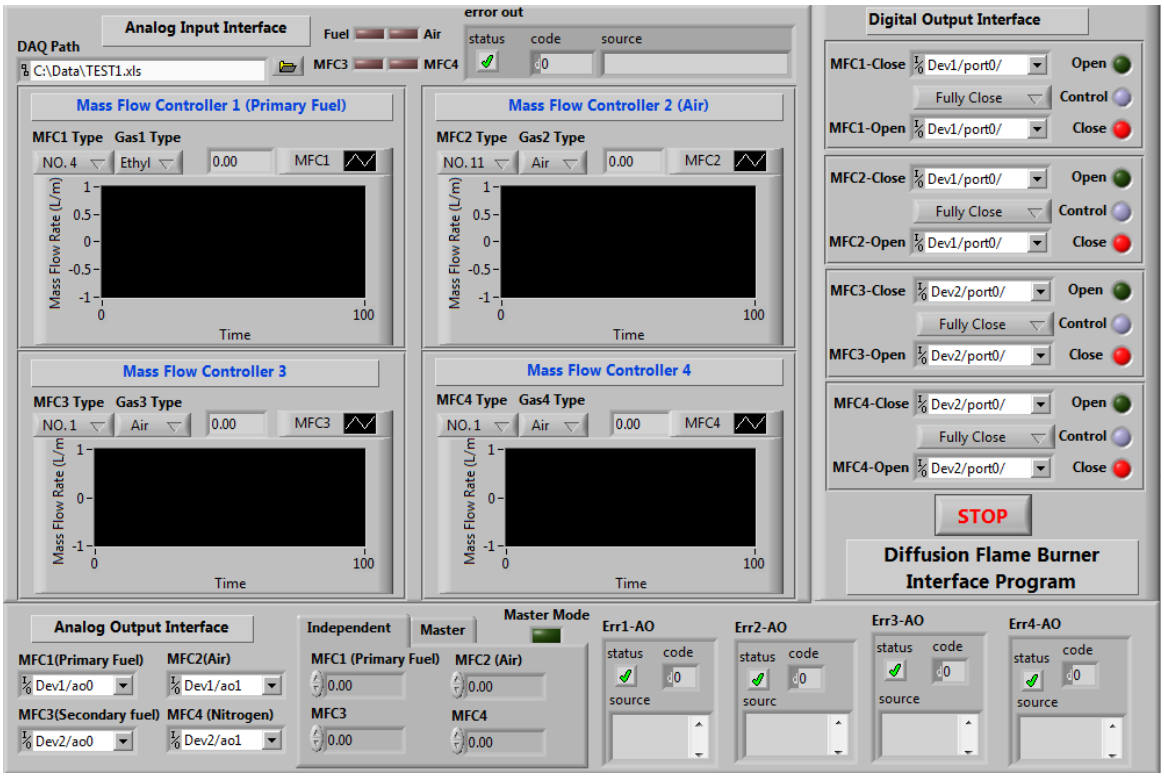

Fig. 3.5: Front panel of the Labview program for controlling the gas flows

The first one is called the "Independent Mode". In this mode, all four mass flow controllers are operated independently so that the air-fuel ratio can be varied. The second mode is the "Master Mode". In this case, only the air mass flow rate is controlled directly, the fuel mass flow rate is calculated by matching the velocity of the air and fuel to achieve a more stable flame. For each mass flow controller channel, there is a menu to identify the particular mass flow controller that has been connected and second menu to identify the gas that will be controlled.

The last part is the digital output interface. All mass flow controllers have two separate digital channels, which are activated by low-state TTL signals, to fully open or fully close the valve inside. A pull-down menu is used to choose between three states: 'fully open', 'fully closed', and 'control'.

The whole program and all four mass flow controllers can be shut down by clicking the "stop" button.

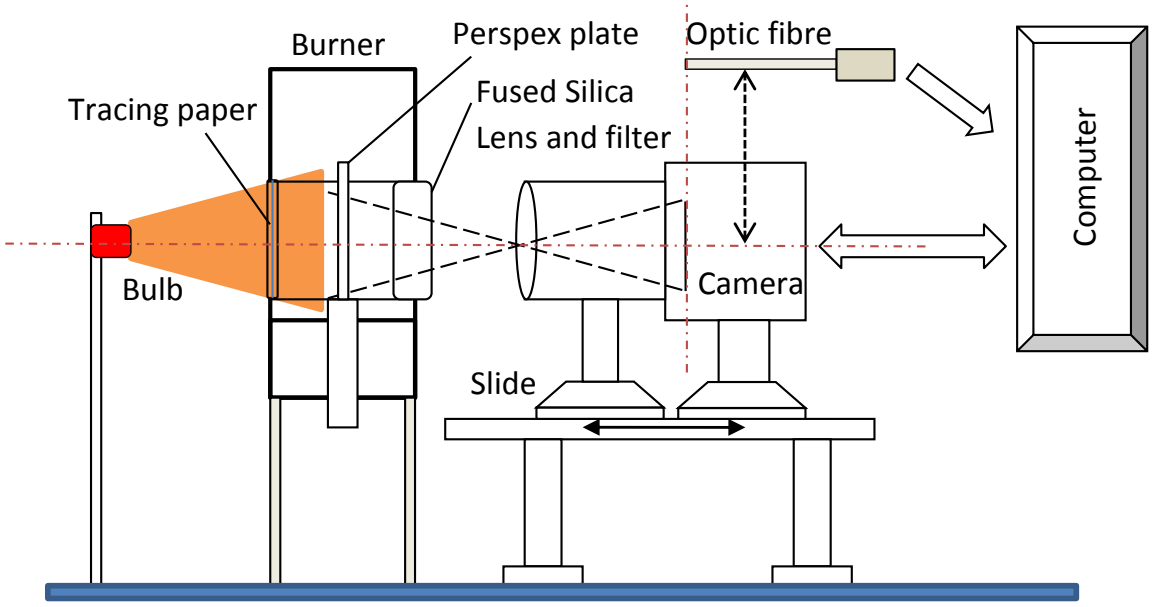

Fig. 3.6: Absolute calibration setup by using a camera

3.2.3 Absolute calibration of the camera sensor

To measure the soot volume fraction, the absolute calibration of the camera CMOS sensor is needed. This is done by using an absolute calibrated spectrometer with a fibre optic input made by Ocean Optics. The *in situ* calibration set-up is shown in Fig. 3.6. Tracing paper was placed between the halogen filament bulb and the Perspex plate to produce a uniform illumination area. The dimension of the camera sensor is 17.4 x 17.4 mm and the full resolution is 1024 x 1024 pixels. Because the diameter of the tip of the optic fibre is 1mm, the required uniformly illuminated area is a circle and its diameter is around 60 pixels.

The camera was firstly used to record the image of the illumination of the opague Perspex plate in Bayer format (raw pixel values only). Then red, green and blue value (R', G', B') at each pixel was calculated by using the bi-linear colour interpolation algorithm as introduced in section 2.2. To reduce the variation of light intensity, 100 images were taken to produce the average image. The false colour images of the pixel value for the separate colour channels of the light source are shown in Fig. 3.7. This figure clearly shows that the intensity variations within the central area of 120 pixel diameters are less than 2%. The average RGB value within this area is [199, 216, 135].

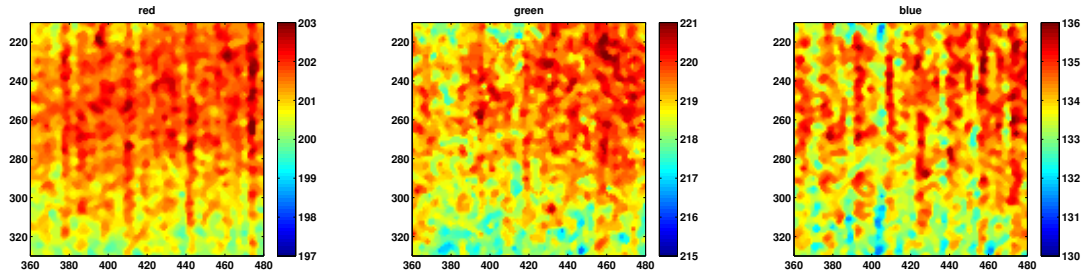

Fig. 3.7: Intensities of separate colour channels in the light source image

Then, the optic fibre replaced the camera to record the raw spectrum. To make sure the optic fibre is in the plane of the camera sensor and is pointing at the central area, a grid with a mark in the central position was stuck to the Perspex plate and some tracing paper was placed at the focal plane behind the lenses to find the centre of the focus plane, as shown in Fig. 3.8. Then, the tracing paper and the grid were removed and the optic fibre recorded the raw spectrum of the light source. To make sure that the optic fibre measured all the light as it passes through the lenses, a small aperture size should be used ($f/32$). The raw spectrum (Fig. 3.9) times the camera response (Fig. 2.3) produced the relative intensity curve. By taking the integral over the visible spectrum and multiplying by the ratio between the area of a single pixel and that of the tip of the optic fibre, the intensities of the red, green, and blue channels (R,G,B) at a single pixel were decided. Then the ratio R/R', G/G', and B/B' were calculated as the relative sensitivity factor of the camera sensor. The relative sensitivity factors for the red, green and blue channels of the camera sensor are [83.6, 83.7, 88.9] aJ/count[2] . The overall mean relative sensitivity factor is 85.4 aJ/count.

The radiance received by the camera sensor (I_s) and that emitted by the flame (I_f) is correlated by the following equation:

$$I_s = I_f \cdot \prod T_{optics} \cdot M^{-2} \cdot \eta_{collection} \tag{3.1}$$

T_{optics} are the transmission efficiencies of the different optical components, such as the lens and the filter. M is the magnification factor for the lens system, and its value for current experiment setup is 0.747. The $\eta_{collection}$ is the collection efficiency, and it is calculated by

[2]aJ/count: attocjoule (1 aJ = $1 * 10^{-18}$ J) per count (the pixel value; ranges from 0 to 255)

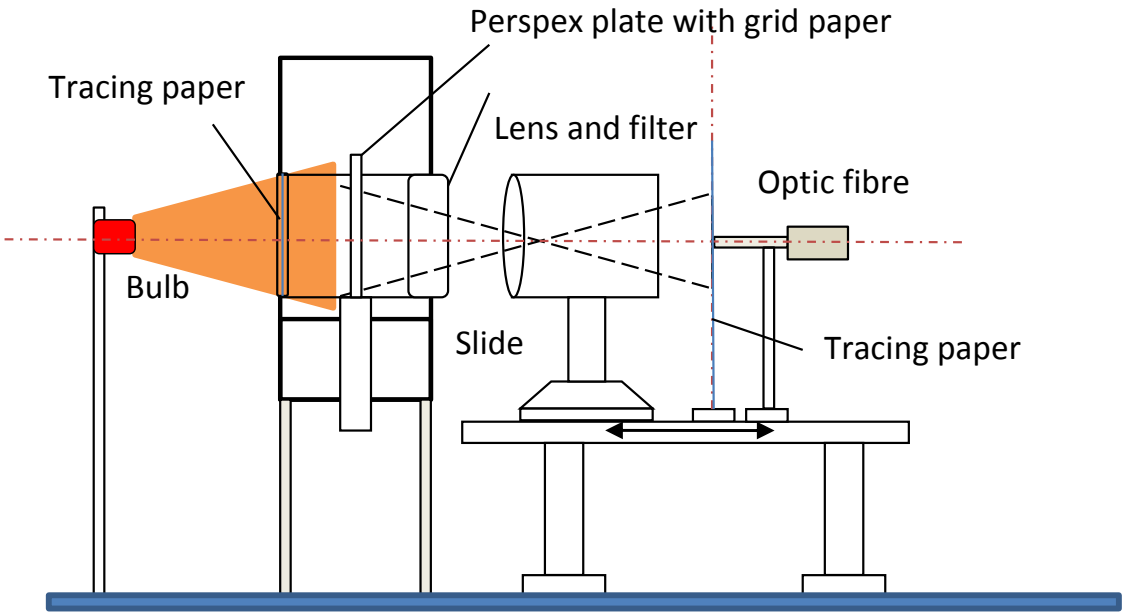

Fig. 3.8: Absolute calibration setup by using an optic fibre

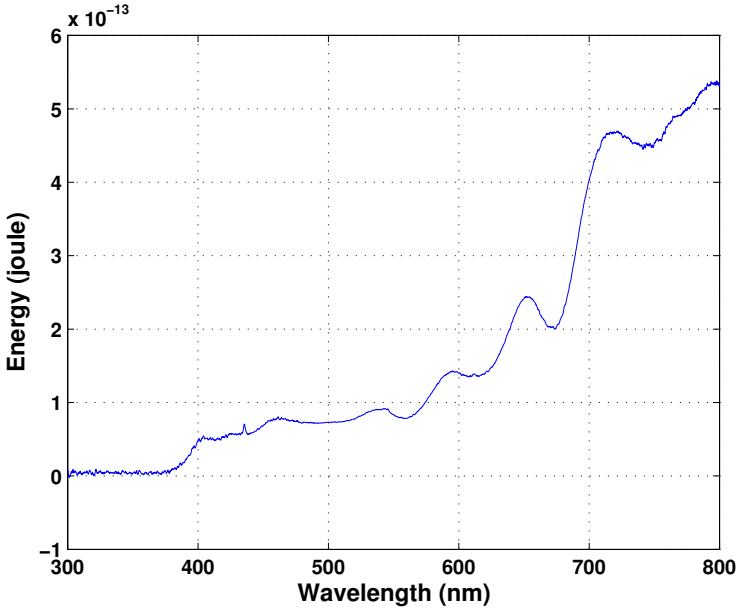

Fig. 3.9: Raw spectrum of the light source detected by the optic fibre

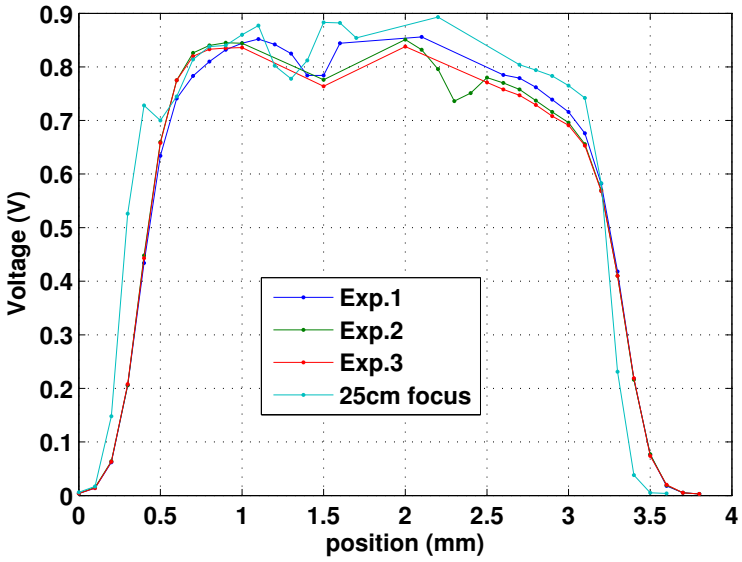

Fig. 3.10: The transmitted laser beam density when the optic system at different radial positions

eq. (3.2)

$$\eta_{collection} = \pi r_{aperture}^2/(4\pi R^2) \tag{3.2}$$

where R is the distance between the lens and the flame. Therefore, to calculate the radiance received by the camera, the absolute transmissions of various optical components and the diameter of the aperture need to be measured. These measurements were carried out using laser beams. To measure the diameter of the aperture, a 644nm He/Ne laser with 0.45 mm beam width was shone through the iris. The whole optical system, including the 50mm lens, a LEE filter and a 2 times convertor, was tranlated horizontally and the energy of the transmitted laser beam was recorded by a photomultiplier, as shown in fig. (3.10).

The horizontal aperture size is determined by the distance between the positions where the intensity is half the maximum intensity because the centre of the laser beams at these two points is coincident with the iris border. The repeatability of this experiment is good, as seen in Fig. 6.10. Similar measurements were carried out at two different heights to decide the aperture diameter since the centre of beam may not be in the same horizontal plane as the aperture centre. According to a simple geometric analysis, the aperture radius (r) can be calculated in terms of two horizontal aperture lengths (d_1 and d_2) and the height between

them (h) by eq. (3.3):

$$r = \sqrt{(\frac{d_2^2 - d_1^2 - 4h^2}{8h})^2 + \frac{d_2^2}{4}} \tag{3.3}$$

The aperture diameter for current optic setup ($f/16$) is 2.93 mm according to the calculation, which is not far from to the theoretical aperture diameter (3.125 mm = f/N = 50 mm/16).

The absolute transmission efficiency of individual optical component was measured by a spectrophotometer. An iris diaphragm was also used to reduce the monochromatic light beam width so as to make sure the light detectors have collected all the transmitted light. Moreover, to test the influence of the internal reflections between the optical components and reduce the uncertainty caused by the positions of the optical components inside the spectrophotometer during measurement, the spectral response of the combined optic component was also measured. The results suggested a 1.22 multiplication factor for calculating the overall transmission efficiency when using individual transmission efficiency of different optical component. The uncertainty in spectrophotometer experiment is around 2%, and is mainly related to the position of the measured objects inside the spectrophotometer. These results were also verified by using three laser sources at different wavelengths (405 nm, 532 nm, and 655 nm). The laser experiment suggested a multiplication factor of 1.18. The uncertainty in the laser experiment is mainly caused by the instability of the laser sources and it is estimated at around 6%. Therefore, the difference in the multiplication factor is well within the uncertainty of the experiment. The transmission efficiency data from both experiment are plotted in Fig. 3.11.

The calibration process is overall accurate, since the uncertainty caused by the misalignment of the optic fibre was estimated at around 1% and the variation of the light intensity in the central area is also around 1% for the camera detector calibration test.

3.3 Optical considerations

To undertake CBT-TCS measurements, the depth of field should be calculated so as to make sure it covers the flame region along an optical path. The lens aberrations, such as chromatic

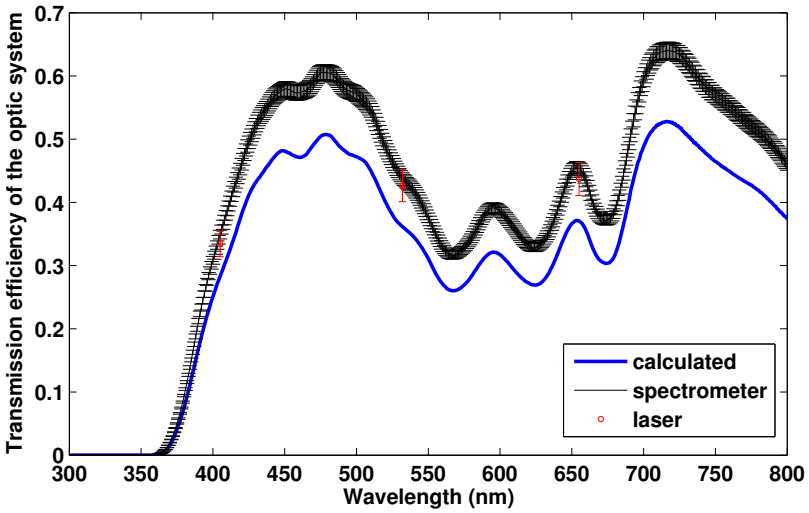

Fig. 3.11: Transmission efficiency of the optic systems (the blue one is calculated by multiplying individual transmission efficiencies; the red one is the blue one times the mutiliplication factor (1.8) suggested by the laser experiment; the black one is the direct measurement data; the errorbars on the red and black curves are experiment uncertainties)

aberration, and diffraction effects, also need to be considered so as to be able to quantify the accuracy.

3.3.1 Depth of field

The depth of field is the distance through which the subject is imaged without becoming noticeably unsharp. Outside this region, the definition falls off progressively. This section provides some simple depth of field calculations (as in Fig 3.12) based on the simple lens formula.

According to the simple lens formula:

$$\frac{1}{u}+\frac{1}{v}=\frac{1}{f} \tag{3.4}$$

Then

$$v=\frac{u\cdot f}{u-f} \tag{3.5}$$

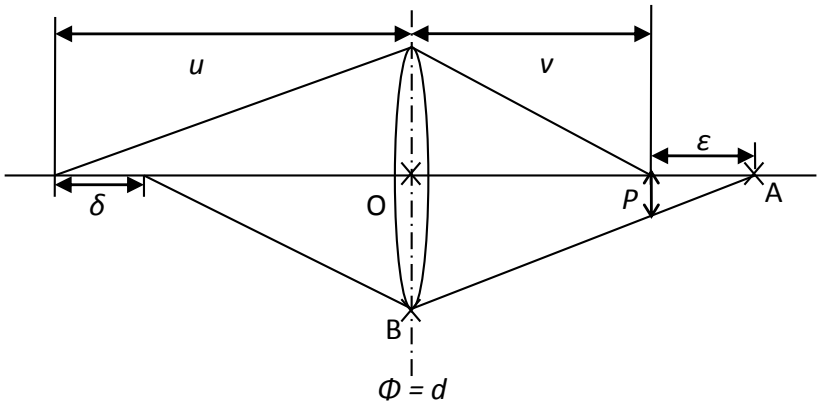

Notes: *u*: distance to object; *v*: distance to image; *f*: focus length; *p*: radius of the image from a point *N*: aperture number (*N*=*f*/*d*)

Fig. 3.12: Depth of field of the camera

Similarly,

$$v + \varepsilon = \frac{(u-\delta)\cdot f}{u-\delta-f} \tag{3.6}$$

Now combine eq. (3.5) & (3.6) and rearrange the formula:

$$\varepsilon = \frac{\delta \cdot f^2}{(u-f)\cdot(u-\delta-f)} \tag{3.7}$$

Consider the similarity of the triangle AOB

$$\frac{p}{d} = \frac{p}{f/2N} = \frac{\varepsilon}{\varepsilon+v} \tag{3.8}$$

Combine eq. (3.7) and (3.8)

$$p = 0.5N^{-1}\cdot f^2 \cdot \frac{\delta}{(u-\delta)\cdot(u-f)} \tag{3.9}$$

Therefore, to use a larger aperture to increase light gain without sacrificing the depth of field, the user needs to either use a close focus lens or increase the distance to the object. In the current experimental setup, the single pixel width in the camera sensor is 17μm, the focal length (f) is 100mm. The aperture size is chosen as $f/32$ to balance the effect of diffraction and other kinds of lens aberrations with the depth of field. If the flame thickness δ is assumed to be around 10 mm, then u and v can be calculated at different resolutions,

Table 3.1: Field of view calculation results

Resolutions (pixel width)	1(1*17μm)	2(2*17μm)	3(3*17μm)
u(cm)	36.1	27.4	23.6
v(cm)	13.8	15.8	17.4

as shown in Table 3.1. To verify the value of u and v in the experimental setup, the height of the real object (h) and the image size (h') need to be measured. Then, according to the simple lens geometry relationship: $h/h' = u/v$, and eq. (3.4), u and v can be checked.

It should be noticed that when different values of u are chosen, the effective aperture size of the lens is different, especially when using close-up lenses or macro extension tubes. The effective aperture size can be estimated using the following equation:

$$\text{effective } f\text{−stop} = f\text{−stop} \times (1+M) \tag{3.10}$$

Usually, the effective f-stop size, which is defined as the ratio of the focus length and the aperture diameter, is calibrated at infinity by the manufacture. For low magnifications (< 0.25), the extension of the focus length is tiny so that the lens is always roughly one focal length away from the camera sensor. But when the magnification becomes larger, the lens becomes so far away from the sensor such that the focal length becomes noticeably longer. As a consequence, the effective f-stop value increases, which means a smaller effective aperture size and less light collected. This effect can be illustrated by fig. 3.13. With the same optical setup and the same nominal f-stop, the pixel value of the image with a small magnification factor (left) is higher than that with larger magnification factor (right).

3.3.2 Lens abberation

Lens aberrations describe the way in which the image departs from ideal, and they can be classified into three main types. The first type is *chromatic aberration*. This is caused by the changes in the refractive index of glass with wavelength. There are many remedies to overcome this kind of aberration. One way is to use a compound achromatic lens, such as

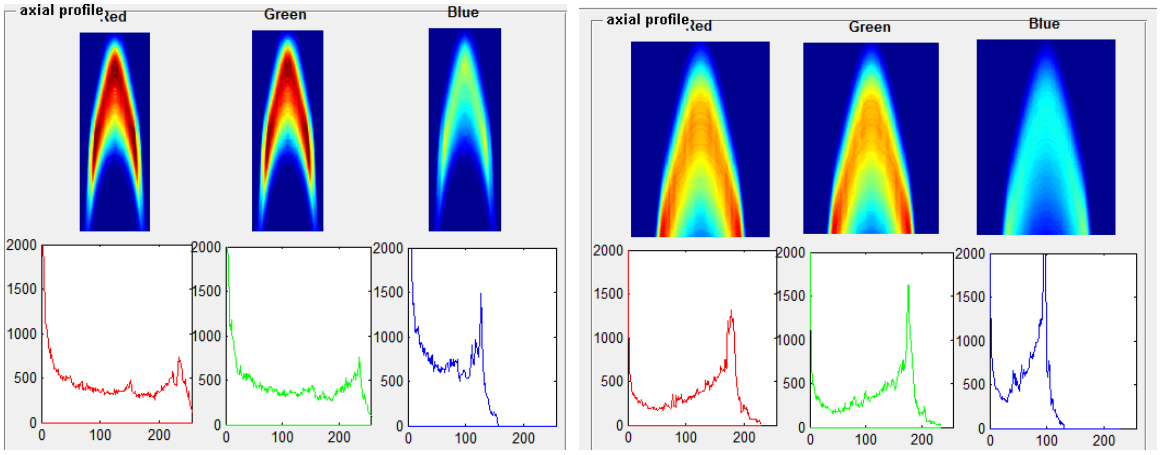

Fig. 3.13: Comparison of recorded pixel value at different field of views (Left is for 2 pixels resolution, and right is for 3 pixels resolution; upper is the false colour intensity distribution, and the lower plots are the histogram of pixel value for the individual colour channels)

the Nikon lens used in this project. But the most convenient way is to reduce the aperture size. The second aberration is *spherical aberration*. This refers to the effect that a spherical lens does not bring light incident onto different parts of the lens into a point focus. This can be corrected by using an aspheric lens. Similarly, using a smaller aperture can also reduce this kind of aberration. The last form of aberration is caused by *diffraction*. This happens when light passes through a very narrow aperture and it can be explained by the Huygens-Fresnel principle. Because of the diffraction, the image of a point source is not a point but a circle, which is called the *Airy Disc*, even with a perfect lens. The diameter (D_A) of the Airy Disc is calculated by:

$$D_A = 2.44\lambda N \tag{3.11}$$

Therefore, the diffraction becomes more significant when using a smaller aperture. As a consequence, balance between the diffraction and other two kinds of lens aberrations need to be carefully addressed when choose the aperture size. Under current optical setup, the diameter of the Airy Disc is between 15.6 – 27.3 μm depending on the wavelength of the incident light beam.

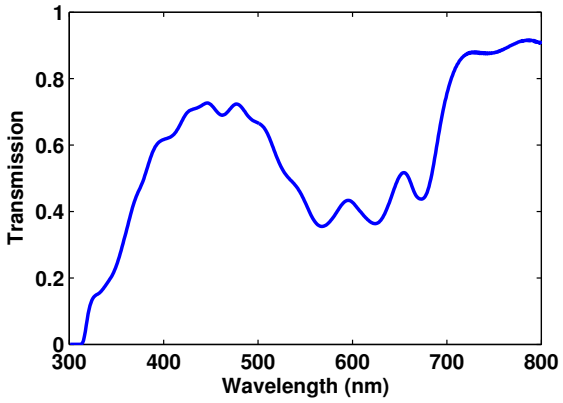

Fig. 3.14: LEE 281 filter transmission efficiency curve

3.3.3 Optical filter

The calibration curve of the camera (Fig. 2.3) shows that the camera has a relatively low blue light sensitivity. To increase the blue light gain and avoid light saturation in the other colour channels, an optical filter (LEE281, Fig. 3.14), which has high blue light transmission efficiency and low red light transmission efficiency, was used. To further reduce the effective aperture size and increase the spatial resolution, a 2^* macro extension tube was used. The effect of the macro extension tube on the effective aperture size can be calculated according to eq. (3.10).

3.4 Implementation in MATLAB

Several MATLAB code packages have been developed to implement the cone-beam tomography to the recorded data and its post-processing. The main program is based on the Open Source Cone-beam Reconstructor (OSCaR), a MATLAB GUI (Graphical User Interface) package written by Rezvani et al based on the FDK tomography algorithm[27][3]. The original OSCaR is used to reconstruct a 3D image from 2D X-ray images gathered by a cone-beam X-ray CT scanner. In this project, the modified OSCaR (OSCaR-P) is used to reconstruct the spatial temperature, soot diameter and soot volume fraction distributions of a laminar diffusion flame from its images taken by a carefully calibrated camera. Several

[3]OSCaR is downloaded from URL: www.cs.toronto.edu/~urezvani/OSCaR.html

other MATLAB GUIs are developed to merge data from different portions of the flame, and to display and save the selected data.

3.4.1 OSCaR-P software package

The main panel for OSCaR-P is shown in Fig. 3.15. It consists of four independent sub-panels to call the other four GUIs. The first GUI is used to create the 2D colour map. The second GUI is used to specify parameters that describe the geometry and resolution of the experimental setup. This GUI is based on the original software package but extends the pre-processing function to all three different colour channels. Then, the FBP algorithms are applied in the third GUI to reconstruct the 3D colour field. This GUI is also based on the original software package and extended the reconstruction function to all three different colour channels independently. But, a slightly different FBP algorithm is applied due to the different experimental setup. In addition, an extra control for the zero padding length has been added compared to the original one. Finally, the fourth GUI can construct the look-up table and find the corresponding property field in each voxel.

3.4.1.1 Data creation GUI

The OSCaR-P data creation GUI is shown in Fig. 3.16.

The background image should be imported first to subtract it from the flame image. Then the net flame image will be displayed on the screen using the jet colour map. Clicking the “Processing” button will do the colour demosaicing (see Fig. 3.16). The reconstructed colour image will be shown on the left figure in the GUI panel. Since the flame is axis-symmetric, the colour flame images taken from different gantry angle are the same, so that the 2D projection data group used to implement the FBP algorithm can be created by duplicating the reconstructed colour flame image over 360 gantry angles. Before exporting the data file, several parameters need to be specified, as listed in Table 3.2.

Fig. 3.15: OSCaR-P Main GUI

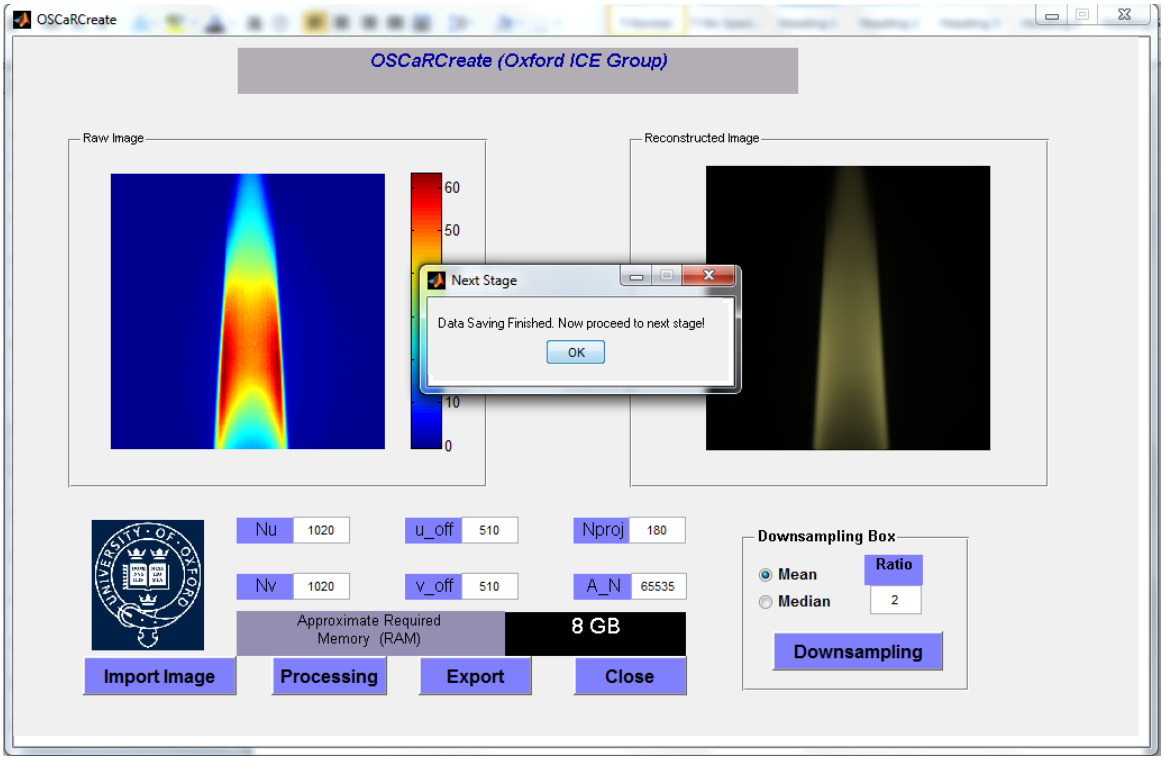

Fig. 3.16: OSCaR-P – data creation GUI

Table 3.2: Parameters in OSCaR-P data creation GUI

Parameters	Description
N_u	Pixel number in the vertical direction
N_v	Pixel number in the horizontal direction
u_off	Vertical postion of the centroid
v_off	Horizontal position of the centroid
N_{proj}	Number of projections
A_N	Air normalization coefficient (for x-ray image only)

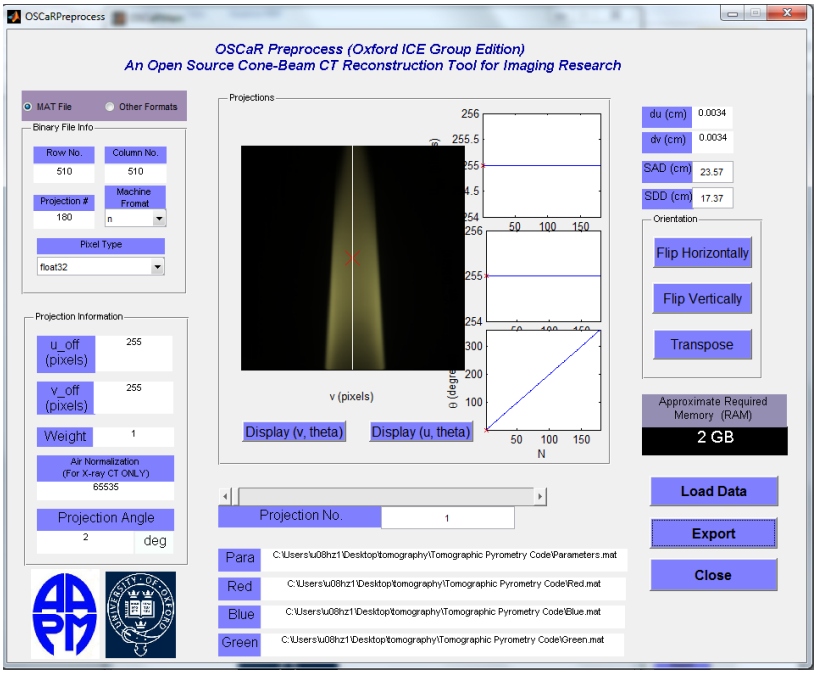

Fig. 3.17: OSCaR-P pre-processing GUI

The GUI also includes the function for downsampling by either applying the mean filter or the median filter, and the downsampling ratio needs to be specified by the user. The approximate memory space occupied by the created data is estimated and shown on the screen. All the data will be exported in MAT format for later processing.

Table 3.3: Parameters in OSCaR-P pre-processing GUI

Parameters	Description
du	Pixel width (cm) in vertical direction
dv	Pixel width (cm) in horizontal direction
SAD	Lens to central axis distance (cm)
SDD	Lens to detector distance (cm)

3.4.1.2 Pre-processing GUI

The OSCaR-P pre-processing GUI is shown in Fig. 3.17. In this GUI, projections from different angles are displayed on the screen. Each projection is a 2D matrix with Nu vertical pixels and Nv horizontal pixels. The user can flip or transpose the data matrix to select an appropriate orientation. The modified data will be displayed and stored. Individual colour channel values either in the vertical or horizontal direction can be displayed.

Extra parameters about the geometry/resolution of the apparatus are required and these are summarized in Table 3.3:

After deciding the approporiate orientation and typing in all the parameters, separate data files for different colour channels are exported in MAT format.

3.4.1.3 Reconstruction GUI

The reconstruction GUI is used to implement the cone beam FBP algorithm, as shown in Fig. 3.18. When this GUI is called, the file input dialog will pop up automatically for the user to input the data file saved in the pre-processing GUI. Then, the user needs to choose the reconstruction volume either by typing in the reconstruction volume by specifying $[xmin, xmax]$, $[ymin, ymax]$, $[zmin, zmax]$, or choosing the volume graphically by using the mouse. The approximate memory to implement the tomography algorithm will be calculated and shown on the screen for the user to decide whether adequate memory space can be allocated or not. Four different window functions are available from the pull-down menu: the Shepp-logan window, the Cosine window, the Hamming window, and the Hanning window. The user can also create a new window function by choosing the 'new filter' option in the pull-down menu. The zero-padding length when doing the fast Fourier transform can also be specified by the user and the total length of the filter will be displayed after choosing the zero-padding length. After finishing the reconstruction process, the 3D colour map can be exported in MAT format and the parameters will be saved in a separate file.

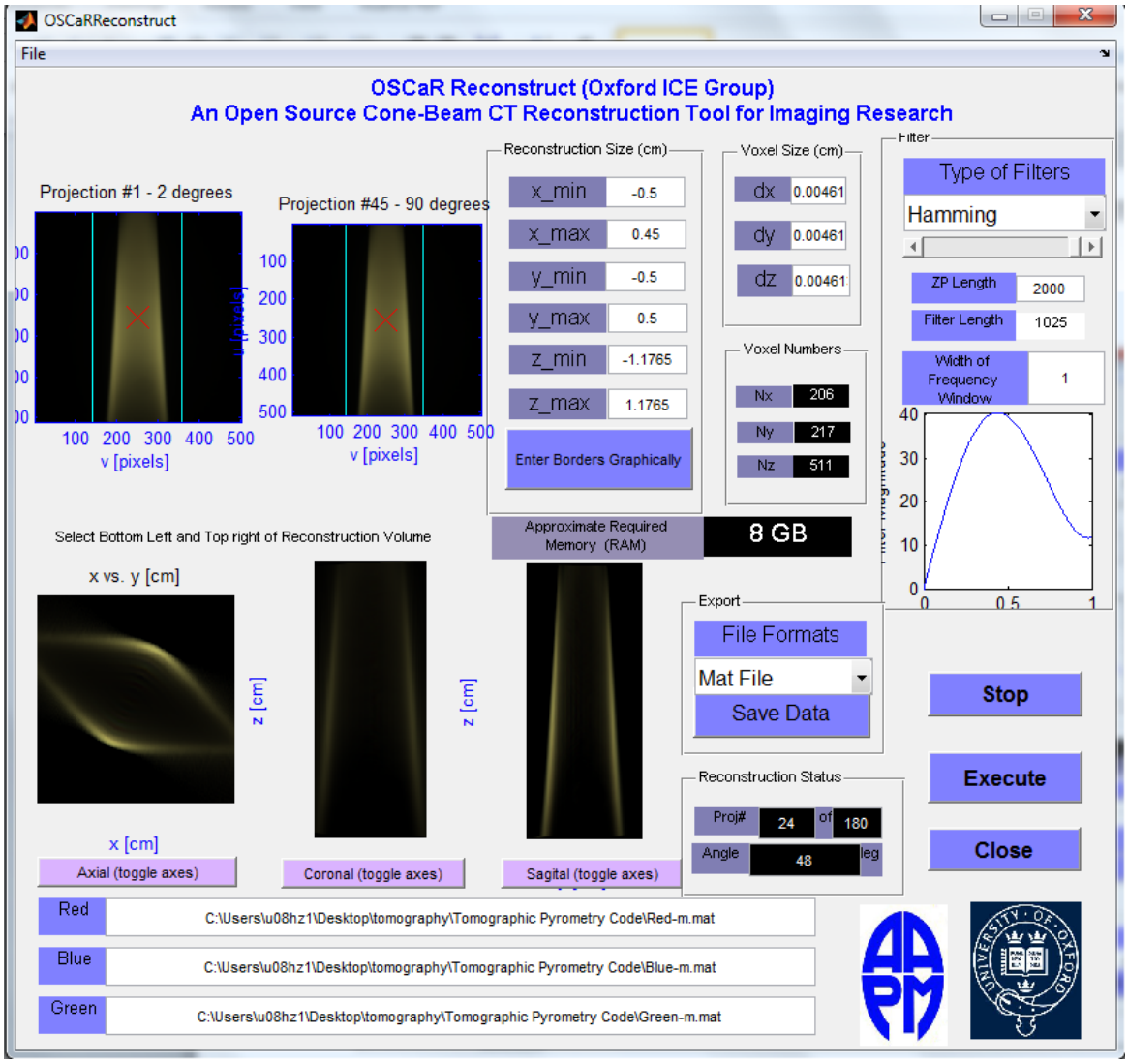

Fig. 3.18: OSCaR-P reconstruction GUI

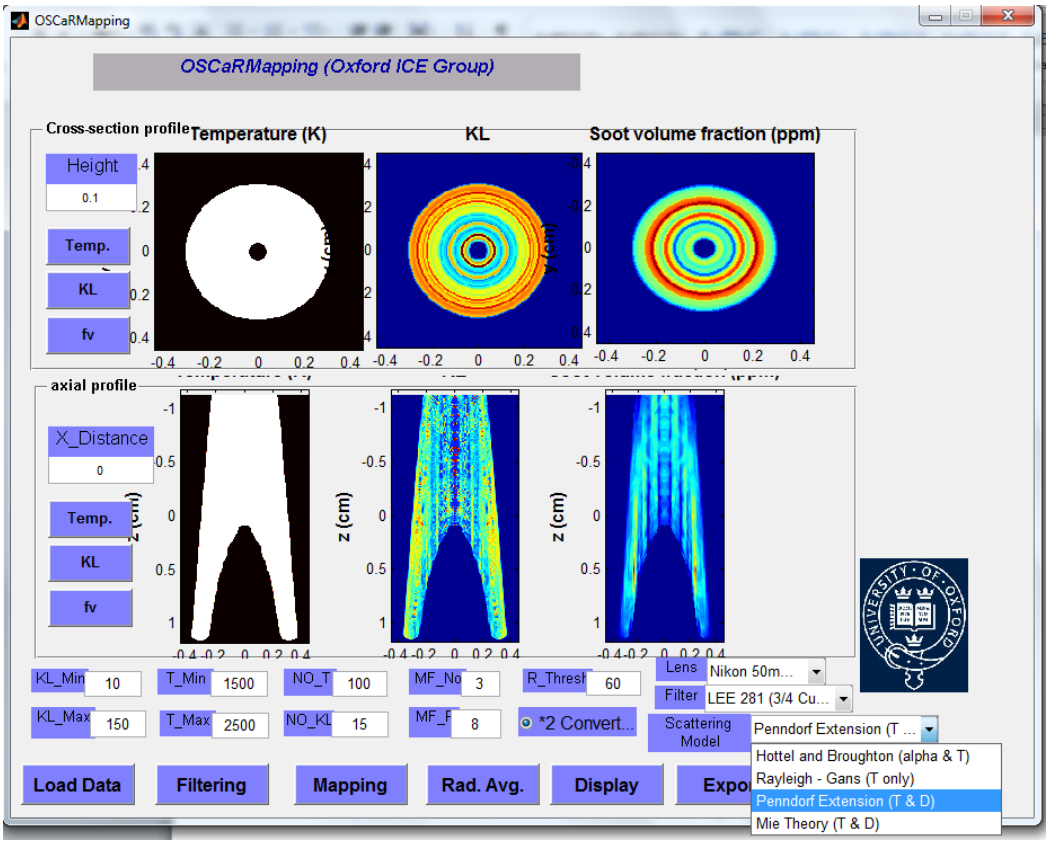

Fig. 3.19: OSCaR-P Mapping GUI

3.4.1.4 Mapping GUI

The OSCaR-P mapping GUI, as shown in fig. 3.19, is used to find the property field (temperature, soot diameter, and soot volume fraction) within the reconstructed volume by using the data from the reconstruction GUI.

The look-up table will be calculated first by using the calibration data of the camera. Several parameters need to be specifed to create the look up table, as summarized in Table 3.4. The transmission efficiency of the lens and any additional optical components (such as any optical filter), need to be taken into account when creating the look up table. Then, by calculating the minimum errors between the reconstructed data and the calculated data, the property values are picked-up from the look-up table as outputs. The error is defined as:

$$\text{error} = \sqrt{((R/B)_d - (R/B)_c)^2 + ((R/G)_d - (R/B)_c)^2} \tag{3.12}$$

The property field at different heights ($x-y$ plane) and at different radial distances ($y-z$

Table 3.4: Parameters in the OSCaR-P Mapping GUI

Parameters	Description
T_Min	Minimum temperature (K)
T_Max	Maximum temperature (K)
KL_Min	Minimum KL (or diameter) value
KL_Max	Maximum KL (or diameter) value
No_T	Number of discrete temperatures
No_KL	Number of discrete KL (or diameter) value
Height	Height above the image centre (z-axis)
X_Distance	Horizontal distance from the image centre (x-axis)

plane) are shown separately on the screen. More detailed property fields can be displayed in a pop-up window. The 3D median filter can be applied after specifying the recursive filter number and filter size. In addition, circumferential averaging can be done to increase the accuracy for axi-symmetric flames. Finally, the 3D property fields can be exported in the MAT format for further analysis and plotting.

3.4.2 Post-processing software package

The post-processing software package consists of several MATLAB GUIs. They can be used to merge the property fields from different parts of the flame when the field of view of the camera cannot cover the whole flame at a single shot. They can also be used to add masks (to see the property field in a specific region). In addition, they can be used to plot 2D false colour property field images at a selected height or radial distance. A separate GUI was developed to compare property fields of different flames.

3.5 Sensitivity and noise analysis

An n-butane laminar diffusion flame was used to investigate the noise level of the results and their sensitivities to different parameters. The flow rates of the butane (~30 mL/min) and the air (~850 mL/min) were chosen to produce a sooting flame. The position of the camera was carefully chosen so that the radius of the circle of confusion (p in Fig. 3.12)

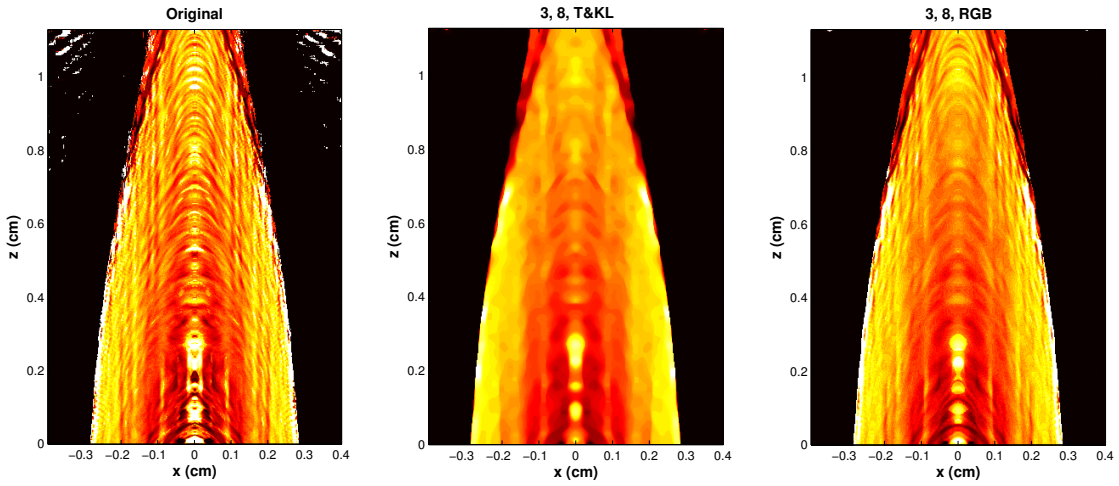

Fig. 3.20: Effect of a 3D median filter on the temperature field

corresponds to three pixels (p = 51 μm, u = 23.57 cm and v = 17.37cm, see Table 3.1). The frame rate was set at 60 frames per second and the aperture size was $f/32$ ($f/16$ with a 2* macro convertor lens). The LEE 281 filter was used to better utilise the range of thecolours in the camera.

3.5.1 Effect of 3D median filter

A 3D median filter was used to reduce the random noise introduced by the tomography technique. Its effect is shown in Fig. 3.20.

The 3D median filter was first applied to the property field data ($T\,\&\,KL$) directly (subplot "3, 8, T&KL"). Median filtering improves the smoothness but it also blurs the image significantly, which means a substantial degradation of the spatial resolution. As an alternative, the 3D median filter was applied to the reconstructed RGB colour map before doing any calculations of the property field (subplot "3, 8, RGB"). In this way, the median filter improves the smoothness effectively without much sacrifice of the spatial resolution. Therefore, applying a 3D median filter to the reconstructed RGB colour map is a better choice for removing the random noise and enhancing the smoothness of the results, so as to indicate the structure of the temperature and soot field within the flame.

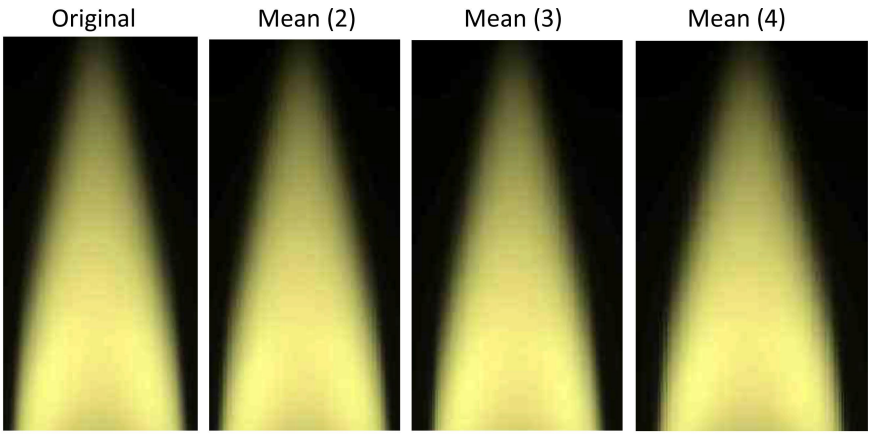

Fig. 3.21: Effect of downsampling on the original flame picture

3.5.2 Effect of parameters in the FBP algorithm

3.5.2.1 Downsampling ratio (DR)

Since the cone beam tomography algorithm used in this project is the extension of the equally spaced fan beam FBP algorithm, the pixel width of the image, or the spacing of the projection points has a great influence on the noise in the deconvoluted field. As the pixel width decreases, the light intensity difference between two adjacent projection points becomes smaller. When the difference is comparable to the noise level, the results will be highly noisy.

Downsampling is a very convenient way to increase the pixel width. Downsampling is carried out by merging multiple pixels into a single one, and the value of the merged pixel is taken as the mean value, or the median value of the original pixels. The downsampling ratio, which is defined as the square root of the ratio between the pixel number of the original image and that of the downsampled image, is used to calculate the final pixel width. For example, if an image with resolution of 1024*1024 is downsampled by a downsampling ratio of 2, the downsampled image has a resolution of 512*512, and the pixel width is doubled. Fig. 3.21 shows the effect of downsampling on the original flame picture. It can be clearly seen from the Fig. 3.22 that the picture resolution is degraded significantly when the downsampling ratio is larger than 3.

Fig. 3.22 shows the effect of downsampling on the reconstructed temperature field. Fig. 3.22

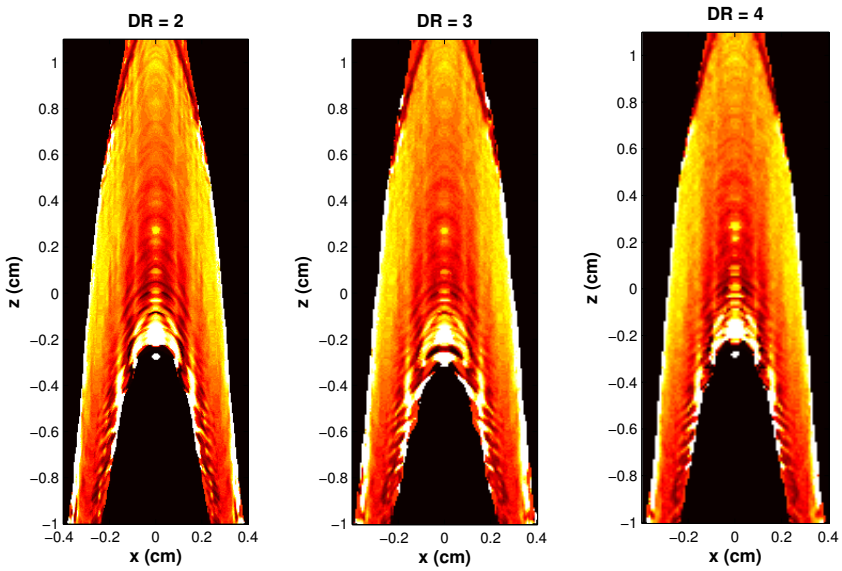

Fig. 3.22: The effect of downsampling on the temperature field

shows that the downsampling is very efficient at enhancing the smoothness of the temperature field at the cost of losing a certain amount of spatial resolution. To balance the trade-off between resolution and smoothness, a downsampling ratio of 2 will be used for later data processing.

3.5.2.2 Projection number

The projection number determines the resolution of the cone beam tomography. Similar to the downsampling ratio, the trade-off between the noise level and resolution should be balanced since a greater number of projections increases the resolution but will introduce more noise, since the difference between two adjacent cone beam projections will be reduced. However, for an axi- symmetric object, such as the laminar diffusion flame, the projection number should have less effect. The effect of projection number on the temperature field is shown in Fig. 3.23 and Fig. 3.24. These figures shows that the difference between temperature fields when using different projection numbers is well below 30 K in most locations except the boundary region, which is comparable to the uncertainty in temperature measurement as indicated by uncertainty analysis (Appendix B).

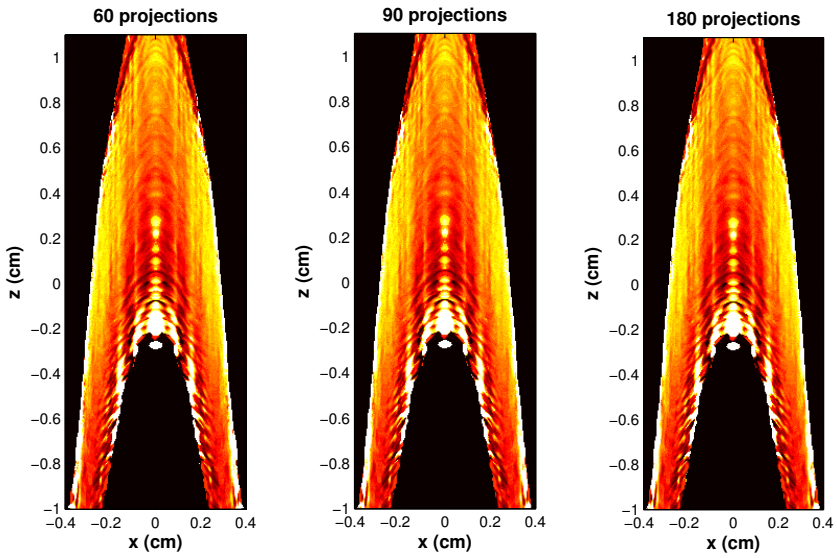

Fig. 3.23: Effect of the number of projections on the temperature field

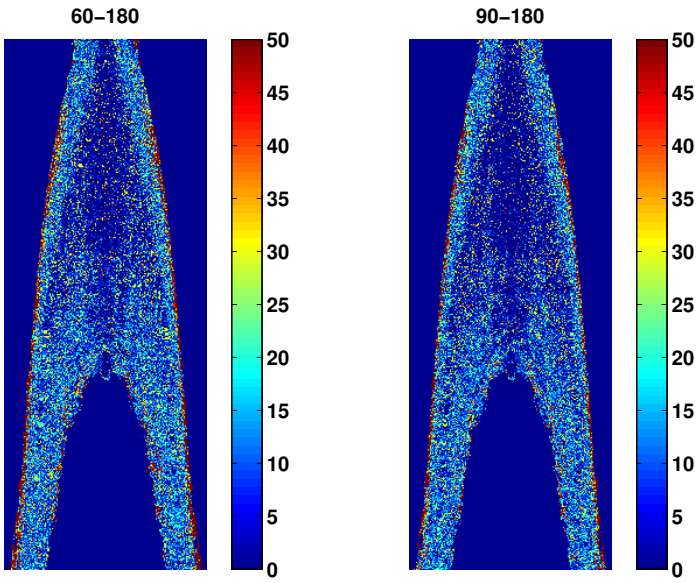

Fig. 3.24: Difference between the temperature fields when using different numbers of projections

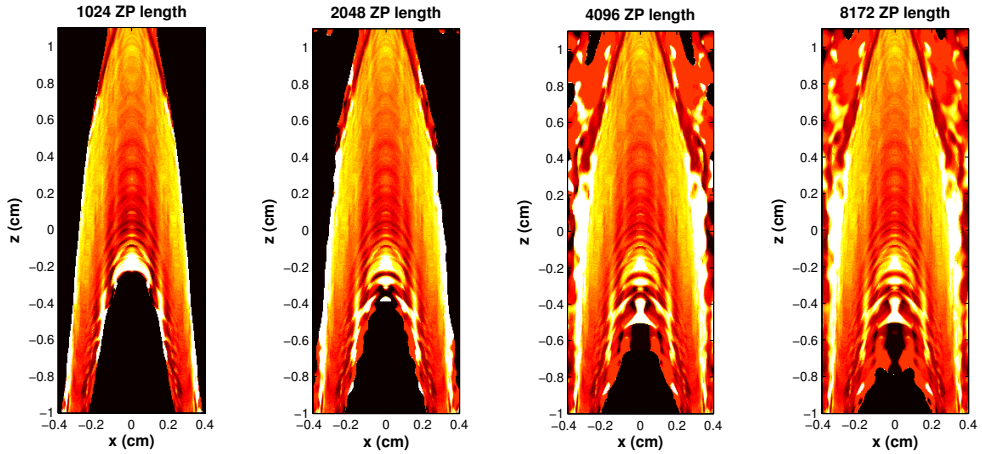

Fig. 3.25: Effect of zero-padding length on the temperature field

3.5.2.3 Zero-padding length

According to eq. 2.35, the FBP algorithm needs to appy a FFT with zero-padding. The zero-padding length determines the resolution in the frequency space. To test the effect of different zero-padding lengths on the results, four different zero-padding lengths (1024, 2048, 4096, and 8172) were used to calculate the temperature field.

Fig. 3.26 shows that zero-padding can enhance the smoothness of the temperature field, but it also introduces a lot of low frequency noise because the zero-padding will introduce interpolation in the frequency domain to increase the resolution.

To remove the noise introduced by the increased longer zero-padding length, a small threshold value [10 (max pixel value is around 300)] for the red pixel was set, and the results are shown in Fig. 3.26. The difference in the reconstructed temperature fields when using different zero-padding lengths is also plotted in Fig. 3.27. It can be clearly seen from Fig. 3.26 and Fig. 3.27 that the temperature field becomes smoother as a longer zero-padding length is used, and the temperature starts to converge once the zero-padding length is greater than 4096. Since increasing the zero-padding length will not increase the computational demand much, the zero-padding length was set as 8173 for subsequent data analysis.

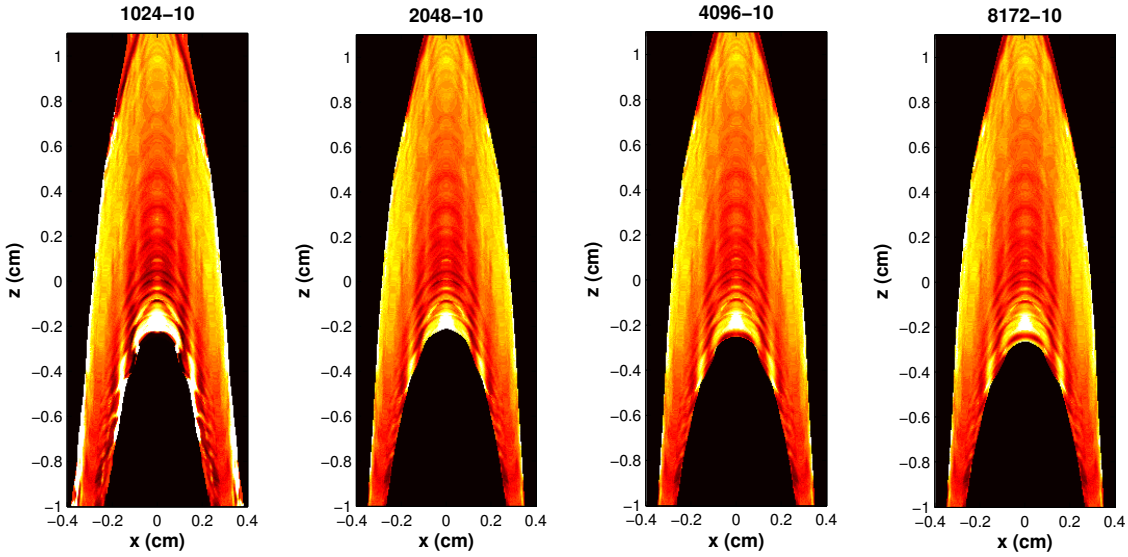

Fig. 3.26: Effect of zero-padding length on the temperature field with a threshold value of 10 for the red channel

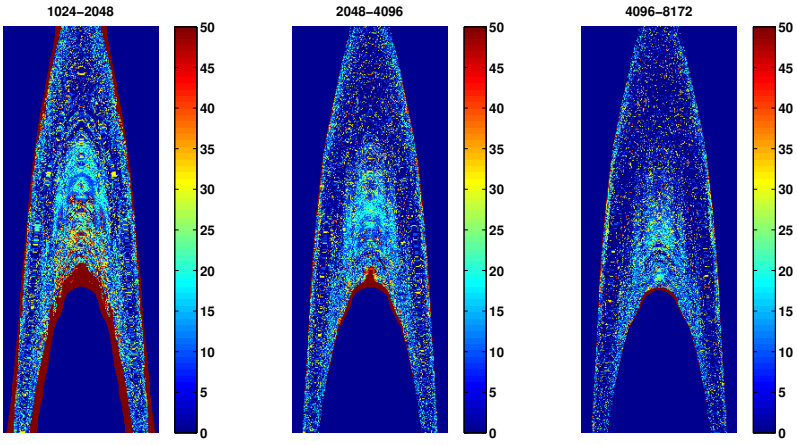

Fig. 3.27: Difference between the temperature fields when using different zero-padding lengths (title of subplots shows the zero-padding lengths)

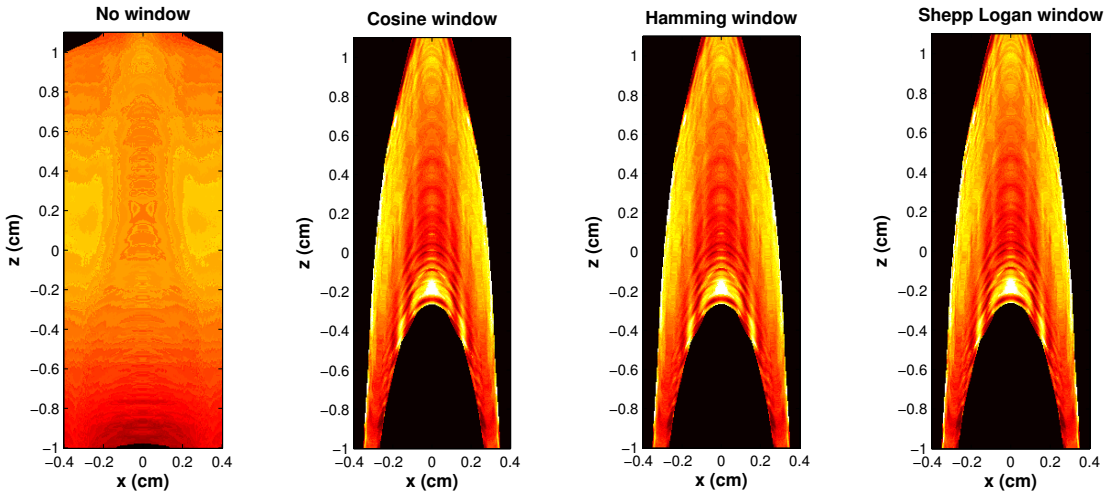

Fig. 3.28: Effect of different window functions on the temperature field

3.5.2.4 Window functions

To reduce the effect of spectral leakage caused by discrete nature of the finite Fourier transform, an appropriate window function needs to be applied. The window function should be chosen to balance the trade-off between resolving the comparable strength of signals with similar frequencies and resolving the disparate strength signals of dissimilar frequency. A good Fourier analysis window function is one which minimizes the side lobes, which cause "cross-talk" in the estimated spectrum from one frequency to another [75]. The effect of different window functions on the temperature fields is shown in fig. 3.28. It can be seen from fig. 3.28 that the effect of the different filters are quite similar. But with no window function, the reconstructed temperature field is highly noisy. The Hamming window is set as the default window function because the reconstructed temperature field when using the Hamming window is most close to the average value of the temperature fields when using different kinds of filter.

3.5.2.5 Position of central axis

Locating the position of the central axis is crucial for tomography since it affects many major parameters used to define the weighting factor in the FBP algorithm. By default, the central axis of the object is set as the central axis of the picture recorded by the camera.

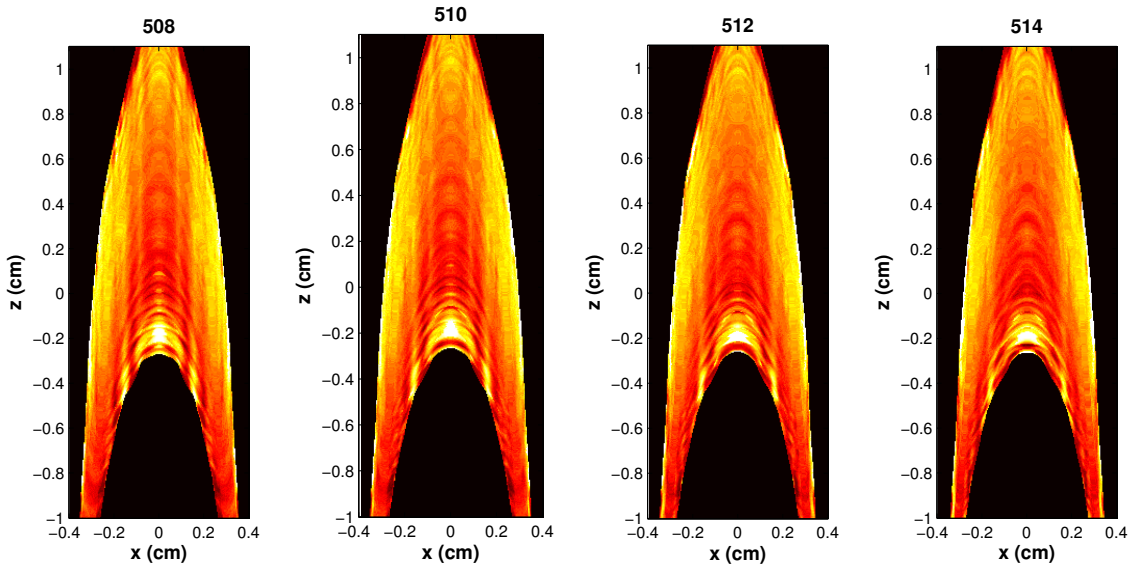

Fig. 3.29: Effect of central axis position to the temperature field

Though before taking the image of the flame, an axisymmetric half-cone pointer was used to calibrate the central axis, a few pixels deviation is almost inevitable. The influence of the position of the central axis of the flame on the temperature field is indicated by Fig. 3.29.

All subplots have been filtered by a 3D median filter with the voxel size [8*8*8]. The central axis of the image taken by the camera is in the 510th pixel. As Fig. 3.29 shows, the position of the central axis would greatly affect the temperature field. After looking at the magnified original flame image, the central axis of the flame should be in around the 513th pixel, and if the central axis is set at this position, the reconstructed temperature field is the smoothest. Therefore, when using cone beam tomography, the optical path alignment should be carefully implemented and the actual central axis of the flame should be double checked by looking at the magnified flame image taken by the camera.

3.5.2.6 Uniformity of projection gantry angles

To investigate the effect of non-uniformity of gantry angles on the temperature field, three different gantry angle distributions (Fig. 3.30) were tested.

The first distribution is called the linear random distribution and it was calculated according to eq. (3.13).

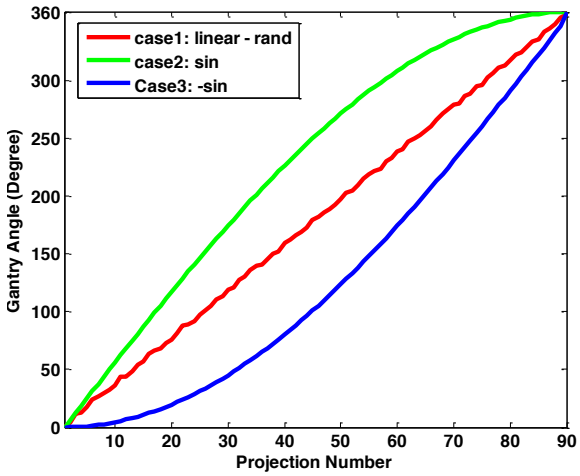

Fig. 3.30: Gantry angle distributions

$$\theta = [\frac{360}{N}, 2 \cdot \frac{360}{N}, ..., (N-1) \cdot \frac{360}{N}, 360] - \text{rand}(N) \cdot \frac{360}{N} \tag{3.13}$$

where θ is the gantry angle; N is the number of projections; rand(N) is a vector with N elements and each element is a random value between 0 and 1. The second distribution is called the sine distribution and it is expressed by eq. (3.14).

$$\theta = \sin([0, \frac{360}{N}, 2 \cdot \frac{360}{N}, ..., (N-1) \cdot \frac{360}{N}] \cdot \frac{2\pi}{360}) \cdot 360 \tag{3.14}$$

The third distribution is the negative sine distribution and its expression is:

$$\theta = (\sin((\frac{[0, \frac{360}{N}, 2 \cdot \frac{360}{N}, ..., (N-1) \cdot \frac{360}{N}]}{4} + 270) \cdot \frac{2\pi}{360}) + 1) \cdot 360 \tag{3.15}$$

The temperature fields for these different cases are plotted in Fig. 3.31.

As Fig 3.31 shows, the non-uniformity of the gantry angles will introduce noise, and the noise level increases as the non-uniformity increases. It can be seen more clearly on the reconstructed RGB colour map in Fig. 3.32.

For the linear random distribution, the noise level is relatively low and can be eliminated by applying a median filter, and the noise level can be further reduced by increasing the projection number. However, the sine and negative sine distributions introduced much higher noise levels. Setting a threshold value for the red channel when doing the mapping can

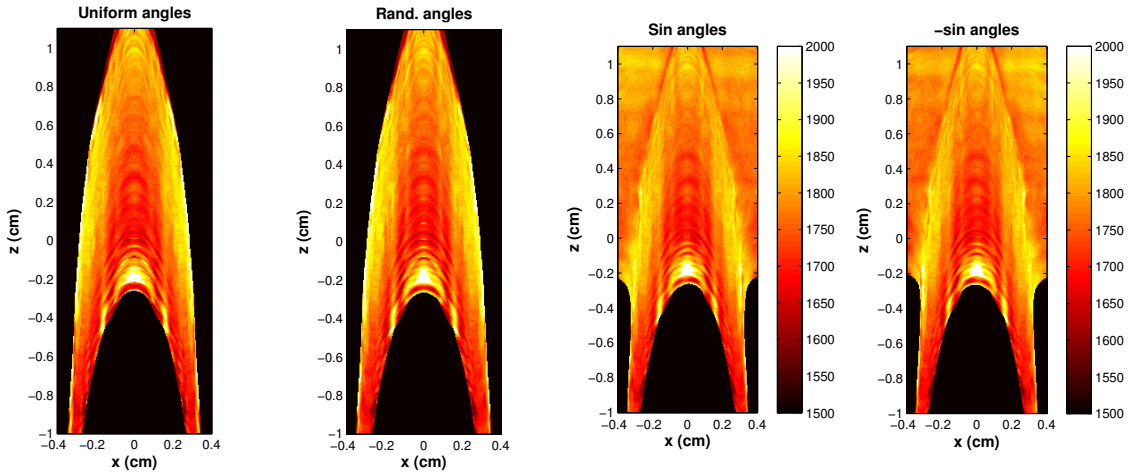

Fig. 3.31: Effect of different distributions of gantry angles to the temperature field

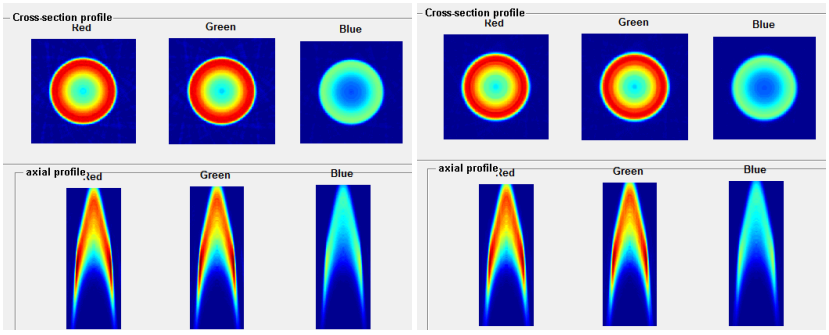

(a) Linear random distribution (90 projections)

(b) Linear random distribution (180 projections)

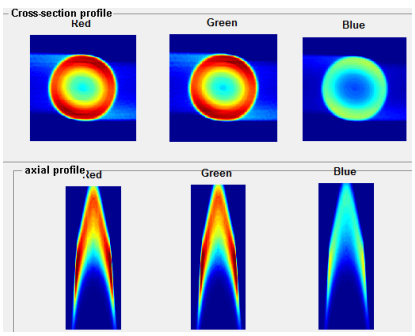

(c) Sine distribution (90 projections)

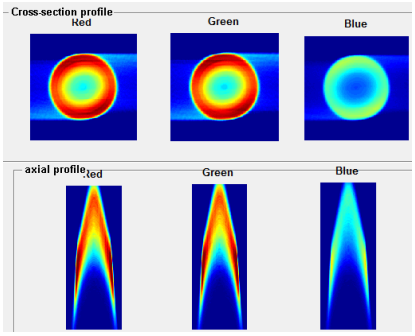

(d) Negative sin distribution (90 projections)

Fig. 3.32: Effect of different distributions of gantry angles to the reconstructed colourmap

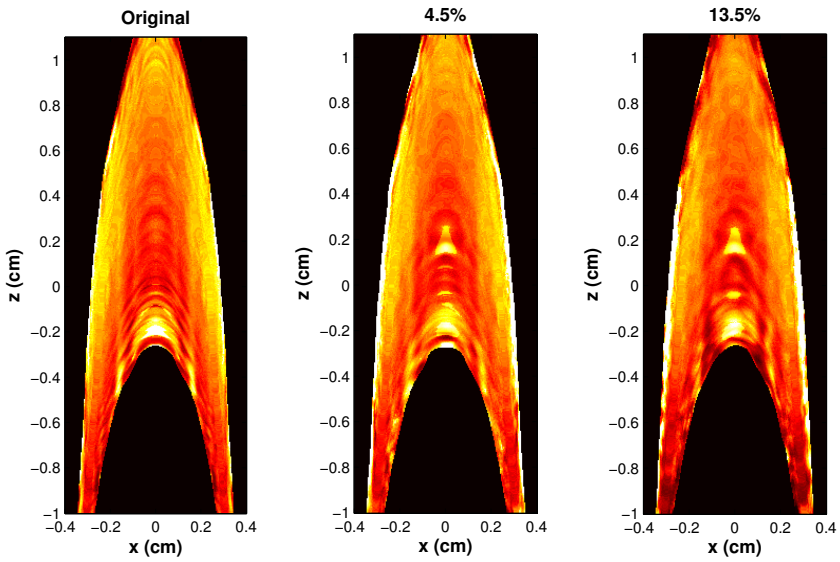

Fig. 3.33: Effect of adding different levels of Gaussian white noise on the temperature field (title is the standard deviation)

reduce the noise, but at a cost of losing effective pixels. For example, when the threshold value is set to 100, most of the noise can be removed, but the temperature field shrinks significantly compared to the original one. Therefore, in practice, the gantry angle should be as uniform as possible when using tomography techniques. Creating a mask may be a better choice to remove the unexpected noise outside the flame region compared to setting a threshold value.

3.5.2.7 Effect of signal-to-noise ratio of the detector

In practice, the detectors have finite signal-to-noise (S/N) ratio and which will introduce some errors on the measured property. To see how the signal-to-noise ratio affects the temperature distribution, different levels of Gaussian white noise were added to the projections taken at different gantry angle. All Gaussian white noise has a mean value of zero but with different standard deviation percentages. The effect of adding Gaussian white noise on the temperature field is shown in Fig. 3.33. The 4.5% of variation in Gaussian white noise corresponds to around 26dB signal-to-noise ratio and 13.5% of variation corresponds to 16dB. The 3D median filter is applied to remove part of the noise introduced. In addition, a threshold value of 10 is set on the red channel to remove noise from outside the flame

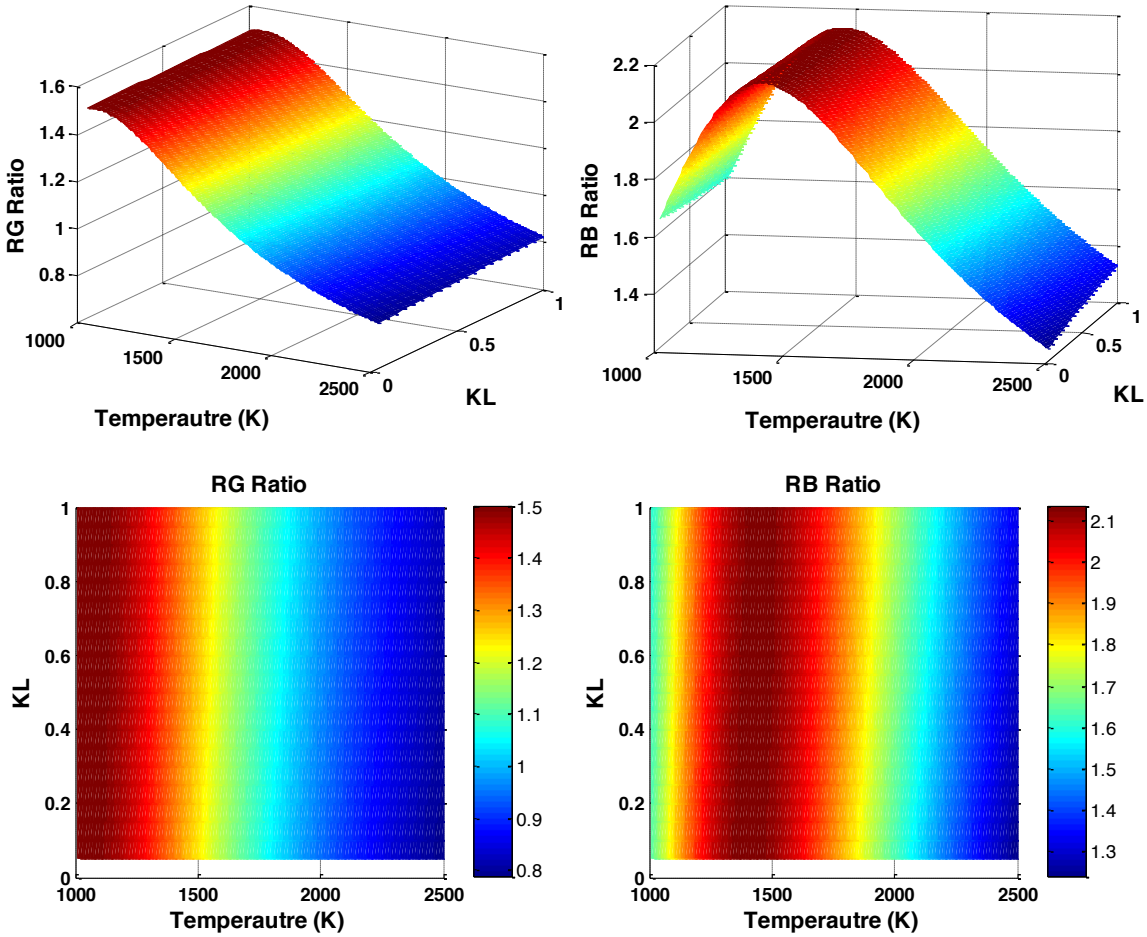

Fig. 3.34: Look-up table method with the Hottel and Broughton correlation

region.

As shown in Fig. 3.33, adding the Gaussian white noise will introduce extra noise near the central axis region, and it is very difficult to eliminate such noise by just using median filter. It also shows that a detector with S/N ratio higher than 26dB will not affect the temperature distribution much.

3.5.3 Sensitivity of the field properties to colour ratios

The accuracy of the CBT-TCS is heavily reliant on the sensitivity of the property field (temperature, KL/diameter) to two different colour ratios (R/G, and R/B). Fig. 2.47-50 shows the response of the colour ratios to the resulting differences in the property field when using different scattering theories.

Fig. 3.34 is the plot when using the look-up table to implement the Hottel and Broughton correlation. According to this figure, both the RG and RB ratios are sensitive to the temperature field. However, they are not very sensitive to the KL value, especially the RG ratio. Therefore, the reconstructed temperature field is much more trustworthy than the KL distribution. In addition, this look-up table can only be used to measure the temperature in the range from 1500 K to 2500 K because there are two identical RB ratios if the temperature ranges is from 1000K to 2500K.

Fig. 3.35 shows the look-up table results when using the Rayleigh-Gans theory. Similar to Fig 3.34, both the RG and RB ratios are very sensitive to the change of temperature. However, they remain unchanged for different Ds because the colour ratio cancels out the soot volume fraction and diameter terms. However, compared to the look-up table using the Hottel and Broughton correlation, this look-up table can be used to measure the whole range of temperature from 1000 K to 2500 K because there is only one possible combination of RG and RB ratio at each temperature.

Fig. 3.36 plots the look-up table results when using the Penndorf extension correlation. The sensitivities of the RG and RB ratios to different temperatures are fairly good but the valid temperature range is from 1400 K to 2500 K. The sensitivities of the RB ratio to different diameters is higher than of the RG ratio, but both the RB and RG ratios are not sensitive enough to give a high resolution diameter distribution, especially in the temperature range below 1700 K.

The look-up table for using the Mie theory is plotted in fig. 3.37. Both the RG and RB ratios are sensitive to the temperature difference when using Mie theory. In addition, the RB ratio is much more sensitive to the diameter difference than the RG ratio. Compared to the look-up table using the Penndorf extension, the resolution of the diameter distribution when using the Mie theory is better. However, there can be two solutions for the diameter from a single combination of R/G, and R/B. Therefore, when doing the calculation of diameter, an upper limit of about 90 nm should be set so as to ensure a more reasonable diameter value. The valid temperature range is also from 1400 K to 2500 K.

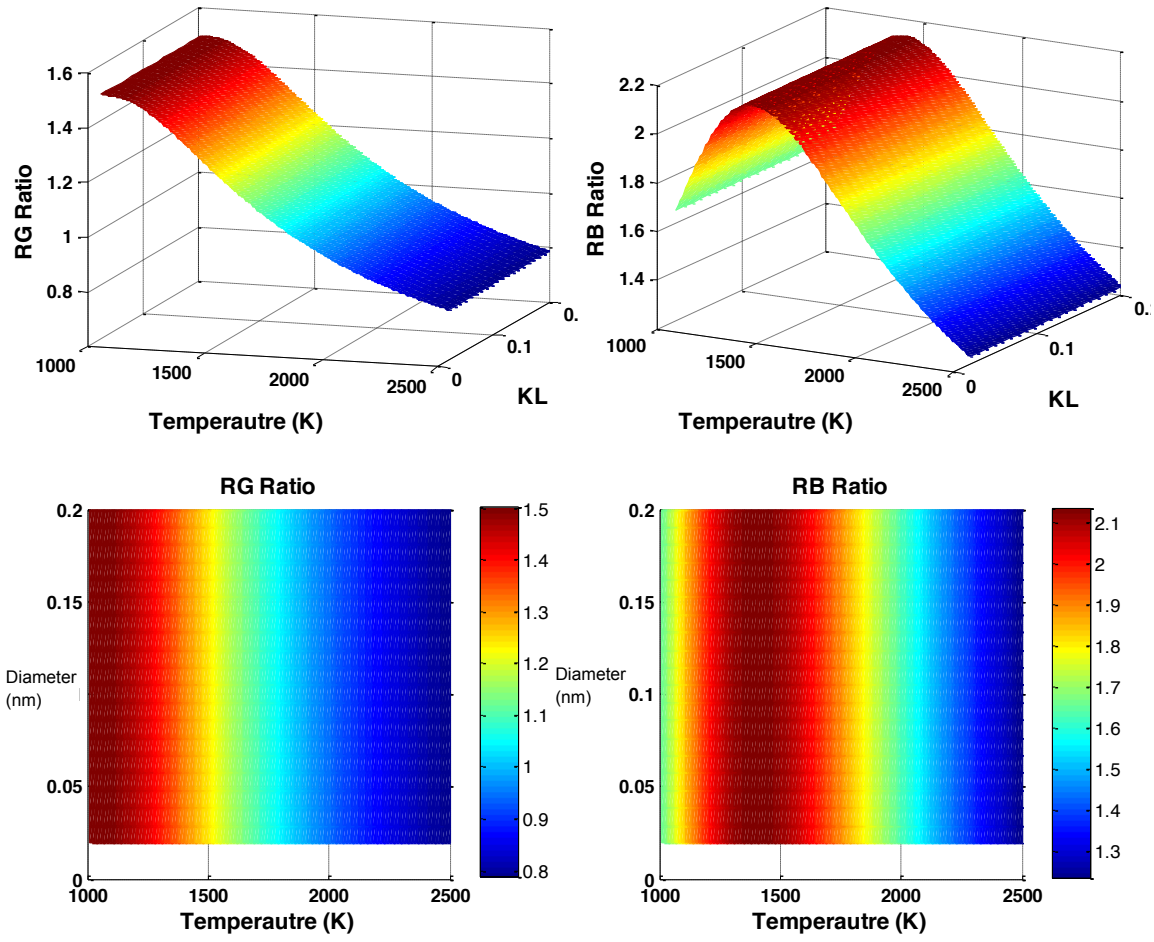

Fig. 3.35: Look-up table results for the Rayleigh-Gans theory

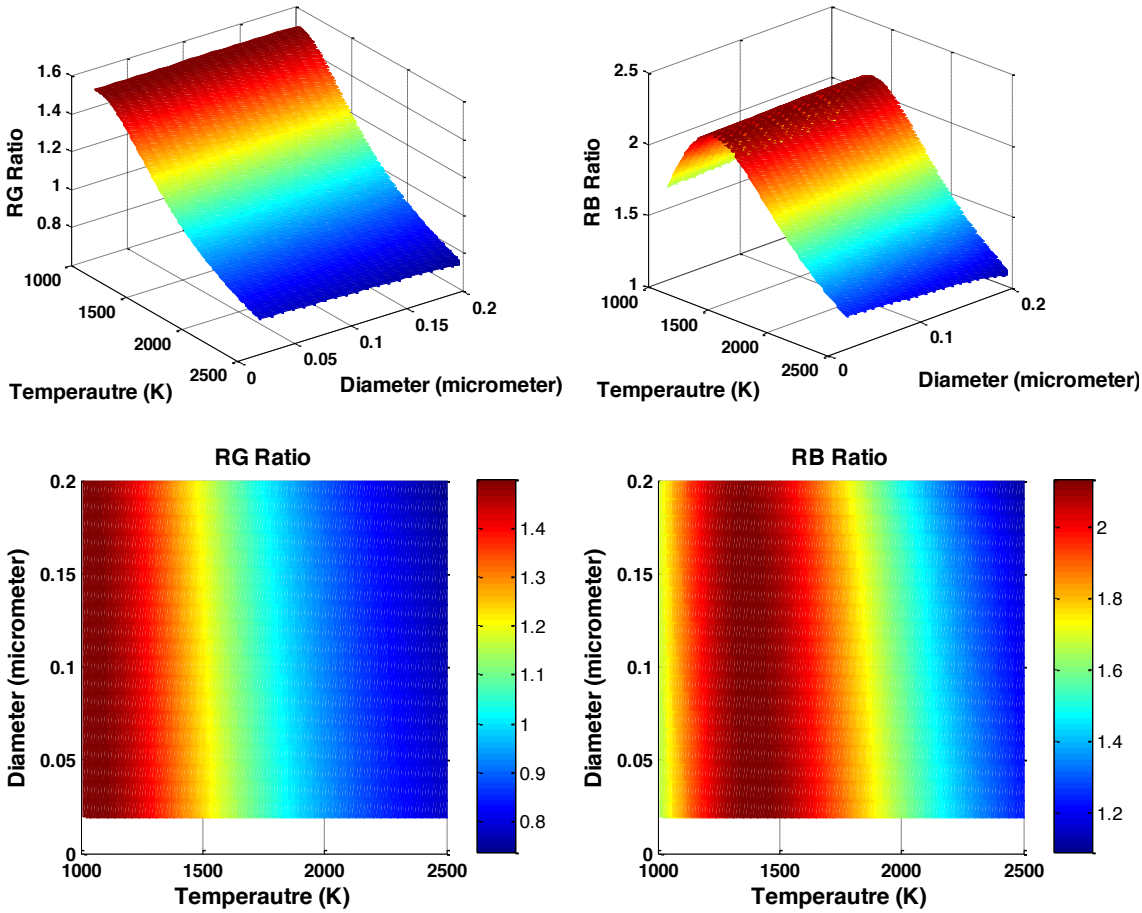

Fig. 3.36: Look-up table results when using the Rayleigh-Gans theory with Penndorf extension

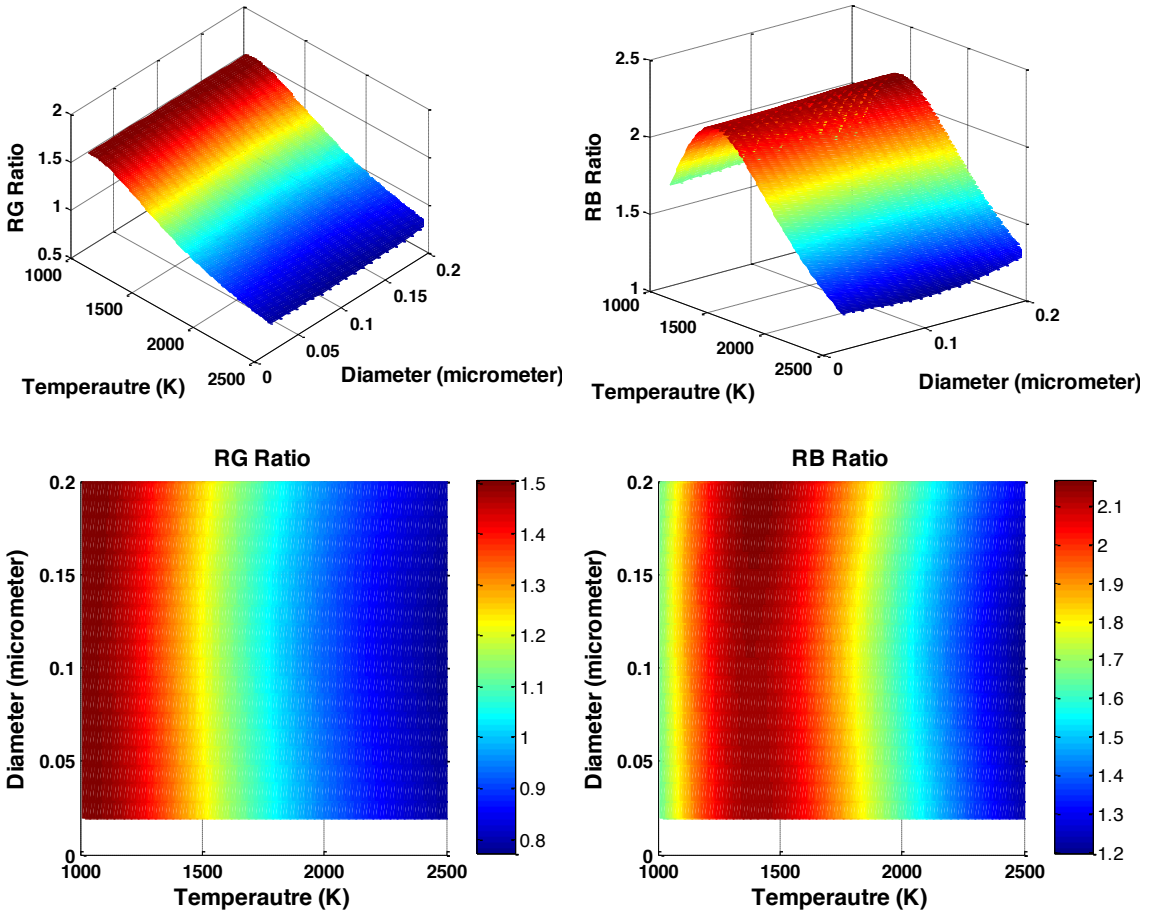

Fig. 3.37: Look-up table results when using the Mie theory

In conclusion, the temperature field is sensitive to both the RG and RB ratios for all these four scattering models. However, the *KL* distribution when using the Hottel and Broughton correlation will have a low resolution. As for the calculation of the diameter distribution, the Mie theory is preferred compared to the Penndorf extension due to its higher sensitivity to the diameter difference if an appropriate cut-off diameter size is chosen.

3.5.4 Effect of using different scattering models

As mentioned earlier, different scattering models can be used to calculate different field properties. This section will compare the results calculated when using different scattering models. The test flames are pure ethylene flames with 200 mL/min fuel flow rate and 45 L/min air flow rate.

Fig. 3.38 shows the temperature and *KL* distributions calculated by using the Hottel and

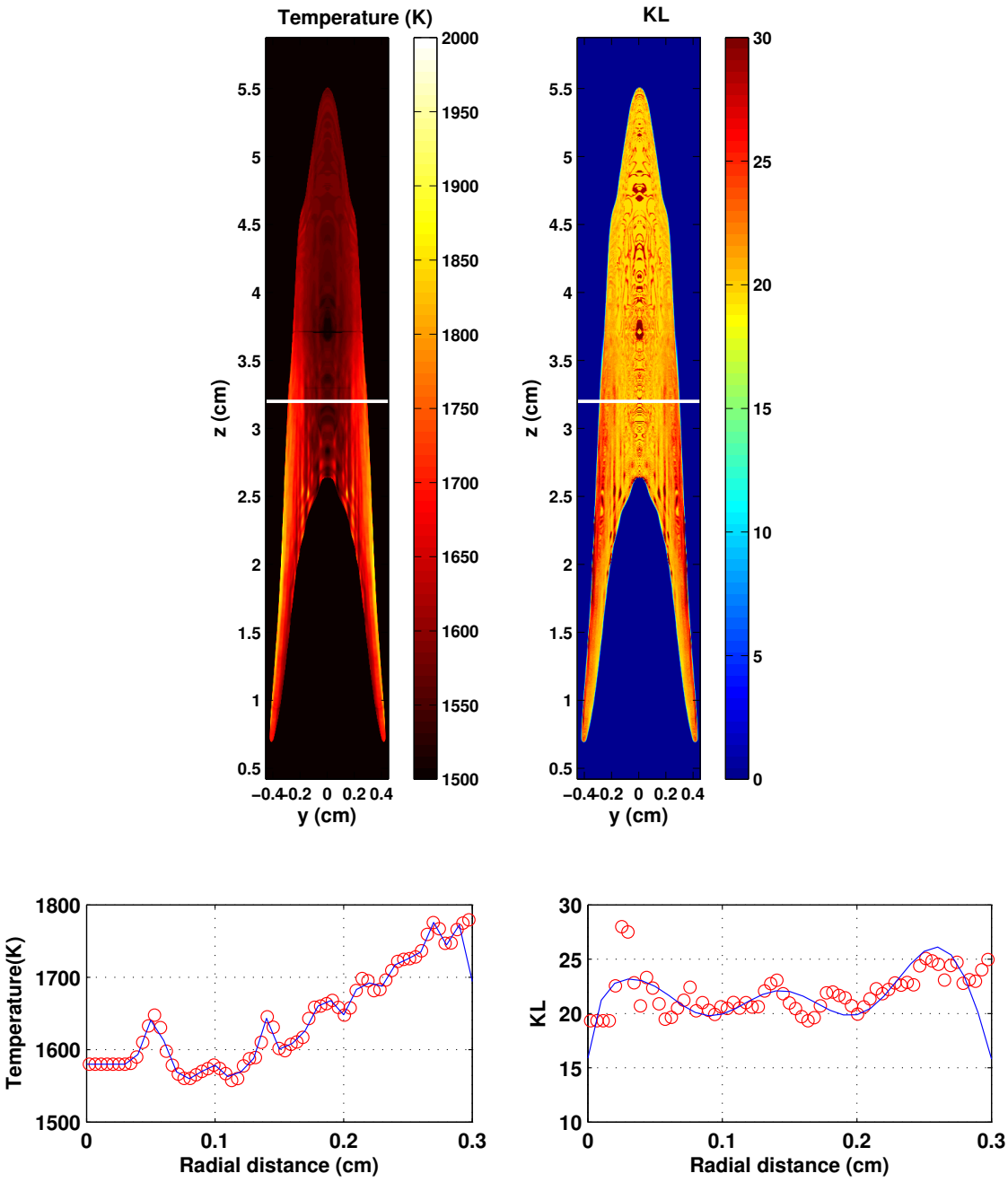

Fig. 3.38: Temperature and *KL* distribution by using the Hottel and Broughton correlation

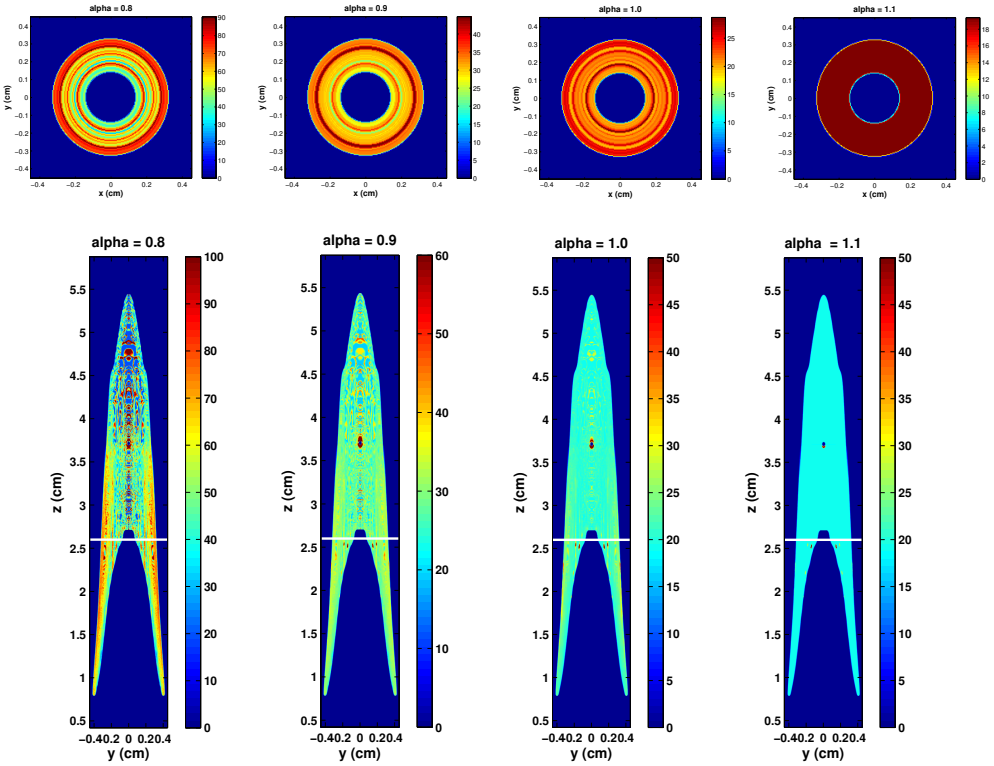

Fig. 3.39: *KL*distributions when using different α values in the Hottel and Broughton correlation

Broughton correlation. Both the temperature and *KL* distributions show very reasonable structures except for some artificial noise in the central axis region. This is due to the effect of diffraction and the low light intensity level in the central axis region. A typical reconstructed colour distributions in a specific height is shown in Fig. 3.40. It clearly shows that the reconstructed colour distributions are very smooth but the colour ratio distributions have several oscillations, especially for the low light intensity region. By carefully checking the light intensity levels of the original flame images, it can be found that the camera sensor does not has sufficient bit-depth to distinguish the light intensity discrepancy, especially for the low light condition. Therefore, a camera with higher bit-depth may need to be used to increase the contrast of the light intensity distributions.

Fig. 3.38 also clearly shows that the most sooting area is also the hottest area where the pyrolysis reaction is most likely to occur to produce the precursors of soot particles. However, the *KL* distribution calculated by the Hottel and Broughton correlation is very sensitive to the exponential coefficient α in eq. 2.7. Fig. 3.39 shows the *KL* distributions when using

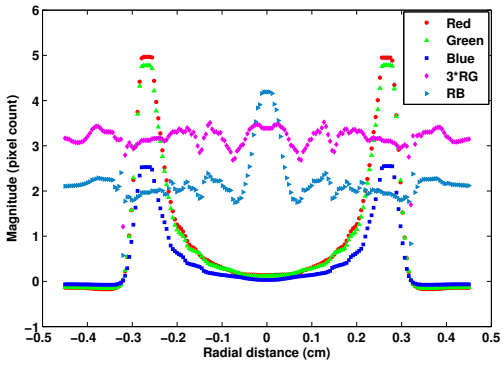

Fig. 3.40: Typical reconstructed colour and colour ratio distributions at a specific height (RG: red/green; RB: red/blue; 3*RG: tripled RG value)

different values of α.

As Fig. 3.39 shows, different α value leads to quite different KL distributions. Since the diameters and compositions of particles in different locations inside the flame are different, using a constant α value will always introduce a certain amount of error.

Fig. 3.41 shows the temperature and soot volume fraction distribution calculated by using the Rayleigh-Gans theory. The temperature obtained by using Rayleigh-Gans theory is a little bit lower (20 K in average) than that using the Hottel and Broughton correlation. The soot volume fraction distribution use a constant soot dimaeter value (50 nm) in this figure also shows that the most sooting region is the hottest part of the flame.

The temperature, soot diameter, and soot volume fraction distribution calculated by the Penndorf extension are shown in Fig. 3.42. The temperature in this figure is lower than that in Fig. 3.38 (Hottel and Broughton correlation) by around 50 K on average. The diameter distribution shows that the average particle size is larger in the upper part of the flame. This is probably due to the longer residence time to allow agglomeration into larger particles. The maximum particle diameter shown in Fig. 3.42 is around 120 nm, which is well above the Rayleigh limit and approaching the upper limit of the Penndorf extension. The soot volume fraction distribution calculated by the Penndorf extension (Fig. 3.42) is very close to that calculated by the Rayleigh-Gans theory (Fig. 3.41), which indicates that the effect of soot diameter upon the soot volume fraction is very small.

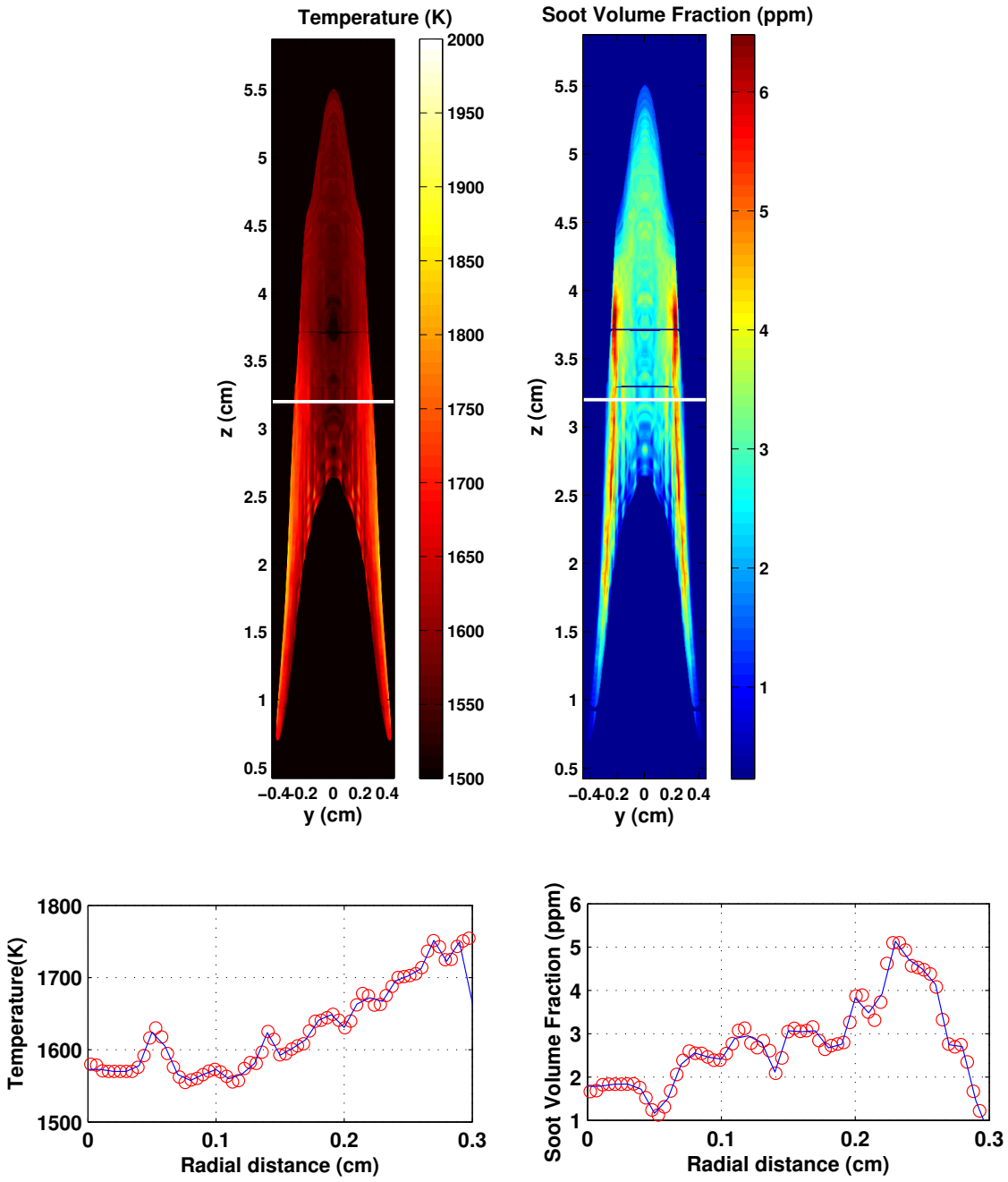

Fig. 3.41: Temperature distribution obtained by using the Rayleigh – Gans Theory

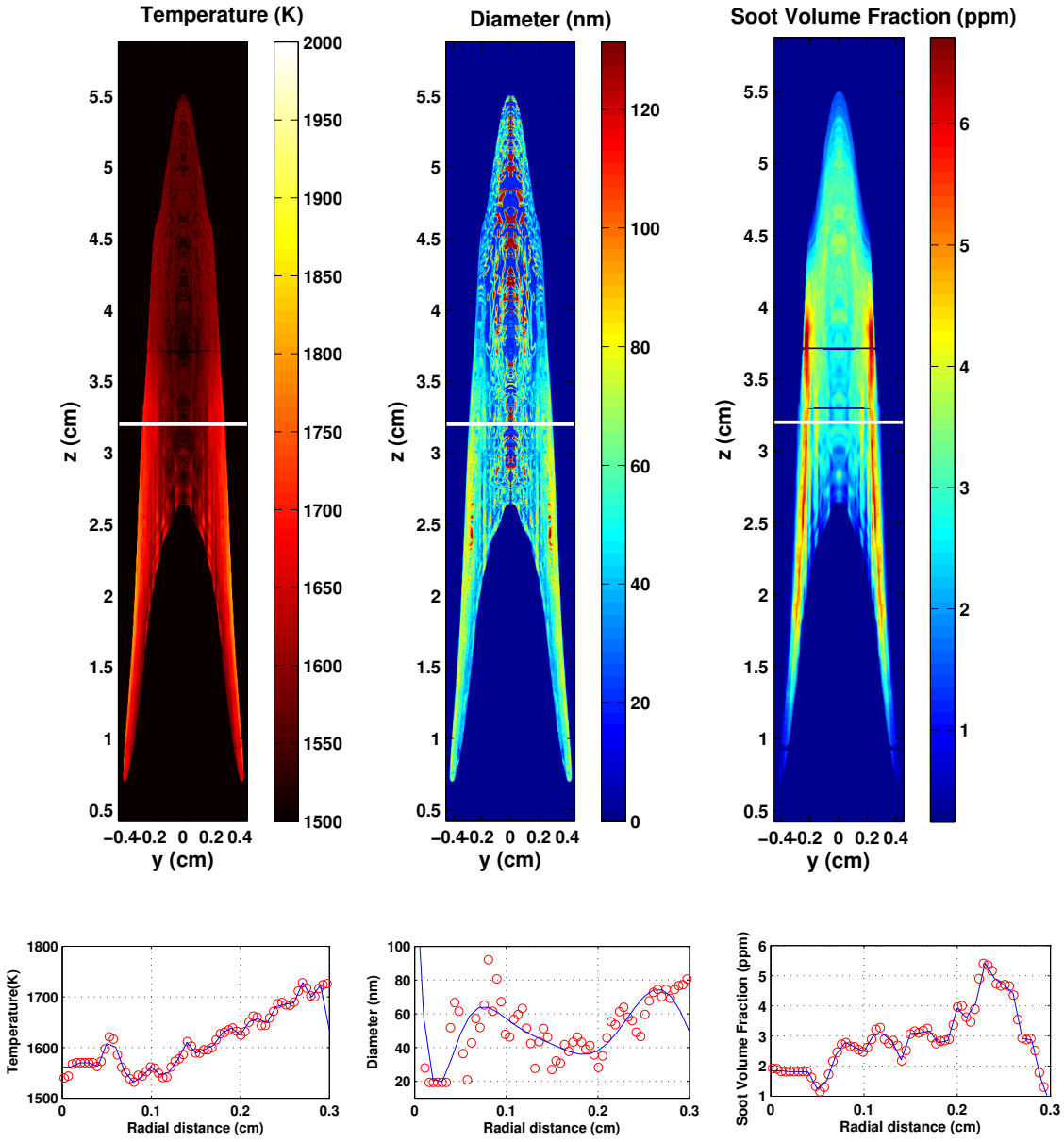

Fig. 3.42: Temperature, soot diameter and soot volume fraction distribution by using the Rayleigh – Gans Theory with Penndorf extension

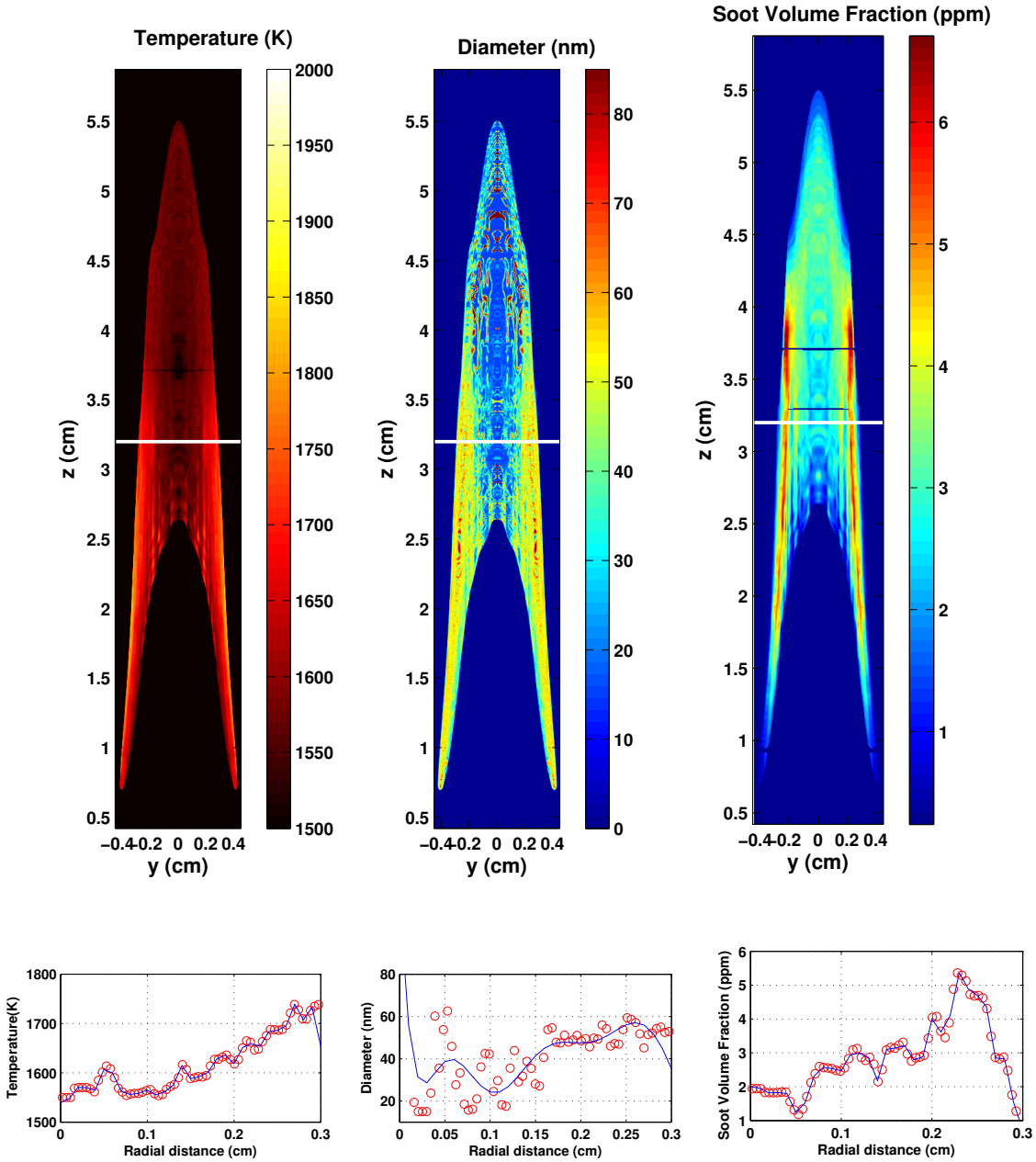

Fig. 3.43: Temperature, soot diameter and soot volume fraction distribution by using the Mie Theory

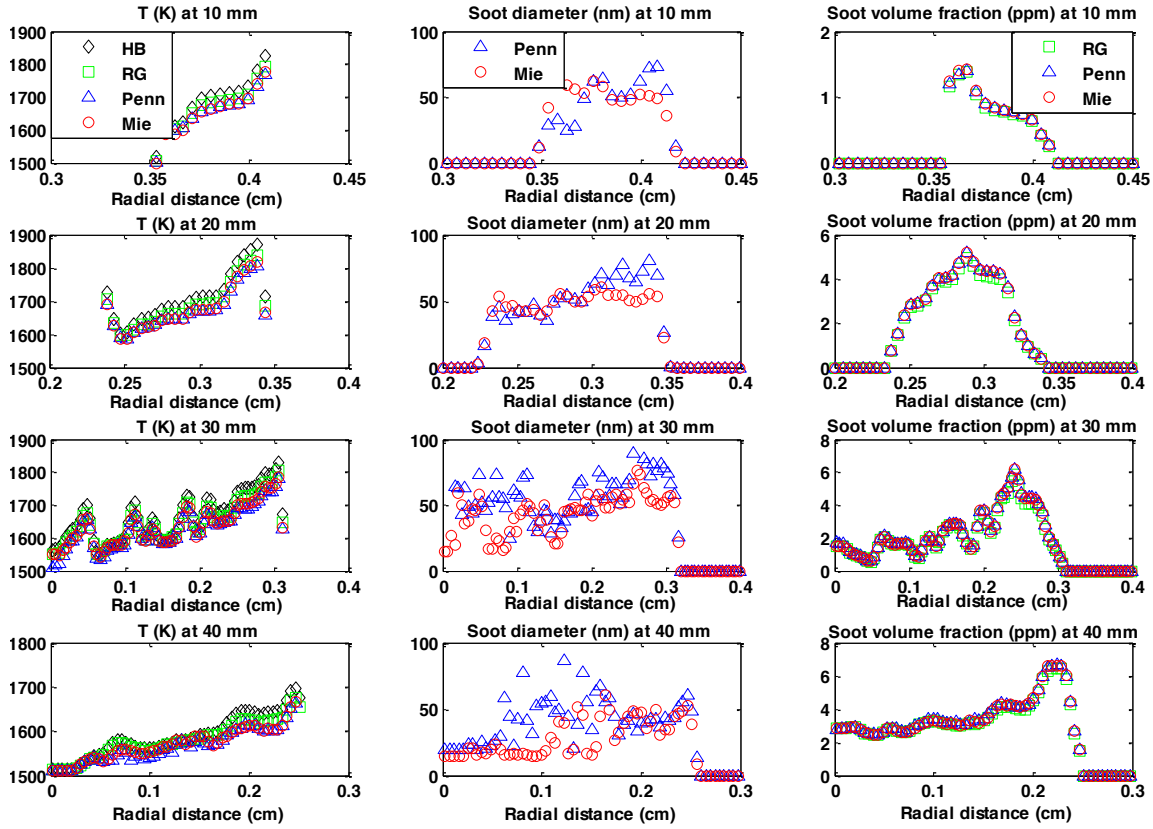

Fig. 3.44: Comparison of temperature, soot diameter and soot volume fraction profiles at different heights when using different scattering models

Fig. 3.43 shows the temperature, soot diameter and soot volume fraction distribution calculated when using the Mie theory. The temperature value in this plot is very close to those in Fig. 3.42(Penndorf extension). The particle size distribution shows a similar trend as in Fig. 3.42 but the value is lower by around 40 nm. Moreover, in the lowest temperature range, the particle size is approaching zero, which indicates very little particle mass in this region.

Comparisons of temperature, soot diameter and soot volume fraction profiles at different heights are shown in Fig. 3.44. In general, the temperature fields reconstructed by using different scattering models show a very consistent structure but the values calculated by using the Hottel and Broughton correlation tends to overestimate the temperatures by around 40-50 K on average, and the Rayleigh-Gans theory also tends to overestimate the temperature by around 20 K if the temperatures calculated by the Mie theory are regarded as the most accurate ones. The particle diameter distributions calculated by using the Penndorf extension and the Mie theory show a very similar structure, but the Mie theory gives a smaller value of particle diameter (by around 40 nm in average). Since the Penndorf extension correlation is a fitting polynomial equation to the experimental data and has no physical meaning, while the Mie theory is the analytical solution to the Maxwell equations, so the size distribution calculated by the Mie theory should be more trustworthy. In addition, because the flame particles are usually smaller than 200 nm, it takes less than 10 iterations to calculate the scattering coefficients in eq. (2.48) and eq. (2.49) so that the Mie theory is the preferred choice for calculating the particle diameter distribution. The Mie scattering models will be used to calculate the soot volume fraction. The *KL* distribution calculated by using the Hottel and Broughton correlation can also give a qualitative estimation of the soot loadings when an appropriate α value is used.

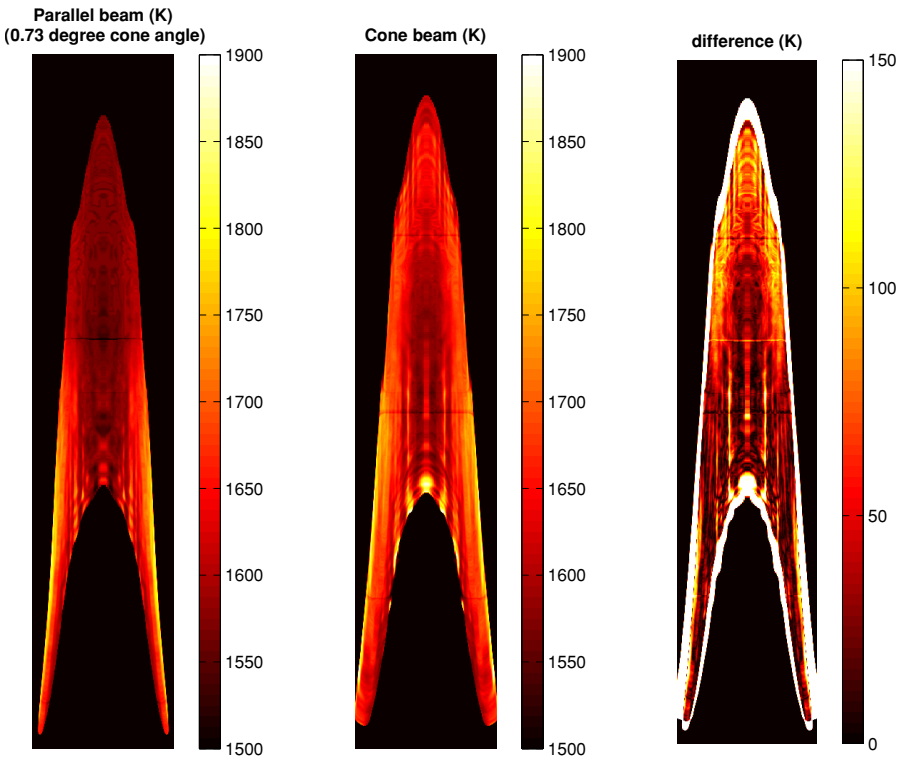

Fig. 3.45: Temperature distributions when using the parallel beam tomography (approximated by cone beam tomography with 0.73° cone angle) and the cone beam tomography

3.5.5 Comparison between parallel beam tomography and cone beam tomography

Some literature suggests that parallel beam tomography can be used as an approximation of the cone beam tomography when cone angle is very small. To investigate how good the parallel beam tomography approximation is, a long focus length (1 m) was used in the cone beam tomography analysis to produce a narrow cone angle about 0.73° as an approximation to parallel beam tomography. The results are plotted in fig. 3.45.

It shows that the overall structure of the temperature distribution can be correctly reconstructed by using parallel beam tomography, and the temperature difference is well below 20 K in most parts of the flame. However, the accuracy is degraded in the regions which are further away from the central of the flame because of the increased cone angle. Therefore, the parallel beam tomography should be used with caution for large flames.

3.6 Summary

The software packages and experimental setup used to apply CBT-TCS has been introduced in this chapter. To find the optimum optical setup, some analyses based on the simple lens theory, including the field of view, lens aberrations, and the effect of optical filters, have been done. These analyses leads to the decision that a Photron camera with a 50 mm Nikon lens, a LEE blue filter, and a 2^*macro converter will be used to capture the image of flames. The values of parameters used in the cone beam tomography, such as the projection number, the zero-padding length, have also been decided by detailed sensitivity analysis. To increase the signal-to-noise ratios, various techniques, such as 3D medium filtering, the downsampling, have been used, and their effects on the measured temperature fields are tested by several sensitivity analysis.

Several tests have been done to investigate the sensitivities of the property fields to the colour ratios. The comparison of different property fields calculated by using different scattering models leads to the decision that in future experiments, the Mie theory will be used to calculate the temperature, soot diameter and soot volume fraction distributions due to its accuracy and the Hottel-Broughton correlation will be used to calculate the KL distribution to give a quanlitative indication of the soot loadings.

Chapter 4

Ethylene Diffusion Flame Experiments

4.1 Introduction

To study Particulate Matter (PM) formation in hydrocarbon laminar diffusion flames, a Santoro burner has been used to produce axisymmetric ethylene diffusion flames. The experimental setup is the same as introduced in the previous chapter (section 2.6.1). The Cone Beam Tomographic Three Colour Spectrometry (CBT-TCS) technique has been used to measure the spatially distributed temperatures, PM diameters, and soot volume fractions. The results from pure ethylene flame experiments produced by a Gulder burner have been compared to the data reported by other workers for similar flames.

Since the effect of adding hydrogen on the PM formation can be divided into three main categories: the thermal effect due to a change in temperature, the dilution effect due to the reduced carbon atom concentrations (especially in the inner region of the diffusion flames) and the direct chemical reaction effect, two groups of experiments were designed. Firstly, different fractions of helium were added into the pure ethylene flame to investigate the dilution effect. Then different fractions of hydrogen were added into the pure ethylene flames to investigate the overall effect. Since the diffusion coefficient of helium is only slightly higher than that of hydrogen, the difference in the results could show the direct chemical reaction effect of the hydrogen.

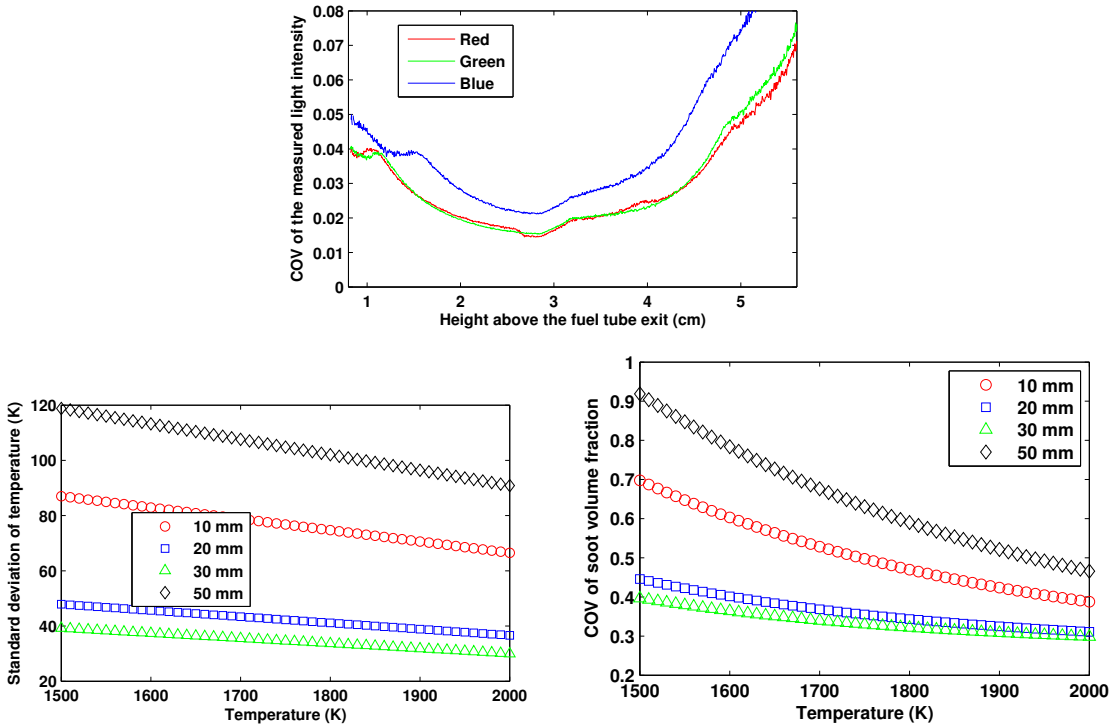

Fig. 4.1: Uncertaities of measurement

To verify the PM diameter distributions, a PM sampling line was designed to collect the PM samples. The samples were analysed using a Cambustion DMS500 to determine the size distributions.

4.2 Pure ethylene flame experiments

The CBT-TCS was applied to a pure ethylene laminar diffusion flame to test whether CBT-TCS can be used to measure the spatially distributed temperatures, soot diameters, and soot volume fractions accurately. The burner used in this experiment was a copy of the burner described by Gulder et al. [31]. It consists of a stainless steel fuel tube of 12.7 mm inner diameter and a air nozzle of 100 mm inner diameter. The ethylene flow rate is 194 mL/min and the air flow rate is 200 L/min. The radial temperature and soot volume fraction distributions at different heights have been compared to the data reported by Snelling et al. [77], as shown in Fig. 4.2.

An uncertainty analysis has been undertaken in order to characterise the precision of the

measurements taken by CBT-TCS. Fig. 4.1 consists of three plots which illustrate in turn flame instability, temperature precision and soot volume fraction uncertainty. The coefficient of variation (COV) o the measured light intensity in fig. 4.1 is obtained by computing the mean and standard deviation at each pixel location through the series of 100 recorded images. At a height of 3cm, the flame luminosity reaches a maximum, and the noise created by the camera is least significant. Below this point, the signal from the flame becomes steadily lower and the COV worsens. Above 3cm, the signal decreases and flame 'flutter' becomes more of a problem, causing up to 8% COV at the flame tip. These fluctuations are amplified throughout the data analysis and lead to height dependence in COV of temperature and soot volume fraction. Fig. 4.1 shows that the best precision for temperature is around 1.5% at a height of 3cm where the flame is very stable. The measurement uncertainty is the worst at the flame tip and is around 8% and this mainly because of the instability of the flame. The uncertainty in the derived soot volume fraction varies from 40-80%. The precisions of the measurements of temperature and soot volume fraction are temperature dependent because of the nonlinear correlation between the thermal radiation and temperature.

Snelling et al. report temperature measurements of this flame using Coherent Anti-Stokes Raman Scattering spectroscopy (CARS) and a 2D tomographic soot spectrometry technique. Spatial soot distributions have been measured using 2D line-of-sight light attenuation (LOSA) and 2D tomographic soot spectrometry. The precision of the CARS measurement was estimated at around ±25-50 K at the flame height of 30 mm [77]; the precision of the 2D LOSA was estimated at around 20-30% and that of the 2D tomographic soot spectrometry was at around 35-45% [82]. The ethylene flow rate in their experiment is also 194 mL/min, but the air flow rate without a chimney is 284 L/min, which is higher than our current experimental setup. The reason our data employs a lower air flow rate is that the flame becomes noticeably unstable for a flow rate higher than 200 L/min. The chimney we used to isolate the flame from air currents in the laboratory constrains the air flow and may be responsible for this difference. This mismatch may also be responsible for a small change in flame height and width, which may be the cause of some of the differences which

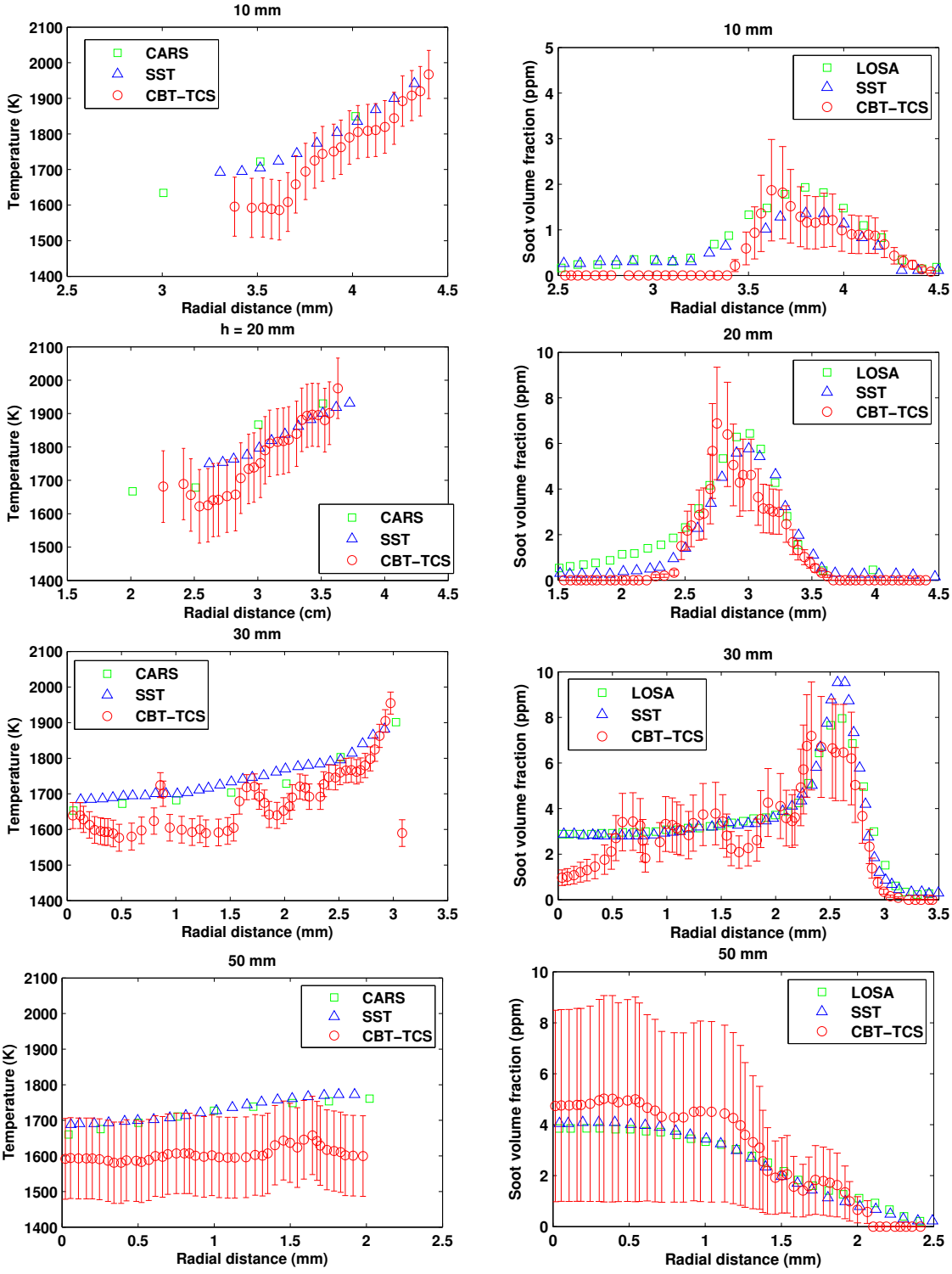

Fig. 4.2: Comparison of the temperature and soot volume fraction profiles at different heights measured by CBT-TCS to that measured by Snelling et al. [77]. (SST: Soot Spectrometry; CARS: Coherent Anti-Stokes Raman Scattering; CBT-TCS: Cone Beam Tomographic Three Colour Spectrometry)

Table 4.1: Summary of test conditions for the helium-ethylene flame experiments

Label	He0	He2	He5	He10	He15	He20
% He	0	2	5	10	15	20
C_2H_4	145	145	145	145	145	145
He	0	2.9	7.5	15.78	25.06	35.5
Air	45×10^3	45×10^3	45×10^3	45×10^3	45×10^3	45×10^3

(a) Flow rates in hydrogen addition tests (mL/min)

Frame rate	Lens	Aperture	Objects-to-lens distance	Lens-to-detector distance	Filter
60 frames/sec	Nikon f 50mm lens; 2* convertor	$f/32$	236 mm	174 mm	LEE E281

(b) Camera and optical system setup

are visible in fig. 4.2. In all cases, the error bars on the CBT-TCS data follow the values presented in fig. 4.1.

In general, fig. 4.2 shows that the radial profiles of both temperature and soot volume fraction at heights of 10, 20, 30 and 50 mm are in good agreement. The differences in the values are largely within the measurement uncertainty. However, the uncertainty in the top region of the flame is much higher than elsewhere, and this is mainly due to the instability of the flame as discussed above. The oscillatory pattern seen most clearly at the 30mm height is thought to be due to the limited dynamic range of the 8-bit CCD sensor which was used to capture the data, since the absolute pixel values at low flame radius are changing by a value which is barely above the digitisation limit. At the edges of the flame, where the luminosity is higher, the CBT-TCS data is stable.

4.3 Diluted ethylene flame experiments

4.3.1 Test conditions

To investigate the effect of dilution on the PM formation, different fractions of helium were added into the pure ethylene. The flow rates of ethylene and helium and the camera setup

are summarized in Table 4.1. A Santoro burner was used in these diluted ethylene flame experiments and the following hydrogen-added ethylene flame experiments.

4.3.2 Results and discussions

In this section, the detailed temperature, soot diameter and soot volume fraction distributions in different helium-ethylene flames are presented. Because of the relatively low signal level near the central axis, the properties within 1mm of the central axis were less accurate.

The flame images taken by the high speed camera show that adding helium increases the flame height slightly. Since helium does not participate in the oxidation process of hydrocarbons directly, the flame heights are mainly decided by the ethylene flow rate and the flame temperature. Fig. 4.3 shows the radial flame temperature distributions at different flame heights. It shows that adding helium does not change the flame temperature distribution much so that the flame heights should not change much if the ethylene flow rate remains constant. The slight increase in the flame heights is due to the dilution effect on the oxidation process of soot particles so that the soot particles have a slightly longer residence time and travel further downstream of the primary reaction region.

The radial soot diameter distributions at different heights are shown in Fig. 4.4. It shows that adding helium does not affect the soot diameter distributions much but it does reduce the total soot concentrations as shown in Fig. 4.5. The detailed radial soot volume fraction distributions at different heights are shown in Fig. 4.6. This shows that adding helium slightly reduces the soot volume fractions in all different regions.

Fig. 4.7 shows the average temperatures, soot diameters, and soot volume fractions at three different heights above the exit port of the fuel tube. It indicates that adding helium has very little effect on the mean temperatures, soot diameter and soot volume fractions.

Fig. 4.8 shows the kernel probability density estimations for different field properties for the whole flame. The kernel used is the Gaussian distribution with a bandwidth calculated

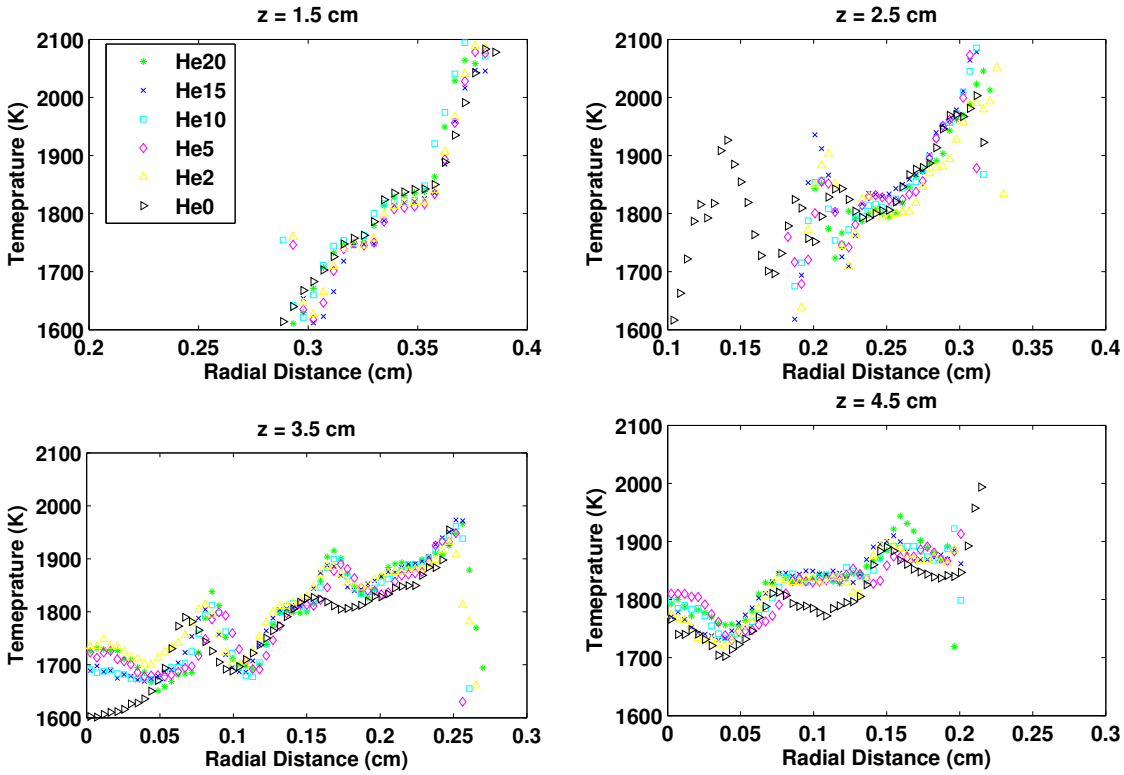

Fig. 4.3: Radial temperature profiles at different heights (z) for helium-ethylene-air flames with a fixed ethylene flow rate as described in Table 4.1

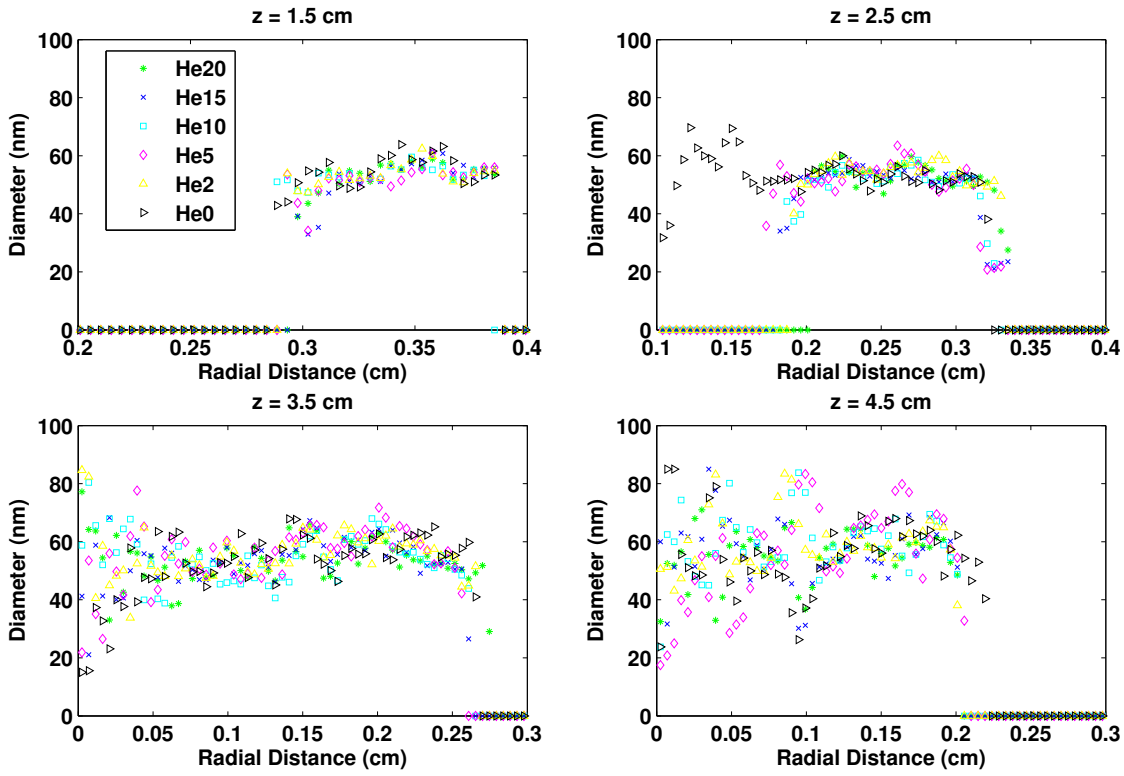

Fig. 4.4: Radial soot diameter profiles at different heights (z) for helium-ethylene-air flames with a fixed ethylene flow rate as described in Table 4.1

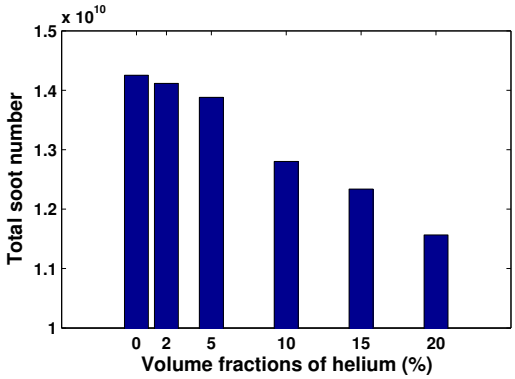

Fig. 4.5: Total soot number concentrations for helium-ethylene-air flames with a fixed ethylene flow rate as described in Table 4.1

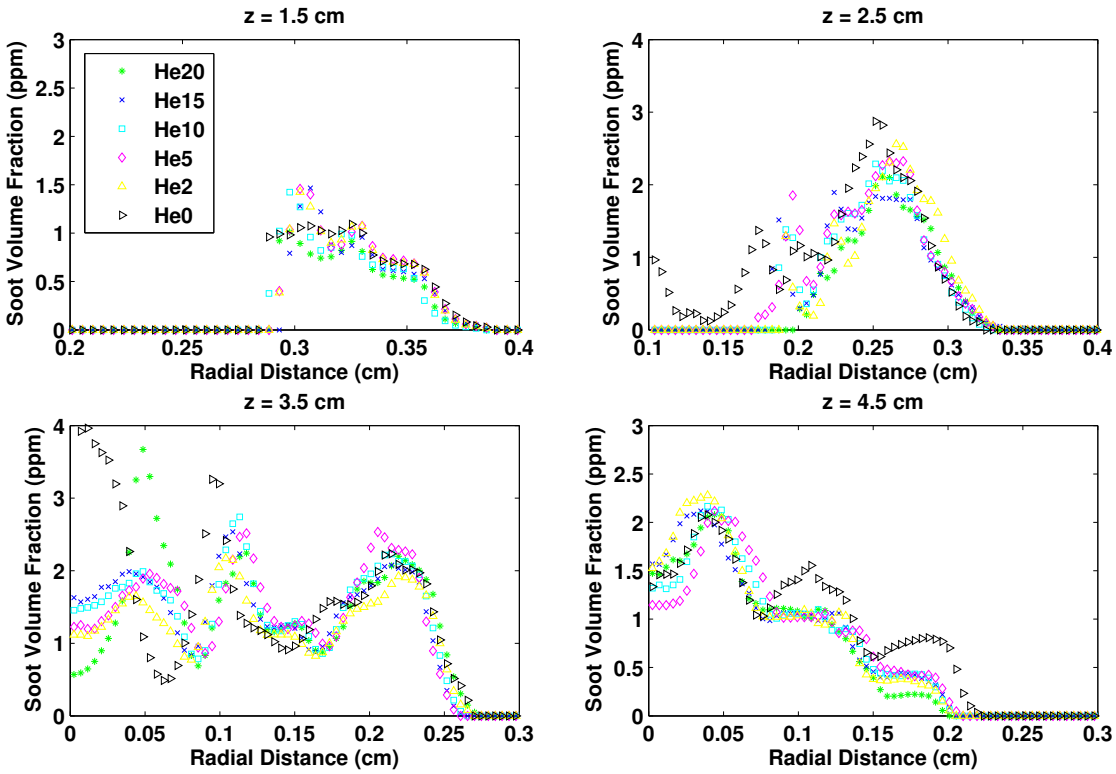

Fig. 4.6: Radial soot volume fraction profiles at different heights (z) for helium-ethylene-air flames with a fixed ethylene flow rate as described in Table 4.1

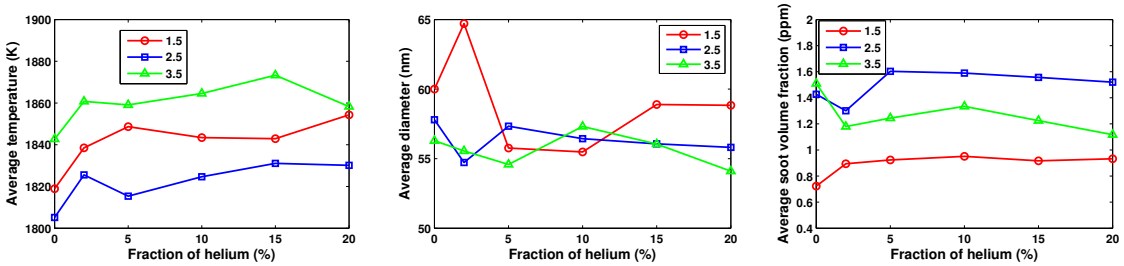

Fig. 4.7: Average temperatures (K), soot diameters (nm) and soot volume fractions (ppm) at three different heights (1.5 cm, 2.5 cm, and 3.5 cm above the exit port of the fuel tube) for the helium-ethylene-air flames

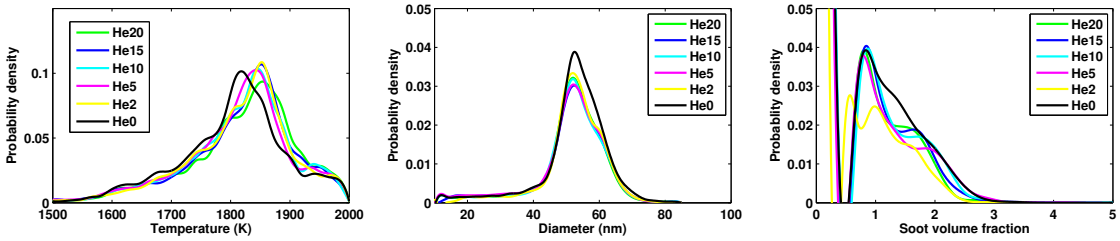

Fig. 4.8: Kernel density estimations of different field properties for helium-ethylene-air flames with a fixed ethylene flow rate as described in table 4.1

Table 4.2: Summary of the parameters used in the kernel probability density estimations

Parameters	Temperature (K)	KL	D (nm)	f_v (ppm)
Kernel Numbers	64	32	32	32
Min. value	1500	15	0	0
Max. value	2000	35	100	220
Resolution	~ 7.8	~ 0.63	~ 3.1	~ 6.9

according to the algorithm suggested in [9]. The detailed kernel numbers and density resolutions are listed in Table 4.2. This shows that adding helium increases the proportion of high temperature regions slightly. Adding helium also increases the fraction of regions with smaller soot diameter and a lower soot volume fraction.

4.4 Hydrogen-ethylene flame experiments

4.4.1 Test conditions

Two groups of hydrogen-ethylene diffusion flame experiments will be introduced in this section. The first group of experiments kept the ethylene flow rate constant and added different fractions of hydrogen. The second group kept the total flow rate of ethylene and hydrogen constant while adding different fractions of hydrogen. The test conditions for these two different groups of experiments are listed in Table 4.3.

Table 4.3: Summary of test conditions for the hydrogen-ethylene flame tests

Label	H0	H2	H5	H10	H15	H20
$\%H_2$	0	2	5	10	15	20
C_2H_4	145	145	145	145	145	145
H_2	0	2.9	7.5	15.78	25.06	35.5
Air	$45*10^3$	$45*10^3$	$45*10^3$	$45*10^3$	$45*10^3$	$45*10^3$

(a) Flow rates in the hydrogen-ethylene flame tests with fixed ethylene flow rate (mL/min)

Label	H0	H2	H5	H10	H15	H20	H25
$\%H_2$	0	2	5	10	15	H20	25
C_2H_4	145	142.1	137.25	130.5	123.25	116	108.75
H_2	0	2.9	7.25	14.5	21.75	29	36.25
Air	$45*10^3$	$45*10^3$	$45*10^3$	$45*10^3$	$45*10^3$	$45*10^3$	$45*10^3$

(b) Flow rates in the hydrogen-ethylene flame tests with fixed total fuel flow rate (mL/min)

4.4.2 Results and discussions

In this section, the detailed field properties of the hydrogen-ethylene flames with a constant ethylene flow rate will be discussed first. Then, the properties of flames with a constant total hydrogen and ethylene flow rate will be presented. As mentioned in the previous section, because of the relatively high noise level near the central axis, the properties within 1 mm of the central axis are less accurate.

4.4.2.1 Constant ethylene flow rate

The flame height does not change much when adding hydrogen according to the flame images. This is because, though the total fuel flow rate increased, adding hydrogen increases the burn rate and the flame temperature (Fig. 4.9) so that the soot particles are oxidized more quickly before they can reach a higher and cooler position. Fig. 4.9 shows the radial temperature distributions at different heights. It shows that adding hydrogen increases the flame temperature in all regions. This is because adding hydrogen increases the heat release rate and the hydrogen also has a higher adiabatic flame temperature compared to ethylene.

Fig. 4.10 presents the radial PM diameter distributions at different heights, and shows that adding hydrogen does not affect the PM size much. The average PM diameter is around 50

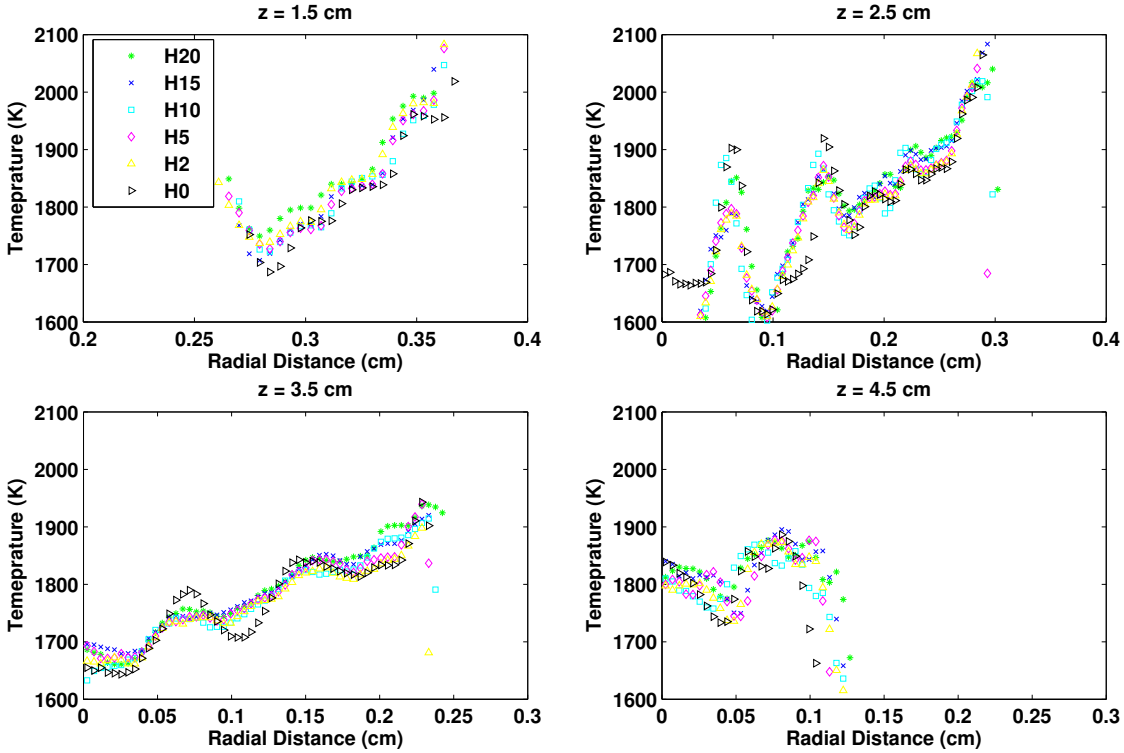

Fig. 4.9: Radial temperature profiles at different heights (z) for hydrogen-ethylene-air flames with a constant ethylene flow rate as described in Table 4.3

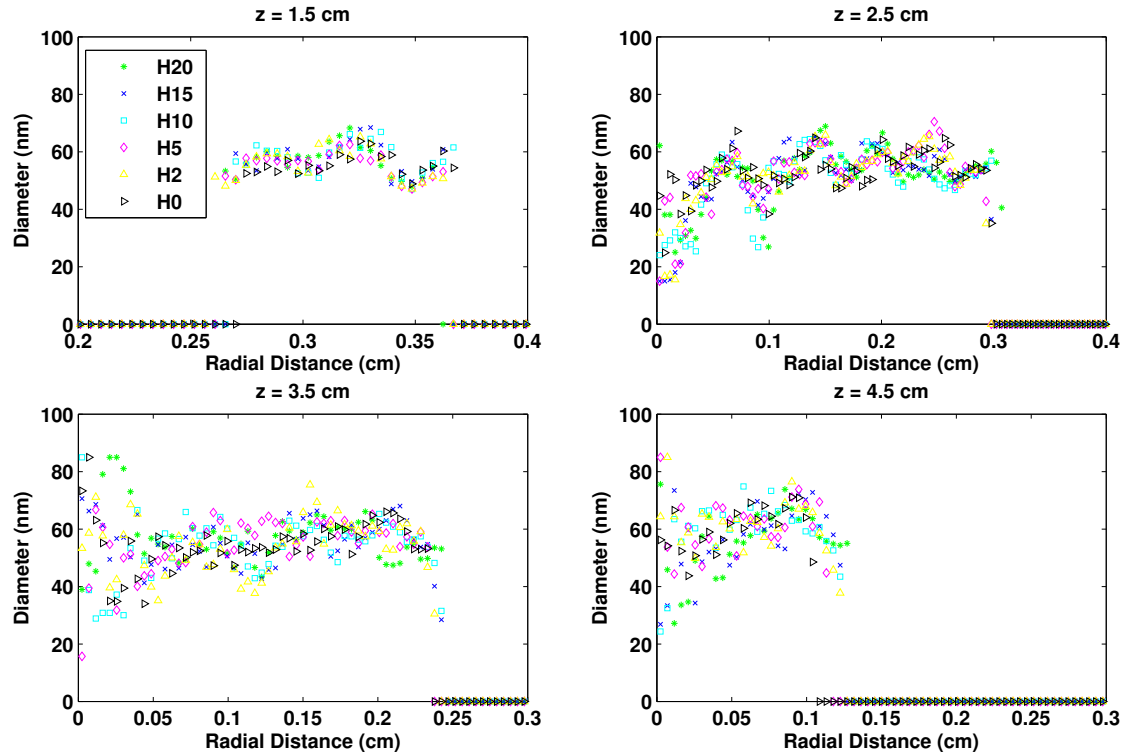

Fig. 4.10: Radial soot diameter profiles at different heights (z) for hydrogen-ethylene-air flames with a constant ethylene flow rate as described in Table 4.3

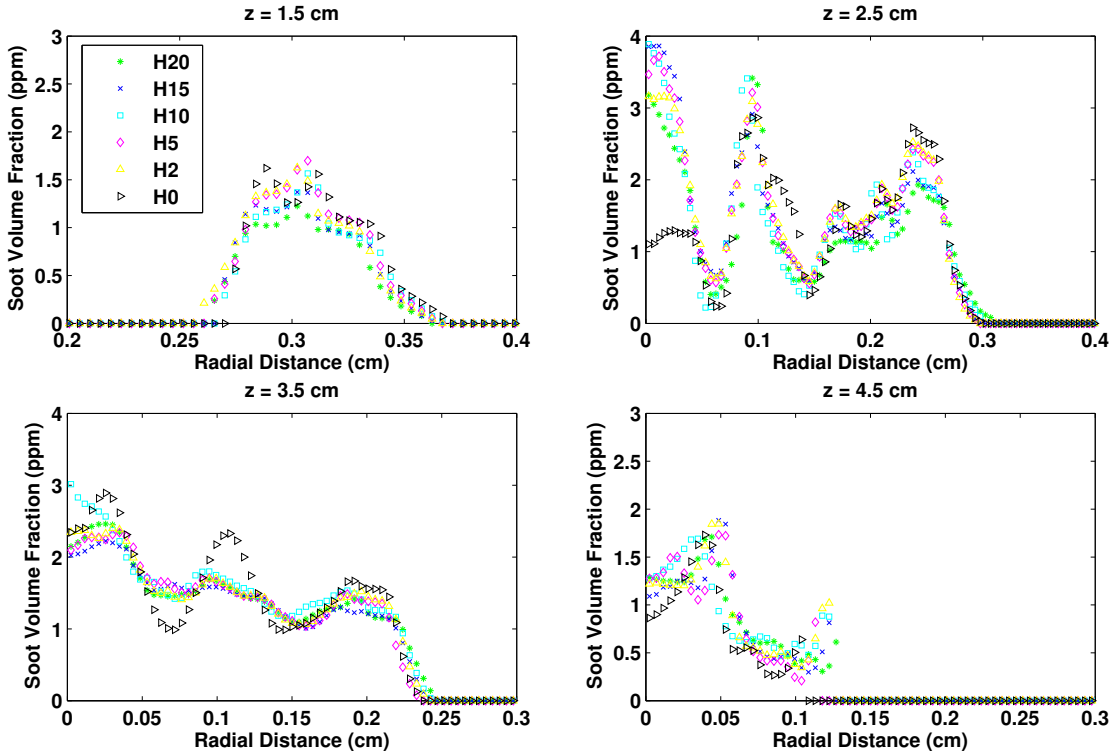

Fig. 4.11: Radial soot volume fraction profiles at different heights (z) for hydrogen-ethylene-air flames with a constant ethylene flow rate as described in Table 4.3

nm across the whole flame.

Fig. 4.11 shows the radial soot volume fraction distributions at different heights. The general trend found in this figure is that adding hydrogen reduces the soot volume fraction except in the noisy central region. Since the temperature in the central region is not high enough for the pyrolysis reactions to take place to produce PM precursors, the PM in this region have mainly diffused from nearby regions and should have a much lower concentration than the reaction zone. A comparison between Fig. 4.9 and Fig. 4.11 shows that the most sooting part of the flame is also the hottest part. This is because the pyrolysis reactions which produce the PM precursors take place in the reaction zone where the temperature is high enough and the oxygen concentration is relatively low. The oxidation of the PM becomes more significant as the height increases. Therefore, the soot volume fraction decreases as the height increases above the reaction zone. Fig. 4.12 shows the total PM numbers within the flame, and it clearly shows that adding hydrogen reduces the total PM number.

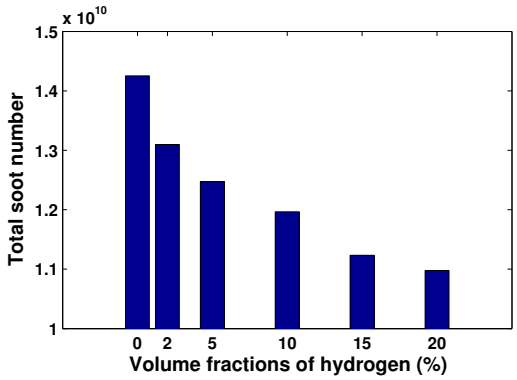

Fig. 4.12: Total soot number concentrations for hydrogen-ethylene-air flames with a constant ethylene flow rate as described in Table 4.3

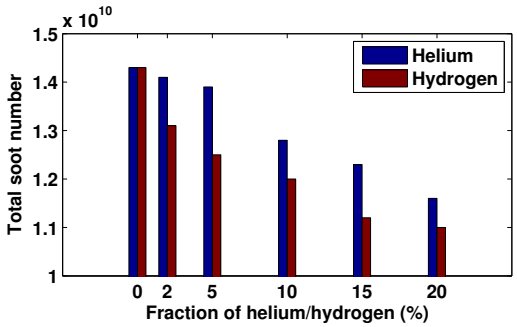

Fig. 4.13: Comparison of the total soot number concentrations when adding different fractions of helium/hydrogen (constant ethylene flow rate)

Fig. 4.13 shows a comparison of the total PM numbers between the diluted ethylene flames and the hydrogen-ethylene flames. It can be clearly seen from this figure that adding the same fraction of hydrogen is more effective in reducing the PM formation due to the combined dilution effect and direct chemical inhibition effect. Similar trends can be found by comparing the detailed radial soot volume fraction distributions at different flame heights (fig. 4.6 and fig. 4.11).

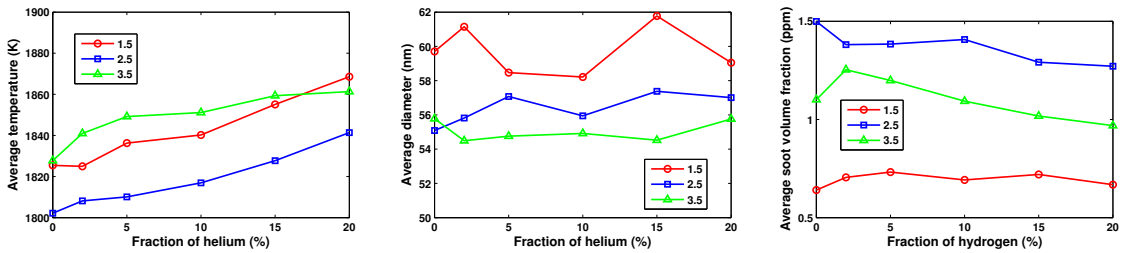

Fig. 4.14: Average temperatures (K), soot diameters (nm) and soot volume fractions (ppm) at three different heights (1.5 cm, 2.5 cm, and 3.5 cm above the exit port of the fuel tube) for the hydrogen-ethylene-air flames with a constant ethylene flow rate as described in Table 4.3

Fig. 4.14 shows the average temperatures, soot diameters, and soot volume fractions at different heights when adding hydrogen. It clearly shows that adding hydrogen generally increases the mean flame temperatures and reduces the mean soot volume fractions in all regions.

Fig. 4.15 shows the kernel probability density estimations for different field properties. The temperature probability density curves in this figure show that adding hydrogen tends to shift the whole temperature probability density curve towards a higher value and distributes the temperature more evenly throughout the flame. The PM diameter and soot volume fraction probability density curves in Fig. 4.15 show that adding hydrogen slightly suppresses the proportion of large particle ($D > 55$ nm) region and effectively reduces the fraction of high soot volume fraction region. According to the HACA (Hydrogen-Abstraction Carbon Addition) model, the formation of PAH (Polycyclic Aromatic Hydrocarbons) depends on the concentration of C_2H_2, H and H_2. Adding hydrogen increases the concentration of molecular hydrogen, which will increase the reverse reaction rate in reaction 1.30. Therefore, the H-abstraction rate is reduced and the available primary particle numbers are reduced. After the primary particles are created, the larger particles are formed through coagulation and surface growth. The coagulation rate is proportional to the number concentration of the primary particles so that the coagulation rate will also be reduced when adding hydrogen. According to the HACA surface reaction model, the surface growth rate is proportional to the acetylene concentration, the active surface site density and the particle surface area. According to the simulations done by Guo et al. (2006)[32], adding hydrogen reduces the active surface site density but increase the acetylene concentration. Therefore, the reduced proportion of larger soot particles can also because of the reduction in active surface sites.

4.4.2.2 Constant total fuel flow rate

The flame height reduced when ethylene is replaced by hydrogen, as shown in Fig. 4.16. This is because of the increased burn rate and flame temperature when adding hydrogen.

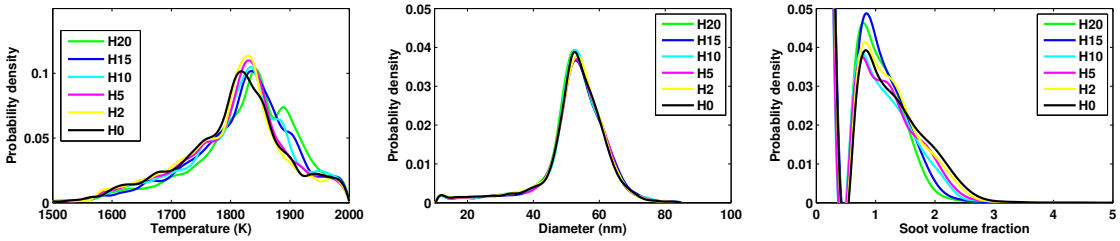

Fig. 4.15: Kernel density estimations of different field properties for hydrogen-ethylene-air flames with constant ethylene flow rate as described in Table 4.3

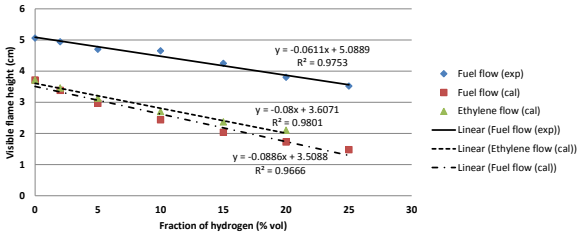

Fig. 4.16: Flame heights when replacing different fraction of ethylene with hydrogens

The fitting curve in Fig. 4.16 shows that the flame height is roughly in a linear correlation with the fraction of hydrogen.

Fig. 4.17 shows the total PM numbers within the flame. It clearly show that replacing the ethylene with hydrogen can significantly reduces the total PM number. Adding 25% of hydrogen can reduce the total PM number by 66%. The reduction is because of the combined effect of reduced amount of carbon atoms and the dilution and chemical inhibation effect when adding hydrogen.

Fig. 4.18 shows the kernel probability density estimations for different field properties.

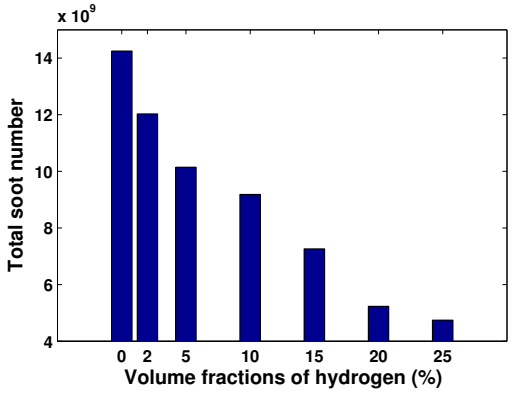

Fig. 4.17: Total soot number concentrations for hydrogen-ethylene-air flames with constant total fuel flow rate as described in table 4.3

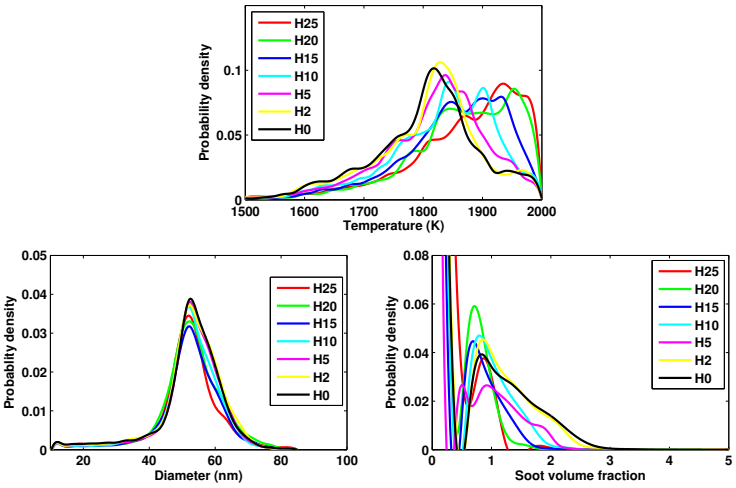

Fig. 4.18: Kernel density estimations of different field properties for hydrogen-ethylene-air flames with constant total fuel flow rate as described in Table 4.3

The temperature probability density curves show that adding hydrogen greatly increases the high flame temperature region. The PM diameter and soot volume fraction probability density curves show that adding hydrogen suppresses the proportion of both large particle regions and high soot volume fraction regions. The reason is similar to the constant ethylene flow rate experiment: adding hydrogen reduces the formation of primary soot particles so that the coagulation rate will be reduced and adding hydrogen may also reduce the surface growth rate so fewer large soot particles can be formed.

4.5 Particulates sampling experiments

To verify the soot diameter distributions inside the laminar diffusion flames, a particulate sampling line has been built to collect a sample which can be analysed by the Cambustion DMS500 particle spectrometer.

4.5.1 Experimental setup

The PM sampling line is shown in Fig. 4.19. As shown in this figure, a brass T-shaped sampling line was used to collect the PM samples. The diameters of the horizontal tube and

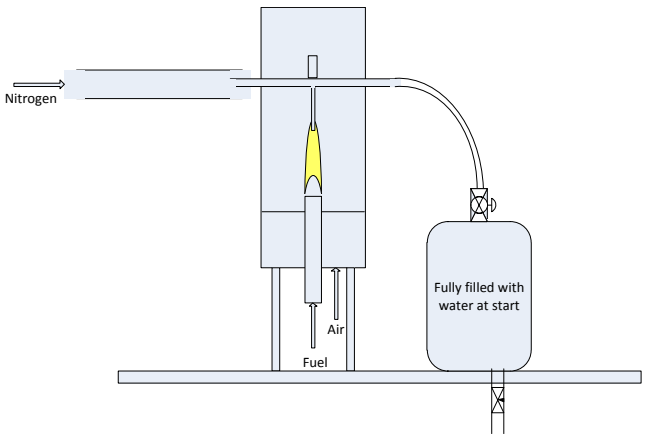

Fig. 4.19: Particulate sampling line for the diffusion flame burner

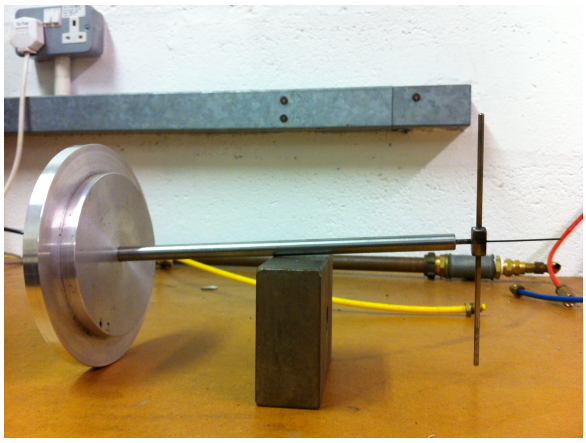

Fig. 4.20: Sampling tube and the central axis alignment facility

the vertical tube were chosen as 3mm and 1 mm respectively to produce a 1:9 dilution ratio. Nitrogen is used as the dilution gas instead of air to reduce the oxidation of the PM and is fed into one end of the horizontal tube where the pressure is at atmosphere pressure. The other end of the horizontal sampling tube is connected to a bottle fully filled with water. After opening the ball valve at both the top and bottom of the bottle, the pressure difference will draw the PM samples into the bottle, with the flow rate controlled by a needle valve. The water leaves through a long vertical pipe, so that the change in water level in the reservoir is not significant. The dilution ratio was double checked by using a gas analyser in the following way: one end of the horizontal tube was exposed to the air and the other end was connected to a gas analyser. When CO_2 is fed into the vertical tube, the gas analyser showed the CO_2 concentration, which can be used to check the dilution ratio.

Fig. 4.20 shows the facility used to align the sampling tube with the central axis of the burner. An alignment bar that is on the same axis as the sampling tube can be inserted into a metal tube, which is aligned to the burner axis by a circular metal plate. The metal plate can be just fitted into the top of the burner, so that the centre of the circular plate coincides with the centre of the burner. The sampling tube is fixed to the burner chimney wall so that the height of the sampling tube can be changed by adjusting the height of the chimney.

When collecting the PM samples from the diffusion flame, the CBT-TCS technique was used simultaneously to measure the temperature, soot diameter and the soot volume fraction distributions. The size distributions of the PM samples collected in the reservoir were measured by using the DMS500: the sampling reservoir was needed as the sampling rate of the DMS500 is about an order of magnitude greater than the sample flow rate.

The pure ethylene diffusion flame was used to generate the sample. The ethylene flow rate was set at 145 mL/min and the air flow rate was 45 L/min. The height of the sampling tube was set at around 35mm away from the outlet of the fuel tube, which is just above the reaction region according to the previous burner tests.

4.5.2 Results and discussions

Fig. 4.21 shows the temperature, soot diameter and soot volume fraction distributions in the central axis plane of the flame measured by using the CBT-TCS technique. As shown in Fig. 4.21, the sampling tube has a significant impact on the temperature, soot diameter and soot volume fraction distributions around the sampling tube (especially around the tip of the sampling tube) because of the heat conduction to the sampling tube and the soot deposition around the sampling tube.

The size distribution measured by DMS500 is shown in fig. 4.22. The red line in Fig. 4.22 is the average value of the PM size distribution. Fig. 4.22 also shows the probability density distribution of the PM size measured by the CBT-TCS. The comparison indicates that the CBT-TCS tends to overestimate the particle size by a factor of two. This is probably because

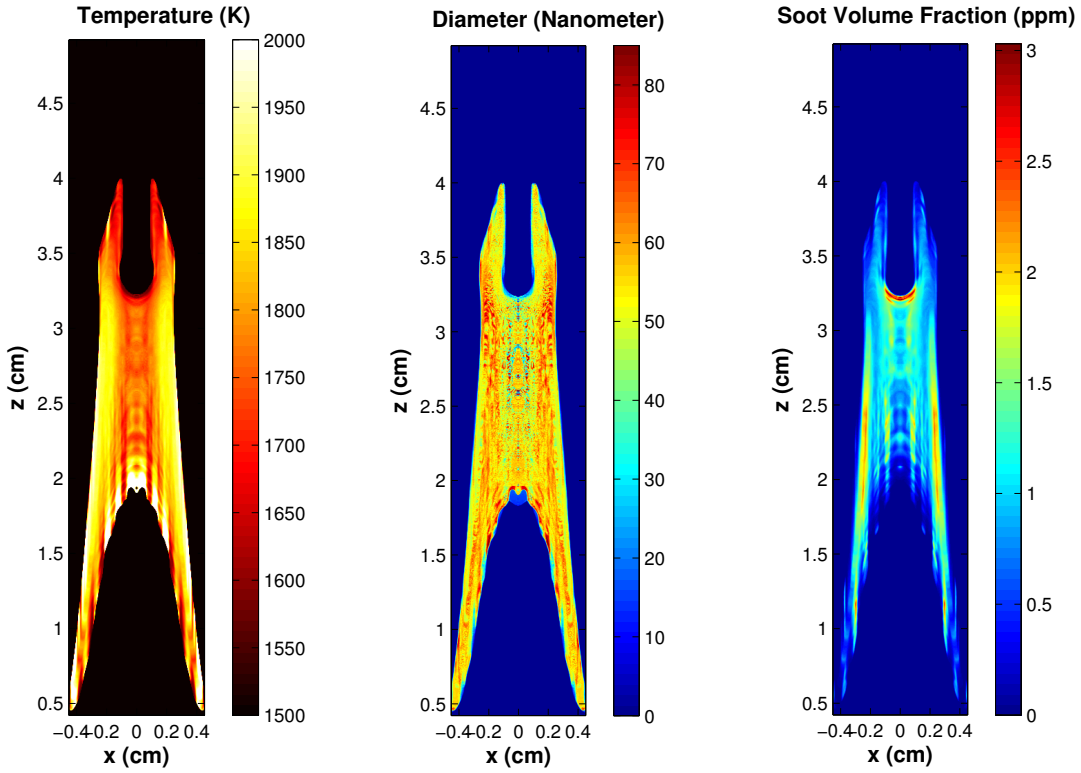

Fig. 4.21: Temperature, soot diameter and soot volume fraction distributions in the central axis plane of the ethylene-air flame (sampling experiment)

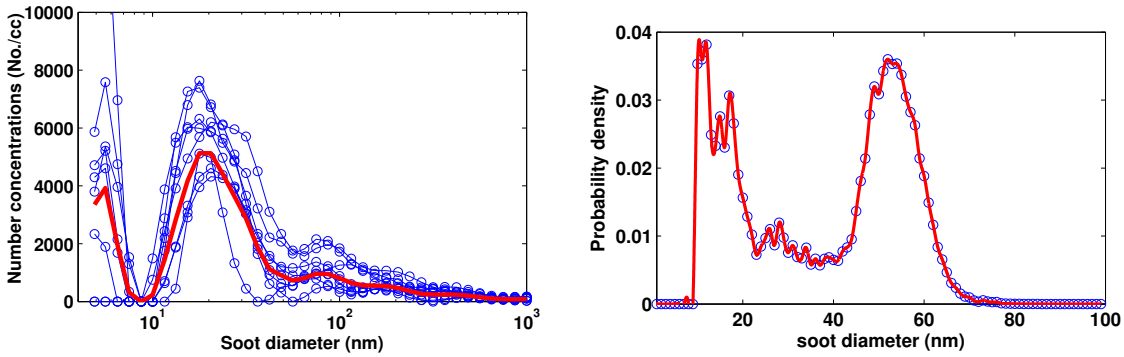

Fig. 4.22: PM number concentration distributions measured by DMS500 and CBT-TCS

the scattering model used in the CBT-TCS assumes single scattering between soot particles but the reality is that there will be multiple scatterings between them. So the light losses due to multiple scattering among soot clouds has been simulated by single scattering among larger soot particles.

4.6 Summary

In this chapter, several different burner experiments have been introduced in detail. To investigate the accuracy of the newly developed optical diagnostic technique — CBT-TCS, this technique has been applied to a Gulder burner to measure the spatially distributed temperature and soot volume fraction profiles. These profiles are consistent with the data reported by Snelling et al. [77]. The difference are well within the experiment uncertainty. The uncertainty analysis also shows that the precision of the CBT-TCS is highly temperature and height dependant and it gets worse in the top part of the flame mainly because of the instability of the flame.

To investigate the dilution effect on the PM formation, different fractions of helium were added into the ethylene flames. The results show that adding helium does not affect the temperature distribution much, but does reduce the soot concentrations. Then, different fractions of hydrogen were added into the ethylene flames to investigate the effect of hydrogen on PM formations. The results show that adding hydrogen has little effect on the flame height, because the increased burning rate compensates for the effect of an increased total fuel flow rate. But adding hydrogen increases the flame temperature because of the increased heat release and the higher adiabatic flame temperature of hydrogen compared to ethylene. Adding hydrogen also reduces the PM concentrations more effectively than adding helium due to the combined effect of dilution and direct chemical inhibition.

To investigate the effect of replacing hydrocarbon fuels with hydrogen on the PM formations, different hydrogen-ethylene mixtures with constant total fuel flow rate were used as the fuel. The results show that increasing the fraction of hydrogen can reduce the PM for-

mation significantly in laminar diffusion flames. This is not only due to the dilution and chemical inhibition effect mentioned earlier, but also due to the reduced amount of carbon atoms.

Finally, a PM sampling system has been built up to collect the samples from an ethylene-air diffusion flame to verify the PM size distributions measured by the CBT-TCS. The samples were analyzed using a Cambustion DMS500, and the results indicate that the CBT-TCS overestimates the soot diameter by a factor of two. This is probably due to the single scattering assumption interpretes the light loss due to multiple scattering as scatter from s single larger soot particle.

To investigate the effect of adding hydrogen on PM emissions in a realistic combustion system, an optical engine has been used to test different hydrogen-hydrocarbon fuels and these experiments will be introduced in the next chapter.

Chapter 5

Hydrogen-Enhanced GDI Engine Experiments and Simulations

5.1 Introduction

The laminar diffusion flame burner tests introduced in chapter 3 show that adding hydrogen reduces the Particulate Matter (PM) emissions, increases the flame temperatures and speeds up the combustion (shorter flame). These results lead to speculation that adding hydrogen in Gasoline Direct Injection (GDI) engines would also reduce their PM emissions. Several groups of engine tests have been carried out to verify this hypothesis. Mixtures of hydrogen and ethylene were used in the first group of engine experiments, as in the burner tests. Then a second group of experiments was conducted by using a mixture of hydrogen and gasoline (represented by a mixture of isooctane and toluene) to investigate the effect of adding hydrogen into gasoline in a GDI engine.

5.2 Experimental setup

All experiments were carried out in a Jaguar optical access engine. This engine can be operated either in direct injection mode or in plenum fuel injection mode. The specification

Table 5.1: Specification of the Jaguar optical engine

Engine Type	Spray-guided direct injection spark ignition engine
Valves	Two intake valves and two exhaust valves
Bore*stroke (mm)	89*90.3
Compression ratio	11.1
Cylinder capacity (cc)	561.8
Injection pressure (bar)	150

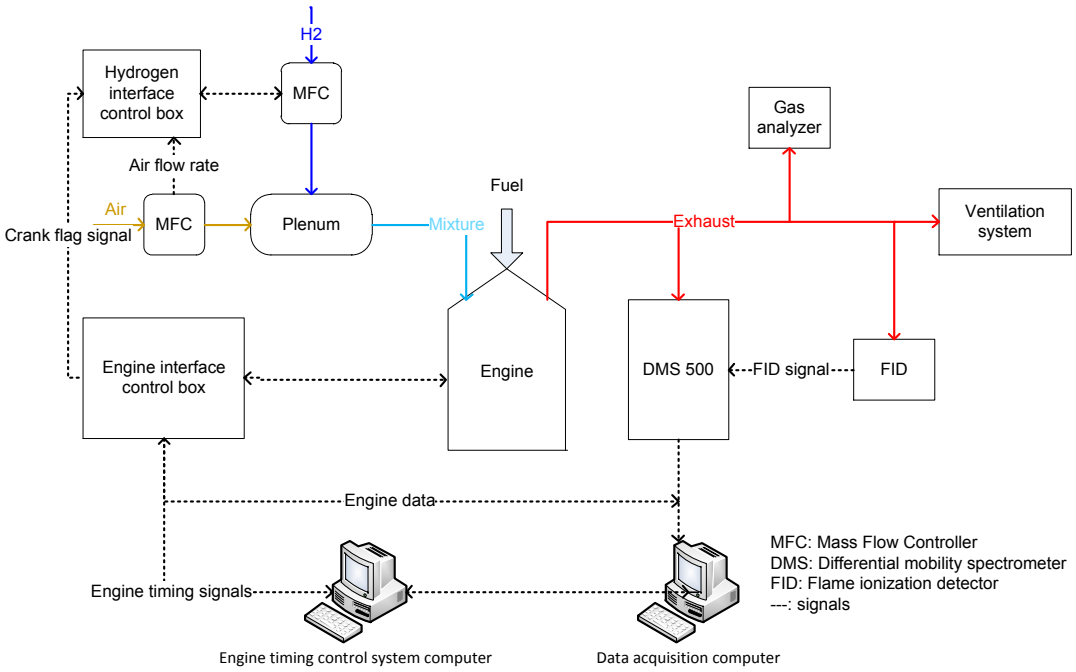

Fig. 5.1: Optical engine experimental set-up

of this engine is summarized in Table 5.1and a schematic picture of the overall experimental set-up is shown in Fig. 5.1.

The fraction of hydrogen is controlled by a mass flow controller from MKS. It was calibrated against air in the first place by using a positive displacement wet gas meter. Then knowledge of the densities and heat capacities of air and hydrogen was used to convert the calibration data from air to hydrogen.

The air flow rate in the intake manifold is measured by a positive displacement flow meter with an output fed back into the hydrogen interface control box to control the hydrogen flow rate. (See Fig. 5.1). According to the energy calculation (Appendix 1) and calibration data, the control voltage for the hydrogen mass flow controller (V_{H_2}) and the output voltage

from the air flow controller (V_{air}) at $x\%$ of stoichiometric hydrogen is correlated by:

$$V_{\text{H}_2}/V_{\text{air}} = 0.0444 \cdot x/C1 \tag{5.1}$$

where C1 is the gain value (2*, 5*, and 10*) from the interface control box. By using a multi-turn potentiometer, the stoichiometric fraction of hydrogen can be controlled.

The Engine Timing Control System (ETCS) is used to control the ignition timings, injection timings, and injection durations etc., and it is also used to trigger the Data Acquisition (DAQ) system. The DAQ system consists of a high speed data acquisition (HDAQ) system and a low speed data acquisition (LDAQ) system. The HDAQ system uses a 12-bit data acquisition card from National Instruments with a maximum sampling rate of 1.25 MS/s. The HDAQ system is for recording high frequency signals, such as the cylinder pressure trace, the trigger signals, or the crank flag signal. A National Instruments PCI-6024E DAQ card (12-bit and 200 KS/s maximum sampling rate) is used in the LDAQ system. The relatively low frequency signals, such as various temperatures, equivalence ratio, and the torque are logged into the LDAQ system.

The emissions are measured by various standard instruments. The PM emissions are measured by a Cambustion DMS500 Differential Mobility Spectrometer. The Unburned Hydrocarbons (UBHC) are measured by a Flame Ionization Detector (FID) and the Nitrogen Oxides (NOx) emissions are measured by a chemical cell gas analyser.

The cylinder pressure trace recorded by the DAQ system is further analysed by a software package called CoBRA (Combustion Burn Rate Analysis, written in MATLAB with a Graphical User Interface). It can be used to calculate the burn rate and the cumulative mass fraction burn according to the approach introduced by Rassweiler and Withrow (1938) [64].

5.3 Results and discussions

5.3.1 Hydrogen-ethylene experiments

The laminar flame burner tests show that adding or blending hydrogen reduces the PM emissions due to both the dilution effect and the direct chemical inhibition effect. To verify whether these effects are still valid in the engine operation environment, a group of engine tests have been done using ethylene-hydrogen mixtures. The optical engine was operated in the plenum fuel injection mode, and the test conditions are summarized in Table 5.3. The case with 5% stoichiometric of hydrogen is equivalent to 24% of hydrogen by volume of the fuel. The combustion related results are shown in Table 5.2.

Table 5.2: Combustion related results from the hydrogen-ethylene engine tests

	fuel	equivalence ratio (λ)	P_{max} (bar)[1]	$IMEP_n$ (bar)	COV_{IMEP_n} (%)	mfb (CA°) 10%	50%	80%
test 1	100% C_2H_4	1.0	25	2.5	2.7	9.9	17	21.6
test 2	100% C_2H_4	0.9	26	2.5	2.6	9	15.9	20.5
test 3	95% C_2H_4+ 5% H_2	1.0	28	2.6	2.9	8.5	15	19.4
test 4	95% C_2H_4+ 5%H_2	0.9	29	2.7	2.9	7.8	14	18.5

As can be clearly seen from table 5.2, blending with hydrogen speeds up the combustion so that the maximum cylinder pressure is increased. The power output from the engine is also increased by adding hydrogen because of the higher calorific value of hydrogen and the increased engine efficiency due to the faster combustion. The cycle-by-cycle variation is already very low and not affected much by adding hydrogen.

[1] P_{max}: maximum cylinder pressure; $IMEP_n$: net indicated mean effective pressure; COV_{IMEP_n}: coefficient of variation of the net indicated mean effective pressure; mfb: mass fraction burned.

Table 5.3: Hydrogen-ethylene engine test conditions

	fuel	equivalence ratio (λ)	air flow rate	fuel injection timing	ignition timing
test 1	100% C_2H_4	1.0	1.0 L/s	265° btdc	20° btdc
test 2	100% C_2H_4	0.9	1.0 L/s	265° btdc	20° btdc
test 3	95% C_2H_4+5% H_2 (by stoichiometric fraction)	1.0	1.0 L/s	265° btdc	20° btdc
test 4	95% C_2H_4+5% H_2 (by stoichiometric fraction)	0.9	1.0 L/s	265° btdc	20° btdc

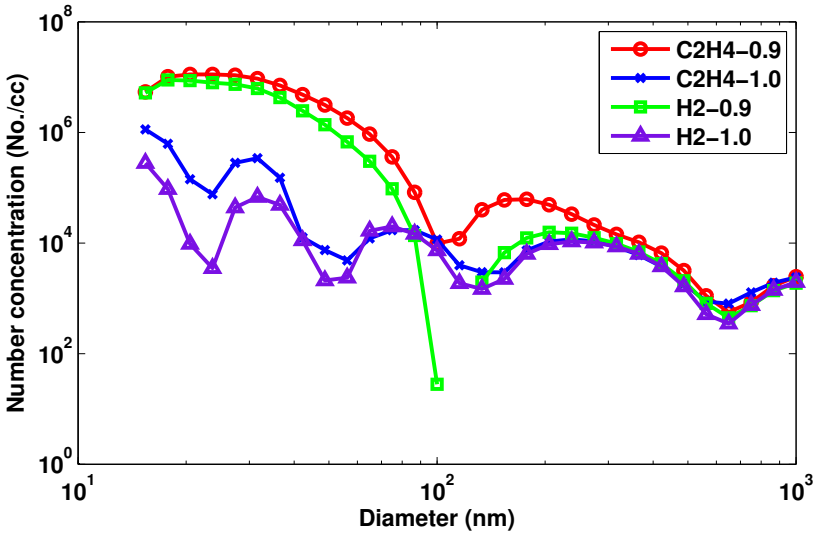

Fig. 5.2: Taipipe particulate matter emissions

The exhaust PM emissions are shown in Fig. 5.2, which clearly shows that adding hydrogen reduces the PM concentrations across the whole size range. Since the background noise level for DMS500 is around 10^4, the concentrations near or lower than this level are not very accurate, which leads to the multiple mode PM emission artefacts for the stoichiometric mixtures shown in Fig. 5.2.

To study the in-cylinder PM formation, a Photron high speed colour camera with Nikon 50mm lens was used to record the combustion process and the flame images were analysed further by using the modified three-colour pyrometry (TCP) technique to deduce the temperature and soot loadings qualitatively. The field of view of the camera is shown in Fig. 5.3.

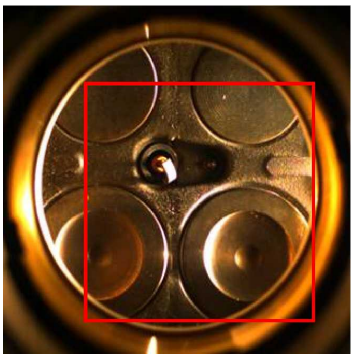

Fig. 5.3: Field of view of the camera (70×70 mm) in the optical engine experiments

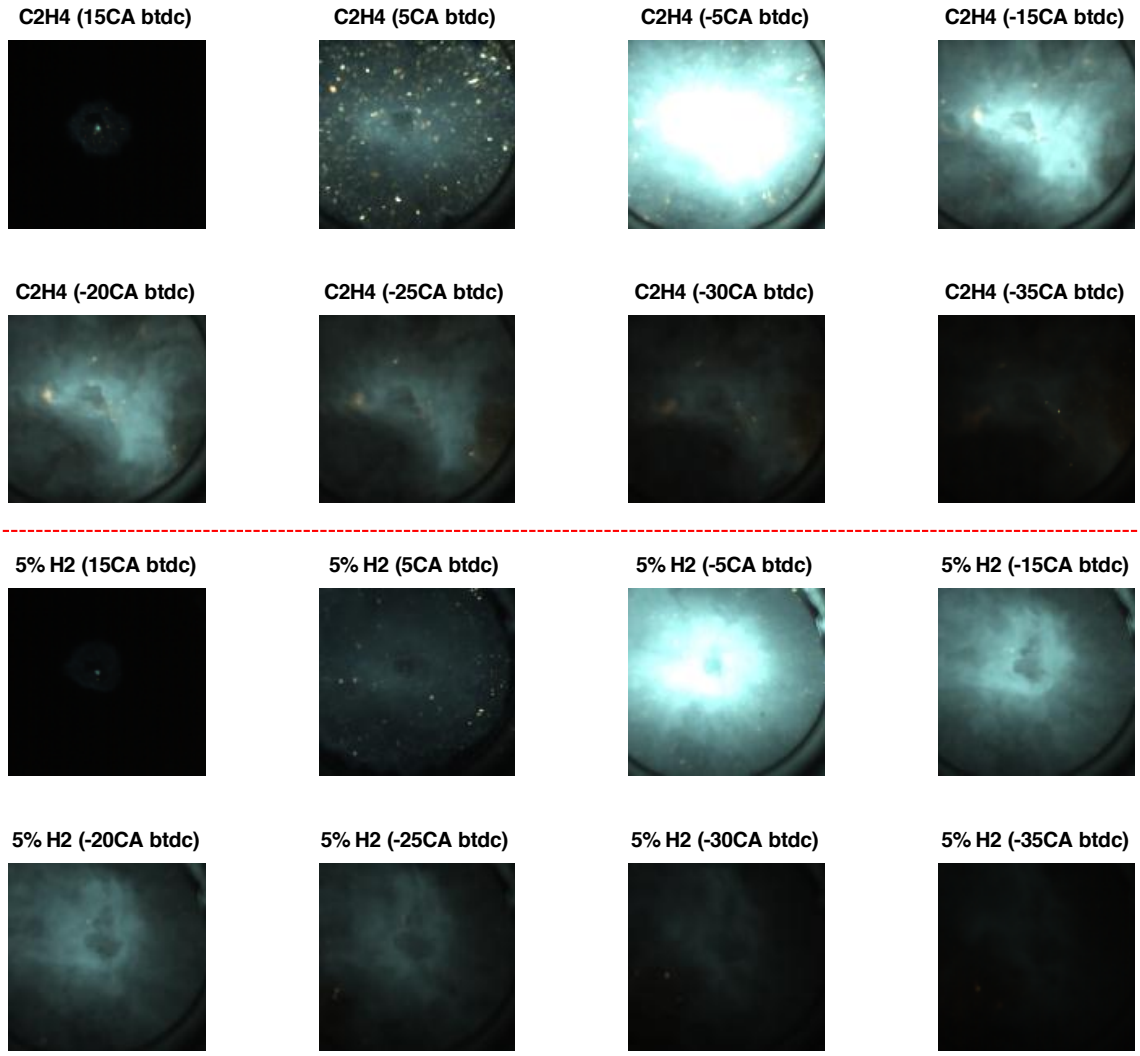

Fig. 5.4: Comparison of pure ethylene flames (top) and 5% H_2 blended ethylene flames (bottom) ($\lambda = 0.9$)

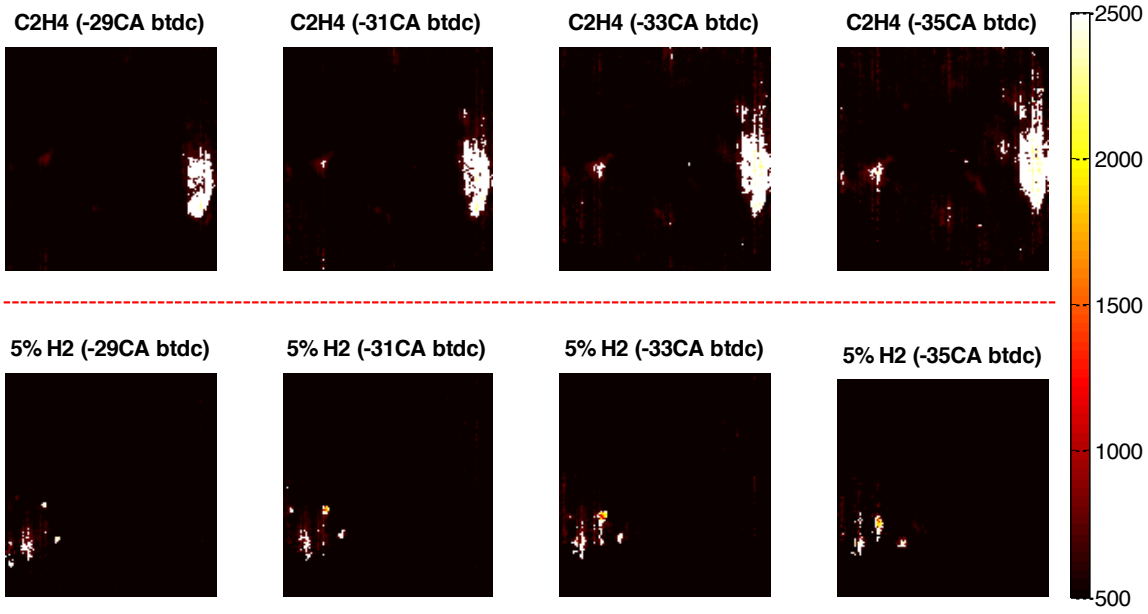

Fig. 5.5: Temperature (K) distributions at selected crank angles ($\lambda = 0.9$, top subplots are for pure ethylene and lower bottom subplots are for 5% hydrogen blended with ethylene)

The flame images from a representative cycle (the pressure trace of the representative cycle is the closest to the average pressure trace) are shown in Fig. 5.4. It clearly shows that adding hydrogen speeds up the combustion and reduces the soot formation (less yellow flame). Though the flame image at 35 CA atdc can be hardly seen, the colour pixel values in the flame region are well above 30 (out of 255) so the soot loadings calculated are still trustworthy.

The temperature and soot loading distributions in the late combustion period and selected early combustion period are shown in Fig. 5.5- 5.9. Since the TCP will break down in the region with a significant amount of chemilluminescence (the blue region in Fig. 5.4) or with saturated light intensity (the white region in Fig. 5.4), it is only valid for moderate light intensity in low level chemilluminescence regions.

Figs. 5.5 and 5.6 show that the most sooting part of the flame was also the hottest part of the flame because of the pyrolysis reaction. The histogram of the *KL* value (fig. 5.7) shows that blending hydrogen can reduce the in-cylinder soot formation effectively. Moreover, the soot particles become smaller as they are partially oxidized during the late combustion period, and blending hydrogen also tends to reduce the soot particle size, as shown in Figs. 5.8

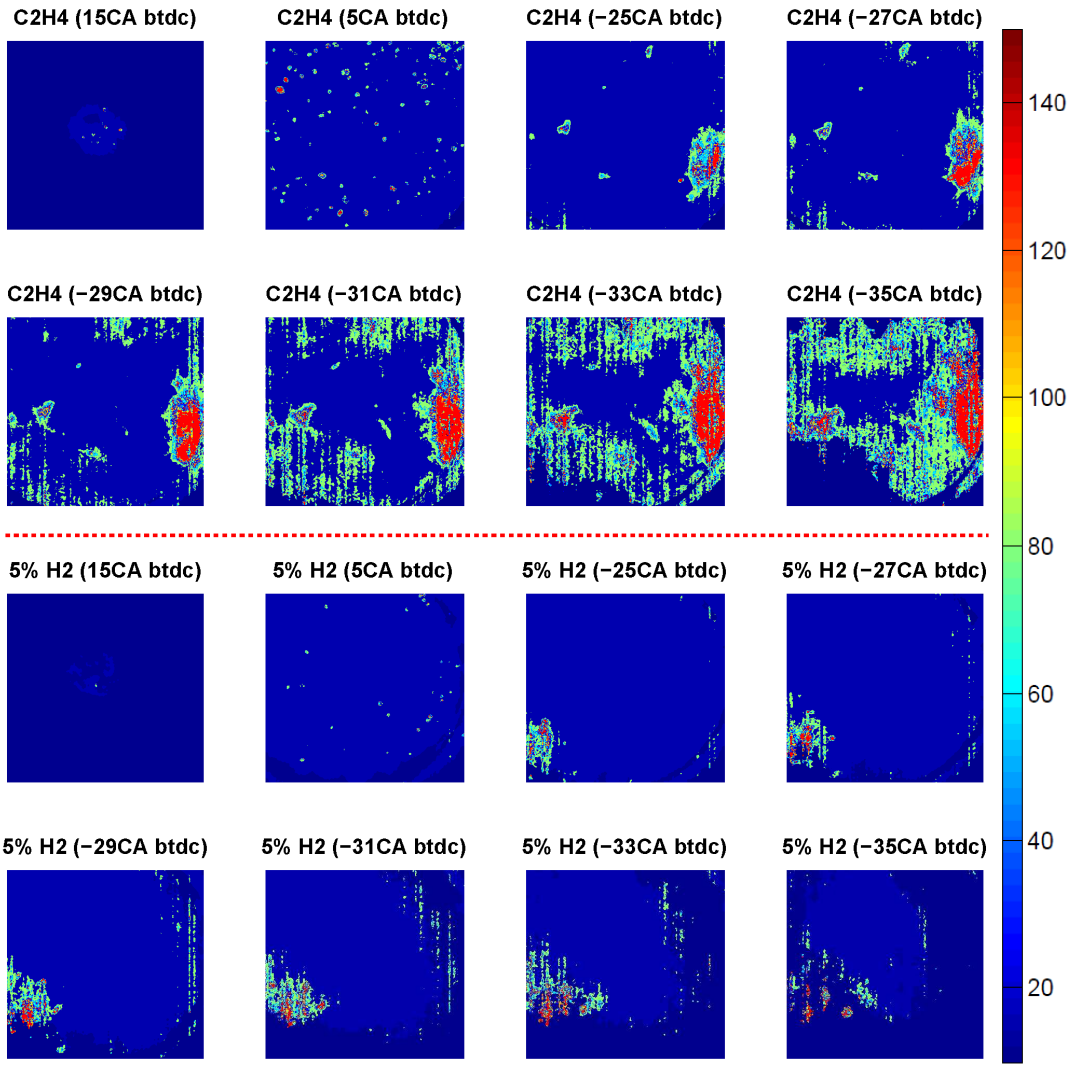

Fig. 5.6: *KL* distributions (soot concentration, in arbitrary unit) at selected crank angles (λ = 0.9, top subplots are for pure ethylene and lower bottom subplots are for 5% hydrogen blended with ethylene)

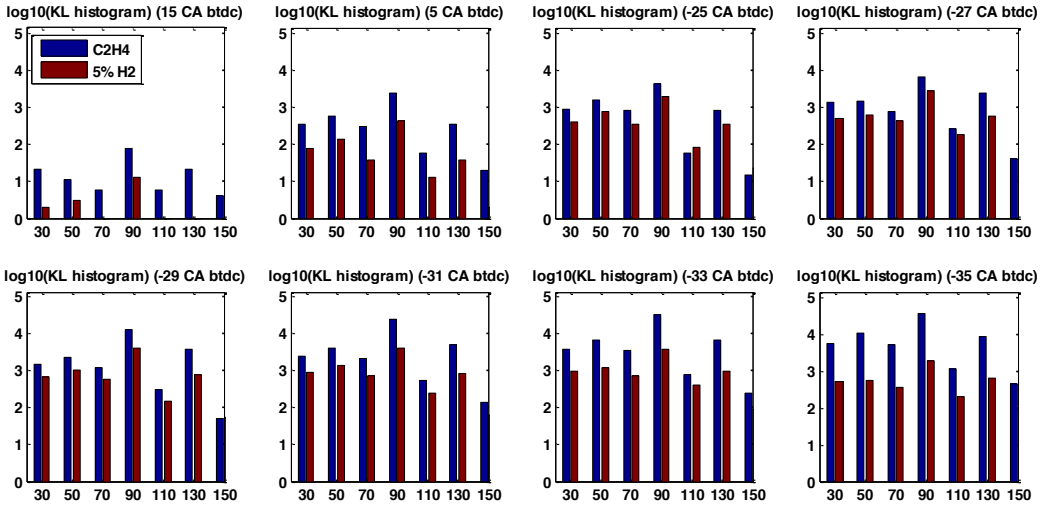

Fig. 5.7: Histogram of the *KL* distributions at selected crank angles (counts are using a log10 scale, the bin widths are 20 and centred on the scales shown in the plot)

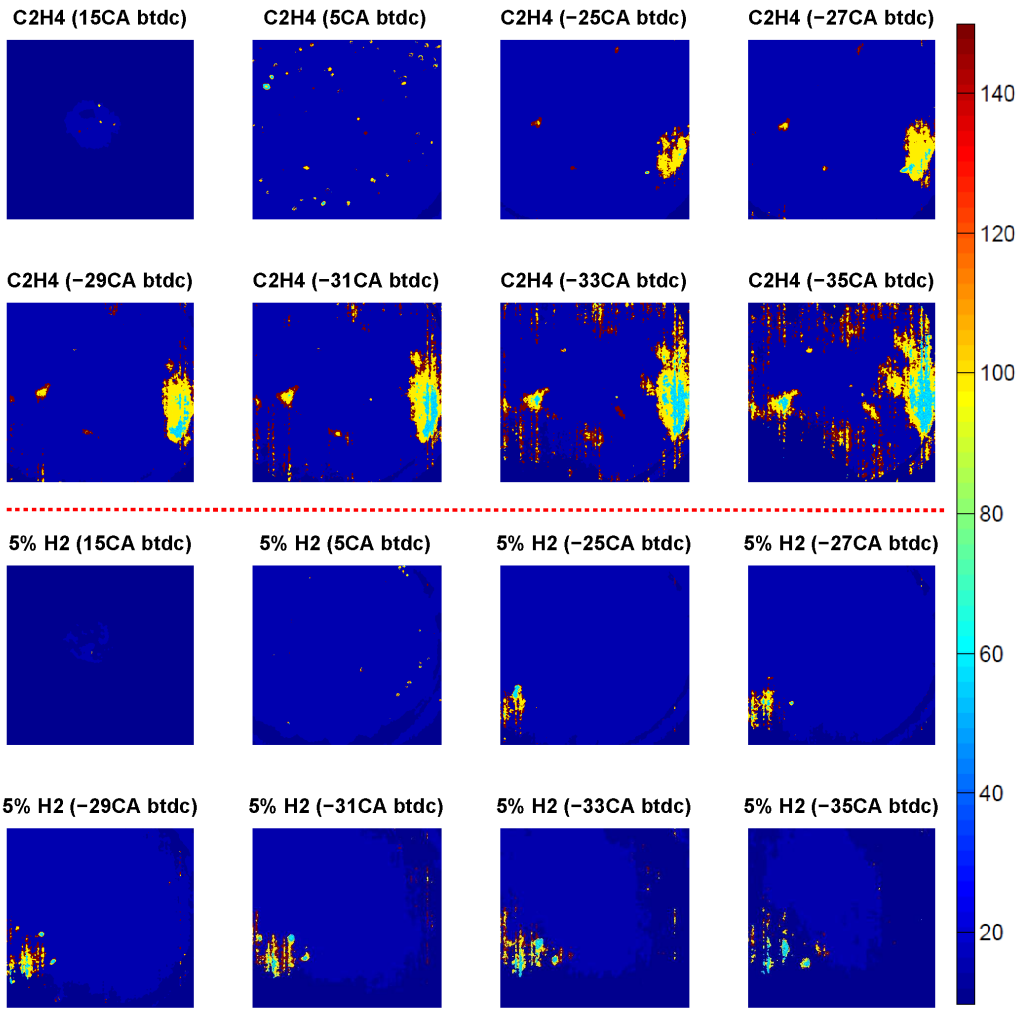

Fig. 5.8: Soot diameter (nm) distributions at selected crank angles ($\lambda = 0.9$, top subplots are for pure ethylene and lower subplots are for 5% hydrogen blended with ethylene)

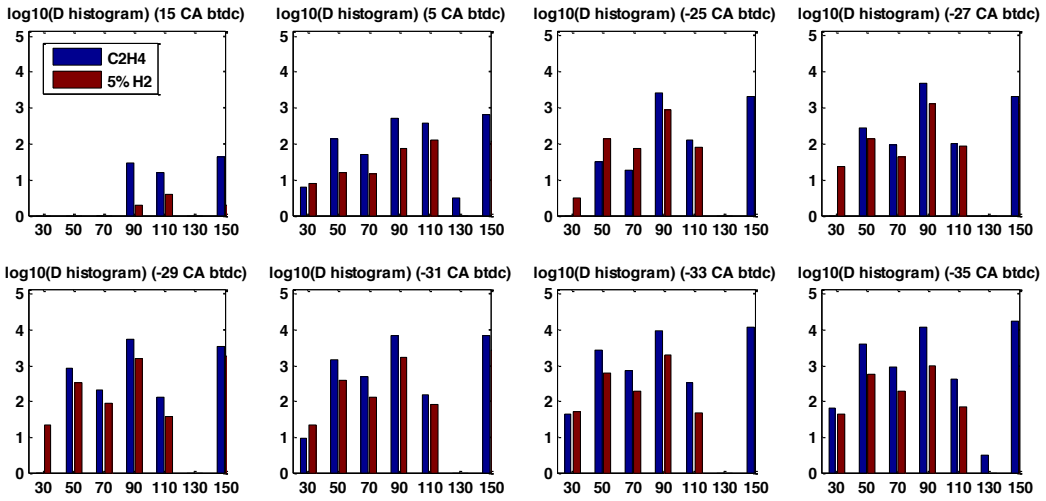

Fig. 5.9: Histogram of the soot diameter distributions at selected crank angles (counts using a log10 scale, the bin widths are 20 and centred on the scales shown in the plot)

and 5.9.

5.3.2 Hydrogen-gasoline experiments

Table 5.4: Hydrogen-gasoline engine tests conditions

	Low load condition	High load condition
Valve timing	IVO: 33.5° atdc; IVC: 241.5° atdc; EVO: 200° btdc; EVC: 50° atdc[2]	
Air flow rate (L/s)	1.5	2.5
Equivalence ratio (λ)	0.9/1.0	0.9/1.0
Injection timing	280° btdc	280° btdc
Ignition timings	5-45° btdc with 5° increment	5-40° btdc with 5° increment
Engine speed	1500 rpm	1500 rpm
Coolant/inlet air temperature (°C)	80/40	80/40

Several groups of experiments have been conducted to investigate the effect of adding hydrogen to the gasoline-based engine in its performance and emission characteristics. The base fuel which consists of 65% iso-octane and 35% toluene by volume was chosen to represent gasoline. The toluene represents the aromatic content and the upper limit of its fraction is 35% according to the regulations. Three different fractions of hydrogen (2%, 5%, and 10% of stoichiometric, or, 2.4%, 5.9%, and 11.7% by energy fraction) were added into the base fuel during the experiments. These four different mixtures are labelled as Base, H2, H5, and H10 respectively. Experiments at two different load conditions have been conducted and the tests conditions are summarized in Table 5.4.

[2]IVO: Intake valve opening; IVC: Intake valve closure; EVO: Exhaust valve opening; EVC: Exhaust valve closure; atdc: after top dead centre; btdc: before top dead centre

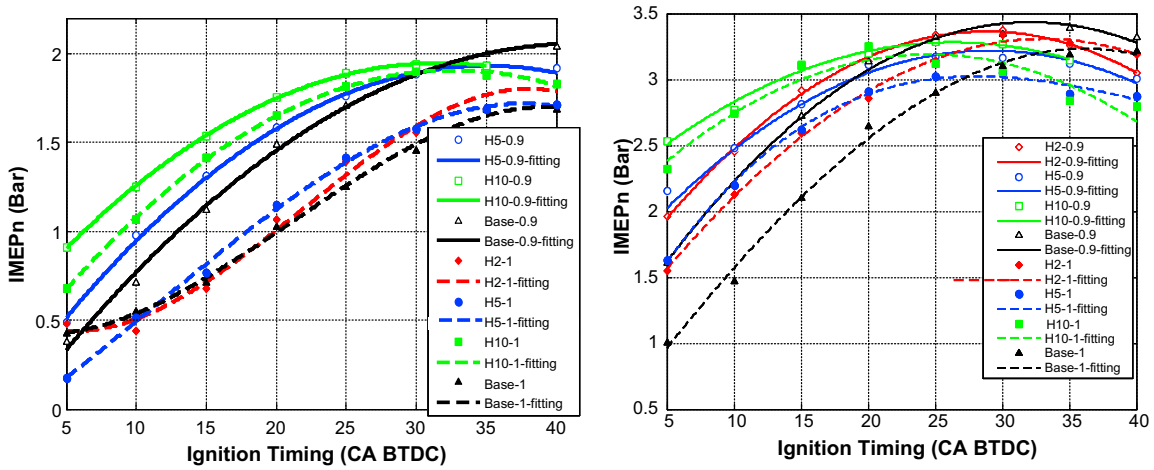

Fig. 5.10: IMEPn (net indicated mean effective pressure). (low load: left; high load: right)

5.3.2.1 Combustion-related results

To find the effect of blending hydrogen on the engine power output and the Minimum (ignition) advance for Best Torque (MBT) ignition timing, the net Indicated Mean Effective Pressures (IMEPn) are plotted versus the ignition timings as shown in Fig. 5.10.

In both load conditions, the IMEPn for the richer mixture (λ = 0.9) is higher than that for the stoichiometric mixture. This is due to the better usage of oxygen in the rich mixture combustion. The effect of blending hydrogen on the maximum IMEPn for different fuels is less obvious. When blending hydrogen, part of the incoming air will be replaced by the hydrogen, and this reduces the IMEPn. Although hydrogen has a much higher calorific value than gasoline, its stoichiometric air fuel ratio is about 34:1. Therefore, its blending decreases the calorific value of a stoichiometric mixture per mole of mixture (see Fig. 5.11). However, the faster combustion when adding hydrogen will increase the IMEPn, so that the reduction in IMEPn is less than the theoretical prediction. The IMEPn value at the high load is higher than at low load as expected, since more mixture is trapped in the cylinder.

The MBT ignition timings are found by looking at the maxima of the second order polynomial fitting curves to the experimental IMEPn data. The results are shown in Table 5.5. The general trend is that blending hydrogen less advanced the MBT ignition timing towards tdc. This is because the higher burn rate (when blending hyderogen) leads to a much higher cylinder pressure during the compression stroke, so that the work gain during the expansion

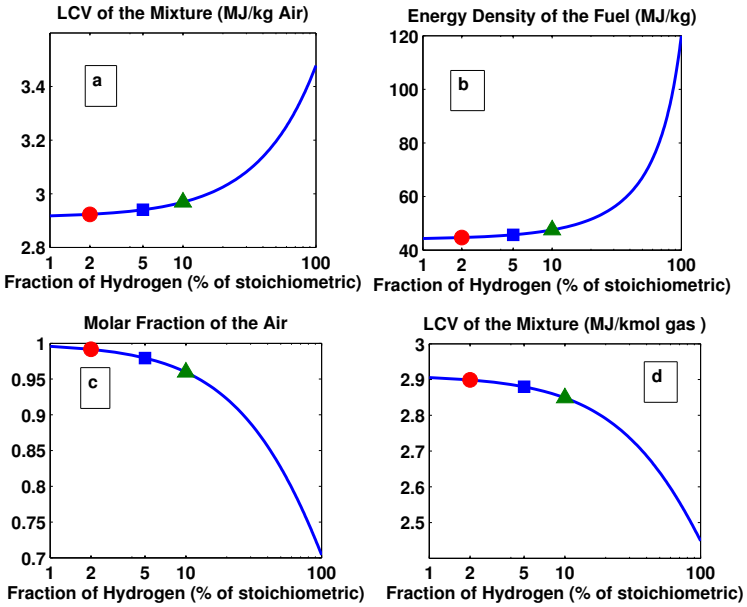

Fig. 5.11: Change of energy content when addding hydrogen (LCV: lower calorific value)

Table 5.5: MBT ignition timings when blending hydrogen (°btdc)

	λ	Base	H2	H5	H10
Low load	0.9	40	39	35	32
	1	41	41	39	33
High load	0.9	33	29	28	26
	1	36	33	28	24

stroke is not enough to compensate for the work loss during the compression stroke. When this occurs, the ignition timing should be retarded to give a lower cylinder pressure. In addition, the effects of blending hydrogen in the MBT ignition timings is less significant for richer mixtures than for a stoichiometric mixture. This is because rich mixtures are inherently faster burning, so blending hydrogen has less effect in reducing the burn duration in richer mixtures.

As for the maximum cylinder pressure, it increases as ignition timing is advanced due to more heat release occurring from combustion during the compression stroke. Except for the extremely retarded ignition timings (later than 10 °btdc), blending hydrogen will increase the maximum cylinder pressure since it speeds up combustion. For very late ignition timings, because the flame propagates so slowly, the pressure rise due to combustion is even less than the pressure drop due to expansion. As a consequence, the maximum cylinder pressure is almost the same as that in motoring and occurs close to tdc. The richer mixture

produces a higher but steady maximum cylinder pressure at the MBT points. This can be explained as the effect of blending hydrogen on increasing the burn rate is more notable at low load, especially with the stoichiometric mixture. At low loads there will be a higher level of exhaust residuals and these impede combustion so the effect of blending hydrogen is greatest.

The angles at which the maximum pressure occurs are affected in different manners by blending hydrogen in three different ignition timing regions. At the low load condition, for very late ignition timing (later than 10° btdc), blending hydrogen has little effect because of the extremely slow combustion. When the ignition timings range from 10 to 25° btdc, blending hydrogen retarded the occurrence of maximum pressure from tdc. This is because blending hydrogen increases the burn rate during the flame development period, which is mostly during the early expansion stroke, so that the pressure rise due to combustion is higher than the pressure drop due to expansion in his period. But as ignition timings is advanced before 25°btdc, hydrogen blending advanced the occurrence of maximum pressure. This is because the pressure rise during the compression stroke becomes more significant since blending hydrogen speeds up the combustion so that the peak heat release rate occurs earlier, which advances the point for peak pressure. A similar trend can be found at high load conditions, but the third range is extended by around 10° (15° btdc to 40° btdc). This is because the burn rate at high load is higher than that at low load, so that the peak heat release rate occurs earlier.

The cycle-by-cycle variation is another important parameter to evaluate whether the engine is operating smoothly. It is usually described by the coefficient of variation (COV). The plots of the COV_{IMEP_n} are shown in Fig. 5.12. As can be seen from this figure, for both load conditions, blending hydrogen improves the combustion stability significantly, especially at the low load/stoichiometric condition. It is generally accepted that the COV_{IMEP_n} should be less than 10% to ensure a good drivability. At low load, the engine has poor combustion stability due to the high percentage of residual gases trapped. Blending 5% of hydrogen at low load reduces the COV well below 10%, and blending 10% of hydrogen can further reduce the COV well below 5%. The COV for the richer mixture is lower than that for

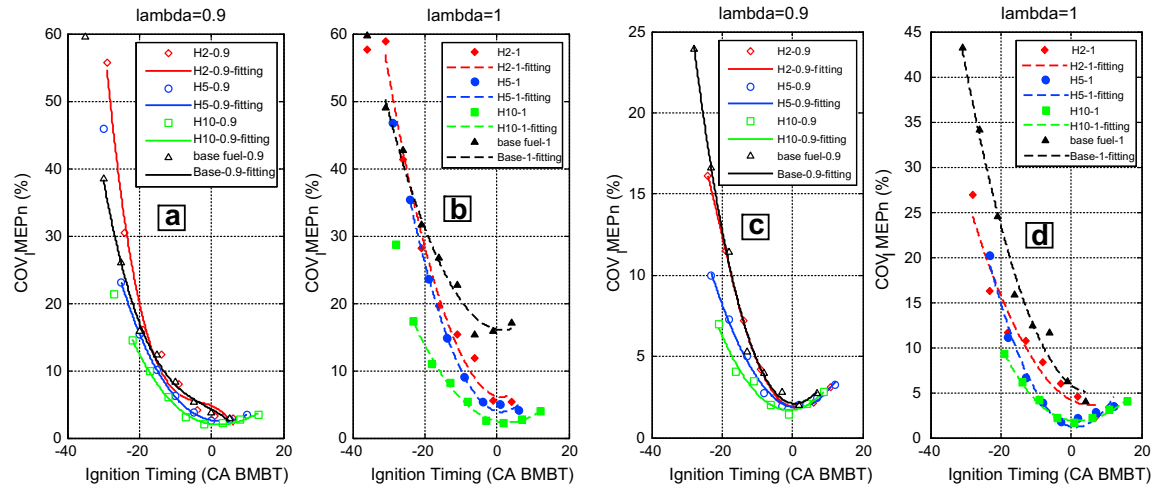

Fig. 5.12: COV (coefficient of variation) of IMEPn (using MBT as the reference ignition timing). (a) and (b) are for the low load condition and (c) and (d) are for the high load condition (as defined in table 1.4).

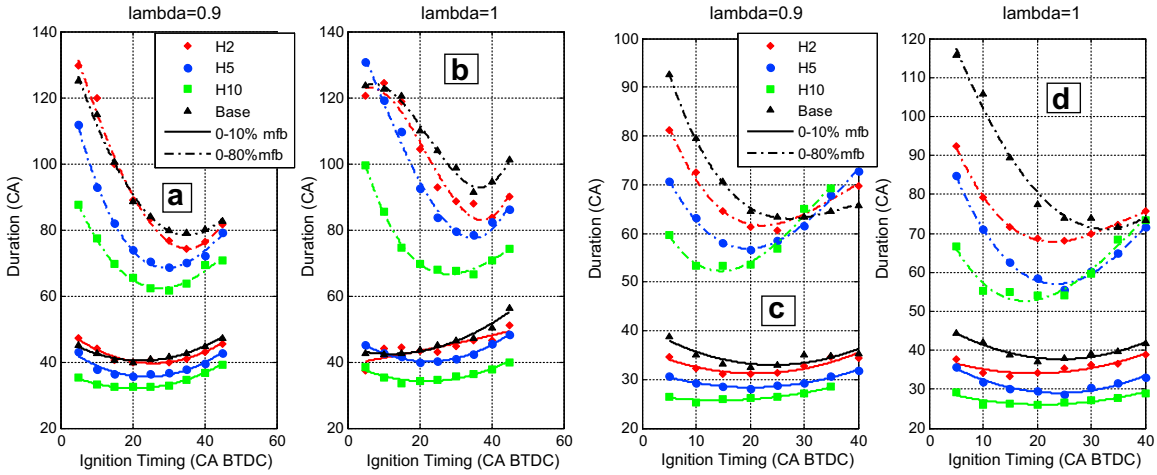

Fig. 5.13: Burn durations. (a) and (b) are for the low load condition and (c) and (d) are for the high load condition (as defined in table 1.4).

stoichiometric mixture as expected because the burn rate is higher with the richer mixture. Moreover, most of the minimum COV_{IMEP_n} occurs around the MBT ignition timings. This is because the combustion in the MBT ignition timing regions is most stable.

Blending hydrogen also speeds up the combustion, as shown in Fig. 5.13. The higher flame speed of hydrogen is believed to be the main reason. By looking at the difference between the 0-80% mfb (mass fraction burned) curve and the 0-10% mfb curve, except for extremely late ignition timings, the 0-10% mfb duration is about equal to the 10-80% mfb duration, and the burn duration for the richer mixture is shorter than that for the stoichiometric mixture. Moreover, the effect of blending hydrogen is more significant for the stoichiometric

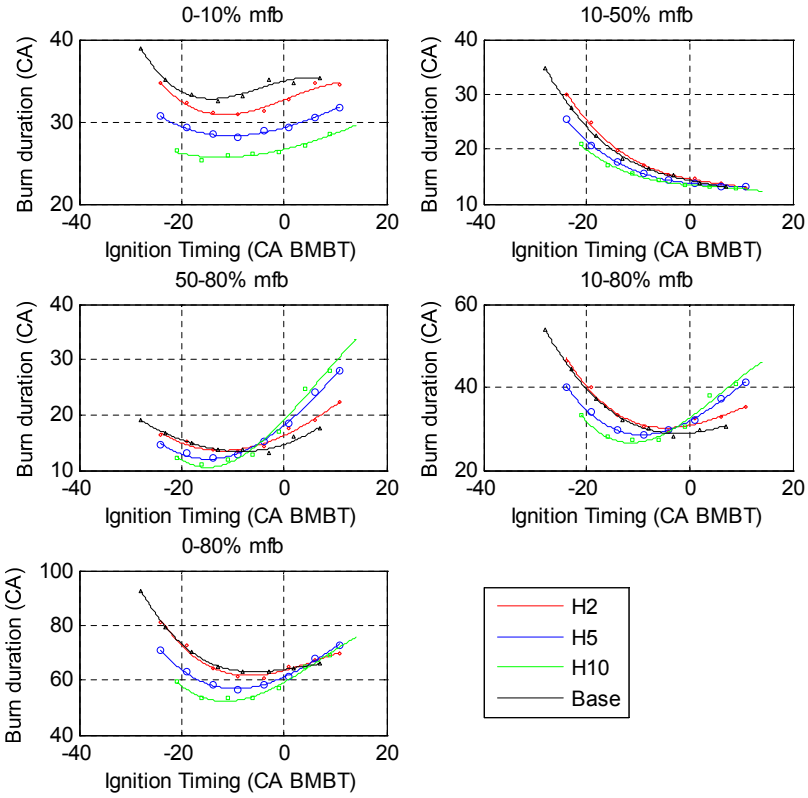

Fig. 5.14: Burn durations at different stages of combustion for the rich mixture ($\lambda = 0.9$) at high load (as defined in table 1.4)

mixtures than the richer mixtures since the burn rate is inherently higher for the richer mixtures. In both load conditions, the ignition timing for fastest combustion is retarded when blending with hydrogen. This response is very similar to the response of the MBT ignition timings. In fact, at the low load condition, the highest burn rate occurs near the MBT ignition timing.

An unexpected result was found for the richer mixture at the high load condition, as shown in Fig. 5.14. As the ignition timing is advanced before a specific timing, blending hydrogen prolongs the 50-80% mfb duration. This is probably due to the large crevice volumes of the optical engine. When blending hydrogen for richer mixtures with the high load condition, more fuel is trapped into the crevices because of the very high cylinder pressure. Since the 50-80% mfb occurs after the maximum cylinder pressure when the temperature is reducing, and the earlier ignition leads to more heat transfer to reduce the in-cylinder temperature, the out-gassing from the crevices will be into cooler gases, so that their post-flame oxidation will be slower.

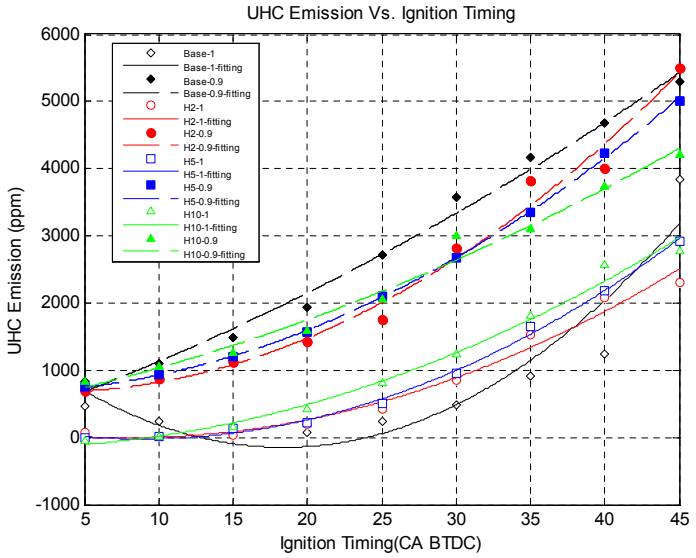

Fig. 5.15: Unburned hydrocarbon (UBHC) emissions at low load (as defined in table 1.4)

Overall, the faster burn rate when blending hydrogen enhances the combustion stability, which will increase the engine efficiency and give a better fuel economy.

5.3.2.2 Gaseous emissions results

The Unburned Hydrocarbon (UBHC) emissions for the low load condition are plotted in Fig. 5.15. The UBHC emission is affected by blending hydrogen in quite different ways for different equivalence ratios. For the stoichiometric mixtures, as the fraction of hydrogen increases, the UBHC emission increase, except for very early or very late ignition timings. The reason is that blending hydrogen speeds up the combustion significantly, which tends to decrease the post-combustion temperatures due to the high heat transfer rates in this engine, especially the exhaust temperature. As a result, the post-flame oxidation effect is reduced as more hydrogen is blended. For the richer mixture, blending hydrogen reduces the UBHC emission. This is because blending hydrogen has less effect on reducing the burn duration, so that the post-flame oxidation is less affected, but the faster flame speed and smaller quenching distance of hydrogen lead to more complete combustion, which reduces the UBHC emissions.

The NOx emission is the major concern when blending hydrogen because it tends to increase the adiabatic flame temperature, which favours the formation of NOx. The results

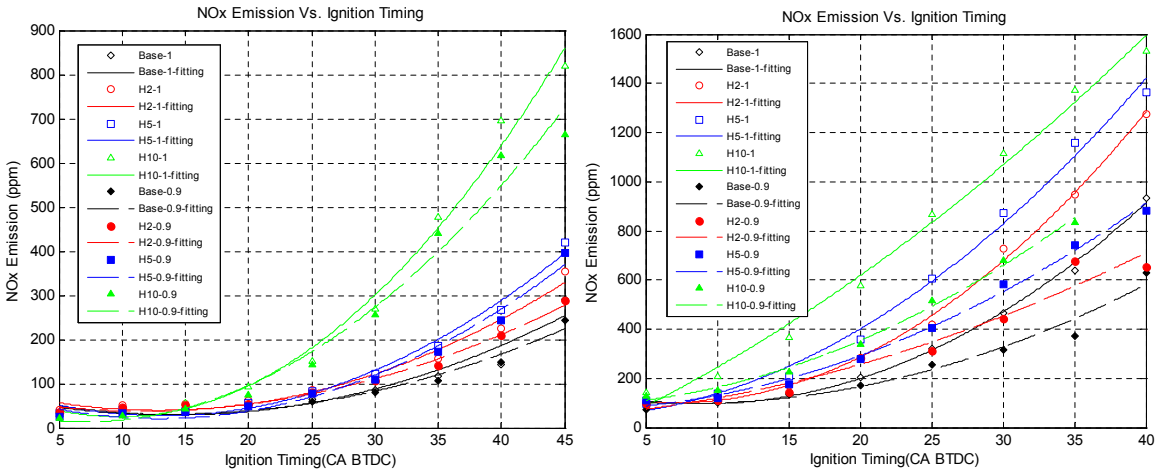

Fig. 5.16: NO_x emissions. Left is for low load and right is for high load (as defined in table 1.4)

in Fig. 5.16 validate this concern. For both load conditions, blending hydrogen increases the NOx emission for both stoichiometric and rich mixtures. However, a higher percent of EGR (Exhaust Gas Recirculation) or further retarded the ignition timings can be used when blending hydrogen because blending hydrogen increase the combustion stability. In this way, the adiabatic flame temperature will be reduced, so as to reduce the NOx emission levels.

5.3.2.3 Particulate Matter (PM) emissions

The PM emission reduction factor (PMRF) of number or mass (calculated) is used to quantify the effect of blending hydrogen, and it is defined as:

$$\text{PMRF} = \frac{\text{PM emissions for the base fuel}}{\text{PM emissions for the hydrogen}-\text{blended fuel}} \tag{5.2}$$

Since PM with diameters less than 23 nm is not taken into account by the European emission legislation, they were excluded when calculating the PMRF. The PM number concentration is measured directly and then the PM mass (m, in kg) is calculated according to the empirical correlation [80]:

$$m = 1.72 \times 10^{-24} \times d_p^{2.65} \tag{5.3}$$

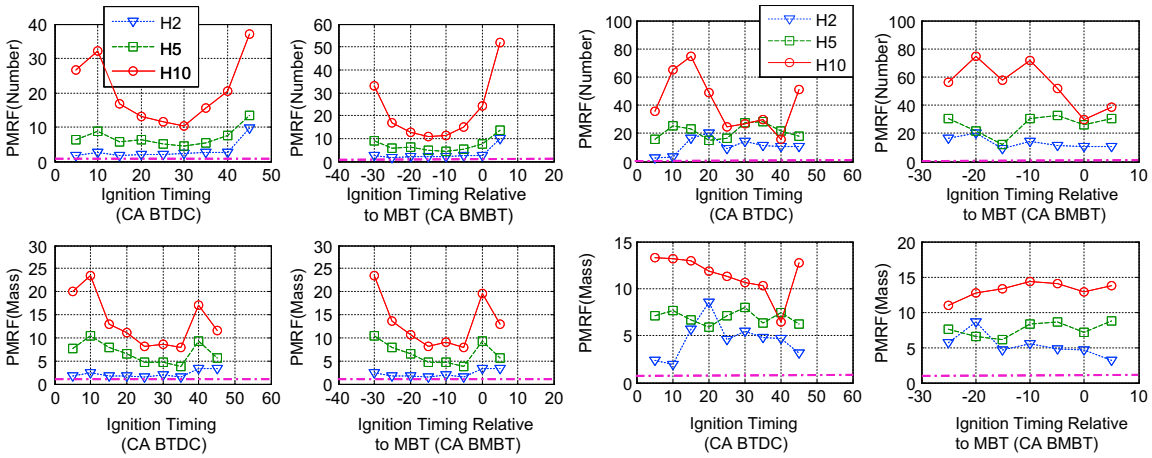

Fig. 5.17: PM emission reduction factor (PMRF) at low load. (left:$\lambda = 1$, right: $\lambda = 0.9$, and the broken line represents PMRF =1)

where d_p is the particualte diameter (nm).

Low load condition Fig. 5.17 shows the effect of blending hydrogen in the PM emissions at the low load condition. At all different operation points, the PM emissions have been reduced significantly when blending hydrogen. For the stoichiometric mixture, blending 5% of stoichiometric hydrogen can reduce the total PM number and total PM mass by up to 90% (PMRF = 10), and 10% of hydrogen can further reduce the total number up to 97% (PMRF = 30), and reduce the total mass up to 95% (PMRF = 20). When compared at the MBT ignition timings, the PMRF is even higher.

For the richer mixture, the hydrogen blending leads to a more remarkable reduction in total PM number. Blending 5% of hydrogen reduces PM by up to 97% (PMRF = 30). But the total PM mass is reduced by less than 90% (PMRF = 10). This is because although the total number concentration is dominated by nucleation mode PM (diameter less than 40 nm), the mass is dominated by the accumulation mode PM (diameter ranges from 40 to 1000 nm), especially the PM with diameter ranges from 100 to 500 nm since the number of particulates larger than 500 nm is very small (see Fig. 5.18 and Fig. 5.19). Blending hydrogen reduces the nucleation mode PM notably, but has less effect on the accumulation mode PM. This can be seen from Fig. 5.20.

Since it is always desirable to operate the engine in the MBT ignition timing region, the PM

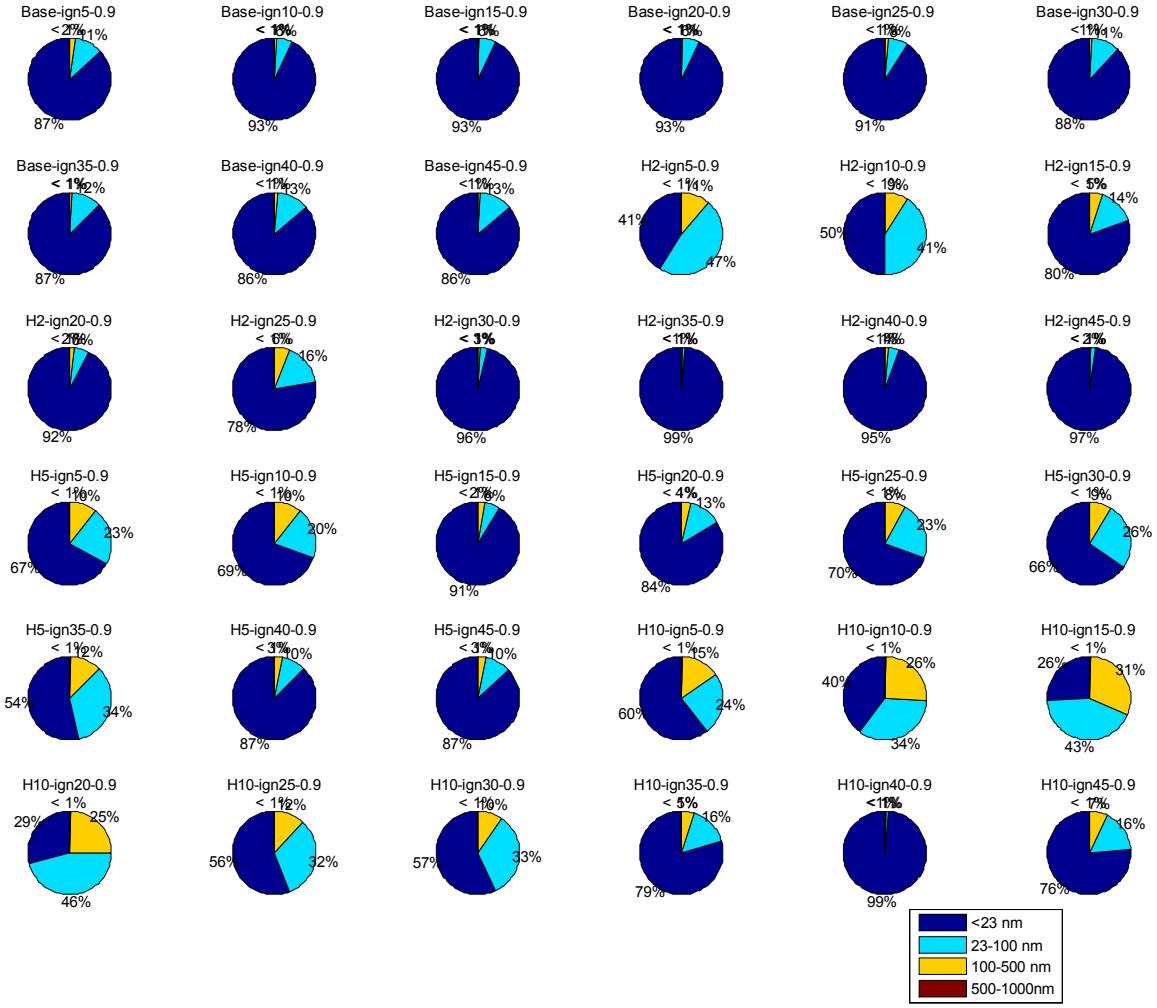

Fig. 5.18: Proportions by number in the different size ranges of the PM (low load, $\lambda = 0.9$)

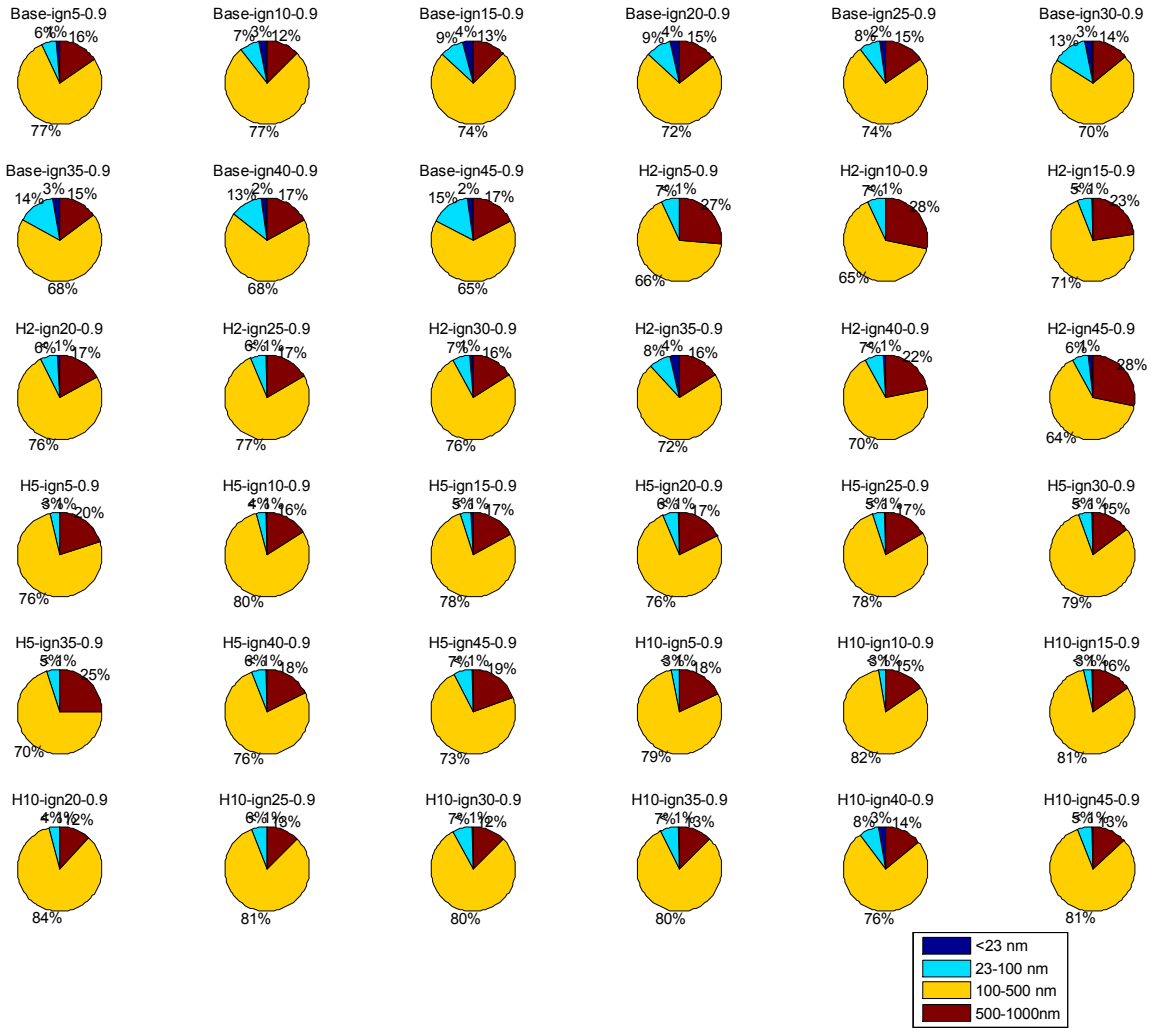

Fig. 5.19: Proportions by mass in the different size ranges of the PM (low load, $\lambda = 0.9$)

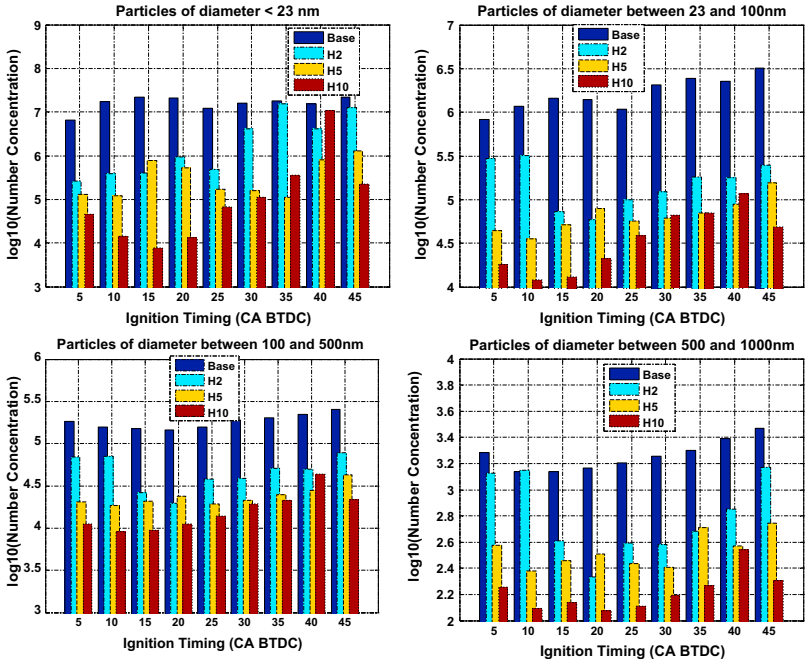

Fig. 5.20: Effect of addding hydrogen in different size ranges of PM (low load, $\lambda = 0.9$)

emissions at MBT ignition timings are plotted separately, as in Fig. 5.21, for comparison. It can be clearly seen that hydrogen blending reduces both the PM number concentration and mass concentration notably: 10% hydrogen blending reduces the total number and mass concentration by more than 95% for the stoichiometric mixture, and for the richer mixture, the number concentration is reduced by 97%, and the mass concentration is reduced by around 92%. As for particulate matter smaller than 23 nm, they are important to the number concentration, but of negligible importance to the mass concentration.

The detailed PM number and mass distributions for the MBT ignition timings are plotted in Fig. 5.22. It can be clearly seen that PM larger than 23nm are effectively reduced over the whole size range as more hydrogen is blended. But for the PM smaller than 23nm, some variation in the results is found. Since smaller particles tend to have charges, the accuracy of the data in this range may not be as good as in other ranges. Furthermore, a slight change in the sampling temperature and dilution ratio can have a large effect on the number of sub-23 nm particles, which is presumably one of reasons that they are excluded in the EU legislation.

Fig. 5.23 shows the typical PM distributions at different ignition timings. The general

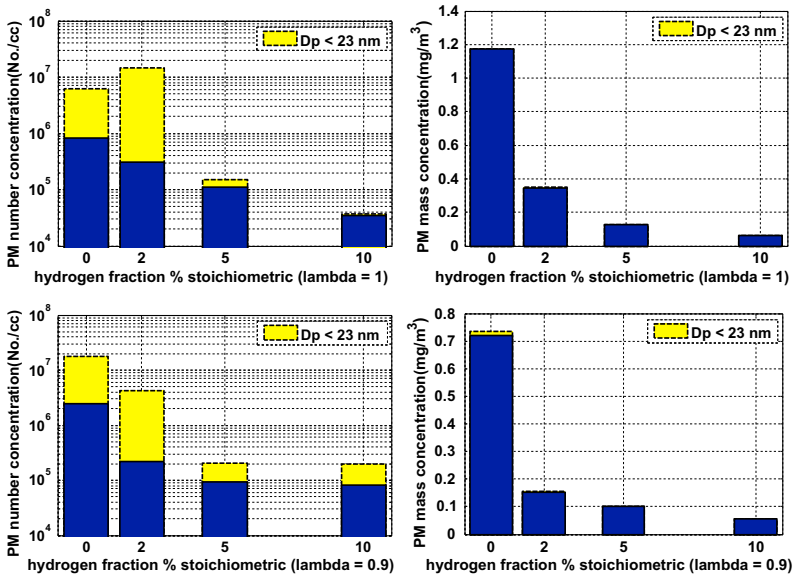

Fig. 5.21: Total PM number and mass at the MBT ignition timing at low load. (Top: $\lambda = 1$, bottom: $\lambda = 0.9$.; the area bounded by dashed line represents PM below 23nm, which is excluded in the EU legislation.

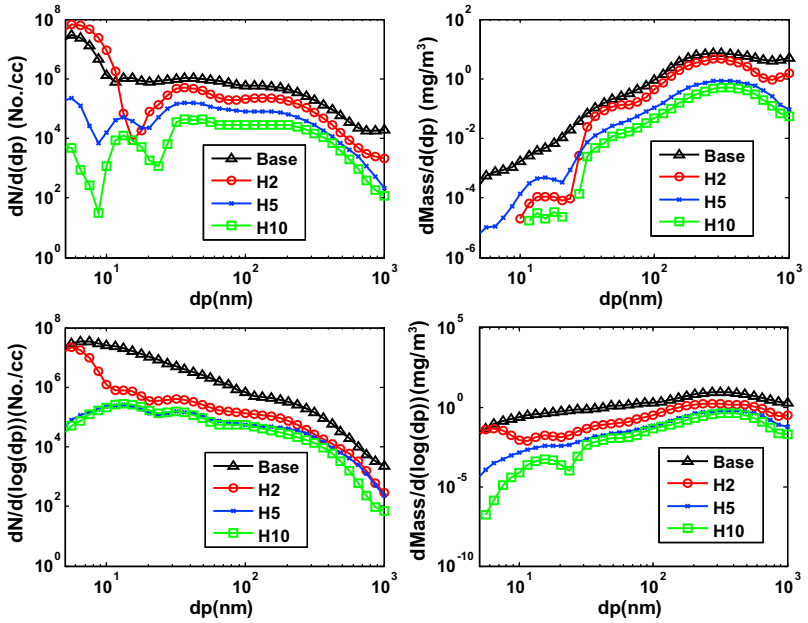

Fig. 5.22: PM number and mass distribution at the MBT ignition timing at low load. (Top: $\lambda = 1$, bottom: $\lambda = 0.9$.

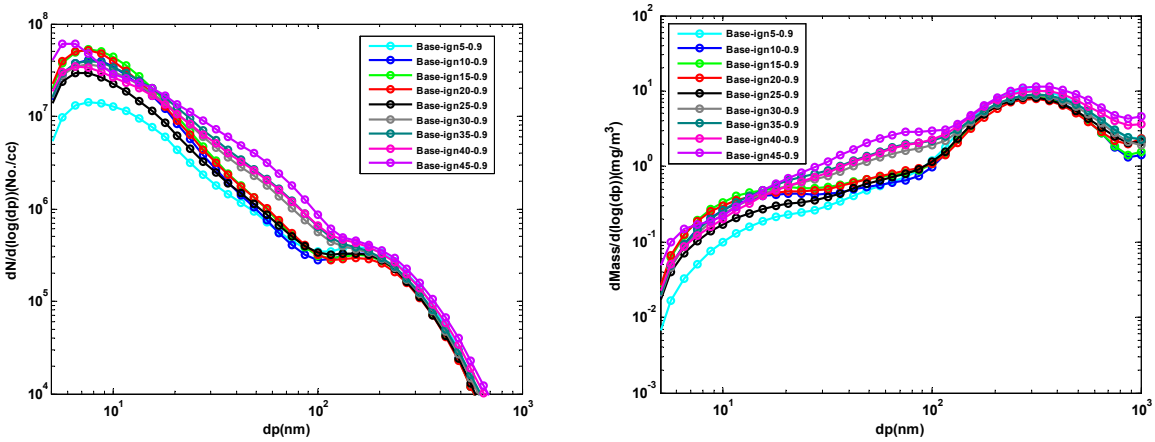

Fig. 5.23: PM number and mass distribution at different ignition timings. (base fuel, low load, $\lambda = 0.9$)

behaviour is that PM emissions are lower at very late ignition timing and higher at extremely advanced ignition timings. This is because at late ignition timings, more time is available for fuel mixing and evaporation, and a late ignition timing gives a higher expansion stroke and exhaust temperature, which promotes the oxidation of PM.

From the above data, it can be safely concluded that blending hydrogen can reduce the PM emissions remarkably at low load conditions for both the stoichiometric mixture and a richer mixture. These results are consistent with the burner test results because of the dilution and direct chemical inhibation effect when adding hydrogen. This is also because the high diffusion coefficient of hydrogen improves the mixing process. In addition, the high flame speed and smaller quenching distance of hydrogen results in a more complete combustion, which reduces the organic PM. In addition, blending hydrogen reduces the amount of available hydrocarbons, which would lead to a lower PM emission level. Another interesting phenomena is that blending hydrogen reduces the nucleation mode particles (below 100 nm) more notably than the accumulation mode particles.

High load condition For the rich mixture, blending 10% hydrogen leads to around an 85% reduction in the total PM number concentration and a 17% reduction in the total PM mass concentration, as in Fig. 5.24. At the MBT ignition timing, blending 10% hydrogen reduces the total PM number by 93%, and the total PM mass by 33%, as in Fig. 5.25. Though the effect is not as remarkable as that at the low load, considering the much higher emis-

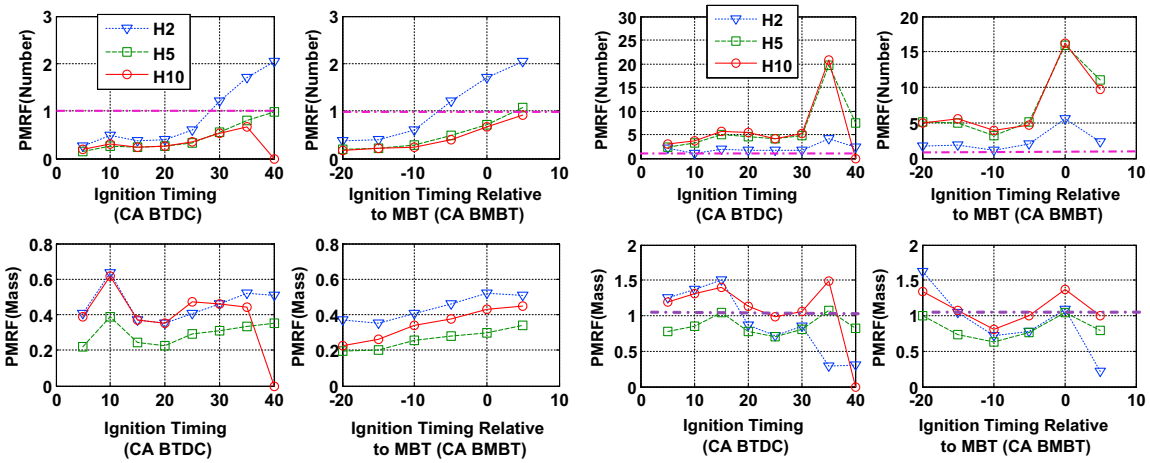

Fig. 5.24: PM emission reduction factor (PMRF) at high load. (Left:$\lambda = 1$, right: $\lambda = 0.9$, and the broken line represents PMRF =1.

sion level, the effect is none the less significant. However, for the stoichiometric mixture, blending hydrogen does not affect the total PM number concentration much, but increases the total PM mass concentration slightly. Fig. 5.26 shows the detailed number and mass distributions at the MBT ignition timing. This figure shows that blending hydrogen does reduce the number of smaller particles, but it also encourages the formation of larger particles. However, for GDI engines there is more concern over meeting the legislation for PM number rather than mass.

As can be seen in Fig. 5.26, for the stoichiometric mixture, blending hydrogen only reduces the PM smaller than 23 nm. This maybe because blending hydrogen speeds up the combustion significantly, so that the post-flame oxidation temperature decreases due to the large heat transfer coefficient in the optical engine. In addition, the higher cylinder pressure when blending hydrogen will force more charge to flow into the crevices so that more fuel can escape the main combustion stage, and the unburned fuel finally experiences gas-to-particle conversion to form particulate emissions.

From the discussion above, it can be seen that blending hydrogen reduces the PM emission level more significantly at low load than at high load. There are many potential causes to this phenomenon. One possible explanation is that different pyrolytic reactions (fragmentation, polymerisation and dehydrogenation) will proceed to form soot only when the cylinder temperature is high enough; otherwise, soot precursors alone are formed and emitted as

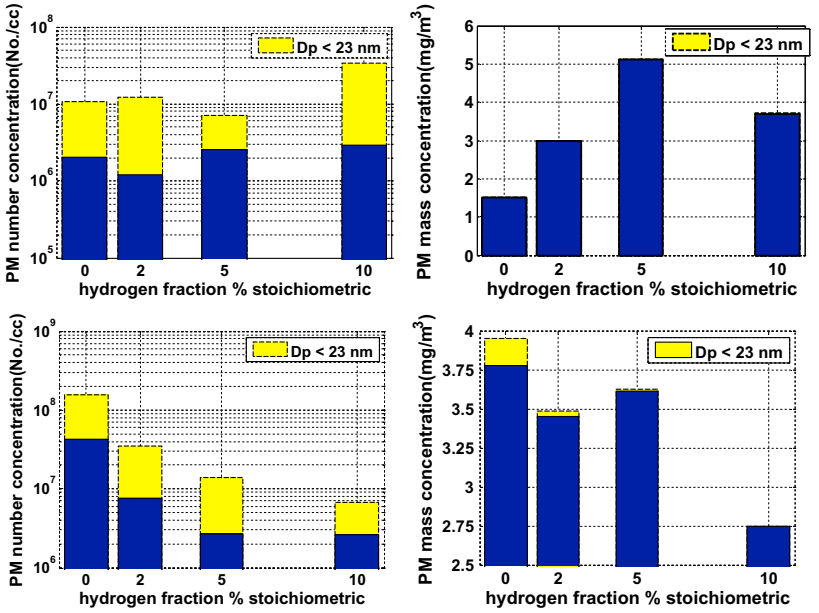

Fig. 5.25: Total PM number and mass at the MBT ignition timing at high load. (Top: λ = 1, bottom: λ = 0.9.; the area bounded by dashed line represents PM below 23 nm, which is excluded in the EU legislation)

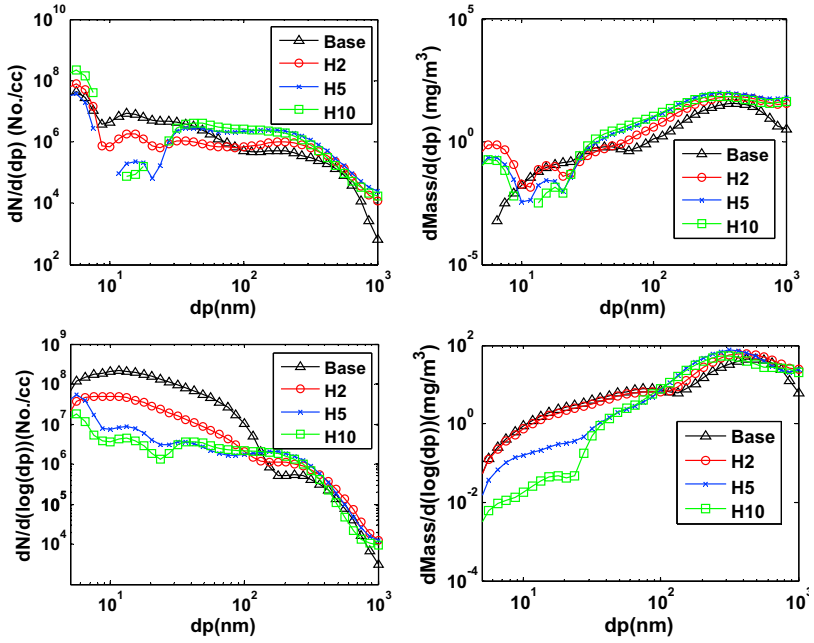

Fig. 5.26: PM number and mass distribution at the MBT ignition timing at high load. (Top: λ = 1, bottom: λ = 0.9)

organic PM (Akihama et al., 2001)[2], the flame temperature at high load is high enough for pyrolytic reactions when blending hydrogen, and this will promote the production of soot nuclei. However, the critical temperature for pyrolytic reaction is seldom reported so more research is needed to validate this explanation. The large crevice volume of the optical engine may also contribute to this effect because the high cylinder pressure in high load conditions enable more hydrocarbon fuel to escape from the main combustion phase and they can form particulates later through gas-to-particle conversion. Therefore, the effect of blending hydrogen to reduce the PM emissions is expected to be more significant for engines designed for commercial vehicles due to their smaller crevice volumes compared to the optical engine. In addition, the poor fuel evaporation due to the more significant charge cooling effect and higher possibility of a pool fire will also reduce the effect of blending hydrogen at the high load condition.

5.4 Summary

The effects of blending hydrogen into the hydrocarbon fuels on the engine performance have been investigated by several groups of optical engine tests and engine simulations and the results are presented in this chapter.

The results of burner tests presented in chapter 3 have shown that adding or blending hydrogen into the ethylene can speed up the combustion (shorter flame heights due to the faster oxidation of the hydrocarbons) and reduce the soot particle formation because of both the dilution effect and the direct chemical inhibition effect. The first group of engine tests reported in this chapter was designed to investigate whether the results of the burner test are still valid in engine environment. Therefore, the pure ethylene and 5% (by volume) hydrogen blended ethylene were used as the fuel and used to give same equivalence ratio. The engine tests show that blending hydrogen increases the burn rate and reduces both the in cylinder soot formation and tailpipe particulate matter emissions. In addition, the three colour pyrometry method used in the optical engine tests shows good temporal response to

the soot concentrations (indicated by the *KL* value) and soot diameter distributions in the regions without a significant amount of chemilluminescence.

To further investigate the effect of blending hydrogen on the performance and emissions, especially the particulate emissions, of the GDI engines, several more groups of engine experiments were conducted using a Jaguar direct injection optical engine. The base fuel used in these engine tests was made of 65% isooctane and 35% toluene (by volume, upper limit of the fraction of the aromatic compounds set by European regulations) to represent the commercial gasoline. Then three different fractions of hydrogen (2%, 5% and 10% by stoichiometric quantity) were blended into the base fuel in the engine tests. The engine was operated at five different ignition timings, two different equivalence ratios and two different load conditions (controlled by adjusting the air flow rate). The results show that blending hydrogen reduces the energy content of the mixture trapped in the cylinder, thereby reducing the IMEP. However, the faster combustion with hydrogen means the reduction in IMEP is less than the simple theoretical prediction based on the energy of the trapped charge. The MBT ignition timing is retarded towards TDC when hydrogen is blended. In addition, the combustion stability is improved greatly as more hydrogen is blended at both load conditions. Using 5% of hydrogen can reduce the COV_{IMEP_n} well below 10% in most cases; 10% of hydrogen can further reduce it below 5% at low load. However, due to the high residual gas level, the COV_{IMEP_n} for a stoichiometric mixture when using the base fuel is unacceptably high at low load. At high load, 5% of hydrogen can assure a very smooth operation since the COV_{IMEP_n} is well below 5% in most cases. Blending hydrogen also speeds up the combustion. This effect is more notable at low load and for the stoichiometric mixture as these have inherently slower combustion. However, blending hydrogen will increase the NOx emissions because of the higher flame temperature. As for the PM emissions, at high load, blending hydrogen reduces the amount of smaller particles, but encourages the formation of accumulation mode particles. For the richer mixture, 10% hydrogen blending leads to around an 85% reduction of total PM number concentration and a reduction of the total PM mass concentration by 17%. But for a stoichiometric mixture, blending hydrogen has a slightly negative effect on PM emissions in terms of total mass concentration. With the

stoichiometric mixture at low load, 5% of stoichiometric hydrogen blending can reduce the total PM number and total PM mass by up to 90% (PMRF = 10), and 10% of hydrogen can further reduce the total number by up to 97% (PMRF = 30), and reduce the total mass by up to 95% (PMRF = 20). When compared at the MBT ignition timings, the PMRF is even higher; for the richer mixture at low load, the hydrogen blending leads to a more remarkable reduction in total PM number. 5% hydrogen blending reduces PM by up to 97% (PMRF = 30). But the total PM mass is reduced by less than 90% (PMRF = 10).

Chapter 6

Conclusions and Future Work

6.1 Conclusions

In this project, the combustion and emission characteristics of various hydrogen-hydrocarbon combustion systems, especially the particulate emissions, have been investigated in detail. Experiments have been carried out in a laminar diffusion flame burner rig and an optical engine rig. In addition, to study the PM formation in laminar diffusion flames, a new optical diagnostic technique, called Cone-Beam Tomographic Three Colour Spectrometry (CBT-TCS) has been developed to measure the spatially distributed temperatures, soot diameters and soot volume fractions. The principles of CBT-TCS, results from diffusion flame tests and some engine tests will be summarized separately in the following subsections.

6.1.1 Cone-Beam Tomographic Three Colour Spectrometry (CBT-TCS)

CBT-TCS can be considered as a technique that integrates the three colour pyrometry and cone beam tomographic techniques. Three colour pyrometry uses the colour ratios of the 2D colour flame image to calculate the mean temperature and soot loadings along the optical path according to Planck's thermal radiation law and the Hottel-Broughton correlation - this is an empirical light scattering model to calculate the emissivity of the soot particle

based on soot concentrations. To measure the 3D distribution of a property field, the cone beam tomography technique can be used to reconstruct the 3D flame image based on the 2D flame images taken by the colour camera.

However, the geometric constant in the Hottel-Broughton correlation was originally decided by optical-path-averaged measurements in acetate flame experiments, and can be different at different positions of the flame. Moreover, this correlation can only be used to calculate the *KL* value, which has an implicit correlation to soot loadings. As a result, a more rigorous light scattering model needed to be used to calculate the soot diameter and the soot volume fraction. The detailed comparison between the Rayleigh-Gans theory, the Rayleigh-Gans theory with Penndorf extension and the Mie scattering theory show that the most commonly used scattering model — the Rayleigh-Gans theory, may not be valid throughout the whole soot diameter range while the Mie scattering theory is the most accurate (it is the analytical solution of the Maxwell equations for spherical particles) and can be used to calculate the soot diameter. Therefore, the Mie scattering model was chosen to calculate the field properties. The calculations and literature reviews also indicate that the emissivity of the soot particle is not sensitive to the complex refractive index and soot particle shape for typical flame temperatures in the visible light spectrum.

The algorithm chosen for the cone beam tomography is the Filtered Backprojection (FBP) algorithm because of its accuracy and calculation efficiency. Detailed sensitivity analyses on the effects of different parameters, such as the projection numbers, the zero-padding length when doing the Fourier Transform, the window function, and the distribution of gantry angles etc., have been undertaken to choose the most appropriate settings for the CBT reconstruction. The sensitivity analysis also shows that the central axis of the flame should be chosen carefully to produce an accurate reconstruction. Various noise suppression techniques, such as downsampling and median-filtering, were also used to increase the signal-to-noise ratio. In addition, detailed field-of-view calculations and careful absolute spectral calibrations have been done to decide the optimal optical setups, such as the distances between flame, lens, and camera, the colour filter, the shutter speed and the aperture size. An experiment to investigate the effect of chemiluminescence shows that the chemilu-

minescence from excited OH, CH and C_2 radicals is only significant along the bottom edge of the flame and is negligible in the main part of the flame.

The overall strategy used in CBT-TCS can be summarized in the following steps:

1. A spectrally-calibrated colour camera is used to take the raw 2D flame images (only one image is needed at an arbitrary angle for an axisymmetric flame).
2. A bilinear colour demosaicing algorithm is used to reconstruct three colour 2D flame images.
3. The 3D FBP algorithm is implemented in MATLAB to reconstruct the 3D colour flame image from a 2D colour flame image.
4. The Planck thermal radiation law and the Mie scattering model are used to construct the look-up table: red/green and red/blue ratios are the inputs; temperature and soot diameter are the outputs.
5. The colour ratios are calculated for each voxel to calculate the temperature and soot diameter by using the look-up table.
6. The temperature, soot diameter and absolute sensitivity factor of the camera sensor are used to calculate the soot volume fraction.

Compared to existing single/multiple wavelength pyrometry, CBT-TCS can measure the 3D temperature, soot diameter and soot volume fraction distributions simultaneously. However, the measurable range of this technique is limited by the signal level. In the current experimental setup, the threshold value for valid temperature measurement is around 1400 K. A camera with a higher sensitivity or a longer measurable wavelength range can be used to measure lower temperatures. In addition, the spatial resolution of the measurement is limited by the bit depth of the camera. For regions with a very low gradient in thermal radiation intensity, a camera with a higher bit depth should be used. The precision of CBT-TCS for the current setup is around 1.5-2.5% for temperature measurements and 35-45% for soot

volume fraction measurement but the precision is better at higher temperatures due to the increased signal levels.

6.1.2 Diffusion flame experiments

The CBT-TCS technique has been applied to an ethylene-air laminar diffusion flame produced by a Gulder burner to measure the 3D temperature, soot diameter and soot volume fraction profiles. A comparison of the temperature and soot volume fraction profiles in the central axis plane of the flame measured by CBT-TCS to measurements reported by Snelling et al. [77] shows consistent temperature and soot volume fraction profiles. The difference in the data are well within the uncertainty of the measurement.

The helium-ethylene-air laminar diffusion flame tests show that adding helium has little effect on the temperature distribution, but slightly increases the visible flame height because of the dilution effect on the oxidation of the soot particles, so that the soot particles can travel further downstream from the primary reaction zone before oxidation is complete. The results also show that adding helium reduces the formation of soot particles across the whole region of the flame.

The hydrogen-ethylene-air laminar diffusion flame tests with a constant ethylene flow rate show that adding hydrogen does not influence the flame height because the increase in burn rate balances the effect of the increased total fuel flow rate. The temperature is increased when adding hydrogen because of the increase in the total heat release and the higher adiabatic flame temperature of hydrogen. Adding hydrogen also reduces the PM formation more effectively than adding helium because of the combined effects of dilution and direct chemical reaction. Adding hydrogen also reduces the proportion of regions with larger soot particles. According to the Hydrogen Abstraction and Carbon Addition (HACA) model, adding hydrogen reduces the formation of primary particles so that the coagulation rate is also reduced. The reduction in the proportion of regions with large soot particles may also be due to the reduced surface growth rate because of the reduced active surface site density

according to the simulation results by Guo et al. [32] The hydrogen-ethylene-air flame tests with constant total fuel flow rates show that both the flame height and the soot volume fraction reduced significantly when adding hydrogen. Besides the reasons mentioned for the constant ethylene flow rate tests, the reduction in available carbon atoms contributes to the reduction in flame height and soot volume fraction.

To verify the soot size distributions measured by the CBT-TCS, a PM sampling system was constructed to collect samples from an ethylene-air diffusion flame. The sample size distribution was analysed using a Cambustion DMS500, and this showed that the CBT-TCS overestimates the soot diameter by a factor of two. This is probably due to the single scattering particle assumption, so that if there is multiple scattering the analysis will attribute this to an increased soot particle size.

6.1.3 GDI engine experiments

The optical engine tests using hydrogen-ethylene blends show that adding hydrogen increases the burn rate and reduces both the in-cylinder and tailpipe soot formation. Three colour pyrometry also has been used in the engine tests and the results show that this technique can give a semi-quantitative indication of the temperature and soot loadings with good temporal resolution in regions with low levels of chemiluminescence.

To further investigate the effect of adding hydrogen on PM emissions for GDI engines, three different fractions of hydrogen (2%, 5% and 10% of stoichiometric, or 2.4%, 5.9% and 11.7% by energy fraction) were added into the base fuel (35% toluene and 65% iso-octane) and the engine was operated at different equivalence ratios, load conditions (controlled by adjusting the air flow rate) and ignition timings. The results show that adding hydrogen reduces the energy density of the mixture and thereby reduces the IMEP, but the increase in the burning rate moderates the reduction in IMEP. Adding hydrogen also retards the MBT ignition timing towards TDC because it speeds up the early flame propagation during the end of the compression stroke, so that the power loss during the end of the compression stroke should be reduced with the less advanced ignition timing to give the maximum

torque output. The burn rate is increased by adding hydrogen because of the higher laminar flame speed of hydrogen and the increased intermediate radical concentrations. In addition, the increased burn rate when adding hydrogen significantly improves the combustion stability, especially at the low load condition. However, adding hydrogen does increase the NOx emissions because the increased flame temperature encourages NOx formation via the thermal mechanism. As for the PM emissions, adding 10% of hydrogen at high load reduces the total PM number concentration by 85% for the rich mixture but has little effect upon the stoichiometric mixture. This is probably because the higher burn rate at high load and large heat transfer coefficient in the optical engine reduce the amount of post-flame oxidation of PM particles. At low load, adding hydrogen can dramatically reduce the PM emissions. Adding 5% of hydrogen can reduce the total PM number concentration by 90% for a stoichiometric mixture and 97% for a richer mixture; adding 10% of hydrogen can reduce the total PM number concentration by 97% for a stoichiometric mixture.

6.2 Future work

6.2.1 Integrate the CBT-TCS to other available optical diagnostic techniques

The uncertainty in the field property measurements when using CBT-TCS can be further investigated by integrating it with other available optical diagnostic techniques. A new optical diagnostic technique, called Laser-Induced Thermal Grating Spectroscopy (LITGS), has been developed by Prof Paul Ewart and Dr Ben Williams in the Department of Physics at Oxford. This technique is based on the measurement of the modulations of a probe laser signal due to the density variations in a thermal grating created by mixing of two pump lasers. LITGS can be used to measure the spatially distributed temperature, pressure, and possibly air-fuel ratio in hydrocarbon flames. LITGS can measure the temperature very accurately because it depends on the frequency of the probe laser modulation, and this has a high signal-to-noise ratio. Therefore, LITGS can be applied to the laminar diffusion

flames to investigate the uncertainty in temperature measurement when using CBT-TCS. Meanwhile, the uncertainty in soot volume fraction measurement by using CBT-TCS can be further verified by taking the line integral and then comparing it to the results measured by the Laser Induced Incandescence (LII).

Moreover, these techniques, along with the Laser Induced Fluorescence (LIF), which can be used to measure the intermediate radical concentrations, can be applied to a diffusion flame burner to investigate the detailed soot formation process when using different hydrocarbon fuels.

6.2.2 Compare the burner test results to simulation results

A collaborative project with the Computational Chemical Engineering Group led by Prof Markus Kraft in University of Cambridge started in April 2011, and this will compare CBT-TCS test results with their simulation results.

They have successfully applied a Lagrangian Flamelet Method to model the temperature field for laminar diffusion flames. The preliminary results from the comparison between burner tests results and simulation results show a consistent temperature profile. The next step is to compare the soot volume fraction distributions measured in the burner tests to those predicted by their models when integrated with soot formation models. Then the new integrated optical diagnostic rig can provide more information about the concentrations of intermediate radicals for comparison to their models.

6.2.3 Diffusion flame experiments with liquid fuels

The laminar diffusion flame burner rig can be upgraded to study the combustion and pollutant formation mechanisms of liquid fuels by using an evaporator. Since a large proportion of industrial combustion systems use liquid hydrocarbon fuels (because of their high volumetric energy density), the upgraded system can provide invaluable information to improve the performance of existing combustion systems.

The simplest liquid fuel evaporation system is the bubbler evaporation system. In this system, a certain amount of carrier gas (usually an inert gas) is introduced into a heated liquid fuel reservoir to produce bubbles of carrier gas and the vapour of the liquid fuels. By precise control of the reservoir temperature and the pressure of the system, the amount of evaporated liquid fuel can be controlled. However, with multi-component fuels the light component of the liquid fuel tends to evaporate first in this system while the heavy components may still be in liquid phase so that the chemical composition of the fuel vapour may not be the same as that of the liquid fuel. The liquid fuel can also be evaporated by using other evaporators, such as the hot plate evaporator, a controlled evaporator mixer, or a capillary force vaporizer etc. In these systems, different methods are used first to increase the surface area of the liquid fuel, such as producing a liquid spray in the hot plate evaporator, premixing the carrier gases and the liquid fuels to produce smaller fuel droplets in the controlled evaporator mixer, or absorbing the liquid fuels into ultrafine pores in the capillary force vaporizer. Then, the liquid fuel will be heated to evaporate. Careful controls of the temperature and flow rates are required to evaporate accurate amount of liquid fuels without deposition or decomposition of any heavy components in the liquid fuels.

6.2.4 Applying the CBT-TCS to non-axisymmetric flames

The CBT-TCS system can also be expanded to measure the 3D distributions of temperature, the soot diameter and soot volume fraction for non-axisymmetric flames by using multiple cameras. The same algorithm can be used to reconstruct the 3D image of the flame by using the 2D images of the flame taken from different angles. To ensure an accurate reconstruction of the flame, at least four cameras are needed and the flame images should cover all 360 degrees angle of view.

6.2.5 Hydrogen enhanced GDI engine research

Hydrogen can be generated on-board by reforming hydrocarbon fuels. Since different reforming techniques will produce different reforming gases, the current research can be extended to investigate the effect of adding different reforming gases on the particulate emissions in GDI engines. In addition, research can be extended to investigate the particulate emissions from hydrogen-enhanced GDI engines running bio-fuels.

Appendix

Appendix A Energy calculation in hydrogen-gasoline engine experiment

Chemical equations in stoichiometric combustion:

$$\mathrm{H_2} + \frac{1}{2}(O_2 + \frac{79}{21}N_2) \longrightarrow \mathrm{H_2O} + 1{\cdot}88\,\mathrm{N_2}$$

$$\mathrm{C_8H_{18}} + 12\,\frac{1}{2}(O_2 + \frac{79}{21}N_2) \longrightarrow 9\,\mathrm{H_2O} + 8\,\mathrm{CO_2} + 47{\cdot}02\,\mathrm{N_2}$$

According to above two equations, the gravimetric mass ratio of hydrogen to air for complete combustion of hydrogen is 1:34.52 (1:2.38 molar basis), and for iso-octane is 1:15.14 (1:59.5 molar basis).

Consider 1 kg of air and x% of stoichiometric of hydrogen, $(x/100)$ kg air is used to oxidize $x/(100 \cdot 34.52)$ kg hydrogen, and the remaining (100-x)/100 kg air is used to oxidize (100-x)/(100·15.14) kg isooctane. Taking into account the calorific values of hydrogen ($Q_{\mathrm{H_2}}$) and that of iso-octane ($Q_{\mathrm{C_8H_{18}}}$), the energy fraciton of hydrogen (y) can be calculated as:

$$y = \frac{x \cdot Q_{\mathrm{H_2}}}{x \cdot Q_{\mathrm{H_2}} + 2.28 \cdot (100 - x) \cdot Q_{\mathrm{C_8H_{18}}}} * 100\%$$

Air flow rate normalized to standard conditions is:

$$V^*_{\text{air}} = \frac{P}{1\text{bar}} \cdot \frac{298.15\text{K}}{T} \cdot (60 \cdot 0.7681 \cdot V_o)$$

where V_o is the output voltage signal from the air flow meter. Then, $x\%$ of stoichiometric hydrogen volume flow rate normalized to standard condition is:

$$V^*_{\text{H}_2} = \frac{57.73P}{T} \cdot V_o$$

Taking P as 1 bar, and T as 300 K, and the proportional constant from calibration data, the input voltage signal for the hydrogen mass flow controller (V_{H_2}) and the output voltage signal from air flow meter (V_{air}) can be correlated as:

$$V_{H_2}/V_{air} = 0.0444 \cdot x/C1$$

where $C1$is the gain value of the interface control box.

Appexdix B Uncertainty analysis in diffusion flame experiments

The uncertainty during the measurement is quantified by the coefficient of variation (COV, CV_x) of the pixel intensity. COV is defined as the standard deviation (SD,S_x) divided by the mean value ($\bar{x}$). Since the uncertainty of the light intensity measured by the camera is due to the unstability of the flame and the noise of the camera detector (similar for different colour channels), the COV for different colour channels (CV_R, CV_G, CV_B) are different because red and green channels pick up more light than Blue channel.

The colour ratios (RG: red to green, RB: red to blue) are used to measure the temperature and soot diameter. The COV of the colour ratios (CV_{RG}, CV_{RB}) are calculated as:

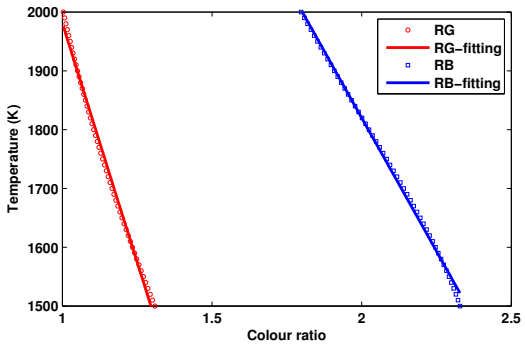

Fig. 6.1: Typical response of the temperature to the colour ratios

$$CV_{RG} = S_{RG}/\bar{RG} = \sqrt{((\frac{\partial(R/G)}{\partial R})_{\bar{R},\bar{G}} \cdot S_R)^2 + ((\frac{\partial(R/G)}{\partial G})_{\bar{R},\bar{G}} \cdot S_G)^2}/(\bar{R}/\bar{G}) = \sqrt{CV_R^2 + CV_G^2}$$

The response of the temperature to the colour ratios for the look-up table is very close to linear, as shown in fig. 6.1. The temperature can be calculated as:

$$T = (T_1 + T_2)/2 = ((k_1 RG + d_1) + (k_2 RB + d_2))/2$$

The SD of temperature is calculate by:

$$S_T = \sqrt{S_{T_1}^2 + S_{T_2}^2}/2 = \sqrt{(k_1 S_{RG})^2 + (k_2 S_{RB})^2}/2$$

According to the Planck thermal radiation law, the radiation (I_λ) is caculated by the formula:

$$I_\lambda = A \cdot f_v \cdot \varepsilon(D) \cdot \frac{1}{\exp(B/\lambda T) - 1};$$

where A and B are two constants, $f_v$is the soot volume fraction, $\varepsilon$is the emissivity of a single soot particle, d is the soot diameter and $\lambda$is the wavelength. The sensitivity analysis show that the emissivity is not sensitive to the diameter and under typical flame temperature and the exponential term is much larger than 1. The COV of theoretical thermal radiation at specific wavelength for unit soot volume fraction is:

$$CV_{I_\lambda} = (\frac{dI_\lambda}{dT})_{\bar{T}} \cdot S_T / \bar{I_\lambda} = \frac{B \cdot S_T}{\lambda \cdot \bar{T}^2}$$

The soot volume fraction is calculated by taking the ratio between the measured light intensity ($I_\lambda^{'}$) to the theoretical thermal radiations for unit soot volume fraction. Taking into account the spectral response of the camera (RS_λ), the transmission efficiencies of the lens

and filter (T_i), and the sensitivity factor of the camera detector (SF). The soot volume fraction is:

$$f_{v,\lambda} = I'_\lambda / I_\lambda = I'_\lambda / [(SF \cdot A' \cdot \exp(-B/\lambda T) \cdot RS_\lambda \cdot \prod T_i]$$

where $A'$is a constant. Assume the COV of the soot volume fraction (CV_{f_v}) across the visible spectrum is close to the value at 500 nm wavelenth. Then CV_{f_v}measured by using the red pixel value is:

$$CV^2_{f_v^R} = CV^2_R + CV^2_{RS} + CV^2_{SF} + CV^2_I + \sum CV^2_{T_i}$$

The soot volume fraction value is taken as the average value of the three independant colour channels. Then,

$$CV_{f_v} = \tfrac{1}{3}\sqrt{CV^2_R + CV^2_G + CV^2_B + 3 \cdot (CV^2_{SF} + CV^2_{RS} + \sum CV^2_{T_i} + (B \cdot S_T/5 \times 10^{-7} \cdot (\bar{T})^2)^2};$$

References

[1] Nitrogen oxides: Impacts on public health and the environment. Technical report, United States Environmental Protection Agency, 1997.

[2] Kazuhiro Akihama, Yoshiki Takatori, Kazuhisa Inagaki, Shizuo Sasaki, and Anthony M. Dean. Mechanism of the smokeless rich diesel combustion by reducing temperature. Technical report, SAE, 2001.

[3] T. Allgeier, M. Klenk, T. Landenfeld, E. Conte, K. Boulouchos, and J. Czerwinski. Advanced emission and fuel economy concept using combined of gasoline and hydrogen in si engine. Technical report, SAE, 2004.

[4] IsIl AyrancI, Rodolphe Vaillon, Nevin Selçuk, Frédéric André, and Dany Escudié. Determination of soot temperature, volume fraction and refractive index from flame emission spectrometry. *Journal of Quantitative Spectroscopy and Radiative Transfer*, 104(2):266 – 276, 2007.

[5] Ludovic Biennier, Farid Salama, Manish Gupta, and Anthony O'Keefe. Multiplex integrated cavity output spectroscopy of cold pah cations. *Chemical Physics Letters*, 387:287–294, April 2004.

[6] H. Bockhorn. *Soot formation in combustion: mechanisms and models*. Springer series in chemical physics. Springer-Verlag, 1994.

[7] Craig F. Bohren and D.R. Huffman. *Absorption and scattering of light by small particles*. Wiley science paperback series. Wiley, 1983.

[8] Probir Kumar Bose and Dines Maji. An experimental investigation on engine performance and emissions of a single cylinder diesel engine using hydrogen as inducted fuel and diesel as injected fuel with exhaust gas recirculation. *International Journal of Hydrogen Energy*, 34(11):4847 – 4854, 2009.

[9] Z. I. Botev, J. F. Grotowski, and D. P. Kroese. Kernel density estimation via diffusion. *Ann. Statist.*, 38:2916–2957, 2010.

[10] T.T. Charalampopoulos, H. Chang, and B. Stagg. The effects of temperature and composition on the complex refractive index of flame soot. *Fuel*, 68(9):1173 – 1179, 1989.

[11] W. K. Cheng, D. Hamrin, J. B. Heywood, S. Hochgreb, K. Min, and M. G. Norris. An overview of hydrocarbon emissions mechanisms in spark ignition engines. Technical report, SAE, 1993.

[12] Ahsan R. Choudhuri and S. R. Gollahalli. Combustion characteristics of hydrogen-hydrocarbon hybrid fuels. *Int. J. Hydrogen Energy*, 25(5):451 – 462, 2000.

[13] Ahsan R. Choudhuri and S. R. Gollahalli. Characteristics of hydrogen-hydrocarbon composite fuel turbulent jet flames. *Int. J. Hydrogen Energy*, 28(4):445 – 454, 2003.

[14] A.R.Ahsan R. Choudhuri and S. R. Gollahalli. Intermediate radical concentrations in hydrogen-natural gas blended fuel jet flames. *Int. J. Hydrogen Energy*, 29(12):1293 – 1302, 2004.

[15] A.R. Chughtai, M.M.O. Atteya, J. Kim, B.K. Konowalchuk, and D.M. Smith. Adsorption and adsorbate interaction at soot particle surfaces. *Carbon*, 36(11):1573 – 1589, 1998.

[16] A. Coderre, K. Thomson, D. Snelling, and M. Johnson. Spectrally resolved light absorption properties of cooled soot from a methane flame. *Appl. Phys. B: Lasers Opt.*, 104:175–188, 2011. 10.1007/s00340-011-4448-9.

[17] Enrico Conte and Konstantinos Boulouchos. Hydrogen-enhanced gasoline stratified combustion in si-di engines. *Journal of Engineering for Gas Turbines and Power*, 130(2):022801, 2008.

[18] W. H. Dalzell and A. F. Sarofim. Optical constants of soot and their application to heat flux calculations. *J Heat Transfer*, 91:100–104, 1969.

[19] T. D'Andrea, P. F. Henshaw, and D. S. K. Ting. The addition of hydrogen to a gasoline-fuelled si engine. *Int. J. Hydrogen Energy*, 29(14):1541 – 1552, 2004.

[20] Cameron J. Dasch. One-dimensional tomography: a comparison of abel, onion-peeling, and filtered backprojection methods. *Appl. Opt.*, 31(8):1146–1152, Mar 1992.

[21] T. P. Davies. Schlieren photography–short bibliography and review. *Opt. & Laser Tech.*, 13(1):37 – 42, 1981.

[22] K. Donaldson and W. MacNee. The mechanism of lung injury caused by pm 10. *Issue in Environmental Science and Technology*, 10:21–32, 1998.

[23] Hai Du, Ru-Chun Amy Fuh, Junzhong Li, L. Andrew Corkan, and Jonathan S. Lindsey. Photochemcad: A computer-aided design and research tool in photochemistry. *Photochemistry and Photobiology*, 68(2):141–142, 1998.

[24] Hong Du. Mie-scattering calculation. *Appl. Opt.*, 43(9):1951–1956, Mar 2004.

[25] P. Eastwood. *Particulate emissions from vehicles*. Wiley-professional engineering publishing series. John Wiley & Sons, 2008.

[26] A.C. Eckbreth. *Laser diagnostics for combustion temperature and species*. Combustion science and technology book series. Gordon and Breach Publishers, 1996.

[27] L. A. Feldkamp, L. C. Davis, and J. W. Kress. Practical cone-beam algorithm. *J. Opt. Soc. Am. A*, 1(6):612–619, Jun 1984.

[28] C.P. Fenimore. Formation of nitric oxide in premixed hydrocarbon flames. *Symposium (International) on Combustion*, 13(1):373 – 380, 1971. Thirteenth symposium (International) on Combustion, Thirteenth symposium (International) on Combustion.

[29] Michael Frenklach, David W. Clary, William C. Gardiner Jr., and Stephen E. Stein. Detailed kinetic modeling of soot formation in shock-tube pyrolysis of acetylene. *Symposium (International) on Combustion*, 20(1):887 – 901, 1985.

[30] I. Glassman and R.A. Yetter. *Combustion*. Academic Press. Academic Press, 2008.

[31] Amer L. Gulder and David R. Snelling. Influence of nitrogen dilution and flame temperature on soot formation in diffusion flames. *Combust. Flame*, 92(12):115 – 124, 1993.

[32] Hongsheng Guo, Fengshan Liu, Gregory J. Smallwood, and Ömer L. Gülder. Numerical study on the influence of hydrogen addition on soot formation in a laminar ethylene-air diffusion flame. *Combust. Flame*, 145(1-2):324 – 338, 2006.

[33] Robert J. Hall and Paul A. Bonczyk. Sooting flame thermometry using emission/absorption tomography. *Appl. Opt.*, 29(31):4590–4598, Nov 1990.

[34] James Hansen and Larissa Nazarenko. Soot climate forcing via snow and ice albedos. *Proc. Natl. Acad. Sci. U. S. A.*, 101(2):423–428, 2004.

[35] Y. Hardalupas and M. Orain. Local measurements of the time-dependent heat release rate and equivalence ratio using chemiluminescent emission from a flame. *Combust. Flame*, 139(3):188 – 207, 2004.

[36] J.B. Heywood. *Internal combustion engine fundamentals*. McGraw-Hill series in mechanical engineering. McGraw-Hill, 1988.

[37] J. C. Hilliard and R. W. Wheeler. Nitrogen dioxide in engine exhaust. Technical report, SAE, 1979.

[38] H. C. Hottel and F. P. Broughton. Determination of true temperature and total radiation from luminous gas flames. *Ind. Eng. Chem. Res.*, 4(2):166–175, 1932.

[39] C. R. Howarth, P. J. Foster, and M. W. Thring. The effect of temperature on the extinction of radiation by soot particles. In *Proceedings of the Third International Heat Transfer Conference*, 1966.

[40] A. Hultqvist, M. Christensen, B. johansson, A. Franke, M. Richter, and M. Alden. A study on the homogeneous charge compression ignition combustion process by chemiluminescence imaging. Technical report, SAE, 1999.

[41] L. Infeld. The influence of the width of the gap upon the theory of antennas. *Q. Appl. Math*, 5:113–132, 1947.

[42] A.C. Kak, M. Slaney, IEEE Engineering in Medicine, and Biology Society. *Principles of computerized tomographic imaging*. IEEE Press, 1988.

[43] G. W. Kattawar and M. Eisner. Radiation from a homogeneous isothermal sphere. *Appl. Opt.*, 9(12):2685–2690, Dec 1970.

[44] K. Kohse-Hoinghaus and J.B. Jeffries. *Applied combustion diagnostics*. Combustion (New York, N.Y. : 1989). Taylor & Francis, 2002.

[45] Katharina Kohse-Höinghaus, Robert S. Barlow, Marcus Aldén, and Jürgen Wolfrum. Combustion at the focus: laser diagnostics and control. *Proc. Combust. Inst.*, 30(1):89 – 123, 2005.

[46] George A. Lavoie, John B. Heywood, and James C. Keck. Experimental and theoretical study of nitric oxide formation in internal combustion engines. *Combust. Sci. Technol.*, 1(4):313–326, 1970.

[47] S. C. Lee and C. L. Tien. Effect of soot shape on soot radiation. *J. Quant. Spectrosc. Radiat. Transfer*, 29(3):259 – 265, 1983.

[48] S.C. Lee and C.L. Tien. Optical constants of soot in hydrocarbon flames. *Symposium (International) on Combustion*, 18(1):1159 – 1166, 1981.

[49] Hua Li, Chao Liu, Lei Bi, Ping Yang, and George W. Kattawar. Numerical accuracy of equivalent spherical approximations for computing ensemble-averaged scattering properties of fractal soot aggregates. *Journal of Quantitative Spectroscopy and Radiative Transfer*, 111(14):2127–2132, September 2010.

[50] Björn-Eric Lindh. Scania fordonshistoria 1891-1991. *Streiffert*, 1992.

[51] Jing Lu, Chun Lou, and Huai-Chun Zhou. Experimental investigation on soot volume fraction in an ethylene diffusion flame by emission spectrometry without optically-thin assumption. *J. Phys. Conference Series*, 147(1):012084, 2009.

[52] Hongrui Ma. *Optical Diagnostics and Combustion Analysis in a Gasoline Direct Injection Engine*. PhD thesis, University of Oxford, 2006.

[53] Yukio Matsui, Takeyuki Kamimoto, and Shin Matsuoka. A study on the time and space resolved measurement of flame temperature and soot concentration in a d. i. diesel engine by the two-color method. Technical report, SAE, 1979.

[54] Yukio Matsui, Takeyuki Kamimoto, and Shin Matsuoka. A study on the application of the two color method to the measurement of flame temperature and soot concentration in diesel engines. Technical report, SAE, 1980.

[55] Gustav Mie. Beiträge zur optik trüber medien, speziell kolloidaler metallösungen. *Annalen der Physik*, 330(3):377–445, 1908.

[56] F. Migliorini, K. Thomson, and G. Smallwood. Investigation of optical properties of aging soot. *Appl. Phys. B: Lasers Opt.*, 104:273–283, 2011. 10.1007/s00340-011-4396-4.

[57] James A. Miller and Craig T. Bowman. Mechanism and modeling of nitrogen chemistry in combustion. *Progress in Energy and Combustion Science*, 15(4):287 – 338, 1989.

[58] Habib N Najm, Phillip H Paul, Charles J Mueller, and Peter S Wyckoff. On the adequacy of certain experimental observables as measurements of flame burning rate. *Combust. Flame*, 113(3):312 – 332, 1998.

[59] S. Pan and A. Kak. A computational study of reconstruction algorithms for diffraction tomography: Interpolation versus filtered-backpropagation. *Acoustics, Speech and Signal Processing, IEEE Transactions on*, 31(5):1262 – 1275, oct 1983.

[60] Robert J Pandya, Gina Solomon, Amy Kinner, and John R Balmes. Diesel exhaust and asthma: hypotheses and molecular mechanisms of action. *Environmental Health Perspectives*, 110:103–112, 2002.

[61] Rudolf B. Penndorf. Scattering and extinction coefficients for small absorbing and nonabsorbing aerosols. *J. Opt. Soc. Am.*, 52(8):896–902, Aug 1962.

[62] Gilbert N. Plass and George W. Kattawar. Monte carlo calculations of light scattering from clouds. *Appl. Opt.*, 7(3):415–419, Mar 1968.

[63] CA Pope and DW Dockery. Health effects of fine particulate air pollution: lines that connect. *J Air Waste Manag Assoc*, 56(6):709–42–, June 2006.

[64] Gerald M. Rassweiler and Lloyd Withrow. Motion pictures of engine flames correlated with pressure cards. Technical report, SAE, 1938.

[65] F. Reif. *Fundamentals of statistical and thermal physics*. McGraw-Hill series in fundamentals of physics. McGraw-Hill, 1965.

[66] K.E. Ritrievi, J.P. Longwell, and A.F. Sarofim. The effects of ferrocene addition on soot particle inception and growth in premixed ethylene flames. *Combust. Flame*, 70(1):17 – 31, 1987.

[67] F.G. Roper. The prediction of laminar jet diffusion flame sizes: Part i. theoretical model. *Combust. Flame*, 29:219 – 226, 1977.

[68] R. Ruiterkamp, T. Halasinski, F. Salama, B. H. Foing, L. J. Allamandola, W. Schmidt, and P. Ehrenfreund. Spectroscopy of large pahs. *Astron & Astrophys*, 390(3):1153–1170, 2002.

[69] R.J. Santoro, H.G. Semerjian, and R.A. Dobbins. Soot particle measurements in diffusion flames. *Combust. Flame*, 51:203 – 218, 1983.

[70] N. Saravanan and G. Nagarajan. An experimental investigation of hydrogen-enriched air induction in a diesel engine system. *International Journal of Hydrogen Energy*, 33(6):1769 – 1775, 2008.

[71] W. Schindler, C. Haisch, H. A. Beck, R. Niessner, E. Jacob, and D. Rothe. A photoacoustic sensor system for time resolved quantification of diesel soot emissions. Technical report, SAE, 2004.

[72] Gary S. Settles. *Schlieren and shadowgraph techniques: visualizing phenomena in transparent media*. Experimental fluid mechanics. Springer, 2001.

[73] H. J. Shafer. Physical optic analysis of image quality in schlieren photography. *Journal of SMPE*, 53, 1949.

[74] T. Shingagawa, T. Okumura, S. Furuno, and K-O. Kim. Effects of hydrogen addition to si engine on knock behaviour. Technical report, SAE, 2004.

[75] J.O. Smith. *Spectral audio signal processing*. W3K Publishing, 2007.

[76] Kermit C. Smyth and Christopher R. Shaddix. The elusive history of m=1.57-0.56i for the refractive index of soot. *Combust. Flame*, 107(3):314 – 320, 1996.

[77] David Snelling, Kevin Thomson, Gregory Smallwood, O. Gulder, E. Weckman, and R. Fraser. Spectrally resolved measurement of flame radiation to determine soot temperature and concentration. *AIAA Journal*, 40(9):1789–1795, 2002.

[78] C. M. Sorensen. Light scattering by fractal aggregates: A review. *Aerosol Science and Technology*, 35(2):648–687, 2001.

[79] T. Suzuki and Y. Sakurai. Effect of hdyrogen rich gas and gasoline mixed combustion on spark ignition engine. Technical report, SAE, 2006.

[80] J.P.R. Symonds, P. Price, and P.I. Williamsand R. Stone. Density of particles emitted from a gasoline direct injection engine. Technical report, 12th ETH-Conference on Combustion Generated Nanoparticles, 2008.

[81] Y. Takeuchi, S. Hirano, M. Kanauchi, H. Ohkubo, M. Nakazato, M. Sutherland, and W. Can Dam. The impact of diesel engine lubricants on deposit formation in diesel particulate filters. Technical report, SAE, 2003.

[82] K. A. Thomson, O. L. Gulder, E. J. Weckman, R. A. Fraser, G. J. Smallwood, and D. R. Snelling. Soot concentration and temperature measurements in co-annular, non-premixed ch4/air laminar flames at pressures up to 4 mpa. *Combustion and Flame*, 140(3):222–232, February 2005.

[83] C.L. Tien and S.C. Lee. Flame radiation. *Progress in Energy and Combustion Science*, 8(1):41 – 59, 1982.

[84] K.S. Varde and G.A. Frame. Hydrogen aspiration in a direct injection type diesel engine-its effects on smoke and other engine performance parameters. *International Journal of Hydrogen Energy*, 8(7):549 – 555, 1983.

[85] Michael Vollmer and Klaus-Peter Mollmann. High speed and slow motion: the technology of modern high speed cameras. *Physics Education*, 46(2):191, 2011.

[86] A. T. Wassel and D. K. Edwards. Molecular gas radiation in a laminar or turbulent pipe flow. *J Heat Transfer*, 98(1):101–107, 1976.

[87] P. Weilmunster, A. Keller, and K.-H. Homann. Large molecules, radicals, ions, and small soot particles in fuel-rich hydrocarbon flames: Part i: positive ions of polycyclic aromatic hydrocarbons(pah) in low-pressure premixed flames of acetylene and oxygen. *Combustion and Flame*, 116(12):62–83, January 1999.

[88] M. Wirth, D. Zimmermann, R. Friedfeldt, J. Caine, A. Schamel, M. Davies, G. Peirce, A. Storch, K. Ries-Muller, K.P. Gansert, G. Pilgram, R. Ortmann, G. Wurfel, and J. Gerhardt. A cost optimised gasoline spray guided direct injection system for improved fuel economy. Technical report, IMech Fuel Economy and Engine Downsizing, 2004.

[89] W. J. Wiscombe. Improved mie scattering algorithms. *Appl. Opt.*, 19(9):1505–1509, May 1980.

[90] Jingde Yan and Gary L. Borman. Analysis and in-cylinder measurement of particulate radiant emissions and temperature in a direct injection diesel engine. Technical report, SAE, 1988.

[91] J. Zeldovich. The oxidation of nitrogen in combustion and explosions. *Eur. Phys. J. A*, 21:577–628, 1946.

[92] Hua Zhao and Nicos Ladommatos. *Engine combustion instrumentation and diagnostics*. SAE International, 2001.